



HAL
open science

Study of reservoir analogues in foreland fold-and-thrust belts: sedimentology, diagenesis, deformation and fracturing of the upper cretaceous-eocene carbonate systems of the ionian zone (Southern Albania)

Nadège Vilasi

► **To cite this version:**

Nadège Vilasi. Study of reservoir analogues in foreland fold-and-thrust belts: sedimentology, diagenesis, deformation and fracturing of the upper cretaceous-eocene carbonate systems of the ionian zone (Southern Albania). Sciences of the Universe [physics]. École Nationale Supérieure des Mines de Paris, 2009. English. NNT: . pastel-00006128

HAL Id: pastel-00006128

<https://pastel.hal.science/pastel-00006128>

Submitted on 8 Jun 2010

HAL is a multi-disciplinary open access archive for the deposit and dissemination of scientific research documents, whether they are published or not. The documents may come from teaching and research institutions in France or abroad, or from public or private research centers.

L'archive ouverte pluridisciplinaire **HAL**, est destinée au dépôt et à la diffusion de documents scientifiques de niveau recherche, publiés ou non, émanant des établissements d'enseignement et de recherche français ou étrangers, des laboratoires publics ou privés.



ED n°398 – Géosciences et Ressources Naturelles, Paris

N° attribué par la bibliothèque

□□□□□□□□□□□□□□□□

T H E S E

pour obtenir le grade de
Docteur de l'École des Mines de Paris
Spécialité “Dynamique et Ressources des Bassins Sédimentaires”

présentée et soutenue publiquement par
Nadège VILASI

le 6 Novembre 2009

Etude d’analogues de réservoirs dans les chaînes plissées et leurs avant-pays : Sédimentologie, diagenèse, déformation et fracturation des systèmes carbonatés crétacés supérieurs - éocènes du Bassin Ionien (Albanie méridionale)

Jury

M. Noël VANDENBERGHE Président
M. Manuel SINTUBIN Rapporteur
M. Philippe MUCHEZ Rapporteur
M. Kristaq MUSKA Examineur
M. François ROURE Encadrant industriel
M. Rudy SWENNEN Directeur
M. Bernard BEAUDOIN Directeur

Acknowledgements / Remerciements

Ce n'est pas vraiment facile de faire une liste des personnes à remercier, tellement elle serait longue, mais je vais faire de mon mieux, en espérant oublier personne....

Merci Rudy pour la confiance et la liberté que tu m'as montrées durant ces 4 années de thèse. Ces moments en quête d'idées innovatrices ont parfois été difficiles à gérer, notamment lorsque l'inspiration ne vient pas, mais à présent, je t'en remercie. Peut être est ce là le secret de l'épanouissement personnel et intellectuel? Merci également de m'avoir montré autant d'enthousiasme à écrire des articles, de m'avoir encouragée à diffuser mes résultats lors de conférences internationales et surtout en anglais! Grâce à toi, j'ai pu découvrir une discipline fascinante qu'est la diagenèse.

A présent, je tiens à te remercier, François, pour tout ce que tu m'as apporté durant ces 4, ou devrais je dire, ces 6 dernières années. Depuis mon master, tu m'as transmis ton optimisme et ta volonté à toujours aller plus loin. Puis en thèse, tes conseils ont toujours été très constructifs et ont largement contribué à améliorer la qualité de mes résultats. Merci également pour la qualité du contact humain qui a été une constante depuis le début de mes travaux au sein de ton équipe.

Je remercie également Bernard Beaudoin pour m'avoir soutenue depuis mon master et permis d'obtenir une cotutelle avec l'Ecole des Mines de Paris (GRN-Paris) qui a été très bénéfique pour mon développement personnel.

Je souhaite aussi remercier les membres du jury, Prof. Philippe Muchez, Prof. Manuel Sintubin, Prof. Noël Vandenberghe, Dr. Kristaq Muska, pour avoir évalué mon travail. Leurs commentaires et corrections ont grandement augmenté la qualité de mon manuscrit.

Un grand merci à toute l'équipe albanaise pour m'avoir tant aidée sur le terrain. Vous m'avez suivi à travers mes diverses périples, vous m'avez transmis toutes vos expériences et connaissances tout en me faisant découvrir votre magnifique pays. Pour tout cela, je remercie spécialement Ajet Mezini, Teuta Shehu et Kristaq Muska ainsi que l'Institut Albanais du Pétrole à Fieri. Vous m'avez été d'une grande aide et j'en garde des anecdotes mémorables.

Pour m'avoir acceptée au sein du département de Géologie-Géochimie-Géophysique de l'IFP, je voudrais remercier Bernard Coletta.

Je tiens à remercier également les personnes ne faisant pas partie intégrante de mon projet, mais qui m'ont grandement aidé à l'améliorer. Je pense tout spécialement à Nicole Guilhaumou, pour m'avoir fait partager son amour des inclusions fluides et à Olivier Lacombe, qui a tant bien que mal essayé de me former sur les macles de la calcite! Désolée Olivier, après avoir passé de longues années à regarder des inclusions, mes yeux n'ont pas pu suivre avec les macles

Pour le côté pratique, je tiens à remercier Herman Nijs et Danny Coetermanns à Leuven pour m'avoir fourni des lames minces impeccables et suivie dans mes analyses géochimiques. Merci aussi à Dirk pour son support informatique.

Thank you, Dr. Joachimsky, for the stable isotope analyses and Rob Ellam for the Sr-isotope analyses. They have been very helpfull. Merci également à Jacques Wautier de l'Université de Louvain. Les nombreuses analyses réalisées à la microsonde ont été déterminantes dans ma thèse.

Ces 2 années de thèse à Leuven et 2 années à l'IFP n'auraient jamais été aussi enrichissantes d'un point de vue professionnel et personnel sans la présence de nombreuses personnes que j'aimerais remercier à présent : la partie « Belgique » avec Helga, Liesbeth, Ben, Pieter, Eva, Gilles et le reste du groupe. Vous avez été d'un grand soutien et support, notamment pour comprendre le néerlandais! Puis le groupe de l'IFP, avec Laure, Nico, Raymi, Khalid, Humberto et Esmeralda Nos pauses café resteront mémorables. Un immense merci à Jean-Paul Callot « l'Expert en Ceressitude! », Benoît Vincent « le diagenetiste », Fadi Nader « le roi de la dolomie », Martin, qui m'a bien fait gagné du temps avec FIT, et aux départements de Sédimentologie et de Géologie Structurale de l'IFP.

Je ne m'en serais jamais sortie toute seule avec Ceres, sans le soutien informatique de Hervé Devoitine, Catherine Marquer et Isabelle Faille. Grâce à vous, j'y suis arrivée !

Comment se seraient passées ces 4 années sans l'aide administrative de Meriem Jehl, Odile Correia, Katrien Smeets, Dovy Tristani, Dominique Vassiliadis et de Marie-Claude Bastok ? Votre aide et votre soutien a été plus que nécessaire. Merci également aux écoles doctorales, qui m'ont permis de faire de nombreuses rencontres et suivre de nombreux cours, très enrichissants d'un point vue personnel et professionnel : Géosciences et Ressources Naturelles (Paris), ADIFP (Rueil-Malmaison) et Leuven Arenberg Doctoral School.

Enfin mes derniers remerciements reviennent à mes parents, ma sœur, et famille, pour m'avoir toujours soutenue, aidée à passer les moments les plus difficiles durant mes études mais qui, malgré tout, ont toujours cru en moi. J'espère qu'à présent, ils comprendront mieux ce qu'est mon métier et qu'ils ne me ramèneront plus des « cailloux » de vacances ! Une petite dédicace également pour Alexia, Armelle et Caro, sans qui peut-être cette aventure n'aurait jamais débutée !

Merci Rémy, pour toute la patience et le soutien que tu m'as témoigné dans les moments les plus difficiles et les plus heureux de ma thèse, mes weekends devant mon pc, mes insomnies, mon stress avant mes conférences. Tu m'as accompagné tout au long de cette aventure et tu as toujours cru en moi. Merci !

Abstract

Although Albania constitutes a relatively small country, it displays a unique petroliferous foreland fold-and-thrust belt (FTB) system. The Albanian fold-and-thrust belt and the Peri-Adriatic Depression are well documented by seismic reflection profiles, GPS reference points, potential data, wells and outcrops. The continuous Oligocene to Plio-Quaternary sedimentary record helps to constrain both the burial history of Mesozoic carbonate reservoirs, the timing of their deformation, and the coupled fluid flow and diagenetic scenarios. Since the mid-90's, the Albanian foothills were used as a natural laboratory to develop a new integrated methodology and work flow for the study of sub-thrust reservoir evolution, and to validate on real case studies the use of basin modelling tools as well as the application of new analytical methods for the study of petroleum systems in tectonically complex areas. The integration of the interactions between petrographic and microtectonic studies, kinematic, thermal and fluid flow basin modelling, is described in detail. The main results of this collaborative study involving scientists from various European countries outline the benefits that any Earth Science project could gain in integrating various techniques and expertise, especially when dealing with sedimentary basins where both deep and shallow processes are involved.

The objective of this PhD is to give a better understanding of the mechanisms and timing of fracturing and fluid flow during the Albanides evolution. Results from structural analyses and petrographic investigations in three selected case studies, which are considered as reservoir analogues for neighboring reservoirs situated in the Ionian Zone, are presented. Their study allows to work out a three dimensional picture of the reservoir features and processes that control porosity and permeability. These analyses have been performed on cemented fractures in the Upper Cretaceous to Eocene deep water carbonates, considered as the best carbonate reservoir intervals in the Mediterranean zone. The results are subsequently replaced into the deformation history of the area in order to place the different fluid migrations into their geological context.

Albania represents a part of the wider Circum-Mediterranean Peri-Tethyan thrustbelts and constitutes a key area for the study of petroleum systems in foothills and thrust front domains (Van Geet et al., 2002). The Ionian tectonic zone corresponds to a foreland fold-and-thrust belt, characterised by a west verging thrusting over the Adriatic foreland. It corresponds to a complex tectonic assemblage, made up of thin-skinned allochthonous units, progressively emplaced during the Neogene deformations. The major décollement level consists of the Triassic evaporites and the major structural fault zones possess a NNW-SSE alignment.

The tectonic evolution of the Albanides included a Middle Liassic–Late Cretaceous phase of oceanic rifting accompanied by a passive margin formation and is divided into two major divisions: the internal and external Albanides. The external zone consists of two platform areas (Sazani and Kruja), which are separated by the Ionian Basin, i.e. the area studied. This basin can be split into three belts: the Berati, the Kurveleshi and the Cika belts. It consists of Triassic evaporite-carbonate and Jurassic to Eocene carbonate sequences in a syn-rift and post-rift setting, covered by Lower Tertiary flysch and/or Neogene clastic deposits. The northern part of the Ionian Zone is marked by the Vlora-Elbasan transfer zone, along which most of the oil and gas fields occur in both carbonate and clastic reservoirs. Their storage is largely improved by the presence of a dual matrix/fracture porosity system. At this place, the Ionian Zone plunges below the Peri-Adriatic Depression (Roure et al., 1995).

The first area studied is located near the hanging-wall of the Berati belt and is made up of Paleocene to Eocene pelagic carbonates. The fracturing of the reservoir interval has a pre-folding origin and relates to the regional flexuring in the foreland. The first recorded cement, postdating the burial stylolites development, has a meteoric signature, implying downward migration and the development of an earlier forebulge in the Ionian Basin. This fluid, which precipitates at a maximum depth of 1.5 km, is highly enriched in strontium with values up to 6960 ppm, attesting for important fluid-rock interaction with the Triassic evaporites, located in diapirs. From this stage, the horizontal tectonic compression increases and the majority of the fluid migrated under high pressure, characterised by brecciated and crack-seal veins. The tectonic burial increased up to 6 km due to the overthrusting that is pointed out

by the increase of the precipitation temperature of the cements. Afterwards, upward migration of SO_4^{2-} , Ba^{2+} and Mg^{2+} -rich fluids, which migrated probably along the décollement level, allow a precipitation in thermal disequilibrium. This period corresponds to the out-of-sequence development of the Berati belt from the Upper Miocene onward, implying the onset of its uplift. From shallower depth to the subsurface, the circulation of meteoric fluid likely develops a selective karstification.

The second area studied is situated in the most western belt, i.e. the Cika belt, and consists of the Saranda anticline, characterised by a NNW-SSE oriented fold hinge. The core of the anticline is made up of Jurassic to Lower Cretaceous carbonates and the flanks consist of Upper Cretaceous to Eocene highly fractured deep marine carbonates. The fracturing of the reservoir interval in the Cika belt has also a pre-folding origin, associated to the flexuring of the foreland during the Lower to Middle Oligocene (Nieuwland et al., 2001). The next fracturing stages are associated to the folding of the area and the subsequent cementations record its progressive burial, indicated by a decrease of the O-isotopic signatures from -1 to -13‰ V-PDB, which is directly related to an increase of the precipitation temperature. This period is also characterised by the development of a conjugated system of tectonic stylolites. From the Serravalian onward, the thrusting phase implies the uplift of the anticline towards the subsurface and the erosion of the Oligocene flysch and the Neogene molasse. The last stage corresponds to the emersion of the anticline and the migration of meteoric fluid into the carbonate system through re-opened fractures. A last tectonic reactivation implies the overthrusting of the western flank on the eastern side. During the Albanide FTB development, no overpressuring period has been recorded in the Saranda area. Moreover some fluids, which migrated during the folding, contain non-euhedral barite, likely originating from the Neogene molasse. This likely suggests downward migration.

The Kremenara anticline, located in the northern part of the Kurveleshi belt at the vicinity of the Vlora-Elbasan transfer zone, has the particularity to demonstrate oil seeps in a dual matrix-fracture porosity system. This anticline is characterised by a NNE-SSW oriented fold hinge, which does not describe the specific NNW-SSE orientation of the main structural features occurring in the Ionian Basin. Here, the main fracturing stages have a post-folding origin and the fractures relate mainly to two main principal stresses σ_1 , oriented N110° and N70°. This area studied is characterised by an early folding and the migration of meteoric fluid, which precipitated non-luminescent calcite cement. The post-folding stage is characterised by a second burial stage, caused by an increase of the sedimentary overburden, and the development of two main overpressuring regimes. The latter compressions are pointed out by the occurrence of crack-seal and brecciated veins, which respectively relate to N110°- and N70°-oriented compressions. An interaction with an evaporitic interval has also been suggested by the less negative and positive O-isotopic signature of the crack-seal veins. From the Serravalian, the N70°-oriented compression developed NNW-SSE transversal faults, which compartmentalise the anticline. Then, an E-W compression generated an overthrusting of the anticline towards the south-west. This period is likely associated to the out-of-sequence development of the Berati belt. The reorientation of the compression during the last stage may be associated to the vicinity of the Vlora-Elbasan transfer zone (Swennen et al., 1998). The Kremenara anticline was not buried deeply, since the Kurveleshi belt has been uplift early in the Albanide development. This is in agreement with the O-isotopic signatures, which plot down to -5‰ V-PDB, and is close to the signature of the Upper Cretaceous to Eocene host-rocks.

The fluid flow modelling allowed to reconstruct the hydrocarbon generation and migration but also to trace the changes in the water flow through time (origin, migration pathways and velocity). The third utility consists of determining the evolution of the overpressuring periods through time and space and then to correlate them to the overpressuring periods determined by studying the fracture-fillings. This will help to place the diagenetic evolution in the tectonic evolution of the FTB. The main results of the hydrocarbon fluid flow modelling show that the Upper Cretaceous-Eocene carbonate reservoirs in the Ionian zone have been charged from the Tortonian onward, and that meteoric fluid migration should have intensely biodegraded the hydrocarbon in place. Concerning the migration paths, it has been demonstrated that the thrusts act principally as flow barriers in Albania, mainly due the occurrence of evaporites (non-permeable), except in the foreland, where they do not occur. The results of the modelling demonstrate that the water migrations are dominantly vertical during the flexure of the

foreland. Then the increase of the sedimentary overburden and the thrusting of the units imply upward water migration under high pore fluid pressure. The development of a high topographic relief caused large downward and lateral meteoric fluid flow, which is characterised by higher velocities. From the thrusting phase onward, the faults act as flow barriers, due to the occurrence of evaporites along the décollement levels and compartmentalise the reservoir interval.

Samenvatting

Ondanks dat Albanië een relatief klein grondgebied bestrijkt, omvat het een vrij unieke olieprovincie in de Albanide voorland plooi- en breukgordel. Dit laatste gebied alsook de Peri-Adriatische Depressie zijn goed gedocumenteerd in seismische reflectie profielen, door middel van GPS referentiepunten, potentiaal data, boringen en ontsluitingen. De continue Oligocene tot Plio-Kwartaire sedimentaire successie laat toe de begravingsgeschiedenis van de Mesozoïsche carbonaat reservoirs te reconstrueren, alsook de periode van deformatie, de gekoppelde fluïdacirculaties en de diagenese te achterhalen. Sinds midden de jaren 90, werden de Albanese “foothills” intens gebruikt als natuurlijk laboratorium om een nieuw geïntegreerde methodologie en werkschema te ontwikkelen betreffende reservoir evolutie in “sub-thrust” exploratie scenario’s. Tevens werd dit gebied gebruikt als een reëel geval om verbeterde bekkenmodelerprogramma’s en nieuwe analytische methodologieën voor de studie van petroleum systemen in tektonisch complexe gebieden te ontwikkelen en te testen.

De voornaamste resultaten van deze studie, waarin wetenschappers van verscheidene Europese onderzoeksinstituten participeerden, tonen aan dat, voor complexe aardwetenschappelijke studies in gedeformeerde sedimentaire bekkens, waar diepe en ondiepe processen optraden, een integratie van verschillende technieken en expertisen steeds een meerwaarde geeft.

De doelstellingen van deze doctoraatsstudie bestaat erin de processen en tijdsrelaties tussen fracturatie en fluïdastromingen in de evolutie van de Albanides te achterhalen. De integratie van petrografische en microtectonische data en kinematische, thermische en fluïdastromingsmodellen in bekken modelleringen wordt dan ook in dit werk in detail beschreven. Resultaten van de structurele analyse en petrografische studie van 3 geselecteerde gevallenstudies, die als analogen beschouwd kunnen worden voor nabijgelegen reservoirs in de Ionische Zone, worden besproken. Onderzoek in deze 3 gebieden liet toe om een drie dimensioneel beeld van de reservoir karakteristieken en processen, die een controle uitoefenen op porositeit en permeabiliteit, te verkrijgen. De analyses werden doorgevoerd op gecementeerde aders in Boven Krijt tot Eocene diep water carbonaten, die als voornaamste reservoirgesteenten gerekend worden in het Mediterrane gebied. Deze resultaten werden vervolgens geplaatst in de deformatiegeschiedenis van het studiegebied met de bedoeling de fluïdamigraties in hun geologische context te plaatsen.

Albanië vormt deel van de Circum-Mediterrane Peri-Tethisch gebergtegordel en vormt een sleutelgebied wat de studie van petroleum systemen in “foothills” en overschuivingszones betreft (Van Geet et al., 2002). De Ionische tektonische zone correspondeert met een voorland plooi- en breukgordel, dat gekarakteriseerd wordt door west-vergente overschuivingen over het Adriatische voorland. Het vormt een complexe tektonische assemblage, dat opgebouwd wordt uit “thin-skinned” allochthone eenheden, die progressief gevormd werden gedurende de Neogene deformatiegeschiedenis. Het voornaamste décollement niveau bestaat uit Trias evaporieten en de voornaamste breukzones bezitten een NNW-SSE oriëntatie.

De tektonische evolutie van de Albaniden bestaat uit een Midden Lias–Laat Krijt fase van oceanische rifting dat gepaard ging met een passieve rand ontwikkeling en dat opgedeeld kan worden in twee gebieden, namelijk de interne en externe Albaniden. De externe zone bestaat op zijn beurt uit twee platformgebieden (Sazani en Kruja), die van elkaar gescheiden worden door het Ionische Bekken, zijnde het gebied dat onderzocht werd. Dit bekken kan opgesplitst worden in drie orogene gordels, met name de Berati, de Kurveleshi en de Cika gordel. Deze bestaan uit Trias evaporiet-carbonaat en Jura tot Eocene carbonaat sequenties die gevormd werden in een syn-rift tot post-rift omgeving, en die bedekt worden door Onder Tertiaire flysch en/of Neogene klastische afzettingen. Het noordelijke deel van de Ionische Zone wordt gekenmerkt door de “Vlora-Elbasan transfer zone”, waarlangs de meeste olie- en gasvelden in zowel carbonaat en klastische reservoirgesteenten zich bevinden. Hun reservoircapaciteit bestaat uit een duaal matrix/fracturatie porositeitssysteem. Nabij deze “transfer zone” duikt de Ionische Zone onder de Peri-Adriatische Depressie (Roure et al., 1995).

Het eerste studiegebied situeert zich in de “hanging-wall” van de Berati gordel en bestaat uit Paleocene tot Eocene pelagische carbonaten. De fracturatie van het reservoir interval heeft een pre-

ploofase oorsprong en kan gerelateerd worden aan de regionale flexuratie van het voorland. Het eerste cement, dat volgt na de ontwikkeling van de begravingsstylolieten, heeft een meteorische signatuur. Dit impliceert een benedenwaartse migratie van fluïda gedurende de vroege voorploofase van het Ionische Bekken. Dit fluïdum, dat precipiteerde op een maximum diepte van 1.5 km, is sterk aangerijkt aan strontium met waarden tot en met 6960 ppm, wat op een belangrijke fluïda-gesteente interactie met Trias evaporieten, gelokaliseerd in diapieren, wijst. De horizontale tektonische compressie neemt vanaf dit stadium toe en de meerderheid van de fluïdamigratie gebeurde vanaf dan onder overdruk, wat aanleiding kan worden uit de gebreccieerde en “crack-seal” aderopvullingen. De begraving ten gevolge van overschuivingstektoniek, zoals afgeleid uit de precipitatie temperatuur van de cementen nam toe tot 6 km. Vervolgens trad er een opwaartse migratie van SO_4^{2-} , Ba^{2+} and Mg^{2+} -rijke fluïda plaats. Dit gebeurde waarschijnlijk langsheen de décollement niveaus, met calciet precipitatie in een thermaal onevenwichtssituatie. Deze periode correspondeert met de “out-of-sequence” ontwikkeling van de Berati gordel vanaf het Boven Mioceen, met de aanvang van opheffing als gevolg. Ondiepe tot diepe circulatie van meteorisch water gaf finaal aanleiding tot selectieve karstificatie.

Het tweede studiegebied situeert zich in de meest westelijke orogene zone, namelijk de Cika gordel. Het bestaat uit de Saranda anticline, welke gekarakteriseerd wordt door een NNW-SSE georiënteerde anticlinaire as. De kern van de anticline wordt opgebouwd uit carbonaten van Jura tot Onder Krijt en de flanken bestaan uit Boven Krijt tot Eocene intens gefractureerde diep marine carbonaten. De fracturatie van het reservoir interval in de Cika gordel heeft een pre-plooiingsoorsprong, en kan geassocieerd worden met de flexuratie van het voorland gedurende de Onder tot Midden Oligoceen (Nieuwland et al., 2001). De hierna volgende fracturatiefasen kunnen geassocieerd worden met de plooiing van het gebied en de aansluitende cementatie reflecteert een progressieve begraving. Dit wordt afgeleid uit de afname van de O-isotopische signatuur gaande van -1 tot -13‰ V-PDB, dat rechtstreeks gerelateerd lijkt te zijn aan een toename van de precipitatie temperatuur. Deze periode wordt ook gekarakteriseerd door de ontwikkeling van een geconjugeerd systeem van tektonische stylolieten. Vanaf het Serravaliaan veroorzaakt de overschuivingstektoniek de opheffing van de anticline tot nabij het oppervlak met de erosie van de Oligocene flysch en de Neogene molasse. De laatste diagenese fase correspondeert met de emersie van de anticline en de migratie van meteorische fluïda in het carbonaatsysteem langsheen gereactiveerde fracturaties. Een finale tektonische reactivatie gaat gepaard met de overschuiving van de westelijke flank van de anticline over de oostelijke zijde. Gedurende de Albanide plooi- en breukgordel ontwikkeling werd in dit studiegebied, in tegenstelling met de andere studiegebieden, geen overdruk ontwikkeling vastgesteld. Verder komen er aders voor, die gevormd werden tijdens de ploofase, welke niet-euhedrale barriet bevatten die naar alle waarschijnlijkheid hun oorsprong vinden in fluïda interactie met Neogene molasse sedimenten. Dit zou dan wijzen op een neerwaartse fluïda migratie.

De Kremenara anticline, zijnde het derde studiegebied, is gelokaliseerd in het noordelijke deel van de Kurveleshi belt nabij de “Vlora-Elbasan transfer zone”. Deze anticline bezit als eigenaardigheid de aanwezigheid van olie “seeps” in een duaal matrix-fracturatie porositeitssysteem. Deze anticline wordt gekarakteriseerd door een NNE-SSW georiënteerde plooi-as, die afwijkt van de gebruikelijke NNW-SSE oriëntatie van de voornaamste structurele structuren van het Ionische Bekken. De voornaamste fracturatie gebeurtenissen hebben een post-plooiingsoorsprong en de fracturaties kunnen voornamelijk gerelateerd worden aan de twee voornaamste stressregimes met een respectievelijke s_1 oriëntatie van $N110^\circ$ en $N70^\circ$. Dit studiegebied wordt gekenmerkt door een vroege plooiing en de migratie van meteorische fluïda, die aanleiding gaven tot de vorming van een niet-luminescerend calciet cement. De post-plooiingsfase wordt gekarakteriseerd door een tweede begravinggeschiedenis, veroorzaakt door de toename van de sedimentaire bedekking alsook door de ontwikkeling van een tweede overdruk periode. Een latere compressie wordt gereflecteerd door de ontwikkeling van “crack-seal” en gebreccieerde aders, die respectievelijk wijzen op een $N110^\circ$ - en $N70^\circ$ -georiënteerde compressie. Een interactie met een evaporitisch interval wordt gesuggereerd op basis van de positieve O-isotopische signatuur van de “crack-seal” aders. Vanaf het Serravaliaan ontstonden NNW-SSE transversale breuken ten gevolge van de $N70^\circ$ -georiënteerde compressie, die aanleiding gaf tot een compartimentalisatie van de anticline. Een latere E-W compressie veroorzaakte een overschuiving van de anticline in een zuidwestwaartse richting. Deze periode is naar alle waarschijnlijkheid geassocieerd

met een “out-of-sequence” ontwikkeling van de Berati gordel. De reorientatie van de compressie gedurende de laatste periode is mogelijk veroorzaakt door de nabijheid van de “Vlora-Elbasan transfer zone” (Swennen et al., 1998). De Kremenara anticline was nooit diep begraven, aangezien de Kurveleshi gordel vroegtijdig omhoog geheven werd tijdens de ontwikkeling van de Albaniden. Dit is in overeenstemming met de O-isotopische signaturen, die plotten tot waarden van -5‰ V-PDB, welke dichtbij de signatuur liggen van de Boven Krijt en Eocene moedergesteenten.

De modellering van de fluïdastromingen liet niet alleen toe de koolwaterstofgeneratie en -migratie, maar ook om de waterstromingen doorheen de tijd (origine, migratie paden en snelheden) te reconstrueren. Een bijkomend nut van deze modelleringen bestaat erin de overdruk periodes doorheen de tijd en ruimte te achterhalen en deze te correleren met de overdruk periodes zoals gedetermineerd op basis van de studie van de aderopvullingen. Dit liet toe een verfijnde diagenetische evolutie uit te werken en deze te koppelen aan de tektonische evolutie van het plooi- en breukgordel gebied. Het voornaamste resultaat van de modellering in verband met de koolwaterstofmigratie toont aan dat de Boven Krijt - Eocene carbonaat reservoirs van de Ionische zone opgevuld geraakten vanaf het Tortoniaan, en dat meteorische fluïdamigratie een belangrijke in situ biodegradatie van de koolwaterstoffen heeft veroorzaakt. Betreffende de migratiepaden kon aangetoond worden dat de overschuivingen vooral als stromingsbarrières fungeerden in Albanië, voornamelijk ten gevolge van de aanwezigheid van (niet-permeable) evaporieten, met uitzondering echter van in het voorland gebied, waar deze evaporieten niet voorkomen. Het resultaat van de modellering toont aan dat de watermigraties dominant vertikaal georiënteerd waren gedurende de flexuratie van het voorland. De toename van sedimentaire bedekking en van de overschuivingseenheden alsook de breukplaatsname van de eenheden impliceert een opwaartse watermigratie onder hoge poriewaterdruk. De ontwikkeling van een hoog topografisch reliëf veroorzaakte een naar beneden georiënteerde en laterale meteorische stroming, welke gekarakteriseerd wordt door hoge stroomsnelheden. Vanaf de overschuivingsfase traden de breuken eerder op als stromingsbarrières, dit ten gevolge van de aanwezigheid van evaporieten langsheen deze décollement niveaus met een compartimentalisatie van het reservoir interval tot gevolg.

Table of contents

ACKNOWLEDGEMENTS / REMERCIEMENTS.....	I
ABSTRACT.....	III
SAMENVATTING.....	VII
TABLE OF CONTENTS.....	XI
TABLE OF ILLUSTRATIONS.....	XV
CHAPTER 1- INTRODUCTION.....	1
CHAPTER 2- GEOLOGICAL SETTING.....	5
2.1- TECTONOSTRATIGRAPHY OF THE ALBANIDES.....	5
2.1.1- The inner Albanides.....	6
2.1.2- The outer Albanides.....	7
2.1.2.1- Krasta-Cukali Zone: deep-water passive margin.....	8
2.1.2.2- Kruja Zone: marginal shallow-water carbonate platform.....	8
2.1.2.3- Ionian Zone: deep water carbonates.....	9
2.1.2.4- Peri-Adriatic Depression.....	9
2.1.2.5- Sazani Zone: Apulian carbonate platform.....	9
2.2- SEDIMENTOLOGICAL AND LITHO-STRATIGRAPHICAL CONTEXT OF THE IONIAN BASIN.....	9
2.3- GEODYNAMICAL BACKGROUND.....	10
2.3.1- Evolution of the Tethyan passive margin and deposition of carbonates.....	10
2.3.2- Foothills development and sedimentary records of the deformation.....	10
2.3.3- Kinematic evolution.....	12
2.4- DÉCOLLEMENT LEVEL.....	12
2.5- THE TRIASSIC INTERVAL: A MAJOR INTEREST FOR PETROLEUM EXPLORATION.....	13
2.5.1- Evaporitic occurrences.....	14
2.5.2- Dolomitic intervals.....	15
CHAPTER 3- PETROLEUM SETTING.....	17
3.1- HISTORY OF PETROLEUM EXPLORATION.....	17
3.2- SOURCE ROCKS.....	17
3.3- RESERVOIRS.....	19
3.4- SEALS.....	20
CHAPTER 4- METHODOLOGY.....	23
4.1- RESEARCH STRATEGY.....	23
4.2- FIELDWORK AND SELECTED CASE STUDIES.....	24
4.3- FRACTURE CHARACTERISATION.....	26
4.4- PETROGRAPHY.....	26
4.4.1- Conventional microscopy.....	26
4.4.2- Cathodoluminescence.....	27
4.4.2.1- "Cold cathodoluminescence microscopy".....	27
4.4.2.2- "Hot cathodoluminescence microscopy".....	27
4.4.3- Scanning Electron Microscope.....	28
4.5- PETROPHYSIC PROPERTIES.....	28
4.6- GEOCHEMISTRY.....	28
4.6.1- Carbon and oxygen isotope analysis.....	28
4.6.2- Sr isotope analysis.....	30
4.6.3- Major to trace elemental analyses.....	30
4.6.3.1- Absorption Atomic Spectroscopy (AAS).....	31
4.6.3.2- Microprobe analysis.....	31
4.7- MICROTHERMOMETRY.....	32

4.8- CONCLUSION	32
CHAPTER 5- DIAGENESIS AND FRACTURING IN THE BERATI BELT: CASE STUDY OF THE KELCYRA OUTCROP	33
5.1- SEDIMENTOLOGY	33
5.1.1- Macroscopic observations	33
5.1.2- Microscopic observations.....	35
5.2- STRUCTURAL ANALYSES	38
5.2.1- Stylolites.....	38
5.2.2- Fracture development	38
5.3- PALEOFLUID CHARACTERISATION	41
5.3.1- Petrography and structural data	41
5.3.1.1- Cal-1 cement.....	41
5.3.1.2- Cal-2a cement.....	41
5.3.1.3- Cal-2b cement and Dol-1 dolomite.....	42
5.3.1.4- Cal-3 cement.....	43
5.3.1.5- Cal-4 cement.....	53
5.3.1.6- Cal-5 cement.....	53
5.3.1.7- Cal-6 cement.....	53
5.3.1.8- Dol-3 cement	53
5.3.1.9- Cal-7 cement.....	53
5.3.2- Stables isotopes	54
5.3.3- Elemental geochemistry	56
5.3.3.1- Calcite cements.....	56
5.3.3.2- Dolomite and barite phases.....	58
5.3.4- Strontium isotopes.....	60
5.3.5- Fluid inclusions	62
5.3.5.1- Results of Cal-2b vein	62
5.3.5.2- Results of Cal-3 vein	63
5.3.5.3- Results of Cal-7 vein	64
5.4- INTERPRETATION	64
5.4.1- Evidences of evaporitic interactions	64
5.4.2- Early marine process	66
5.4.3- Compaction and fracturing	66
5.4.4- Early meteoric fluid.....	66
5.4.5- First main compressive stress	69
5.4.6- Evidences of a second overpressure regime	71
5.4.7- Change of the main tectonic stress	72
5.4.8- Dolomitic fluid, Dol-3.....	72
5.4.9- Late calcite cement	73
5.4.10- Selective dissolution stage.....	73
5.5- CONCLUSIONS	74
5.5.1- Evolution of the fluid flow versus kinematic evolution.....	74
5.5.2- Characterisation of the evaporitic interactions	75
CHAPTER 6- DIAGENESIS AND FRACTURING IN THE CIKA BELT: THE SARANDA ANTICLINE CASE STUDY	77
6.1- GENERAL CHARACTERISTICS	78
6.1.1- Description of the studied areas (macroscopic observations).....	78
6.1.2- Microscopic observations.....	82
6.1.3- Porosity versus permeability	82
6.2- STRUCTURAL ANALYSES	83
6.2.1- Stylolites.....	84
6.2.2- Joint and fracture development.....	87
6.3- PALEOFLUID CHARACTERISATION	90
6.3.1- Petrography and structural data	91
6.3.1.1- Cal-1 cement.....	91
6.3.1.2- Cal-2 cement.....	91

6.3.1.3- Cal-3 cement.....	93
6.3.1.4- Cal-4 cement.....	93
6.3.1.5- Cal-5 cement.....	93
6.3.2- Stables isotopes	97
6.3.3- Elemental geochemistry	99
6.3.4- Strontium isotopes	100
6.3.5- Fluid inclusions	103
6.4- DISCUSSION	104
6.4.1- Paleofluid characterisation	104
6.4.1.1- Cal-1.1 cement.....	104
6.4.1.2- Cal-1.2 cement.....	104
6.4.1.3- Cal-2 cement.....	106
6.4.1.4- Cal-3 cement.....	107
6.4.1.5- Cal-4 cement.....	108
6.4.1.6- Cal-5 cement.....	108
6.4.2- Origin and relative timing of the vein formation	108
CHAPTER 7- DIAGENESIS AND FRACTURING IN THE KURVELESHI BELT: THE KREMENARA ANTICLINE CASE STUDY	113
7.1- GENERAL CHARACTERISTICS.....	114
7.1.1- Lithologies of the Upper Cretaceous-Eocene interval	114
7.1.2- Previous work: Matrix porosity of carbonate turbidites	119
7.2- STRUCTURAL ANALYSES	122
7.2.1- Stylolites.....	122
7.2.1.1- Burial stylolites.....	122
7.2.1.2- Tectonic stylolites.....	122
7.2.2- Fractures	124
7.2.3- Oil occurrences.....	127
7.3- VEIN DEVELOPMENT IN THE KREMENARA ANTICLINE.....	127
7.3.1- Cal-1 cement	127
7.3.2- Cal-2 cement	127
7.3.3- Cal-3 cement	127
7.3.4- Cal-4 cement	128
7.3.5- Cal-5 cement	128
7.3.6- Cal-6 cement	130
7.3.7- Cal-7 cement	131
7.4- STABLE ISOTOPES.....	132
7.5- INTERPRETATIONS	134
7.5.1- Pre-folding stage	134
7.5.2- Post-folding stage.....	135
CHAPTER 8- FLUID-FLOW MODELLING.....	137
8.1- PREVIOUS WORK: COUPLED 2D-KINEMATIC/STRATIGRAPHIC MODELLING	137
8.1.1- Edition of the section.....	137
8.1.2- Coupled Thrustpack-Dionisos forward kinematic and stratigraphic modelling.....	137
8.2- CERES WORKFLOW	140
8.2.1- Edition of the initial Ceres section	140
8.2.2- Restoration of the section	140
8.2.3- Forward simulations	142
8.3- CASE STUDY: THE ALBANIDES TRANSECT CR13.....	143
8.3.1- The initial section	143
8.3.2- Geological attributes.....	144
8.3.2.1- Distribution of the lithologies and porosities	144
8.3.2.2- Distribution of the source rocks, reservoirs and seals	146
8.3.3- Burial curves of the studied tectonic units.....	147
8.3.4- Limitations of the model	147
8.4- THERMAL REGIME	147
8.4.1- Initial data.....	148

8.4.2- Thermal Calibration	148
8.4.3- Maturity of the source-rocks	150
8.4.3.1- Vitrinite reflectance	150
8.4.3.2- Transformation ratio	152
8.5- PRESSURE EVOLUTION	154
8.5.1- Hydraulic head	154
8.5.2- Generation of overpressure	158
8.5.3- Fracturing episodes.....	159
8.6- FLUID FLOW	159
8.6.1- Water migration.....	161
8.6.2- Oil migration and HC charge through time	163
8.6.2.1- Incidence of the oil density	164
8.6.2.2- Function of the fault behaviour.....	165
8.7- CONCLUSIONS	169
CHAPTER 9- DEFORMATION / FLUID FLOW HISTORY	173
9.1- FRACTURING VS. KINEMATIC EVOLUTION OF THE ALBANIDES	173
9.1.1- Pre-orogenic stage	174
9.1.2- Generation of overpressures	174
9.1.3- Thrusting stage	174
9.1.4- Overthrusting and out-of-sequence development	175
9.1.5- Onset of an E-W compression	175
9.2- GENERAL CONCLUSION	175
BIBLIOGRAPHY	176

Table of illustrations

Figure 2.1. Geological map of the Alpine orogen, comprising the Albanides (UNESCO/CGMW).....	5
Figure 2.2. Structural map of the outer Albanides with the locations of the studied areas, i.e. Kelcyra area , Saranda and Kremenara anticlines (modified after Roure et al., 1998). The CR13 line indicates the location of the studied seismic profile, used for the fluid flow modelling	6
Figure 2.3. Structural interpretation of an E-W seismic profile, passing through the Vlora-Elbasan transfer zone, where all the major oil fields occur (from Roure et al., 1998).	7
Figure 2.4. Schematic representation of the carbonate paleogeographic sequences during the rifting stage (modified from Zappatera, 1994).	7
Figure 2.5. Overview of the stratigraphic evolution in the outer Albanides (Swennen et al., 1998).....	8
Figure 2.6. Schematic evolution of the Albanides from the Lower Triassic to Present-day (from Barrier et al., 2003; and reference therein). Notice that the thicknesses are not to scale.	11
Figure 2.7. Kinematic evolution of the Ceres model along the CR13 section from the Aquitanian to present-day.	13
Figure 2.8. Evolution of the dolomitic interval, characteristic for Upper Triassic interval and showing the dissolution of the evaporite.	14
Figure 2.9. Pictures of the Triassic interval. Notice that the base is more siliciclastic with green marls (picture on the left), indicating an anoxic environment, whereas the top of the formation evolves towards carbonate system and displays red marls (picture on the right) due to the sea level fluctuations.	15
Table 3.1. List of the main Albanian oil and gas fields (based from Sedjini, 1990; Petroconsultants, 1991; Flores et al., 1991; Albpetrol, 1992). Abbreviations: Frac. carbonate = Fractured carbonate, mainly Eocene to Cretaceous limestones; Late Miocene Sst. = Messinian, Tortonian (Serravalian) deltaic to shallow marine sandstones; Plioc. Turb./ Molasse Sst. = Pliocene turbiditic deep water fan sands and occurrence of shallower water sandstones.	18
Figure 3.1 Map of Albania showing major oil and gas fields and selected deep exploration wells (from Petroconsultants, 1991).	19
Figure 3.2. Schematic lithostratigraphic log, characterising the sedimentary evolution of the outer Albanides, with the main source rocks and oil/gas reservoirs. On the right side, a brief kinematic evolution of the Ionian Zone is given (modified from Dalipi et al., 1971; Albpetrol, 1992).	20
Figure 3.3. Rock sample of the Posidonia shale, i.e. Toarcian serie, accounting for most oil production in the Ionian Zone	21
Figure 3.5. Pictures of the Patos field. Oil seeps in sandstone interval occur in the matrix and fracture porosity.21	
Figure 3.4. Picture of the Male I Gjere reservoir analogue for the main Upper Cretaceous to Paleocene reservoir interval. Notice that two main slumping horizons occur in the Uppermost Cretaceous to Paleocene intervals.	21
Figure 4.1. Methodology followed to characterise the fluid flow	23
Figure 4.2. Schematic map with indication of the studied locations: i.e. the Saranda and Kremenara anticlines and the Kelcyra quarry.	25
Table 4.1. Stable isotope composition of Cretaceous and Paleocene marine constituents and carbonates (after Van Geet et al., 2002).	29
Figure 4.3. Variations in $\delta^{13}\text{C}$ values (Hudson, 1977; Moore, 2001).....	30
Figure 5.1. Geological map (from the Geological survey of Albania) of the central part of the Berati belt, showing the hanging wall and the footwall of the main thrust fault. The letters from (A) to (D) refer to the position of the main faults, which are described on the NE-SW geological cross-section in Figure 5.2 (black line). The black square indicates the location of the studied quarry.	34
Figure 5.2. NE-SW cross-section through the Berati unit. The location of this transect is shown on Figure 5.1. The main faults are designed by a letter from (A) to (D). The main (C) fault is thrusting the Neogene deposits and borders the western part of the Berati belt. The (B) backthrust fault, occurring in the Kurveleshi belt, is also thrusting the Neogene deposits.	34
Figure 5.3. Satellite image of the studied area; the quarry is indicated by a blue square (from Google Earth 4.3, 2007). The scale of the quarry is of 70m in height and about 120m long.	35

Figure 5.4. Outcrop and petrographic features of the Upper Paleocene-Eocene limestones in the Kelcyra quarry: (A) Macroscopic view of a fractured Upper Paleocene-Eocene mudstone with stylolite. (B) Transmitted light view of wackestone with planktonic foraminifera. (C) Transmitted light view of mudstone with dispersed planktonic foraminifera. (D) Transmitted light view of fine-grained limestone with silica (S), overlain by foraminiferal packstone. The top is towards the right. (E) Transmitted light view of planktonic foraminiferal packstone. (F) Transmitted light view of wackestone with foraminifera.	36
Table 5.1. Porosity and permeability data. Only samples where some porosity could be seen macroscopically were analysed (see column "Selected samples"). M = Mudstone; W = Wackestone; P = Packstone; LPS = Layer Parallel Shortening; BPS = Bedding Parallel Stylolites.	37
Figure 5.5. Crossplot between porosity and log (permeability) with data for various lithologies. (M = mudstone, W = wackestone, P = packstone with or without TS = Tectonic stylolites). The arrows indicate the increase of the K-Phi properties with the occurrence of tectonic stylolites.	37
Figure 5.6. Lower hemisphere stereonet projections of raw and backtilted data: bedding (So), fracture generations and stylolites (i.e. burial and tectonic). The colored planes represent a mean of each fracture set.	39
Table 5.2. Raw data of bedding, stylolites and fractures of the Kelcyra quarry (present day orientations, <i>raw data</i>).	40
Table 5.3. Relative timing of the different vein types compared to stylolites and fracture generations, principally based on crosscutting relationships.	42
Figure 5.7. (A) Photograph of crosscutting relationship between vein generations and tectonic stylolites (TS). Here, TS are cutting a Cal-2 vein and predate a Cal-5 vein. (B) Photomicrograph of Cal-5 vein crosscutting Cal-2 vein. (C) Transmitted light view of Cal-2a and Cal-2b vein generations, showing highly twinned calcite crystals. Note the continuity between both phases and the occurrence of Dol-1 inclusions. (D) CL view of picture (C). A distinction between Cal-2a and Cal-2b can be made. Cal-2a cement displays a sector zoning, whereas Cal-2b is recrystallised as attested by the varying CL characteristics. It contains many scattered red luminescent dolomite crystals. (E) CL microscopic view of Cal-2a cement, which has precipitated in a vug. (F) Transmitted light view of Cal-2a and Cal-2b cements, stained with Alizarin Red-S and K-ferricyanide. Cal-2a is relatively more enriched in Fe than Cal-2b, attested by the blue coloration of the calcite crystals. (G) CL view of Cal-2a cement, which precipitated in a reused Cal-1 vein. Cal-2a cement displays undefined brecciated fragments.	43
Figure 5.8. (A) CL view of a contact between Cal-2a and Cal-2b with red-dull dolomite crystals (Dol-1) precipitated into Cal-2b calcite cement. (B) Transmitted light view of unstained dolomite crystals scattered into pink-coloured calcite crystals (Cal-2b cement). (C) and (D) SEM views of euhedral dolomite crystals. The crystals are partially corroded due to the polishing and the etching by HCl in the Alizarin Red-S stain. (E) & (F) Backscattered Electron (BSE) images of Dol-1 crystals, which have precipitated parallel to the twinning planes. In (E), it is clear that the dolomite precipitates close to the dissolved area of the Cal-2b vein. (G) & (H) CL and transmitted light views respectively of a rest of sector-zoned luminescent calcite into the Cal-2b cement. Notice that this sector zoned luminescent calcite part remains more transparent on normal view.	43
Figure 5.9. (A) Backscattered electron (BSE) image of acicular strontianite, which has precipitated along calcite twins in Cal-2b cement. (B) Photomicrograph of strontianite in Cal-2b cement. Strontianite remains uncoloured after Alizarin Red-S staining. (C) BSE image of strontianite crystal associated with barite in Cal-2b cement. (D) BSE image of celestite.	46
Figure 5.10. Transmitted light (A) and CL (B) views of a crack seal texture in the Cal-3b cement. Notice the fracture opening, characterised by a dull luminescent calcite cement, into the Cal-3b filling. On picture A, the twinning is continuous through the orange and the dull luminescent cements. It demonstrates that the fluid has nucleated in crystallographic continuity with host phases along the fracture wall as a crack-seal texture. Notice also that the Dol-1, i.e. the micrometric red-dull luminescent dolomites, occur only in the orange luminescent calcite (i.e. early growth), whereas they do not occur in the dull luminescent calcite, i.e. late growth phases.	47
Figure 5.11. Images of Cal-3 cement. (A) Photograph of Cal-3 cement on polished sections. The vein is up to 2 cm wide. (B) Photomicrograph of Cal-3 cement, displaying highly twinned calcite crystals. The centre of the vein is characterised by longitudinal dissolution features, giving rise to a grainy texture. (C) & (D) Respectively transmitted light and CL views of dolomite crystals (Dol-1), scattered in Cal-3 calcite cement. Notice the presence of a relict texture of sector zoned calcite. (E) & (F) Respectively transmitted light and CL views of Cal-1 cement (dull luminescence) reused by Cal-3 cement (yellow luminescence) that contains many brecciated Cal-1 vein fragments (shown with arrows).	48

Figure 5.12. Cal-5 and Cal-6 veins. (A) Photograph of a vein filled by Cal-5 cement crosscutted by a vein with Cal-6 cement. (B) Transmitted light view of Cal-5 vein crosscutted by Cal-6 veins. (C) Transmitted light view of Cal-5 vein, showing many host-rock fragments, which are parallel to the fracture opening. (D) Transmitted light view of stained Cal-5 vein. The pink colour of the calcite crystals reflects a low Fe-content. (E) and (F) respectively transmitted light and CL views of Cal-6 vein postdating Cal-5 vein. Notice the occurrence of barite (Ba) in Cal-5 cement (i.e. non-luminescent crystal in F) adjacent to the Cal-6 vein.	49
Figure 5.13. (A) Transmitted light view of Cal-5 cement, surrounding subhedral dolomite crystals. (B) Transmitted light view of the fibrous antitaxial texture of the Cal-5 cement, showing many trails of pieces of wall-rock. (C) Enlargement of regularly trails of pieces of wall-rock in Cal-5 cement. (D) Transmitted light view of Dol-2 crystals emplaced into Cal-5 cement. The dolomite is non-transparent and possesses a subhedral shape. The calcite cement is highly twinned. (E) Backscattered electron (BSE) image of barite, located in Cal-5 cement. (F) Photomicrograph of stained Cal-2 cement cut by Cal-4 vein. The latter displays fibrous and elongated non-ferrous calcite crystals and contains some barite phases.	50
Figure 5.14. (A) & (B) Respectively transmitted light and CL views of Cal-3 cement, displaying brecciated fragments in a dull luminescent calcite cement. Here the fragments are composed of dolomite crystals, which are partially dedolomitised (bright luminescent calcite). (C) Transmitted light view of pink-stained Cal-5 cement with an unstained euhedral dolomite crystal (Dol-2). (D) & (E) Respectively CL and transmitted light views of Dol-3 cement, which precipitates in a re-activated fracture. The unstained dolomite crystals are subhedral, and display a red dull luminescence. This generation predates Cal-7, which consists of dull sector zoned calcite crystals. In picture (E), the unstained dolomite (Dol-3) is clearly visible. (F) Detail of twinned and partially dedolomitised Dol-3 in contact with Cal-7.	51
Figure 5.15. Backscattered Electron (BSE) images. (A) Occurrence of altered cubic fluorite and feldspath phases (Fld K.) associated with detrital phyllosilicates at the grain boundaries in Cal-7 cement. (B) Corroded barite crystals associated with oxy/hydroxides (FeO). (C) Detrital phyllosilicates associated with euhedral pyrite.	52
Figure 5.16. Carbon and oxygen isotopic crossplot with compositions of the Upper Paleocene-Eocene limestones (Im, Veizer et al., 1999) from the Kelcyra outcrop and their diagenetic products. Notice that the isotopic data for the dolomite phases have not been corrected with the fractionation factor of the dolomites of about 3 ‰ (Land, 1980).	54
Table 5.4. Minimum, maximum and average data for the major and trace elements in ppm based on microprobe analysis of the main diagenetic phases in the Kelcyra area. Values below detection limit are indicated with "< dl" (about <10 ppm). The sign "-" means the lack of analytical results. Additionally, 14 samples of diagenetic phases have also been analysed by using AAS. Their average measurements are given in Average AAS. In the case of data below the detection limit, <dl has been replaced by 10 ppm, consisting of the average lowest limit, to calculate the average value.	55
Table 5.5. Major and trace element data in ppm (microprobe data) of diagenetic phases of Kelcyra area. Values below detection limit are indicated with "<dl"	57
Table 5.6. Major and trace element data in ppm (AAS analyses) of major diagenetic phases of Kelcyra area.	58
Figure 5.17. Elemental composition in magnesium versus strontium of the successive vein filling calcite generations.	59
Table 5.7. Major and trace element data (in ppm) of barite and dolomite (Dol) crystals in the Kelcyra area. Values below the detection limit are indicated with "<dl" (about <10 ppm).	59
Figure 5.18. Elemental composition in strontium versus aluminium of the barite crystals.	60
Figure 5.19. Elemental composition in strontium versus silica of the dolomite crystals.	60
Table 5.8. AAS trace element geochemical data from dolomites from southern Albania (Mali Gjere section, Swennen et al., 1998). IR = Insoluble Residue in %; all trace element concentrations in ppm.	61
Table 5.9. Sr ⁸⁷ / Sr ⁸⁶ ratio of limestone (mudstone) and some vein-filling calcite samples from the Kelcyra outcrop (Upper Paleocene to Eocene age). For reference also the Late Paleocene-Eocene marine water values are given (McArthur and Howarth, 2004) as well as measured for Triassic dolomite and evaporites from the south of Albania (Swennen et al., 1998).	61
Figure 5.20. Plots of Sr ⁸⁷ / Sr ⁸⁶ secular variation, compiled after McArthur and Howarth (2004) with enlargement of specific time intervals, i.e. a), b), and c), with indication of measured Sr-isotopic composition of Triassic dolomites and evaporites (Swennen et al., 1998), and of the three main vein-filling (i.e. Cal-2b, Cal-3 and Cal-7 cements).	62
Figure 5.21. Photomicrograph of primary inclusions into Cal-2b cement.	63

Figure 5.22. T_h (°C) versus salinity (eq. wt.%NaCl) diagram of F2 fluid inclusions in Cal-2b.	63
Figure 5.23. T_h (°C) versus salinity (eq. wt.% NaCl) diagram of the two generations of fluid inclusions. Note the 2 clusters attesting of a variation in salinity.	64
Figure 5.24. T_h (°C) versus salinity (eq. wt.% NaCl) diagram of solitary fluid inclusions of Cal-7.	64
Figure 5.25. Histogram of fluid inclusion homogenisation temperatures of Cal-7 cement.	64
Table 5.10. Summary of the petrographic, cathodoluminescence, geochemical, isotopic data and fluid inclusion for calcite and dolomite cements.	65
Figure 5.26. Paragenesis of Late Paleocene – Eocene deep marine carbonates in the Kelcyra area.	68
Figure 5.27. Conceptual model for the diagenetic study. (s.l.: sea level). Red and green coloured arrows relate respectively to down- and upward fluid migrations. For explanation see text: the step A corresponds to the pre-deformational period; B and C indicate the onset of thrusting respectively in the hinterland and in the Ionian basin; “D” shows the out-of-sequence development of the Berati belt; “E” corresponds to the uplift of the Berati belt.	70
Figure 5.28. Fluid flow evolution versus burial history. The construction of the burial curve is discussed in the chapter on fluid flow modelling. “T” corresponds to homogenisation temperatures, which were measured within fluid inclusions.	74
Figure 6.1. Simplified structural map of the southern part of the Ionian zone (based on the geological map of Albania, 2002). The Saranda anticline is indicated by a dashed square. The indicated NE-SW transect is shown in the Figure 6.3.	78
Figure 6.2. Detailed geological map of the Saranda anticline. The studied outcrops are indicated on the map and identified by numbers 1 to 8.	79
Figure 6.3. SW-NE geological transect (modified from Roure et al., 1995) of the southern part of the Ionian Zone, which is located on the Figure 6.1. A detailed zone of the Saranda anticline, showing its asymmetric structure, is also given in the lower part.	79
Figure 6.4. Overview of the study areas in the Saranda anticline: Satellite image of the northern (A), central and southern (B) parts of the Saranda anticline (Google Earth 4.3, 2007); (C) Field picture of the Upper Cretaceous carbonates, which are located in the central part of the anticline (location 7, Figure 6.2). (D) Outcrop located in the western side (location 1), where the Upper Cretaceous to Paleocene fine-grained limestones and debris flow are characterised by beds slightly dipping towards the SW. (E) Overview of a studied quarry (location 3), where Eocene limestones are cropping out. The limestones display a pinkish colour. (F) Quarry of well-bedded Eocene carbonates (location 4), consisting of pink to white limestones and characterised by steeply dipping beds towards the NE.	80
Figure 6.5. Schematic sedimentary log based on own data of the Saranda anticline.	81
Figure 6.6. Petrographic characteristics of Upper Cretaceous to Eocene limestones in the Saranda area: (A) Transmitted light view of planktonic foraminiferal Upper Cretaceous packstone; (B) Transmitted light view of Paleocene wackestone and recrystallised foraminifera; (C) and (D) Respectively transmitted light and cathodoluminescence (CL) views of Paleocene grainstone (i.e. debris flow); (E) and (F) Transmitted light views of Eocene mud- to wackestone with benthic and planktonic foraminifera.	83
Figure 6.7. Crossplot of the porosity versus permeability for various lithologies (W = Wackestone; G = Grainstone; P = Packstone; BPS = Bedding Parallel Stylolites; open fract = open fractures).	84
Table 6.1. Porosity and permeability data (W= Wackestone; BPS= Bedding Parallel Stylolites; G= grainstone; P= Packstone).	84
Figure 6.8. Lower hemisphere stereonet projections of the pre- (TS 1, backtilted data) and post-folding (i.e. TS2, raw data) tectonic stylolites. The coloured-planes identify the mean tectonic stylolite orientations. The black planes show the orientations of the recorded tectonic stylolitic planes.	85
Figure 6.9. Macroscopic observations of cross-cutting relationships between fractures and with stylolites.	86
Figure 6.10. Raw and backtilted data of the recorded fractures.	87
Figure 6.11. Synthesis of the successive sets of fractures in relation to its position in the Saranda anticline.	88
Figure 6.12. Models of fracture sets associated with folding: (A) Summary taken from Griggs and Handin (1960) based on laboratory rock mechanical testing of cylindrical samples; (B) Stearns (1968) model of primary fracture sets during folding. The maximum and minimum principal stresses lie within the bedding. (C) Spatial relationship of fractures and fold of the Stearns (1968) model (modified from Bergbauer and Pollard, 2004).	89
Table 6.2. Raw and backtilted data of bedding (So), tectonic stylolites (TS) and fractures, according to their locations (i.e. from 1 to 8, Figure 6.2). Yellow-highlighted raw data corresponds to the post-folding	

fractures; green-highlighted data consists of TS 1 interpreted as pre- to syn-folding. The blue colour data shows TS, interpreted as post-folding but where the timing is not constrained. They probably reflect a syn-folding development.....	90
Table 6.3. Relative timing of the different vein generations compared to fracture sets, principally based on cross-cutting relationships.....	91
Figure 6.13. Photomicrographs of the Cal-1 cement: (A) and (B) Respectively transmitted light and CL views of recrystallised calcite crystals. Note the presence of a relic of zoned calcite pattern under CL. The twinning planes partially disappear in the recrystallised calcite, showing that recrystallisation likely postdates the twinning. (C) - (D) Respectively transmitted light and CL views of a typical recrystallised pattern of Cal-1 cement. (E) CL view of zoned-calcite with bright to dull luminescence; (F) Transmitted light view of highly twinned and deformed calcite crystals. The twins are closely spaced; (G) Detailed area, showing two sets of thin twinning planes in Cal-1; (H) Transmitted light view of calcite, displaying thicker and less numerous twins.....	93
Figure 6.14. Photomicrographs of the Cal-2 cement: (A) and (B) Transmitted light views showing thin and numerous twinning planes in the calcite crystals; (C) and (D) Respectively transmitted light and CL views of the recrystallised Cal-2 cement. Notice that the centre of the crystals are more recrystallised than the border, which likely relates to differences in the initial composition; (E) and (F) Respectively CL and transmitted light views of Cal-2 cement, displaying a sector zoned pattern under CL. On the right side, the cement is more twinned along a reopening zone in Cal-2. The same observation has been encountered along tectonic stylolites. This process occurs due to pressure building afterwards.....	94
Figure 6.15. Photomicrographs of Cal-3 cement: (A) and (B) Transmitted light views of transparent calcite crystals, characterised by thin twinning planes; (C) and (D) Respectively transmitted light and CL views of Cal-3 cement, showing a characteristic dull to orange zoning. Notice that Cal-3 crystals are not or only weakly recrystallised; (E) CL view of N110° oriented tectonic stylolitic planes, filled with Cal-5 cement, crosscutting Cal-3 cement; (F) CL view of Cal-3 predating undefined dull luminescent calcite vein.....	95
Figure 6.16. Photomicrographs of Cal-4 and Cal-5 cements: (A) and (B) Transmitted light and CL views of a continuous precipitation from Cal-2, overgrown by Cal-4 and Cal-5, without any corrosive contact between these cement generations. Cal-2 is highly recrystallised compared to the later cements. (C) and (D) Respectively CL and transmitted light views of Cal-4, precipitating upon Cal-1. Here, Cal-1 is highly recrystallised. (E) and (F) Respectively CL view of Cal-5 vein crosscutting Cal-1 vein. Both cements occur in different oriented fractures, i.e. in FRACT2 (Cal-1) and FRACT6 (Cal-5).....	96
Figure 6.17. Photomicrographs of the Cal-4 and Cal-5 cements, precipitating upon Cal-1. (A) & (B) Respectively transmitted light and CL views of zoned Cal-4 and non-luminescent Cal-5 cement, which precipitated upon Cal-1. A straight contact between these phases exists. Cal-1 demonstrates a typical CL pattern of recrystallisation. The second set of twins postdates the Cal-5 cement; (C) & (D) Respectively transmitted light and CL views showing the first set of twins, which does not occur in Cal-5. Consequently, this set of twin developed before Cal-5 precipitation; (E) CL view of Cal-1 cement, which is overgrown by Cal-5 cement.....	97
Figure 6.18. Backscattered electron images of the Cal-4 and Cal-5 cements, which precipitate upon Cal-1 and Cal-2 cements: (A) Partial dissolution of the Cal-1 cement; (B) – (C) Acicular and micrometric calcite crystals (likely Cal-5 cement), which precipitate upon Cal-1 calcite crystals.....	98
Figure 6.19. Carbon and oxygen isotopic crossplot with compositions of the Upper Cretaceous-Eocene limestones and their diagenetic products from the Saranda anticline study area.....	99
Table 6.4. Minimum, maximum and average data for the major, minor and trace elements in ppm based on microprobe analysis of the main diagenetic phases in the Saranda anticline. Values below the detection limit are indicated with <dl.....	100
Table 6.5. Major, minor and trace element data in ppm, measured with microprobe. Values below the detection limit are indicated with "<dl".....	101
Table 6.6. Major, minor and trace element data in ppm of the main recorded cement generations, based on AAS analyses.....	102
Table 6.7. Sr ⁸⁷ /Sr ⁸⁶ ratio of some vein-filling cements from the Saranda anticline.....	102
Figure 6.20. Plots of Sr ⁸⁷ /Sr ⁸⁶ secular variation and Sr-isotopic composition of the vein infillings (i.e. Cal-1.1; Cal-1.2; Cal-2 and Cal-3). The secular trend is compiled after McArthur and Howarth (2004).....	103
Table 6.8. Melting temperature (T _m) and homogenisation temperature (Th) in °C measured in Cal-1 and Cal-2 cements. The salinity, expressed in eq. wt.% NaCl, was calculated based on the equation described by Bodnar (1993).....	104

Table 6.9. Summary of the petrographic, cathodoluminescence (CL) and geochemical data for the successive calcite cements. Minimum and maximum contents for Cal-1.1, Cal-1.2, Cal-2 and Cal-3 are measured by AAS. Measurements for Cal-4 and Cal-5 cements were made with microprobe.	105
Figure 6.21. Paragenesis of the Upper Cretaceous-Eocene deep marine carbonates in the Saranda area. The depth for the maximum burial has been estimated based on the analysis of calcite twins. See text for explanation.	106
Figure 6.22. Geographical repartition of the C- and O-isotopic results of the successive vein-fillings. Notice that each studied location is characterised by a similar isotopic trend.	110
Figure 6.23. C- and O-isotopic signature of the different vein-fillings, regrouped according to the studied areas (bold numbers) and associated to the fracturing stages. The arrow suggests a parallel evolution of the fracture generations with the burial of the Saranda anticline.	110
Figure 6.24. Summary of the deformation history, which characterised the Saranda area. The successive steps are described in the text.	111
Figure 7.1. Geological map of the Kremenara anticline (from Swennen et al., 1998). Profiles 4-4' and 5-5', described in Figure 7.5 and Figure 7.6, are indicated by red-lines on the map. Note the three NW-SE faults, which compartmentalise the anticline into four compartments.	114
Figure 7.2. W-E geological profile through the Kremenara anticline (Swennen et al., 1998).	115
Figure 7.3. Field pictures of oil seeps, occurring in the dual matrix-fracture porosity system of the Upper Cretaceous - Paleocene interval: (A) Oil seeps in fractures and burial stylolites; (B) Upper Cretaceous carbonate turbidites, where the matrix porosity is partially stained with oil; (C) Oil seep in fractures.	115
Figure 7.4. Field pictures of (A) Upper Cretaceous carbonate turbidites, characterised by the development of Bouma sequences (Deweever et al., 2007); (B) Unconformable draping of the Serravalian deposits on the Eocene carbonates (cb); and (C) Barnacle assemblages in the Serravalian sandstone, which covers unconformably the Lower Cretaceous carbonates.	116
Figure 7.5. NW-SE geological transect of the central part of the Kremenara anticline, i.e. compartment 2 (Figure 7.1). The location of the 4-4' transect is given in the Figure 7.1. (based on own and wells data).	116
Figure 7.6. NE-SW geological transect of the central part of the Kremenara anticline, located in the Figure 7.1. , i.e. compartment 3 (based on own and well data).	117
Figure 7.7. Sedimentary log of the Fratari area (eastern flank), based on well data and own field observations.	117
Figure 7.8. Sedimentary log of the Greshica area, in the northern part of the Kremenara anticline (based on well data and own observations).	118
Figure 7.9. Schematic drawing of the present-day situation of the carbonate series in the Kremenara area, covered unconformably by the Oligocene flysch.	119
Figure 7.10. Photomicrographs in transmitted light view of the Upper Cretaceous and Paleocene limestones from the Kremenara anticline: (A) and (B) Basal part of the turbidites with matrix supported wackestone, stained with hydrocarbon (HC); (C) Wackestone to mudstone from the upper part of the turbiditic interval; (D) Paleocene mudstone/wackestone lithology with foraminifers; (E) Oil impregnated packstone with hydrocarbon in the Paleocene interval; (F) Packstone located in the Paleocene interval.	120
Figure 7.11. Photomicrographs of the Eocene limestones: (A) Eocene mudstone lithology with foraminifers; (B) Eocene wackestone with foraminifers, such as Nummulites sp.; (C)-(D) and (E)-(F) Respectively transmitted light and CL views of Nummulites with intraparticle porosity cemented with calcite.	121
Figure 7.12. Backtilted data of the recorded tectonic stylolites, which have been previously assumed to be pre-folding.	123
Figure 7.13. Raw data of the tectonic stylolites dated as post-folding.	123
Figure 7.14. Backtilted data representation for recorded fractures.	124
Figure 7.15. Presentation of the raw data of fractures, determined as post-folding.	125
Table 7.1. Relative timing of the fracture generations in relation to the tectonic evolution of the Kremenara anticline.	126
Figure 7.16. Photomicrographs of the Cal-1 cement: (A) - (B) Respectively transmitted light and CL views of the orange luminescent zoned calcite, precipitating along the border, whereas the central part displays a typical CL pattern of recrystallisation. (C) - (D) Respectively transmitted light and CL views displaying the crosscutting relationship of Cal-1 and a non-luminescent calcite vein, i.e. Cal-3.	128
Figure 7.17. Photomicrographs of the Cal-2 cement: (A) CL view of Cal-2 cement, re-opened and filled by the same cement, suggesting a crack-seal process. The yellow luminescent areas display typical CL pattern of	

recrystallisation; (B) Transmitted light view of a brecciated fragment into Cal-2 vein; (C)-(D) Respectively transmitted light and CL views of Cal-2 vein, where brecciated fragments of the former cement occur. ...	129
Figure 7.18. Respectively transmitted light and CL views of the Cal-3 cement. Notice the brecciation of the non-luminescent calcite cement by a younger bright luminescence cement.	129
Figure 7.19. Transmitted light and CL views of Cal-3 cement, which postdates the previously brecciated Cal-2 cement.	130
Figure 7.20. (A) & (B) Respectively transmitted light and CL views of the Cal-4 cement, characterised by numerous brecciated fragments, which likely originate from the former veins or can be attributed to sparitised micritic fragments. (C) & (D) Respectively transmitted light and CL views of the Cal-4 cement, displaying regularly spaced trails of wall rock, parallel to the opening of the vein (arrows). These fragments may contain pieces of micritic matrix and non-carbonate impurities.	130
Figure 7.21. Respectively transmitted light and CL views of the Cal-5 cement, which brecciates the initial Cal-2 cement. Notice the intense brecciation of the vein and the occurrence of Fe-oxides (non-luminescent crystals). The matrix fragments in the brecciated vein display the same luminescence as the surrounded matrix.	131
Figure 7.22. Respectively transmitted light and CL views of the Cal-6 cement, characterised by numerous brecciated fragments, which originate from the former veins.	132
Figure 7.23. Photomicrographs of the Cal-7 cement. Respectively transmitted light and CL views: (A) – (B) of Cal-7 cement, which crosscut Cal-6 vein; (C) – (D) view on elongated calcite crystals, characterised by orange to non luminescent sector zoning.	132
Figure 7.24. Carbon and oxygen isotopic signature of the matrix carbonates, which occur in the Kremenara anticline.	133
Figure 7.25. Carbon and oxygen isotopic crossplot of the successive calcite veins.	133
Figure 7.26. Summary of the paleofluids and coeval paragenesis and its relationship with the tectonic evolution of the Kremenara anticline (adapted from Van Geet et al., 2002).	134
Figure 8.1. Two seismic profiles, which are located in the Outer Albanides, interpreted by Barrier et al. (2003).	138
Figure 8.2. Workflow of the coupled structural/stratigraphic forward modelling. See explanation in the text. .	138
Figure 8.3. Main steps, defining the work flow of the section editor: (A) – (B) edition of the present-day geometry and the definition of segment points; (C) to (F) edition of the geological attributes; (G) definition of the kinematics blocs and building of the meshing for each bloc.	141
Figure 8.4. Structural map of the Albanides with location of the CR13 line, which represents the geological profile interpreted from seismic line.	142
Figure 8.5. Successive steps for the simplification of the profile from the seismic interpretation to the Ceres section. The upper figure (A) represents the interpreted seismic profile, displaying its detailed geometry (from Barrier et al., 2003). The middle transect (B) is the regional balanced cross-section (from Barrier et al., 2003) and the lower profile (C) is the simplified section used for Ceres (fluid flow modelling). All the layers are represented but only the main faults can be implemented in the Ceres profile, due to numerical complexities. The areas with simplifications are indicated by red circles in the upper seismic profile.	143
Figure 8.6. Distribution of geometries and lithologies of the present day CR13 section. The four main source rocks are indicated, i.e. the Upper Triassic, the Middle Cretaceous, the Paleocene-Eocene (Pal-Eocene), and the Tortonian source-rocks (SR). The locations “1”, “2”, and “3” were chosen to work out the distribution of the (over)pressure in the focussed Upper Cretaceous-Eocene carbonates interval along the profile through time.	144
Figure 8.7. Distribution of the lithologies and of the resulting porosities in the CR13 section (Vertical and horizontal scales are respectively in kilometres and in meters).	145
Figure 8.8. Distribution of the thermal conductivity (in $W.m^{-1}.^{\circ}C^{-1}$). Vertical and horizontal scales are respectively in kilometres and in meters.	145
Figure 8.9. Burial curves of the main tectonic units, i.e. the foredeep, the Kurveleshi and the Berati belt. Two curves representing respectively the evolution of the geothermal gradient (input data) and the modelled temperature evolution through time (output data) are also indicated.	146
Figure 8.10. Actual geothermal gradient distributed in the southern part of Albania (from Frasheri et al., 1995). The black line represents the location of the CR 13 profile.	147
Figure 8.11. Geothermal profile from a well (i.e. Ard-18) located in the southern part of the Peri-Adriatic Depression (from Frasheri et al., 1995).	148

Figure 8.12. Heat flow variations through time for the studied E-W CR13 transect. Both hypotheses provide a good fit between the computed temperature and the present day data.	149
Figure 8.13. Present-day temperature and maturity evolutions for the two hypotheses, shown in Figure 8.12. The actual geothermal gradient and the thermal data, from industry data, used to calibrate the model are indicated in the diagrams. The dash line represents the modelled geothermal gradient from the computed temperature.....	150
Figure 8.14. Ceres section showing the distribution of the temperature in °C (top) and the Ro in % (bottom) for the hypothesis 2. The productive wells used to constrain the model are indicated in red.	151
Figure 8.15. Repartition of the maturity (Vitrinite reflectance in %) along the CR13 profile from the Aquitanian to the Early Tortonian.	152
Figure 8.16. Continuation of the Figure 8.15, showing the Ro evolution from the Tortonian to the present-day.	153
Figure 8.17. Distribution of the transformation ratio in the frontal thrust units at present-day.....	153
Figure 8.18. Evolution of the transformation ratio for the Triassic to Lower Jurassic sources rocks, located in (A) the foreland and in (B) the upper part of the Kurveleshi belt. The peak oil corresponds to the main transformation phase, varying between 25 and 65% of transformed organic matter (Houseknecht and Hayba, 1998). The vertical and horizontal scales correspond respectively to the transformation ration in % and the time in Ma.....	154
Figure 8.19. The diagram shows the variation of the eustatism, i.e. sea level, for the two tested scenarios. The dashed and the black lines correspond respectively to the first and the second scenarios described in the text. The second hypothesis is defined relatively to the sea level evolution used for the first hypothesis. .	155
Figure 8.20. Evolution of the hydraulic head (water pressure) through time (Scenario 1). For explanation, see text.....	156
Figure 8.21. Hydraulic head (water pressure) evolution through time (Scenario 2). For explanation, see text. .	157
Figure 8.22. Evolution of the overpressure in MPa through time for the two hypotheses discussed in the text, based on the bathymetry evolution (Figure 8.19). The black and red lines characterise the overpressure evolution for respectively the first and the second hypotheses. The simulated locations, i.e. foredeep (1), Kremenara (2) and Kelcyra (3), are indicated on the interpreted profile. They have been chosen with regard to the actual position of oil reservoirs and to check the lateral overpressure variation through time.....	158
Figure 8.23. Evolution of the fracturing during the main steps of the deformational period, based on the second hypothesis (i.e. shallower marine sedimentation). The fracturing ratio is an estimate of the possible intensity of fracturing and is purely indicative. It is based on overall physical-mechanical properties of rocks, since no input data was used to calibrate the model.	160
Figure 8.24. Water migration pathways from the Burdigalian until the Early Tortonian shown by red arrows The water flow is expressed in m/My. For discussion, see text.	161
Figure 8.25. Water migration pathways from the Tortonian onward, described by red arrows. The water flow is expressed in m/My. For discussion, see text.	162
Figure 8.26. Modelled velocity of the water flow (in m/My) through time. The dashed lines and the full lines correspond respectively to the eastern and western part of the Upper Cretaceous intervals for each tectonic units.....	163
Figure 8.27. Distribution of the water saturation at present-day for the two tested oil densities, i.e. 33 and 15 °API. Notice that the decrease in water saturation is complementary to the oil saturation. A density of 33°API corresponds to light oil and 15°API characterises heavy oil. The main differences are highlighted by red circles.	164
Figure 8.28. Evolution of the water saturation for light oil density from the Aquitanian to present-day, for estimating time of oil expulsion of a source rock and primary migration. Notice that the accumulations of hydrocarbon in the Upper Cretaceous to Eocene carbonates are located beneath the thrusts, sealed by Triassic evaporites and the Oligocene flysch.	167
Figure 8.29. Water saturation (= oil accumulation) with the oil migration pathways from the Aquitanian to the present-day with illustrations of some detailed zones. The size of the arrows is proportional to the migration velocities, varying approximatively from 0.04 to 4.5 m/My.....	169
Table 8.1. Characterisation of the main steps of the deformation. PAD, Krm and Kel refer to the three main studied areas, which are respectively the Peri-Adriatic Depression, Kremenara and Kelcyra.	170
Figure 8.30. Summary of the main steps in the water flow modelling according to the tectonic evolution of the Albanides.	172

Figure 9. 1. Summary of the main diagenetic processes determined in the three studied areas, placed into the tectonic evolution of the Albanides. Processes taking place in the beginning of the diagenetic history are indicated in the upper part of the figure, those that occurred at the end are given in the lower figure part. 173

CHAPTER 1- INTRODUCTION

Classical applied geological research on reservoir characterisation often relies on the study of core material in conjunction with the interpretation of log-data. However, since an economic oil reservoir often covers an area of 5 by 5 km, the representativity of such type of reservoir geological study can be questioned, especially since in the exploration stage only a limited number of core intervals of the reservoir are available for research. Consequently, there is a need for fundamental scientific research of natural analogues. These are outcropping reservoir structures, which are representative for neighbouring reservoirs in the subsurface. To make it clear, a reservoir analogue is not equivalent to an outcrop where the reservoir interval is exposed. It rather corresponds to a system of several tens of outcrops covering a wide geographical area and where major topographical differences occur, allowing also to study the vertical characteristics on a reservoir scale. The study of these reservoir analogues should allow to work out a 3 dimensional picture of the reservoir features and processes that control porosity and permeability. This is especially of importance for the study of complex oil and gas reservoirs, as they occur for example in foreland fold-and-thrust belts.

The main challenge for the study of sedimentary basins relates to the coupling and interactions between various processes, acting either deep in the lithosphere and crust (i.e., the heat flow and tectonic subsidence), at shallower burial levels in the sediments (i.e., the diagenesis), or eventually at the surface (i.e., erosion and sedimentation), in the course of ongoing deformation. The more we learn on sedimentary basins, the more we identify the need for integration of data and expertise from various disciplines such as (1) geophysics, structural geology and sedimentology, to properly describe at different scales the architecture, dynamic and sedimentary infill of the basin, but also (2) petrography, geochemistry and basin modelling, that are ultimately required to reconstruct the evolution of the porous medium through times and to provide realistic predictions (quantification) of present-day characteristics of the reservoirs in

areas which have not yet been investigated by drilling.

In this scope, the yearly workshops of the ILP Task Force on Sedimentary Basins and GeoFluids constitute excellent opportunities to develop and consolidate an efficient network, involving scientists from different background, to help initiating new collaborations and to disseminate new techniques and methodologies applied to the study of sedimentary basins and reservoir appraisal. From 1996 to 2002, collaborative studies dedicated to the prediction of reservoir characteristics, coupling both petrographic work and basin modelling, have also been the driving force of the SUB-Thrust Reservoir APpraisal Joint Industry Project (SUBTRAP Consortium; Roure et al., 2005), with case studies dedicated to sandstone reservoirs in Sub-Andean Basins in Venezuela and Colombia, and to carbonate reservoirs in Pakistan, Mexico, Canada, as well as in Albania (Benchilla et al., 2003; Breesch et al., 2006, 2007; Dewever et al., 2007; Ferket et al., 2002, 2003, 2006; Swennen et al., 2000; Van Geet et al., 2002; Vandeginste et al., 2005, 2006; Vilasi et al., 2006, 2009).

Thanks to the support of Bernard Durand (IFP) and Ilia Fili (Albania), first collaboration between IFP and the Albanian Petroleum Institute in Fieri started in 1992, focusing on the regional cross-section balancing done by Irakli Mio with Locace, forward modelling coupling kinematics, thermal evolution and petroleum generation with Thrustpack, revision of Neogene bio-stratigraphic correlations made on nannofossils by Carla Müller, as well as on oil and source rock characterizations. This pioneer phase ended with a field trip and workshop organized on site in 1995 (Roure et al., 1995), which helped to promote the Subtrap proposal and gain the interest of more than 15 participating companies. During the Albanian part of the Subtrap project and subsequent collaborations with the Petroleum Institute in Fieri, Triassic dolomites (Muska, 2002) and Late Cretaceous carbonate turbidites were successively studied (Swennen et al., 2000; Van Geet et al., 2002; Dewever et al., 2007).

This work was then extended to the quantitative kinematic and sedimentary modelling coupling Thrustpack with Dionisos (Barrier et al., 2005), as well as the fluid flow, pore fluid pressure and hydrocarbon migration modelling with Ceres. During this project, the Albanian Petroleum Institute gave access to subsurface data (seismic and well data), and provided the requisite regional expertise and logistics for the field work, whereas basin modelling tools were operated at IFP. Additional analytical work focusing on paleo-thermometers, microfabric and evolution of reservoir characteristics through time was performed at KU-Leuven (with support from Rudy Swennen for the diagenesis of carbonates), UMPC-Paris VI (with support from Olivier Lacombe for calcite twins) and the Museum National d'Histoire Naturelle (MNHN, Nicole Guilhaumou; fluid inclusions).

In addition to these rather applied projects involving the petroleum industry, other recent earth science projects supported by NATO (Science for Peace Programme) have also provided new information on tectonically active features of the Albanian foothills (synthesis on current seismicity, focal mechanisms and GPS measurements; Nieuwland et al., 2001; Kiratzi and Muço, 2004; Jouanne et al., in press), as well as on the timing of tectonic uplift and unroofing of the hinterland (Apatite Fission Tracks; Muceku, 2006; Muceku et al., 2006), making Albania one of the best documented natural laboratory for the study of active European onshore compressional systems.

This Ph.D. project consisted in an integrated structural-diagenetic-basin modelling approach, involving different techniques applied at different scale, i.e. from thin section to basin-scale, which are precisely described below to demonstrate how a pluridisciplinary study can help in reservoir appraisal in terms of architecture, geodynamic and thermal evolution, in relation to regional tectonic evolution (i.e. individual tectonic unit) as well as fluid migration and fluid rock interaction (composition of the fluid, open-closed system, etc...). Specific attention was paid also to the characterisation of the hydraulic fracturing, which testifies of overpressure regimes during the onset and subsequent evolution of the tectonic deformation.

The aim of this Ph.D. is to determine and discuss the possible relationship between the geodynamic evolution of the FTB and the fluid

migration through time, with special emphasis on the creation and destruction of porosity. This study combines field work, structural analysis, detailed petrography and geochemistry of the fracture fillings for three selected case studies, and fluid flow modelling. In this specific research project, three objectives were considered: (i) first to give a better understanding of the fracture genesis and fluid flow through time during the FTB development in Albania, (ii) secondly to determine the major diagenetic stages, which have an important impact on present-day reservoir characteristics of nearby oil producing reservoirs (i.e. porosity development or destruction) and (iii) thirdly to model the kinematic evolution of the FTB and the fluid flow (i.e. oil/water) in order to determine the possible fluid pathways, oil accumulations, the velocity of the fluid migrations and to discuss the fault behaviours.

Chapter 1 forms the introduction to the Ph.D. Chapters 2 and 3 provide the geological and petroleum settings, which occurs in Albania, to place the studied areas in a regional and local stratigraphical, paleogeographical and structural framework. Chapter 4 describes the work flow and techniques involved in my research project and documents the three selected areas studied.

Chapters 5 to 7 focus on the diagenesis of the Upper Cretaceous to Eocene carbonates, which constitute the most important reservoir intervals in the Ionian Zone, and thus for the three selected studied areas, i.e. Berati outcrop, Saranda and Kremenara anticlines. These chapters aims to answer to the first two objectives described previously. Pluridisciplinary studies, comprising structural, sedimentological and geochemical approaches were performed in order to determine the successive diagenetic processes, and their relationships with the tectonic evolution. At the end of each chapter, the successive diagenetic processes are placed within the tectonic evolution of the area, leading to some local specific conclusion.

Chapter 8 that deals with the third objective presents the workflow and regional 2D fluid flow modelling, using the Ceres software. In this specific study, basin-scale modelling was mainly used to propose a timing for the major fluid migrations determined diagenetically. These fluid migrations were placed into the geological evolution of the FTB based on major regional hydrofracturing processes, determined

petrographically and numerically. More generally, basin-scale modelling techniques are also required to understand the velocity and trends of fluid migrations, pore fluid pressures and temperature evolution of the basin as well as natural hydrofracturing and the hydrodynamic behaviour of faults.

Chapter 9 summarises the regional/local diagenetic processes, evidenced in the different studied areas. Here, the three case studies and the fluid flow model are integrated thanks to good time markers, which relate the overpressuring periods, regional stylolitisation with the main trends of fluid migrations. The main differences and similarities are discussed and placed into the geodynamic evolution of the Albanides FTB.

CHAPTER 2- GEOLOGICAL SETTING

Albania constitutes a key area to study the petroleum systems in foothills domains, where deformation is still currently active (Sorel et al., 1991; Tagari, 1993; Muço, 1994; 1998; Roure et al., 2000). Together with the Apennines and Romanian Carpathians, the Outer Albanides constitute one of the European foredeep basins

where the synorogenic series are well preserved. Due to these unusual conditions, it is possible to constrain accurately the kinematics of the deformation, understand the tectonic control on the architecture of synorogenic sequences, and trace the burial and thermal evolution of potential source-rocks and reservoirs.



Figure 2.1. Geological map of the Alpine orogen, comprising the Albanides (UNESCO/CGMW).

Situated on the eastern border of the Adriatic Sea, between the Dinarides in the north (former Yugoslavia) and the Hellenides in the south (Greece), the Albanides constitute a segment of the wider Circum-Mediterranean Peri-Tethyan thrustbelts (Figure 2.1). In fact, the Albanian foothills correspond to a typical foreland fold-and-thrust belt, characterised by a west verging thrusting over the Adriatic foreland.

2.1- Tectonostratigraphy of the Albanides

The Albanides include a flexured foreland domain in the west, frontal thrusts and foothill structures involving the Mesozoic series of the former Tethyan passive margin in the east. The hinterland consists of an ophiolitic suture, i.e. the Mirdita ophiolite, which is well preserved.

The Ionian tectonic zone consists of a thrust front zone, characterised by a complex geology, where the main tectonic feature is a west verging thrust with the Triassic evaporite acting as the major décollement level. The major structural fault zones in Albania possess a NNW-SSE alignment (Figure 2.2), which can be easily demonstrated by orientation of thrust sheets or fold hinges. Several secondary features and processes related to this thrusting, such as backthrusts, fold structures, triangle zones, carbonate duplex structures, local unconformities, evaporitic diapirs, etc ..., are also present. A general east-west geological transect through Albania is illustrated in Figure 2.3.

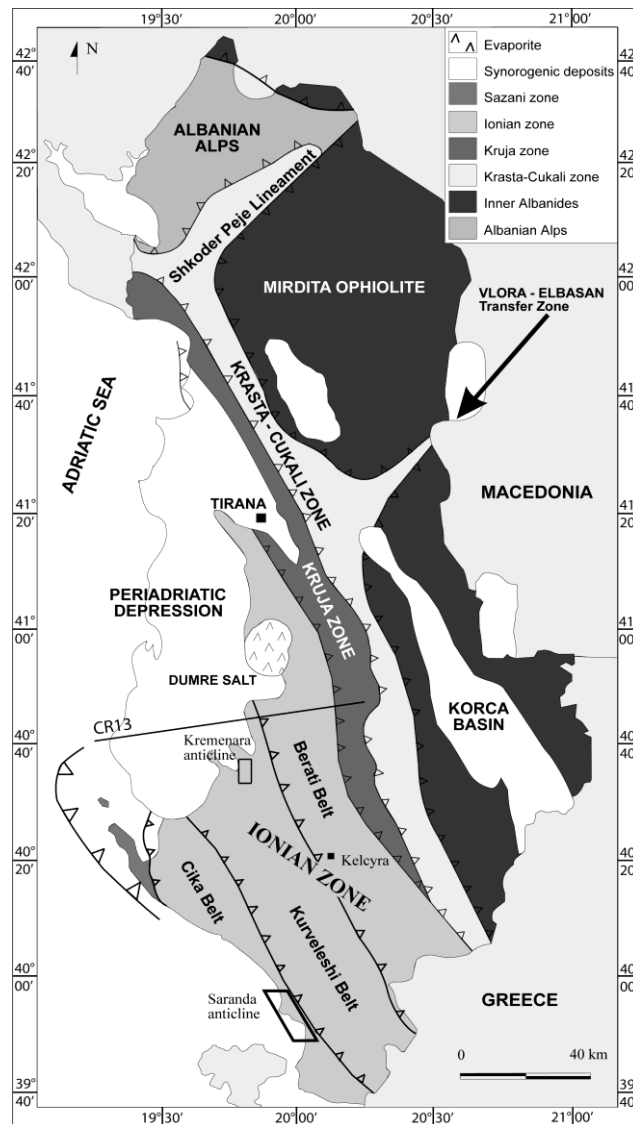


Figure 2.2. Structural map of the outer Albanides with the locations of the studied areas, i.e. Kelcyra area, Saranda and Kremenara anticlines (modified after Roure et al., 1998). The CR13 line indicates the location of the studied seismic profile, used for the fluid flow modelling.

The Albanides are derived from a former Mesozoic (Tethyan) passive margin and can be divided into two major divisions: the *inner* (i.e. eastern part) and *outer* (i.e. western part) *Albanides* (Papa, 1970; Shallo, 1991). These two major units can be split into several tectonostratigraphic sub-units, each of them being characterised by a former typical paleogeographic environment. Only the geology of the outer Albanides, which constitute a major petroleum province at the scale of the Mediterranean, will be presented in detail below. The outer Albanides are divided by a major transfer zone, i.e. the Vlorë-Elbasan lineament,

along which most of the oil and gas fields occur (Figure 2.2).

2.1.1- The inner Albanides

The inner Albanides are characterised by basic to ultrabasic magmatic rocks (ophiolite), derived from a former oceanic basin to the East (Shallo, 1992; Kodra and al., 1993) and some Palaeozoic to Mesozoic sediments. They are subdivided in four major tectonic thrust zones (Figure 2.2), the Mirdita zone (the main ophiolitic bearing zone), the Korabi zone and in the north, the Albanian Alps and the Gashi zone.

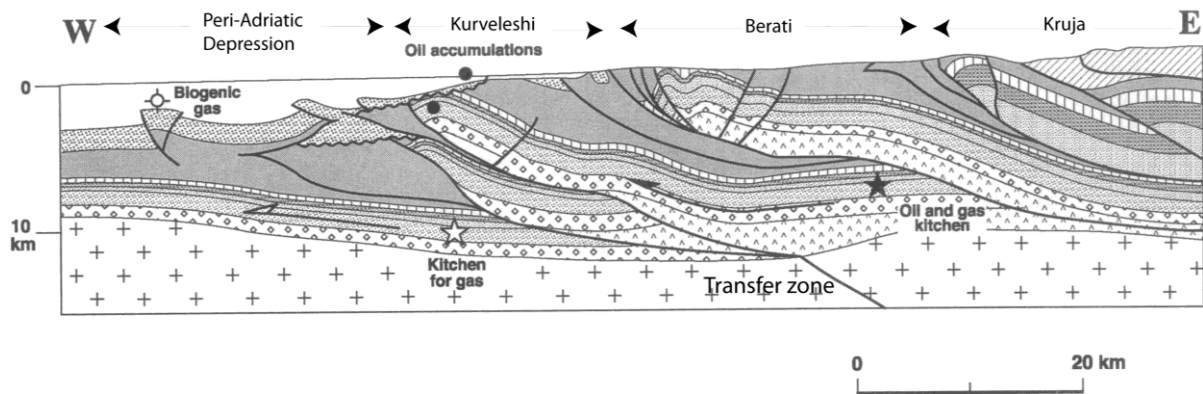


Figure 2.3. Structural interpretation of an E-W seismic profile, passing through the Vlora-Elbasan transfer zone, where all the major oil fields occur (from Roure et al., 1998).

2.1.2- The outer Albanides

The outer Albanides comprise a complex tectonic assemblage, made up of thin-skinned allochthonous units, progressively emplaced during Neogene deformations and mainly derived from the former Mesozoic passive margin of the Adriatic plate.

The northern part of the outer Albanides comprises two distinct domains: the Peri-Adriatic Depression in the west, which consists of Oligocene flysch and Neogene molasse deposits, and the Kruja zone, comprising thrust anticlines made up of Mesozoic platform carbonates (Figure 2.2).

The southern part of the outer Albanides, located south of the Vlora-Elbasan transfer zone, consists of Mesozoic-Paleogene basal units, which are detached from their former substratum

along intra-Triassic evaporitic series. Only the western part, consisting of the Sazani zone, is autochthonous and forms the extension of the Apulia platform. The Vlora-Elbasan lineament marks the transition area, where the Ionian Zone plunges below the Peri-Adriatic Depression.

From east to west, the Krasta-Cukali, the Kruja, the Ionian and the Sazani Zones have been differentiated (Roure et al., 1995; Swennen et al., 1998; Velaj et al., 1999; Meço and Aliaj, 2000). These zones correspond to horst- and graben structures (Figure 2.4) resulting from extensional tectonic regimes, dated as Early Middle Cretaceous (Gealey, 1988). The Sazani (i.e. Apulian platform) and the Kruja belts represent two former carbonates platforms, bordering the Ionian basin, which is at present split into three belts: the Berati, Kurveleshi and Cika belts (Meco, 1988; Shallo, 1990; Roure et al., 2004).

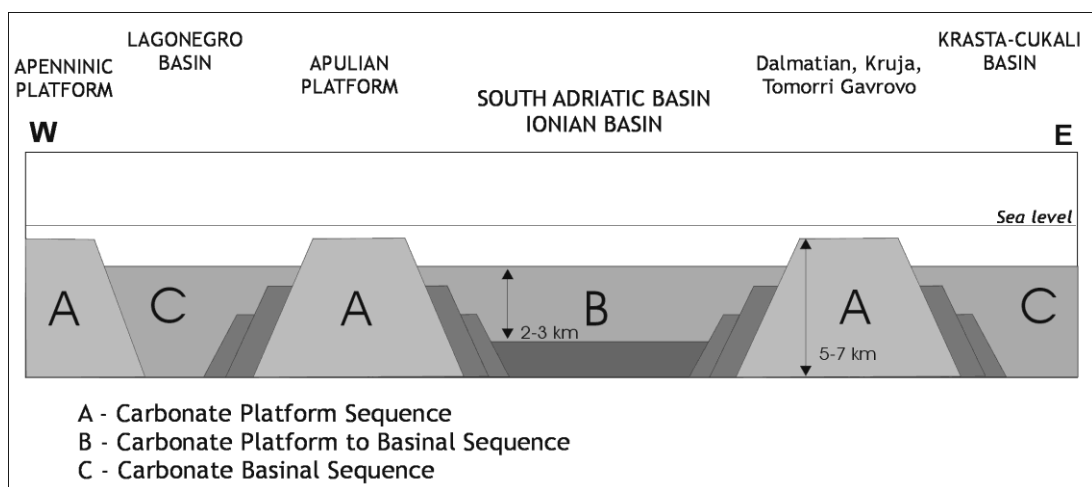


Figure 2.4. Schematic representation of the carbonate paleogeographic sequences during the rifting stage (modified from Zappatera, 1994).

Stratigraphically, the outer Albanides comprise a Triassic to Eocene carbonate sequence deposited in syn-rift and post-rift settings, covered by a thick Oligocene to basal Miocene flysch and early Miocene to recent molasse sedimentary succession (Figure 2.5).

2.1.2.1- Krasta-Cukali Zone: deep-water passive margin

The Krasta-Cukali zone has an intermediate location between the inner and the outer

Albanides. It is composed of Triassic terrigenous rocks and neritic limestones, Jurassic deep-sea sediments, Lower Cretaceous flysch, Upper Cretaceous pelagic limestones and Maastrichtian to Eocene flysch (i.e. 2 to 2.5km of siliciclastic turbidites). The Krasta-Cukali zone is underthrust in the east beneath the inner Albanides and is thrust over the Kruja unit in the west.

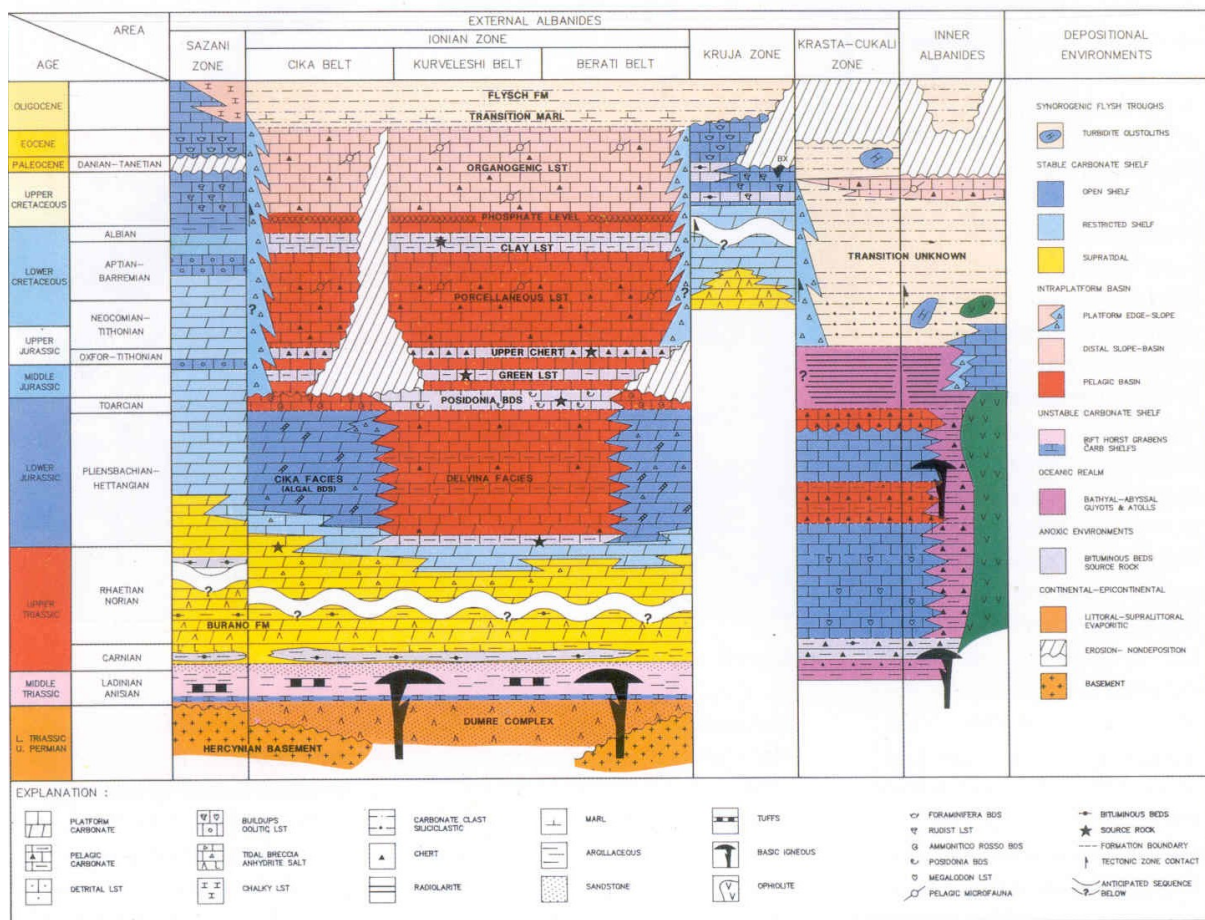


Figure 2.5. Overview of the stratigraphic evolution in the outer Albanides (Swennen et al., 1998).

2.1.2.2- Kruja Zone: marginal shallow-water carbonate platform

The Kruja zone, corresponding to a ridge, comprises a stack of duplexes, which have been partially identified by drilling. These structures have been detached from their Cretaceous substratum along Lower Cretaceous anhydritic horizons (well known in former Yugoslavia). It is characterised by several NW-SE oriented anticlines, which are overturned along their western flanks and wide synclines. The

geological sequence consists of a succession of Cretaceous to Paleocene-Eocene shallow marine limestones with rudists, bioclastic layers, dolomitic limestones and dolomites (Lula, 2002; Godfroid, 2007), intercalated with subaerial surfaces, bauxitic intervals, as well as frequent stratigraphical hiatuses. These shallow marine limestones are covered by the Oligocene transgressive series, made up of deep water turbidites (flysch). The latter records the progressive flexuring of the foreland and then, the involvement of the Kruja zone in the

Albanides foredeep. The upper part of the succession consists of the Tortonian to Pliocene series, deposited in piggy-back basins, attesting ongoing deformation.

2.1.2.3- Ionian Zone: deep water carbonates

The Ionian zone, located south of the Vlora-Elbasan transfer zone, corresponds to a broad trough. The Vlora-Elbasan lineament is a NE-SW trending zone, which separates the Ionian Zone in the south from the Peri-Adriatic Depression in the north. Most of the oil and gas fields occur along this lineament, where the Ionian Zone plunges below the Peri-Adriatic Depression.

The accumulations occur in both carbonate and clastic reservoirs. Their storage is largely improved by the presence of a dual matrix/fracture porosity. The Ionian Zone represents a thin-skinned fold-and-thrust belt with an evaporitic décollement level (Fraseri et al., 1996; Roure et al., 1998, 2005). It is dominated by large-scale folds, forming large synclines, filled with Early Tertiary flysch or Neogene clastics and anticlines, cut by high-angle reverse faults. The Ionian Zone is divided in three structural sub-zones, which are:

- the Berati anticline belt, corresponding to its eastern margin;
- the Kurveleshi anticline belt, in the central zone of the former basin;
- the Cika anticline belt, representing its western margin.

The oldest rocks are the Permian-Triassic evaporitic sediments, which are overlain by thick deposits made up of Upper Triassic-Lower Jurassic dolomitic limestones and by Upper Jurassic-Paleogene deep marine carbonates. Subsequently, a siliciclastic overburden, which consists of the Oligocene to Early Miocene flysch sequence, gradually changes to pre-molasse, which is subsequently overlain by coarse-grained porous Miocene molasse. This succession reflects the overthrusting that prograded from the east to the west of the Ionian basin.

2.1.2.4- Peri-Adriatic Depression

The overlying Peri-Adriatic Depression covers the Ionian, Sazani and part of the Kruja tectonic zones in the northern part of the outer Albanides. The Peri-Adriatic Depression consists of a foredeep filled with thick terrigenous syn-

flexural Oligocene flysch and a syn-kinematic Neogene molasse that is covered by Quaternary deposits. This unit is at present detached from its former Mesozoic - Paleogene carbonate substratum. From south-east to north-west, the thickness of the molasse increases. The total thickness of these siliciclastic deposits can exceed 7 km, based on seismic profiles. However, unlike in the Ionian Basin, no intra-Triassic décollement has ever been evidenced beneath the Peri-Adriatic Depression, accounting for a major paleogeographic change occurring on both sides of the Vlora-Elbasan transfer zone.

2.1.2.5- Sazani Zone: Apulian carbonate platform

In the south-western coastal area of Albania, the Sazani Zone belongs to the south-east prolongation of the Pre-Apulian and Apulian Zones of southern Italy (Papa and Kondo, 1968; Dercourt et al., 1980, 1986, 1993; Aliaj, 1987). It corresponds to the western margin of the Ionian Basin and forms a large anticlinal structure. The Sazani succession (Robertson and Shallo, 2000) consists mainly of Late Triassic-Jurassic limestones and dolomites, Cretaceous to Eocene neritic carbonates, unconformably overlain by thickening and coarsening-upward Early Miocene shallow-marine to fluvial, terrigenous clastics.

2.2- Sedimentological and litho-stratigraphical context of the Ionian Basin

The lithostratigraphy of the Ionian Zone (Figure 2.5) is well known from outcrop sections in central and southern Albania (Moorkens and Döhler, 1994). The stratigraphic column can be split into three major units: (1) Evaporites and dolomites representing the oldest rocks cropping out in the Ionian Zone, (2) a carbonate serie and (3) the siliciclastic overburden. Both of them reflect different structural stage during the formation of Albanides mountain range.

The lower part of the succession is made up of Triassic to Lower Jurassic dolomites and evaporites and reflects the rifting stage. The Early to Middle Triassic series consist of evaporite with some carbonate intercalations. Upwards an alternation of dolomite and evaporite beds occurs, which is followed by a massive crystalline dolomitic interval in the uppermost Triassic. These deposits reflect shallow water to lagoonal conditions.

This period is followed by a final break-up episode and by a post-rift subsidence after the Early Jurassic. Accumulation of Lower Jurassic to Upper Eocene deep water carbonates reflects predominantly basinal conditions and can be subdivided into two parts: the first one consists of pelagic limestone, containing several chert intervals. Two distinct phosphatic horizons occur regionally during the Albian, creating a characteristic marker bed for correlation. Above this level, the second part of the Ionian sequence extends from the Upper Cretaceous onward and consists of deep water carbonates, best described as an organogenic limestone (Van Geet et al., 2002).

Subsequently, the siliciclastic overburden, which consists of an Oligocene to Early Miocene flysch sequence changes gradually to pre-molasse, which is overlain upwards by a coarse-grained Miocene molasse. This period records the overthrusting from the east of the Ionian Zone.

2.3- Geodynamical background

The Albanian foothills result from the Neogene deformation of the former eastern passive margin of Apulia. Located west of the Mirdita ophiolite and Kruja Zone (Figure 2.2), the outer zones of the Albanian thrust belt are subdivided in two very distinct tectonic provinces by the NE-trending Vlorë-Elbasan lineament, with up to 10 km of Oligocene to Plio-Quaternary clastics being still currently preserved in the Peri-Adriatic Depression in the north, and Mesozoic carbonates of the Ionian Zone being directly exposed at the surface in the south (Figure 2.2). As evidenced on seismic profiles, the main décollement level is localised within Triassic evaporite and salt in the south, ramp anticlines accounting for the tectonic uplift of Mesozoic carbonates in the Ionian Zone. In the north, the main décollement level is located within the Cenozoic clastics, where no carbonate reservoirs are exposed at the surface. Accordingly, the Vlorë-Elbasan transfer zone is best described as a lateral ramp connecting these two distinct décollement surfaces (Roure et al., 1995, 2005). A schematic evolution of the development of the Albanides is described in Figure 2.6.

2.3.1- Evolution of the Tethyan passive margin and deposition of carbonates

Tethyan rifting (Figure 2.4, Figure 2.6) accounts for the development of Late Triassic to Liassic

tilted blocks and grabens, thick organic-rich dolomitic platform carbonates characterising the paleo-horsts and Liassic blackshales (Posidonia Shales) deposited in the grabens (Karakitsios, 1989, 1990; Zappatera, 1994; Meço and Aliaj, 2000). These organic layers account for the two main source rock intervals of the basin. Post-rift thermal subsidence resulted in the formation of deep water cherts during the Middle and Upper Jurassic in the Ionian Basin (Xhomo et al., 1971), whereas prograding Cretaceous carbonate platforms from the Kruja Zone in the east, and from the Sazani Zone in the west, contributed as a distal source for the thick carbonate turbidites deposited in the Ionian Basin during the Late Cretaceous and Paleocene (Velaj et al., 1999). These turbidites, which reworked platform carbonate material (Van Geet et al., 2002), are interbedded within finer grained pelagic carbonates, and constitute the main hydrocarbon reservoirs onshore Albania, but also offshore in the Italian part of the Adriatic.

2.3.2- Foothills development and sedimentary records of the deformation

Up to 10 km of synflexural and synkinematic siliciclastic series have been deposited in the Peri-Adriatic Depression, ranging from near-shore and littoral facies in the east and south, towards deeper water and turbiditic facies in the north and in the west (offshore), providing a unique and continuous sedimentary record of the deformation (Frasheri et al., 1996). Sequence stratigraphy and bio-stratigraphy by means of foraminifer and nannoplankton studies in pelagic facies are able to provide accurate correlations of very good resolution for the dating of geologic events in this basin:

- Tectonic loading applied by the hinterland (Mirdita ophiolite) from the Late Cretaceous onward and westward thrusting of far-travelled basinal units of the Krasta Zone induced the progressive development of a wide flexural basin, which ultimately impacted the outer Albanides lithosphere in Oligocene times (Kodra and Bushati, 1991; Mello et al., 1991a, 1991b; Shallo, 1991, 1992; Swennen et al., 1998). The first deformations affected the Kruja platform during Middle Eocene times.

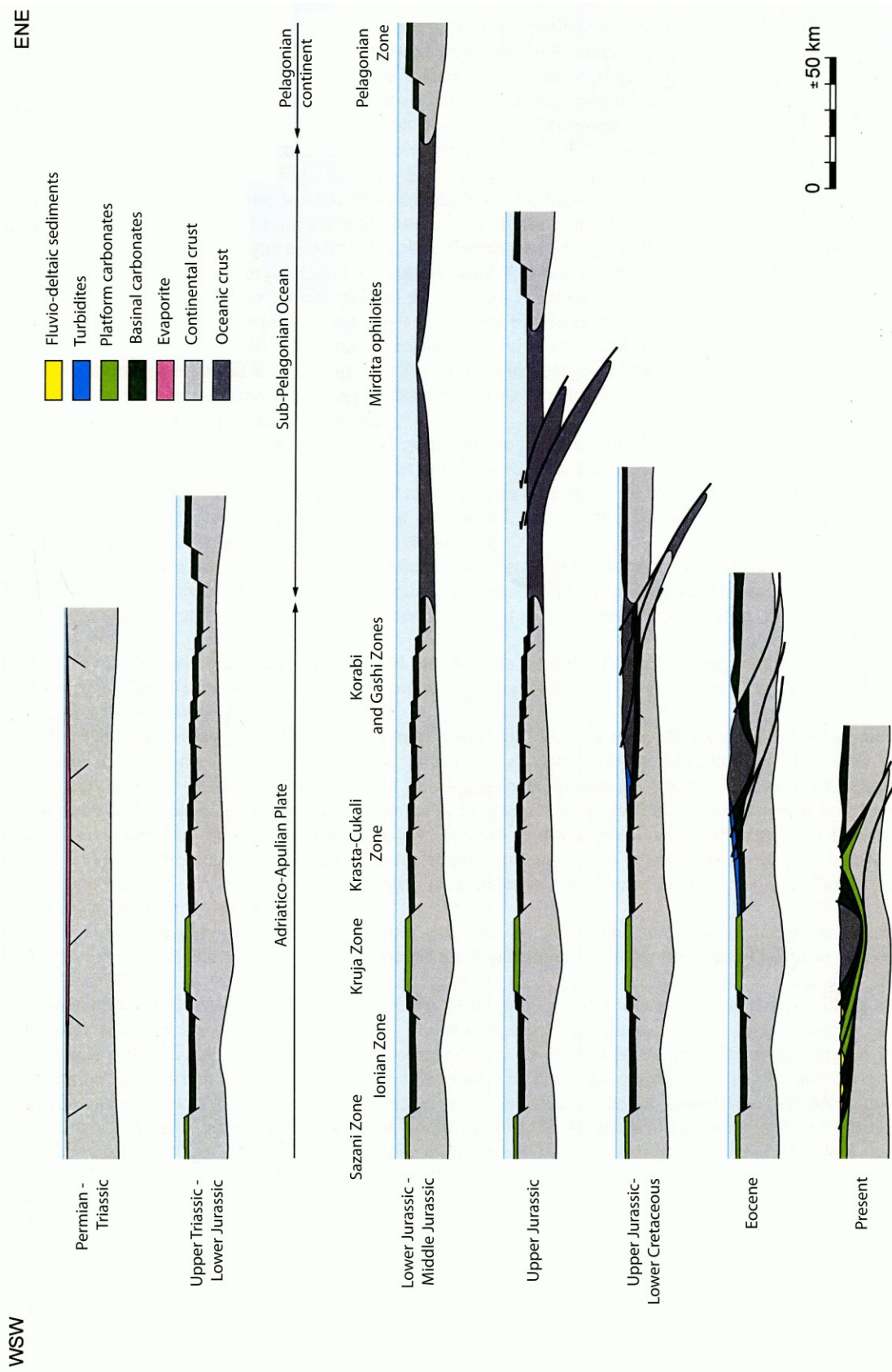


Figure 2.6. Schematic evolution of the Albanides from the Lower Triassic to Present-day (from Barrier et al., 2003; and reference therein). Notice that the thicknesses are not to scale.

- Growth anticlines started to develop in Late Oligocene-Aquitainian in the Ionian Basin (Velaj et al., 1999; Meço and Aliaj, 2000; Robertson and Shallo, 2000; Nieuwland et al., 2001), accounting for the development of Burdigalian reefal facies and paleokarst at the crest of the Kremenara anticline. This main episode of shortening being sealed by Langhian - Serravalian clastics (Swennen et al., 1998).

The second episode of tectonic shortening is best documented near the Vlora-Elbasan transfer zone (Roure et al., 1995, 2005) and farther north in the Peri-Adriatic Depression, where Pliocene backthrusts account for major lateral and vertical offsets of a pre-Messinian erosional surface. Although Neogene deposits are mostly absent from the Ionian Zone itself, it is obvious that this post-Messinian tectonic episode strongly affected also the southern part of the Albanian Foothills, thus increasing the deformation in both Kremenara and Saranda anticlines, which will be further discussed in more detail (Tagari, 1993; Breesch et al., 2007).

Apart of thrusting and development of ramp anticlines, these Neogene episodes of deformation have also contributed to remobilise former salt diapirs, i.e. in the Dümre area (Monopolis and Bruneton, 1982; Underhill, 1988; Bakiaj and Bega, 1992; Velaj and Xhufi, 1995), where an allochthonous salt unit has been thrust along a low-angle fault over underlying carbonate duplexes and deformed Cenozoic clastics. At this stage however, it is difficult to date the onset of the salt motion, and at which time Triassic salt indeed breached the surface (Velaj et al., 1999).

2.3.3- Kinematic evolution

The Ceres model, which was inferred from the Thrustpack kinematic modelling (Barrier et al., 2003, 2005), is illustrated in Figure 2.7. It comprises seven major episodes, summarising the geodynamic evolution of the Albanides:

- End of the passive margin (i.e. Eocene) and flexuring of the foreland basin, which was filled by the Oligocene flysch, due to the active folding in the inner Albanides until the Aquitainian (-20.52 Ma).

- Thrust emplacement of the Kruja belt, resulting in the flexuring and turbiditic

sedimentation in the Ionian Basin from the Burdigalian onward (-16 Ma).

- Onset of the thrusting in the Ionian zone during the Serravalian (-11.6 Ma) and subsidence of the foreland.

- Out-of-sequence thrusting, accounting for the development of an intermediate tectonic unit in the Ionian Basin (i.e. Berati belt) during the Early Tortonian (-8.5 Ma), causing the tectonic subsidence of the Kurveleshi unit.

- Maximum shortening of the Ionian zone recorded during the Tortonian (-7.5 Ma), causing an important flexural subsidence in the foreland. At the same time, the eastern thrust units were uplifted and partially eroded.

- Burial increases related to thrusting and coeval syn-orogenic sedimentation in the foreland, which amplified the flexural subsidence. The compressive front was still active and many compressive structures were growing in the foreland during the Messinian (-5.3 Ma). This period is also characterised by an important erosion of the Kruja unit.

- The present day profile shows partial erosion of the Oligocene seals located at the top of the tectonic units that allows the unroofing and emersion of the main reservoir interval in the Kruja and Berati belts. The compressive structures located in the Peri-Adriatic Depression are still active.

2.4- Décollement level

Five major décollement levels, characterised by a regional distribution, were determined in the Albanides, accounting for the development of thin-skinned structures. They consist of the (1) Triassic evaporite (Roure et al., 1995; Velaj et al., 1999); (2) the Toarcian Posidonia Schist; (3) the Aptian-Albian shales, all of them occurring within the Ionian Basin (Swennen et al., 1998).

Another major décollement level in the Ionian Basin is defined by the Oligocene flysch and pelitic interbeds of the Neogene molasse (Roure et al., 1995). The latter occurs in the Peri-Adriatic Depression and also accounts for localised backthrusts along the western flank of the Kremenara anticline. A last decoupling horizon occurs in the Kruja belt in the Cretaceous evaporites.

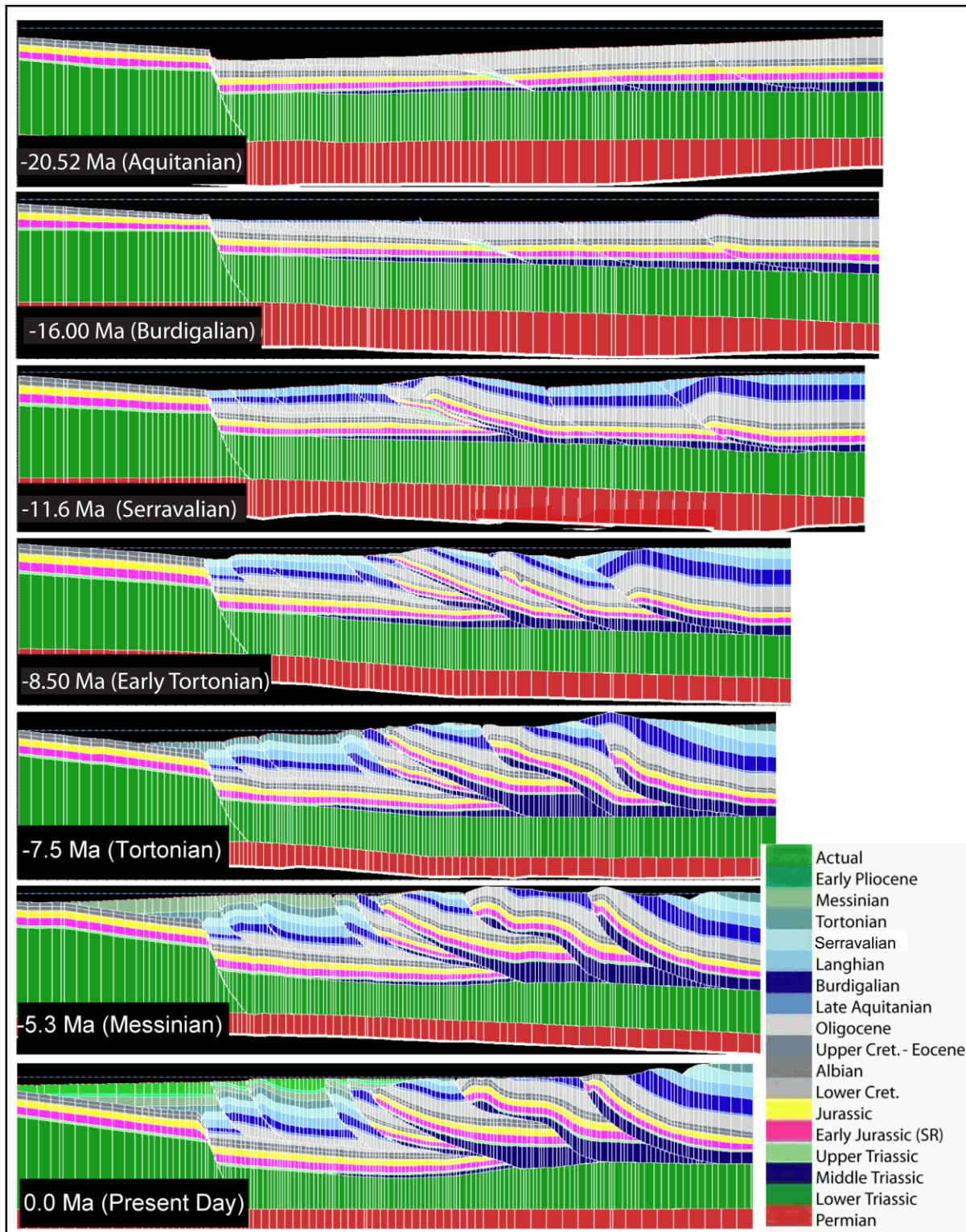


Figure 2.7. Kinematic evolution of the Ceres model along the CR13 section from the Aquitanian to present-day.

2.5- The Triassic interval: a major interest for petroleum exploration

Since many years, the Triassic platform carbonates associated with evaporites have been of major interest for petroleum exploration in the Mediterranean region (e.g. Italy, Spain, Greece;

Travé et al., 2000; Marfil et al., 2005). The interplay between carbonates and evaporites is very significant during any orogeny, as it controls the seal characteristics of the reservoirs, their ductile behaviour during tectonic deformation, the occurrence of high thermal

conductivities, and diagenetic processes (i.e. tectonic-induced dolomitisation).

Sometimes the potential reservoir qualities of carbonates can improve, especially in relation to the dehydration of the gypsum that can create pore fluid overpressure and consequently hydrofracturing (De Paola et al., 2007) during the burial stage. At present, the Upper Triassic dolomitic interval (Van Geet et al., 1997) consists of cyclic sequences, characterised by the occurrence of mud at the base, followed by evaporitic strata, containing many dissolved chicken-wire fabrics, and dolomite collapse breccias at the top, testifying of the dissolution of the evaporite (Figure 2.8).

In the Ionian Zone, the Triassic evaporitic succession (i.e. an alternation of gypsum-anhydrites, dolostones and clays) is locally up to

2.5 km thick. The latter reflects hypersaline, shallow-water depositional conditions.

2.5.1- Evaporitic occurrences

Lower Triassic evaporite (i.e. mainly gypsum) is widespread in the Albanides and constitutes the main décollement level of the Albanides foreland fold-and-thrust belt (FTB). Triassic evaporite locally crops out but is more common in the subsurface, where it either forms diapirs or flows along main faults. Two main types of diapirs (Velaj, 2001) are recognised in the Ionian Basin: (a) those that are emplaced along longitudinal tectonic faults (i.e. NNW-SSE thrust faults), where they intersect transversal ones (i.e. NE-SW rifting faults), as the Dümre diapir (Figure 2.1); and (b) diapirs that are located in local structures such as in the core of anticlines (i.e. the Delvina, Bashaj, Fterra diapirs).

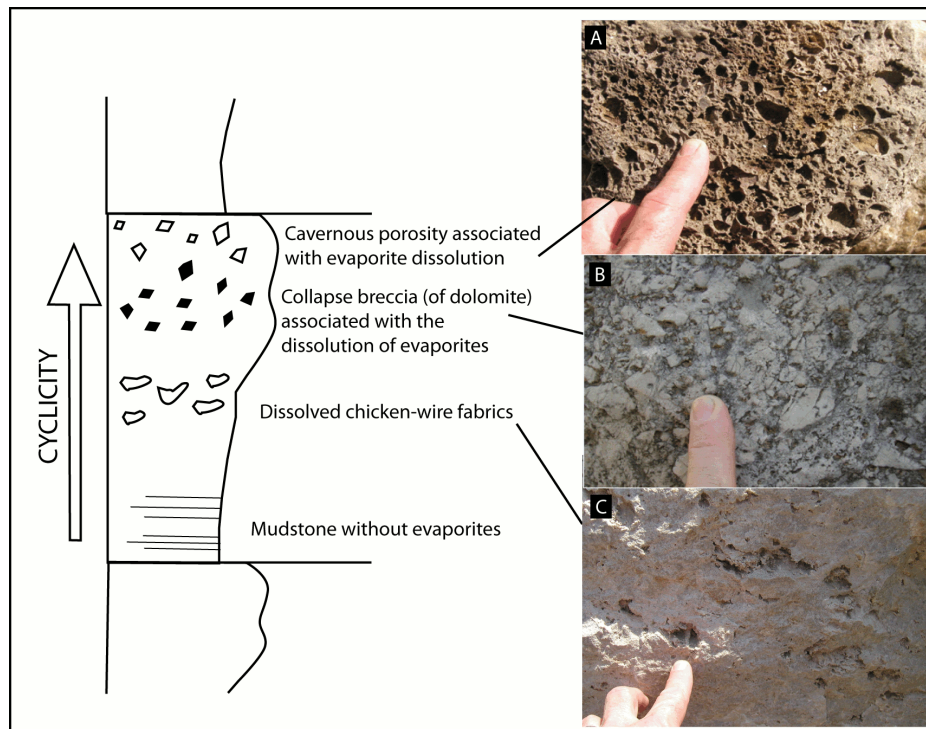


Figure 2.8. Evolution of the dolomitic interval, characteristic for Upper Triassic interval and showing the dissolution of the evaporite.

Since the mechanical properties of the evaporites changed through the geodynamic evolution of the basin, according to the applied stress, pressure and temperature regimes, the mode of formation of diapirs is actually still discussed. After sedimentation the first step of their formation occurred prior to the orogeny during the extension stage (i.e. rifting period) from the Late Triassic till the Early Cretaceous (Figure

2.9). During this period, the light evaporites have migrated vertically according to the gravitational forces. They have been subsequently affected from the Oligocene onward by folding and thrust tectonics. The normal faults were then reactivated and inverted as thrusts or strike-slip faults, forcing the evaporites to move towards lower pressure gradients. According to Velaj (2001), most Albanian diapirs have been thrust

westward with a displacement exceeding 20-30 km, which is in agreement with the average shortening of the main thrust units.

2.5.2- Dolomitic intervals

Recently, Triassic evaporitic, shaly and dolomitic intervals, cropping out in the south-western part of the Ionian Basin (Kurveleshi unit, Delvina area) have been investigated by Muska (2002), especially in an attempt to understand the formation of the Upper Triassic dolomites and the thermal evolution of the Kurveleshi tectonic unit. It appears, based on petrographic studies, that the dolomites formed by dolomitisation of an initial limestone, deposited during the rifting stage. This early diagenetic process occurred before the dissolution and brecciation of the

Triassic evaporites. The fluid inclusion analyses, performed on these dolomites, display a maximum homogenisation temperature of 80°C (Muska, 2002), which can be related to the maximum burial during the Late Oligocene. However, the thermal evolution of the Triassic interval is not homogeneous along the Albanides, since the tectonic units have not been formed and thrust simultaneously. In fact, the Kurveleshi unit was the first unit to be uplifted with the Cika belt, whereas the Berati and Kruja units have been developed out-of-sequence (Chapter 8). Finally, even if only low temperature dolomites occur in the Delvina oil field (in Kurveleshi unit), high temperature dolomites may exist locally in deeper buried structures (i.e. Berati and Kruja units).

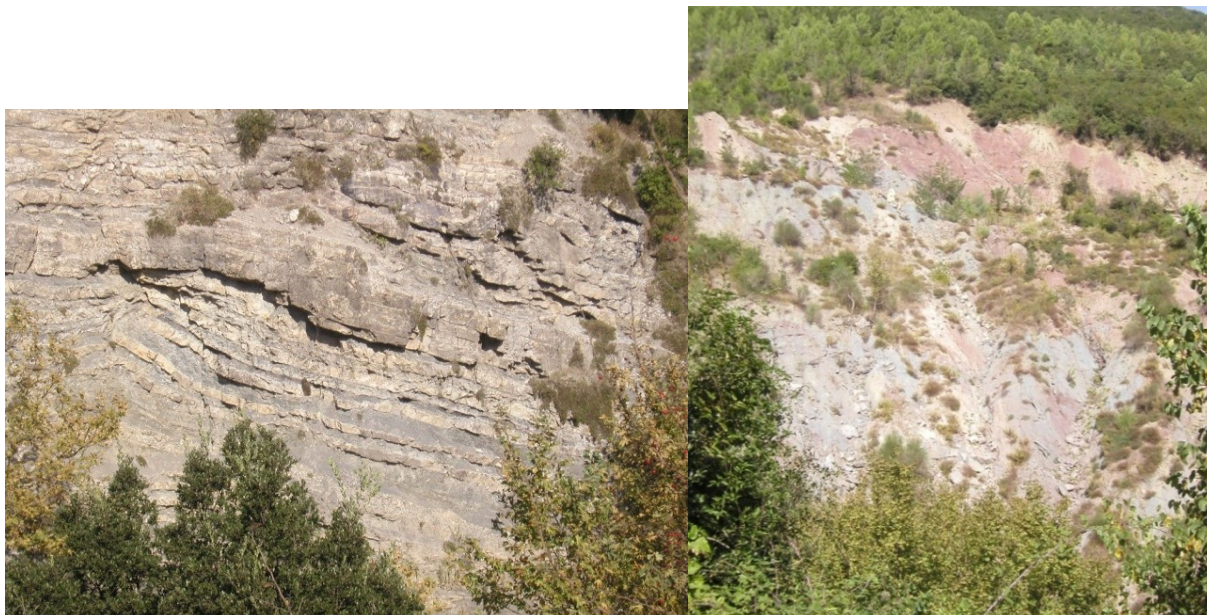


Figure 2.9. Pictures of the Triassic interval. Notice that the base is more siliciclastic with green marls (picture on the left), indicating an anoxic environment, whereas the top of the formation evolves towards carbonate system and displays red marls (picture on the right) due to the sea level fluctuations.

CHAPTER 3- PETROLEUM SETTING

Petroleum exploration started at the beginning of the XX century in Albania (Ineichen, 1934; Macovei, 1938; Mayer-Gürr, 1953; Lazzari, 1964; Marku, 1992; Moorkens and Döhler, 1994). Over 1000 exploratory wells and some 3500 oil and gas production wells have been drilled. However, since 1991, the drilling activity has practically stopped, because of financial and technical supply problems and the high costs that are linked with drilling subthrust exploration plays.

3.1- History of petroleum exploration

The first Albanian oil discoveries were made by Italians in the 20's in bituminous Messinian sandstones (i.e. Drashovice oil field). Subsequently, the Patos (1926), and the Kuçova (1928) fields were discovered within the Miocene sands onlapping older rock sections.

In the 50's, Russian technology allowed to carry out onshore seismic operations, promoting the discovery of the Marinza oil field (1958) within the Tortonian sandstone, helping to considerably increase the production.

In the 60's, a more realistic image of deep structures led to the first discoveries within deep carbonate reservoirs, i.e. Cretaceous to Eocene intervals, in the Ionian Zone, such as the Gorisht-Koculli (1963), Cakran and Ballsh (1964) fields. Until 1975, ten more fields within carbonates, were brought on stream and the production increased up to approximately 2 250 000t/year. Additionally, gas fields, i.e. Frakulla and Divjaka-Ballaj, were discovered in anticlinal structures within the Mio-Pliocene intervals in the western part of the Peri-Adriatic Depression (PAD).

From the 80's, intense exploration in the known areas led to the discovery of other fields, such as Durrës, Ballaj, Frakülle, Povelcë and Panaja gas fields, as well as the Delvina gas and condensate field in southern Albania. Since then, a large coverage of seismic profiles has been recorded onshore, some regional profiles being even recorded and processed down to 7s twt, thus imaging the entire sedimentary column.

Since 1995, foreign companies, i.e. Occidental, OMV, Chevron, Deminex, Hamilton, Shell and Agip have been invited to operate in Albania, providing for the first time seismic images of the offshore domain. At present, however, no deep well has yet been drilled to reach subthrust objectives below the Kruja allochthon, nor in the tectonic windows where the outer zones are again exposed, east of the Mirdita ophiolite. From a petroleum point of view, the External Albanides, comprising also the Neogene molasse basins, represent the main interest in Albania.

A summary of the main oil and gas reservoirs in the Albanides are described in the Table 3.1 and located in Figure 3.1.

3.2- Source rocks

Potential source rocks (Figure 3.2) have been identified in both Mesozoic carbonates and Cenozoic terrigenous series. The Upper Triassic to Upper Cretaceous carbonates of the Ionian Zone contain several rich to very rich source rock intervals (Curi, 1993; Dulaj and Basha, 1998), the principal being:

- The Upper Triassic and Liassic series represent the oldest potential source rocks in most Apulia. Bituminous Upper Triassic dolomitic schists were reached in the Sazani Zone and are expected to be equivalent to the Burano Formation in Italy (Paulicci et al., 1988; Mattavelli et al., 1991). Contemporary bituminous rocks, up to 15m thick, crop also out in the Cika belt, in the Ionian Zone. These Upper Triassic source rocks contain up to 4.96% TOC, whereas Ro (vitrinite reflectance) grades from 0.7 to 0.87, which indicates a mature source.

- Toarcian shales indicate an immature source-rock in surface conditions, with TOC values of 5% and Ro as low as 0.55 (Danelian et al., 1986; Baudin et al., 1988, 1989, 1990; Jenkyns, 1988). These Toarcian series correspond to the widespread Posidonia Shale (Figure 3.3), up to 300m thick, accounting probably for most oil production in the Ionian Basin (Albpetrol, 1995).

Oil field	Reservoir	HC type	Disco. year	Reservoir depth (m)	Permeability (mD)	Porosity (%)	Density (°API)	Cumul prod. (MMbb)
AMONICA	Frac. Carbonate	oil	1981	1000-3000	40-300	4 to 5	13	32.8
BALLSH	Frac. carbonate	oil/gas	1966		200-400	10 to 25		
BUBULLIMA	Frac. carbonate							
CAKRAN	Late Mioc. Sst. +	oil/gas/cond.	1963	> 1800				
DELVINA	Frac. carbonate	oil/gas/cond.	1977	3000-4500	2-600	4 to 5	11.5 to 37	19.3
DRASHOVICA	Frac. carbonate	gas/cond.	1987		0.2	3 to 5	23.5 to 26	2.5
FINIQ	Oligocene Flysh Sst.	heavy oil	1919	200-1000		10 to 25		
GERNEC	Frac. carbonate	oil	1970	800-2000		3 to 4		
GORISHT-KOCUL	Frac. carbonate	oil			300	4 to 5	13 to 16	78
HEKAL	Frac. carbonate	partly heavy oil	1965	1000-2500	40-300	4 to 5	13	32.8
KARBUNARA	Frac. carbonate	oil	1966					
KOLONJA	Late Mioc. Sst.	oil						
KRANE	Frac. carbonate	oil						
KRESHPAN	Frac. carbonate	oil + gas	1970	800-2000		3 to 4		
KUCOVA	Late Mioc. Sst.	oil	1929	surface to 1500	70	22.8	14.5 to 22	23.3
MARINZA	Late Mioc. Sst.	partly heavy oil	1957	1200-1800	550	24.2	9 to 24	28
MOLLAJ	Frac. carbonate	oil	1957					
PATOS	Frac. carbonate	oil + gas	1977		2-600	4 to 5	11.5 to 37	19.3
PEKISHT-MURIZ	Late Mioc. Sst. +	partly heavy oil	1927	surf. To 1200		10 to 30	012-24	
VISOKE	Late Mioc. Sst.	oil	1963		200	4 to 5	5 to 16	37.6

Gas field	Reservoir	HC type	Discovery year	Permeability (mD)	Porosity (%)	Cumul prod. 10 ⁶ m ³	Depth reservoir (m)
BALLAJ	Plioc. Turb. Sst.	gas	1983	2 to 35	16-32	331	300-1700
DIVJAKA	Plioc. Turb. Sst.	gas	1963	2 to 35	16-32	371	300-1700
DURRES	Late Mioc. Sst.	gas	1970	7-300	13-30	1371	2400-3100
FRAKULLE	Late Mioc. Sst.	gas	1989	2200			
PANAJE	Late Mioc. Sst.	gas	1965	7-300	13-30	240	270-2500
POVELCE	Late Mioc. Sst.	gas/cond.	1989			16	2500
SELENICA	Plioc. Molasse + Oligocene Flysh Sst.	gas bitumen	1987	7-300	13-30	160	1800-3500

Table 3.1. List of the main Albanian oil and gas fields (based from Sedjini, 1990; Petroconsultants, 1991; Flores et al., 1991; Albpetrol, 1992). Abbreviations: Frac. carbonate = Fractured carbonate, mainly Eocene to Cretaceous limestones; Late Miocene Sst. = Messinian, Tortonian (Serravalian) deltaic to shallow marine sandstones; Plioc. Turb./ Molasse Sst. = Pliocene turbiditic deep water fan sands and occurrence of shallower water sandstones.

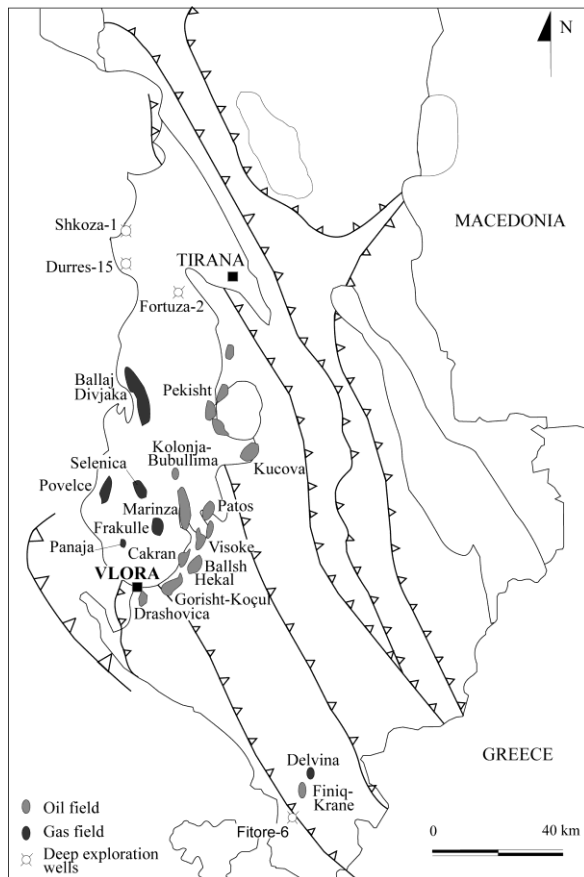


Figure 3.1 Map of Albania showing major oil and gas fields and selected deep exploration wells (from Petroconsultants, 1991).

According to some Albanian geologists (Albpetrol, 1992), TOC values average up to 5% and may locally reach 29%.

- - Middle Jurassic bituminous black shales and clays occur in the Kurveleshi belt and consists of thin, organic-rich intercalations. TOC values reaches up to 5.25% with R_o ranging from 0.52 to 0.57.

- Upper Jurassic organic-rich horizons can reach a maximum TOC of 1.5% with R_o values of 0.51.

- Bituminous Cretaceous schists, with TOC of 1 to 27% and vitrinite reflectance of 0.41-0.44%.

For all the detailed source-rocks, the kerogen is predominantly of type I or of type II.

In the Peri-Adriatic Depression, two other source-rocks occur:

- the Early Tortonian shales.
- the Late Neogene part, containing some lignites and brown coal deposits. It generates gas from type III kerogen, characterised by a low

TOC (below 0.4%). They occur mainly below the Messinian evaporite, in the deltaic sediments of the Early Messinian and the Pliocene. As they were never deeply buried, they are still immature, characterised by vitrinite reflectance of 0.3-0.4%. Based from Valbona and Nazaj (1990), they are assumed to be the source of the biogenic gas.

3.3- Reservoirs

In Albania, oil and gas accumulations (Figure 3.2) are present in carbonates and sandstones of the molasse formation (Curi, 1993; Misha et al., 1999; Sazhdanaku et al., 1999). Some petrophysical studies were done near productive fields in the Kruja and Ionian Zones, as well as in the Peri-Adriatic Depression. Some results are summarised on the Table 3.1.

Fractured carbonate reservoirs range in age from Cretaceous to Eocene and consist essentially of pelagic facies of the Ionian Basin, associated with slumping horizons and turbidites. One of the most famous reservoir analogues (Figure 3.4) of the Upper Cretaceous to Paleocene reservoir interval is located in the Male I Gjere section, south of the Ionian Zone, i.e. the Kurveleshi belt. Typically, carbonate reservoirs have low matrix porosity, however, their storage is largely improved by the presence of open fractures, developing a dual porosity.

As observed in the Cakran, Gorisht and Ballsh fields (Albpetrol, 1992), fracture porosity generally averages up to 4 or 5% in the top of the anticlinal structures, with permeabilities between 44 and 224 mD.

Clastic reservoirs of the Peri Adriatic Depression occur in the terrigenous flysch and molasse sequences, mainly in the Tortonian-Pliocene interval, which can be divided into 2 groups:

(1) a transgressive Messinian molasse. These reservoirs are formed by deltaic sandstones with porosities comprising between 10 and 30% and permeabilities of 200-2000mD. All these sandstone reservoirs are at least locally oil-bearing;

(2) the gas-condensate bearing fields of the Peri-Adriatic Depression occur in Late Miocene molasse sandstones or in Pliocene turbiditic sandstones. The Pliocene sandstone presents porosities ranging from 15 to 30%, and low permeabilities with values up to 45mD.

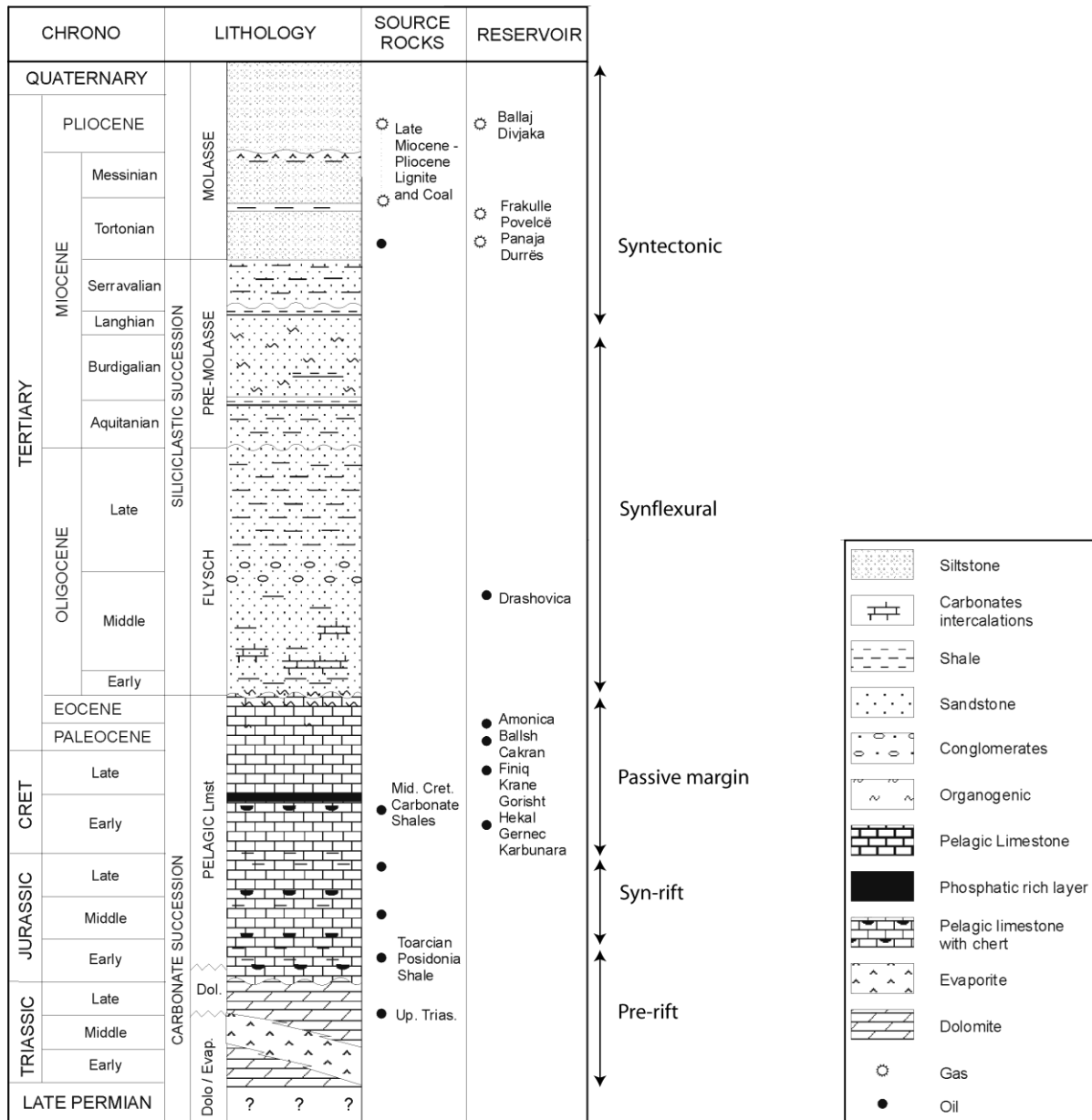


Figure 3.2. Schematic lithostratigraphic log, characterising the sedimentary evolution of the outer Albanides, with the main source rocks and oil/gas reservoirs. On the right side, a brief kinematic evolution of the Ionian Zone is given (modified from Dalipi et al., 1971; Albpetrol, 1992).

3.4- Seals

Numerous stratigraphic intervals have good seal capacities, with some having a wide regional extent. Generally, the Oligocene flysch constitutes the best stratigraphic seal for underlying fractured carbonate reservoirs, located in the Ionian Zone. Oil and gas accumulations occur generally in anticlines, partially or totally sealed by the Oligocene flysch or even the Neogene molasse, such as the

following reservoirs: Ballsh, Visoka, Cakran, Gorishit, Hekal and Delvina fields.

However, where the Oligocene flysch has been tectonically removed, the Upper Triassic evaporite of overlying allochthonous units also constitutes a composite stratigraphic and structural seal, as it is the case for the Pekist and the Delvina oil fields.



Figure 3.3. Rock sample of the Posidonia shale, i.e. Toarcian serie, accounting for most oil production in the Ionian Zone

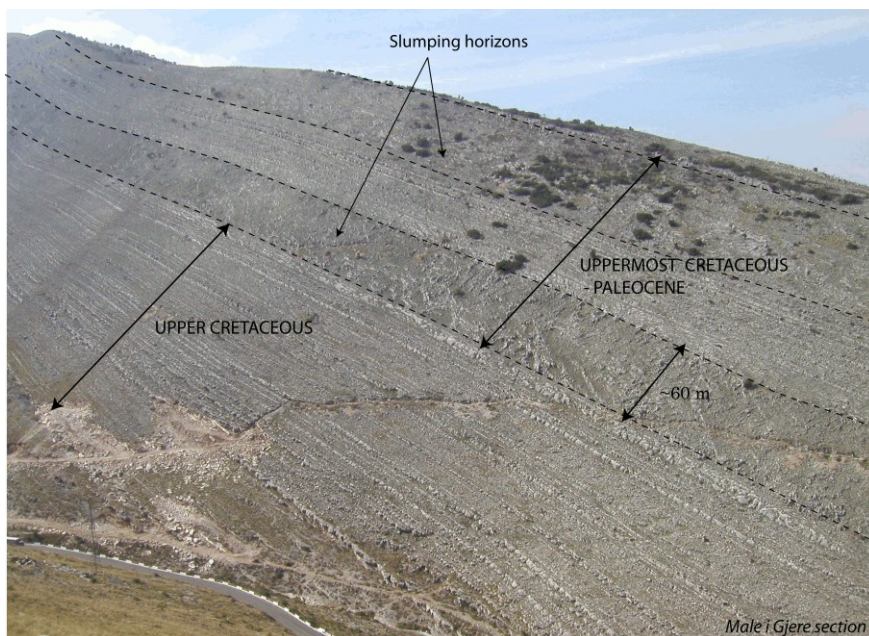


Figure 3.4. Picture of the Male I Gjere reservoir analogue for the main Upper Cretaceous to Paleocene reservoir interval. Notice that two main slumping horizons occur in the Uppermost Cretaceous to Paleocene intervals.



Figure 3.5. Pictures of the Patos field. Oil seeps in sandstone interval occur in the matrix and fracture porosity.

In the Peri-Adriatic depression, and even in the Neogene piggyback basins, i.e. the Marinza field, the traps are stratigraphic and structural-lithological, and formed during Pliocene or post-Pliocene tectonism. Here, the Messinian and Pliocene shaly interbeds constitute the major

seals for sandstone reservoirs. However, lateral facies variations occur, limiting the petroleum storage. At least, large amounts of bituminous deposits generated during heavy oil expulsion (Langhian and Messinian) constitute good superficial seals (i.e. Patos field, Figure 3.5).

In brief, the four major petroleum plays in Albanian consist of:

- the Messinian oil-bearing and tar-sands at the base of piggyback basins overlying the Ionian units;
- the gas-bearing Pliocene sandstones of the Peri-Adriatic Depression;
- the oil-bearing Cretaceous to Eocene carbonate in anticline structures in the Ionian zone;

- the Paleocene-Eocene platform carbonate reservoirs in the duplex zone of Kruja.

Some other places, as in the Vlora area, i.e. Ardenica and Fitore (Sejdini, 1990), have some oil occurrences but they are actually considered to be non-commercial.

CHAPTER 4- METHODOLOGY

4.1- Research strategy

One of the most important objectives of this research is to unravel the paragenetic sequence in the different areas studied, mainly based on field and petrographic observations, and to evaluate possible fluid sources and flow pathways by using mainly geochemical and microthermometric analyses of fluid inclusions. Figure 4.1 represents briefly the work flow and methodology followed.

The characterisation of the nature/origin of the fluids and water-rock interactions is necessary to obtain a precise chronology as well as information of potential cementation, diagenetic alteration and/or porosity development. This requires an integration of many elaborated techniques, including: (1) a detailed field survey

to establish a primary chronology of the diagenetic features observed. At the same time a thorough field sampling is realised and fracture orientations are recorded as well as the cross-cutting relationships between the different veins (i.e. fracture fillings) and diagenetic phases; (2) an accurate petrographical (e.g. classical petrography, cathodoluminescence microscopy, scanning electron microscopy) and geochemical study (e.g. stable isotopes, Sr-isotopes, multi-element characterisation by means of electron microprobe analysis) and other techniques (e.g. porosity - permeability measurements, microthermometry, ...) in order to characterise the different generations of diagenetic phases and veins and to link this to their fluid composition and origin.

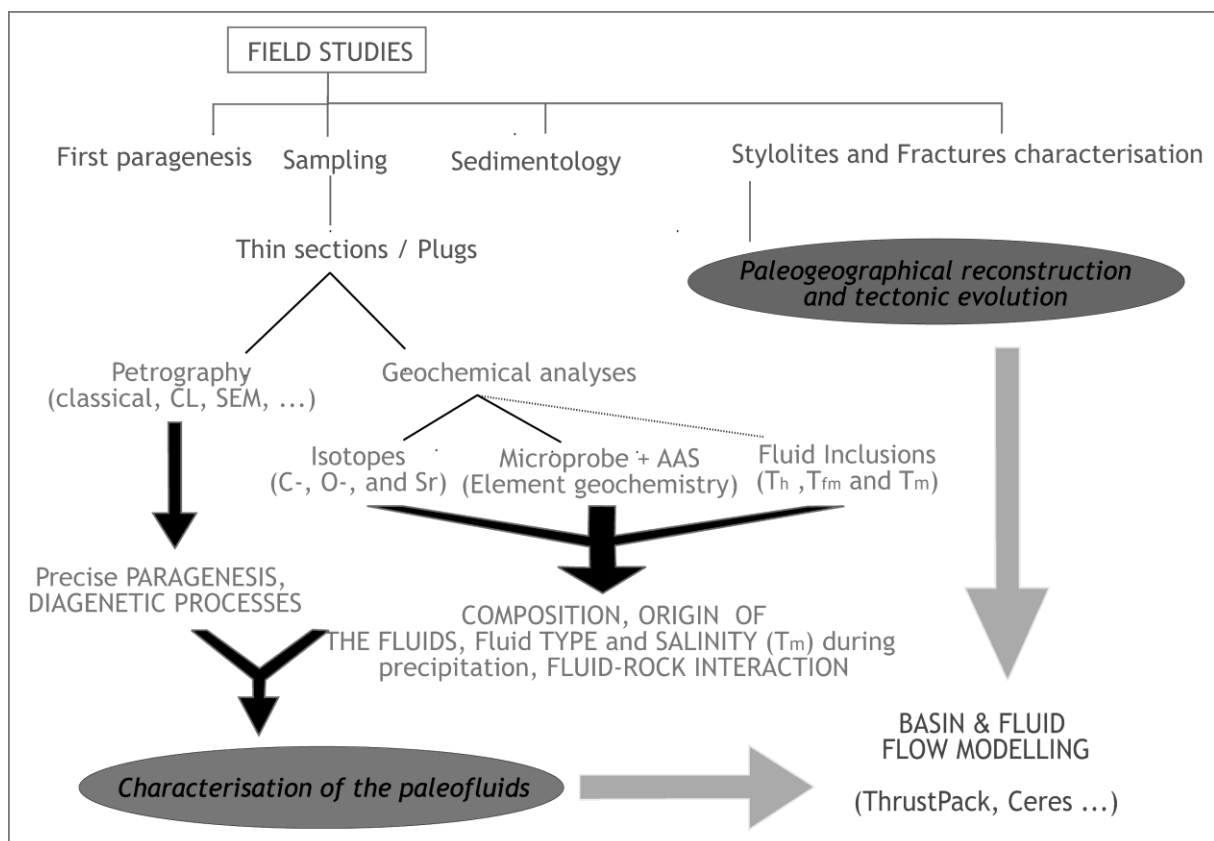


Figure 4.1. Methodology followed to characterise the fluid flow.

Cemented fractures can also be classified based from a structural point of view; they can be grouped according to their orientations.

However, the structural measurements have not been determined for all vein sets. Moreover, many veins, which are grouped in the same

generation from a structural point of view, display strongly different petrographical and geochemical characteristics, complicating the subdivision of the veins.

Veins have been sampled to characterise the fluid flow evolution and the water-rock interactions as well as the main migration pathways for the water and other fluids during the successive steps of the kinematic evolution of the Ionian Zone.

Based on field observations, mutual cross-cutting relationships between veins and/or with stylolites, cathodoluminescence (CL) and stable isotope analyses, the main episodes of porosity development and destruction and of related fluid migration during the evolution of the FTB can be subdivided into distinct stages. A list of cements and some other post-depositional events are enumerated below, arranged in a chronological order, which represents the paragenetic evolution of the fluid flow in the studied area. Cement generations in the following chapters are numbered chronologically (Cal-1, Cal-2..., Dol-1...) in order to enhance the readability of the petrographical section and to allow to compare phases of the paragenetic sequences and geochemical signatures. It should be stressed however, that numbering of vein generation is made separately for each case-study and identical numbers do not allow any correlations between the studied areas.

The coupling of the diagenesis to the deformation history is made easier by differentiating between several sets of stylolites (i.e. pressure-solution structures), which relate either to burial compaction or tectonic compression. These pressure solution structures are of particular interest since they are pervasive in carbonate rocks (see Rutter, 1983; Groshong, 1988, for reviews of pressure solution phenomena) and often act as discrete and preferential fluid conduits, affecting the porosity and permeability (Bathurst, 1971, Evans, 2006). The stylolites themselves consist of non-carbonate 'insoluble' rock residue left behind. Two families can be differentiated in FTB setting, namely:

(1) **Burial stylolites**, also called Bedding Parallel Stylolitic planes (BPS), develop parallel to

bedding. Their formation is dependant to the timing of the foreland development but usually occurs prior to tectonic deformation due to vertical compression (i.e. burial compaction). These features start to form in limestones at a burial depth of 500 m (Lind, 1993; Railsback, 1993; Nicolaidis and Wallace, 1997; Drivet and Mountjoy, 1997; Duggan et al., 2001).

(2) **Tectonic stylolitic planes** (TS) generally develop sub-perpendicular to bedding as a result of horizontal compression during tectonic activity (Railsback & Andrews, 1995; Andrews & Railsback, 1997; Whitaker & Bartholomew, 1999; Sans et al., 2003).

Crosscutting relationships between veins and one or both sets of stylolites (i.e. BPS and TS) allow to constrain diagenetic events relative to shallow burial (pre-BPS veins), intermediate to deep burial to pre-orogenic (post-BPS and pre-TS veins) and post-orogenic events (post-TS veins; Van Geet et al., 2002; Breesch et al., 2007, ...). Significant amounts of host-rock may be dissolved during pressure-solution episodes. This rock material, liberated during pressure solution, either precipitates locally in inter/intra-particular porosity or in veins ("internal recycling"; Dewever, 2008) and/or is carried out of the local system by advecting fluid flow.

4.2- Fieldwork and selected case studies

In the framework of this study, eight weeks of fieldwork have been carried out in Albania. The goal was to work out a sedimentological-diagenetic field model on reservoir scale, during which the stratigraphical and sedimentological variations as well as the mutual relationships between diagenetic products were defined. A precise sampling was done in three reservoir analogues, which are shown in the Figure 4.2. Attention especially focussed on mapping out the porous reservoir intervals and to better understand the paleo-geographical evolution of each studied area.

Additionally, a large number of structural geological measurements on veins were carried out. A lot of attention was spent to study the relationship between vein type, host rock type, relative timing and the relative timing with regard to burial and tectonic stylolites.

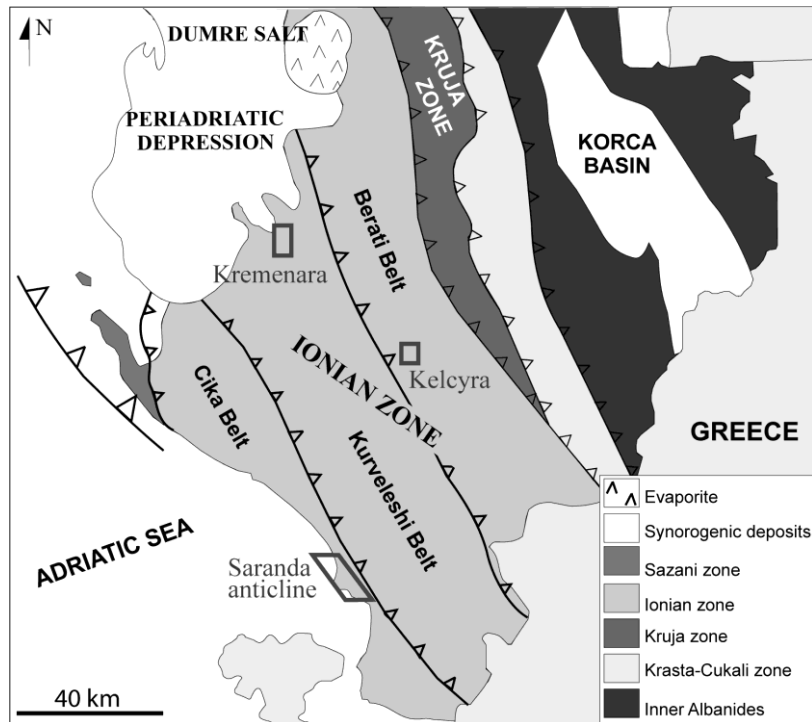


Figure 4.2. Schematic map with indication of the studied locations: i.e. the Saranda and Kremenara anticlines and the Kelcyra quarry.

Two fieldwork campaigns were organised in:

- **Kelcyra, a surface reservoir analogue of deep marine carbonates: 2 weeks, September 2004**

The first studied area corresponds to a surface analogue of the Late Paleocene-Eocene deep marine carbonates close to the city of Kelcyra (Chapter 5). This syncline structure is located in the Berati belt that forms the eastern-most unit of the Ionian Zone and belongs to the external Ionian sub-zone. These sediments crop out at the surface, but were previously buried beneath the Oligocene flysch. Its main specificity consists of its emplacement close to the hanging wall of the Berati thrust belt. Consequently the carbonates are intensely fractured. During the first fieldwork, the goal was to acquire an overview of the different lithologies present in the Ionian Basin as well as the tectonic structures, which compose the Albanides fold-and-thrust belt. A second aim was to sample an outcrop in the Kelcyra area (Figure 4.2), which represents a surface reservoir analogue of the Late Paleocene-Eocene deep marine carbonates. Structural measurements of veins and stylolites were carried out.

- **Saranda - Kremenara anticlines (deep marine carbonates): 4 weeks, April 2005**

Sampling, mapping and structural measurements were carried out in 2 studied areas: i.e. the Kremenara anticline and the Saranda anticline.

The Saranda anticline (Chapter 6) is located in the south-west of the Ionian zone, more specifically in the Cika belt. It belongs to the frontal unit of the Albanides FTB system and is situated next to the Sazani platform, which limits the Ionian Basin to the west. The anticline covers an area of 7 by 16 km. Its main axis reflects a south-east to north-west trend, which is parallel to the main thrust fronts of the Ionian Basin. Here, pelagic carbonates of the Lower Jurassic are exposed in the core of the anticline, whereas the highly fractured Upper Cretaceous to Eocene deep marine carbonates and debris flows are well exposed in the eastern and western flanks.

The research goal here was to map out this structure from sedimentological and stratigraphical point of view with special attention to the Upper Cretaceous-Eocene intervals in order to compare this anticlinal setting with the Kremenara anticline (see below). A representative sampling (veins and matrix) and geological measurements (fractures and bedding)

were carried out in order to distinguish the various sets of lithofacies and to examine the diagenetic and deformation features, such as fractures, veins and stylolites.

The Kremenara anticline (Chapter 7) is located in the northern part of the Kurveleshi belt, close to the Vlora-Elbasan transfer zone, where the major Albanian oil fields are located. It represents a reservoir analogue of 5 by 8 km for nearby and underlying hydrocarbon fields. The main anticlinal axis trends towards the southwest. Pelagic carbonates of the Middle Jurassic are located in the core of the anticline, whereas deep marine Upper Cretaceous to Eocene fractured carbonates and debris flows are exposed in the flanks. These Mesozoic and Paleogene series are unconformably covered by Serravalian deposits. The core of the anticline was first mapped. A precise sampling was realised in the different stratigraphical units and a large number of structural geological measurements on different types of veins was carried out. A first paragenesis of the successive vein generations (e.g. hydrofractures, syn-burial veins, or open veins filled with oil) was established, especially by unravelling the relationship between vein types, with host-rocks and the crosscutting relationship with tectonic and burial stylolites. Another essential aspect was to understand the tectonic deformation of this complex area and to place each stage of fracturing into the overall kinematic evolution of this thrust unit. Additionally the evolution of the paleogeographical setting was established by the interpretation of the depositional facies.

During these field campaigns, some time was also spent to work at the Geological and Petroleum Institute of Fier (QKSHH, Fier) to collect data and discuss preliminary interpretations with Albpetrol geologists.

4.3- Fracture characterisation

In petroleum exploration and production, fractures and stylolites are among the most common and important geological structures, since both may have a significant effect on production. Despite their importance, characterisation of fractures remains a difficult problem. The word "Fractures" is used here as a general terminology to indicate a brittle failure in a geologic formation. They can be differentiated by their displacement mode: the fractures may be dilatational, i.e. joints (a natural mode I rock

fracture) or exhibit a shearing with components parallel or perpendicular, i.e. faults (mode II or III rock fractures) to the direction of fracture front propagation. In this study, fractures terminology is mainly used to characterise the occurrence of "joints" (dilatational displacement), since no appreciable lateral displacement occurred. No faults, demonstrating a "significant" displacement, have been observed within the studied beds. These "joints" (i.e. fractures) are usually filled by a cement that is defined by the term "veins", i.e. fracture infilling. The relative timing of the fractures is essentially based on the occurrence of veins, since mutual cross-cutting relationships can be observed. However, fracture development and vein formation are not necessarily synchronous. A same generation of veins may have different orientations. The non-synchronous cementation of the fractures points to the occurrence of opened or non-cemented fractures during certain time intervals during the FTB evolution.

During field work, structural characterisation of stylolites and fractures (orientations, azimuth and dip and density measurements) were realised, based principally on mutual cross-cutting relationships between fractures and stylolites. To account for the presence of post-cementation folding and current dipping attitude of the beds, field data (i.e. dip and azimuth) have been rotated back to their initial attitude by restoring the reference bedding surfaces to a horizontal position (Ramsay, 1967).

4.4- Petrography

First observations were made in outcrop and were further refined by using polished samples and thin sections.

4.4.1- Conventional microscopy

After sawing and polishing of the samples, petrographical inspection of carbonate rocks is realised on thin sections to study sedimentary facies, diagenesis, deformation structures and particularly cross-cutting relationships in more details. For this project, a total of 95 thin sections, with matrix porosity or containing veins, were studied with transmitted light. Some of them have been stained with alizarin-red S solution and potassium ferricyanide (Dickson, 1965 and 1966). This method allows to distinguish between calcite (pink to red colour), ferroan calcite (purple colour in function of the increase of iron content), dolomite (uncoloured)

and ferroan dolomite (pale to intense blue colour).

4.4.2- Cathodoluminescence

Cathodoluminescence (CL) microscopy is an extremely important and essential tool in the investigation of various processes occurring in carbonate sedimentary rocks (Nickel, 1978; Richter & Zinkernagel, 1981; Marchal, 1988; Pagel et al., 2000; Boggs and Krinsley, 2006), such as crystal growth (Walkden and Berry, 1984), replacement, recrystallisation, deformation and provenance.

A cathodoluminescence microscope is a combination of an electron gun device and a classical light microscope. CL reveals many detailed cement petrographical features by illuminating different mineralogical phases (e.g. crystal growth zones), which often remain undistinguishable under normal light petrographical examination. When combined with other petrographic and geochemical information, CL allows to work in detail and helps to constrain and interpret paleofluid flow regimes.

The method of CL involves electron bombardment of uncovered and unstained thin or polished sections in a vacuum chamber. The latter results in the emission of an electromagnetic radiation of the bombarded material. This cathodoluminescence emission can be in the visible range (400-700 nm), ultraviolet (UV: <400 nm) and infrared (IR: >700 nm) and depends on the operating conditions, on a variety of defects (e.g., various structural imperfections, such as poor ordering, radiation damage, shock damage) and on the presence of activators (e.g. Mn^{2+} , Cr^{3+} , Fe^{3+} , Ti^{4+} and Rare Earth Elements (REEs)) or quenchers / inhibitors (e.g. Fe^{2+} , Co^{2+} and Ni^{2+}) (e.g. Miller, 1988; Barnaby and Rimstedt, 1989; Machel and Burton, 1991; Machel et al., 1991; Tucker, 1995; Kaufmann et al., 1999; Cazenave et al., 2003).

The luminescence in carbonates ranges from yellow-orange to black colours and reflects the presence of major to trace elements. Mn^{2+} is known to be the most effective activator of luminescence for calcites and dolomites, whereas Fe^{2+} is regarded to be a quencher of luminescence. In the framework of this project, two types of CL microscopy have been used: i.e. "cold cathodoluminescence microscopy" and

petrographical analysis making use of a "hot-cathode".

4.4.2.1- "Cold cathodoluminescence microscopy"

Cold cathodoluminescence (CL) microscopy generates positive ions along with electrons, which neutralize surface charge buildup and consequently eliminate the need for conductive coatings to be applied on the specimens. The cold cathode generates an electron beam by a corona discharge tube that takes place between two electrodes (Marshall, 1988).

Cold-CL petrography was performed on a Technosyn Cold Cathodoluminescence (CCL) device Model 8200, Mark II (IFP), operating under 10-15kV gun potential and 600 μA beam current, 0.05 Torr vacuum and 5 mm beam width.

4.4.2.2- "Hot cathodoluminescence microscopy"

CL colour and intensity are not only dependent on the characteristics of the sample but also on the working conditions of the microscope in use. Acceleration voltage and beam current of the electron beam are of major importance. When relating to "hot cathodoluminescence", the CL microscope is equipped with a "hot cathode", which is an electrically heated tungsten filament (<http://www.lumic.de/>). The hot CL enables excitation of luminescence on the surface of a polished thin section by electron bombardment, and by emitting electrons due to thermo-ionic emission by an electron gun. Hot cathodes typically achieve much higher power density than cold cathodes, emitting significantly more electrons from the same surface area. All electric parameters, which are decisive for the intensity of the emitted luminescence, can be exactly controlled. Therefore the most appropriate beam current density for each specific sample is obtained by varying acceleration voltage and beam current. To avoid electrical charging of the samples, the latter are previously coated with a conductive layer of for example gold or carbon. For this study, only carbon coating was used.

The microscope used is a HC3-LM type and all observations were carried out under 0.2 mA beam current and 14kV gun potential with a turbo-molecular pump. Most of the pictures in this project were realised with the "hot cathode", since the calcite crystals display usually dull sector zoning.

4.4.3- Scanning Electron Microscope

The scanning electron microscope (SEM) produces high resolution images of a sample surface (from plugs or thin sections) with a high 3D quality. It is useful for studying the surface structure of a sample, especially with regard to the shape of crystals, the existence of secondary porosity, diagenetic alterations, etc ...

The principle of the technique is the excitement of a sample by a high-energy electron beam under vacuum. These interactions cause the subsequent emission of secondary electrons from the sample surface, which are subsequently detected to produce an image. The electrons are detected by a scintillator-photomultiplier device. By using this technique, resolutions can be of the order of 5 nm.

The intensity of high-energy backscattered electrons (BSE), essentially elastically scattered primary electrons, is processed to obtain an image of a polished surface that reflects chemical contrasts according to the atomic number. Consequently some contrasts in grey-shade can be observed between areas with different chemical compositions.

Moreover the presence of an Energy Dispersive X-ray (EDX) detection system allows to determine semi-quantitatively the composition of minerals. This characterisation relies on the principle that each element has a unique atomic structure, allowing element specific X-rays to be identified individually from each other. X-rays are detected and analysed by an energy dispersive spectrometer.

SEM observations are made using a JEOL 840-A Scanning Electron Microscope at the University Paris VI, providing Back Scattered Electron (BSE) imaging and EDX analysis. It generally operates under 15-20 kV accelerating voltage for a working distance between 8 and 39 mm. Samples have been coated with carbon to guarantee a sufficient conductivity of the surface of the sample.

4.5- Petrophysic properties

Some porosity-permeability characterisation of the carbonate matrix was made. However, samples where no porosity could be seen macroscopically have not been studied. Thus non-porous samples are under-represented in the studied dataset. In total, 32 samples from the three reservoir analogues have been analysed

with regard to their "horizontal air permeability (800 psi NOB)" and "Ambient porosity (Helium)" at Corelab. Samples were kept at ambient temperature and pressure during the measurements.

4.6- Geochemistry

4.6.1- Carbon and oxygen isotope analysis

Carbon and oxygen stable isotopes are commonly used in diagenetic research in most natural systems. Variations in isotopic ratios are small but they can be precisely measured. These ratios are compared to a standard, for carbonates typically to the V-PDB (Vienna Pee Dee Belemnite, South Carolina USA) and for waters to the V-SMOW (standard mean oceanic water). The results are reported using δ -values, i.e. the delta notation, in which the isotope ratio of a sample is expressed in terms of its deviation, in part per thousand (‰), from the same ratio of isotopic values with regard to an internationally accepted standard (Hudson, 1977):

$$\delta_A = 1000 \times \frac{(R_A - R_{std})}{R_{std}}$$

where R_A is the ratio of the heavy isotope to the light isotope for phase A (e.g. $^{18}\text{O}/^{16}\text{O}$); R_{std} represents the same ratio for a standard material.

These data commonly plot on a cross plot of $\delta^{18}\text{O}$ versus $\delta^{13}\text{C}$. The data could allow to infer the diagenetic environment responsible for specific diagenetic products. Oxygen-isotopic values of marine Phanerozoic waters normally vary around 0‰ V-SMOW, depending on temperature, evaporation and dilution from sea ice (Anderson and Arthur, 1983). Table 4.1 gives an overview of reference values for calcite precipitated in equilibrium with marine water at different periods that are relevant for this study. Under conditions of heavy evaporation, marine waters can exhibit relatively high $\delta^{18}\text{O}$. Inversely, burial fluids display a wide range of $\delta^{18}\text{O}$ values (Moore, 2001), often reflecting precipitation at elevated temperature and/or different degrees of water/rock interaction.

The $\delta^{18}\text{O}$ -signature of meteoric waters is relatively low, but can exhibit a wide range of oxygen isotopic compositions due to latitude and altitude effects (evaporation, amount of precipitation ...) (Anderson and Arthur, 1983).

	$\delta^{18}\text{O} \text{ ‰ V-PDB}$	$\delta^{13}\text{C} \text{ ‰ V-PDB}$
Shackleton & Kennett (1975): Late Paleocene foraminifera	-0.5 to -1.7	+0.2 to +1.4
Frank & Arthur (1999): Upper Maastrichtian	-1.7 to +1.0	+0.5 to +2.2
Swennen & Dusar (1997): Maastrichtian chalk	-1.2 to -2.6	+1.9 to +2.4
Shackleton (1986): Paleocene carbonates	0.0 to -0.5	+1.0 to +3.5
Jørgensen (1987): Upper Cretaceous chalk	-0.5 to -2.0	+0.5 to +3.0
Veizer & Hoefs (1976): major population Cretaceous carbonates	-1.0 to -4.2	0.0 to +3.1
Scholle & Arthur (1980): Aptian - Albian carbonates	-2.5	+2.5 to +4.0
Moldovanyi & Lohmann (1984): Lower Cretaceous carbonates	-2.0	+4.0
Luciani (2007): Late Paleocene – Early Eocene		-2.0 to +2.1

Table 4.1. Stable isotope composition of Cretaceous and Paleocene marine constituents and carbonates (after Van Geet et al., 2002).

The oxygen isotopic fractionation between water and calcite is highly dependent on temperature (Friedman and O'Neil, 1977) with $\delta^{18}\text{O}$ of the calcite becoming increasingly lower with increasing temperature. The following fractionation equation, developed by O'Neil et al. (1969), gives the relationship between temperature, $\delta^{18}\text{O}$ of calcite and water:

$$1000 \ln \left(\frac{1030.91 + 1.03091(\delta^{18}\text{O calcite})}{1000 + \delta^{18}\text{O water}} \right) = \frac{2.78 \times 10^6}{T^2} - 2.89$$

with T in Kelvin

While the oxygen isotopic fractionation is mainly dependent on temperature, the carbon isotopic equilibrium fractionation is less temperature dependent but here often kinetic biological fractionations occur (Anderson and Arthur, 1983). Marine dissolved inorganic bicarbonate is characterised by a $\delta^{13}\text{C}$ value around 0‰ V-PDB and marine limestone by approximately -2 to +4 ‰ V-PDB (Figure 4.3.). However this marine signature can be altered by respired CO_2 from photosynthesis ($\delta^{13}\text{C}$ between -23 and -33‰ V-PDB) and by CO_2 from oxidation of organic material (between -20 to -25‰ V-PDB). Extremities reflect the methanogenesis, characterised by a large kinetic fractionation between CH_4 (-60 to -80‰ V-PDB) and CO_2 (from +5 to +15 ‰ V-PDB). CH_4 and CO_2 migration and mixing through the sediments result in a very wide range of $\delta^{13}\text{C}$ values,

varying from very depleted (CH_4 -oxidative dominated) till positive values (methanogenic CO_2 dominated).

Meteoric diagenesis in a carbonate displays a typical isotopic evolution, which is called the "meteoric calcite line" or "inverted-J curve" (Lohmann, 1988). This line points to different degrees of water-rock interactions and the amount of light ^{12}C from soil- CO_2 . The C-signature can be buffered by the host-rock or reflect a value on the mixing trend between both extremities, i.e. marine and soil CO_2 .

Procedure:

For carbon and oxygen isotope analyses of calcites and dolomites, 1 to 5 mg of sample was carefully drilled and analysed at the University of Erlangen (Germany). Carbonate powders were reacted with 100% phosphoric acid (density >1.9, Wachter and Hayes, 1985) at 75°C using a Kiel III online carbonate preparation line connected to a ThermoFinnigan 252 massspectrometer. All values are reported in per mil relative to V-PDB by assigning a $\delta^{13}\text{C}$ value of +1.95 ‰ and a $\delta^{18}\text{O}$ value of -2.20 ‰ to NBS19. Reproducibility was checked by replicate analysis of laboratory standards and is better than ± 0.03 ‰ for $\delta^{13}\text{C}$ and ± 0.01 ‰ for $\delta^{18}\text{O}$ (σ_1). The oxygen isotopic composition of dolomite was corrected using the fractionation factors given by Rosenbaum & Sheppard (1986). In some samples, a chemical separation of calcite and dolomite was done prior to the isotopic

analyses, when fine crystalline dolomites were scattered in calcites (Nader et al., 2008). The latter is based on a sequential extraction procedure (modified from Burns and Baker, 1987) of samples, containing only calcite and dolomite. The calcite phase is removed by leaching and shaking the sample in an acetic acid-buffered ammonium acetate solution (pH 5) for 5 hours. The calcite is consequently totally removed, whereas the dolomites remain not or partially affected by this dissolution (Nader et al., 2008).

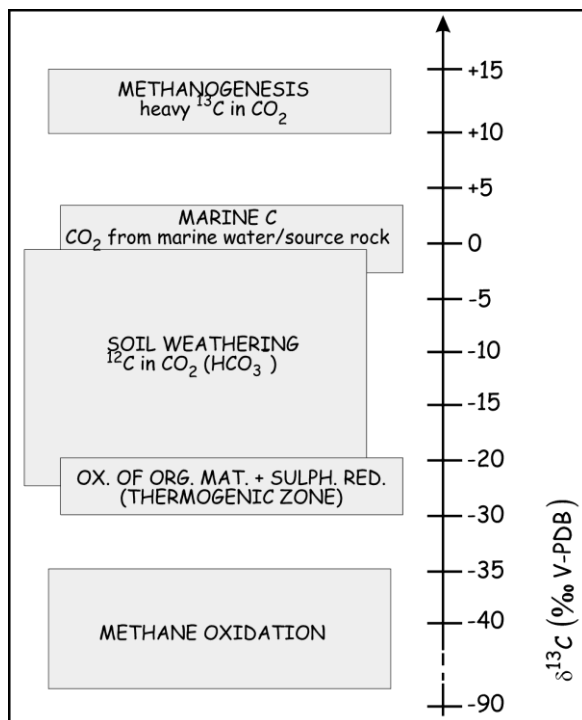


Figure 4.3. Variations in $\delta^{13}\text{C}$ values (Hudson, 1977; Moore, 2001).

4.6.2- Sr isotope analysis

The fundamental concept in strontium isotope geochemistry of carbonate rocks is that ocean water is well mixed and consequently has a uniform $\text{Sr}^{87}/\text{Sr}^{86}$. This ratio changes through time in response to the relative contribution of Sr from continental crust and upper mantle sources. These variations over time may be recorded and preserved in marine limestones or cement phases, when they contain negligible amounts of non-carbonate material. The $\text{Sr}^{87}/\text{Sr}^{86}$ ratio of seawater throughout the geological history has been established, especially for the last 70 Ma. The latter is now used for stratigraphic and absolute dating purposes (e.g. Burke et al., 1982;

Elderfield, 1986; Hess et al., 1986; McArthur et al., 2004). Today this variation is known with high accuracy especially for the Cenozoic (Elderfield, 1986; Veizer et al., 1999).

The measurements of $\text{Sr}^{87}/\text{Sr}^{86}$ in non-altered marine limestones allow the datation of samples. Moreover organisms could inherit the marine $\text{Sr}^{87}/\text{Sr}^{86}$ ratio at the time of their carbonate skeleton precipitation. Other interest using $\text{Sr}^{87}/\text{Sr}^{86}$ ratios in carbonates is the possibility to associate cementation or diagenetic processes to subsurface influx of water from specific sources or ages (e.g. fluid-rock interaction). Diagenesis generally leads to an increase in $\text{Sr}^{87}/\text{Sr}^{86}$ ratio by interaction with fluids enriched in radiogenic Sr (especially if the latter interacted with siliciclastics). However, marine diagenetic fluids or brines with a lower $\text{Sr}^{87}/\text{Sr}^{86}$ ratio may also be involved in diagenesis (Brand, 1991; Denison et al., 1994; Banner, 1995; McArthur, 2004).

The use of Sr isotope in conjunction with stable isotopes can constrain the degree of fluid-rock interaction and sometimes migration pathways. Oxygen and carbon values are essential indicators for the origin of the fluid, whereas the Sr ratio reflects sources of dissolved Sr and both can provide information on water mixing and migration, the degree and nature of water-rock interaction and the chemical evolution of waters (Connolly, 1990).

Sr-isotope analyses were carried out at the Scottish Universities Environmental Research Center. The carbonate samples were leached in 1N of NH_4 acetate prior to acid digestion in 6M of HCl. Sr was separated in 2.5M of HCl using Bio-Rad AG50W X8 200 - 400 mesh cation exchange resin. The Sr samples were loaded onto Ta filaments with 1N phosphoric acid and analysed in a VG Sector 54-30 multiple collector mass spectrometer, with the $^{87}\text{Sr}/^{86}\text{Sr}$ ratio normalized to 0.1194. Total procedural blanks for the sequential leach and digestion procedure contained < 100 pg of Sr.

4.6.3- Major to trace elemental analyses

During precipitation, carbonate cements incorporate various trace and minor elements proportionally to their concentration in the fluid. The incorporation of elements in calcite is dominated by substitution for Ca^{2+} , rather than interstitially between lattice planes, at site defects, as adsorbed cations or within inclusions (e.g. Na^{2+} mainly in inclusions) (Veizer, 1983b;

Dickson, 1990; Banner, 1995). The lattice parameters of a specific mineralogy plays a major role in determining the distribution coefficient: a crystal with a large unit cell can accommodate cations larger than Ca (such as Sr, Na, Ba...), while the smaller unit cells, as rhombohedral crystals, preferentially incorporate smaller cations, such as Mg, Fe and Mn (Veizer, 1983).

Waters from the major diagenetic environments are so different in trace and minor element composition that the cements precipitated from these diverse waters should easily be recognizable by their trace element signature. However the distribution coefficients of the elements are relatively crude estimates and can be dramatically affected by temperature, major element composition of the solid phase (stoichiometry and degree of ordering), the rate of precipitation of the cement (Mucci and Morse, 1983; Given and Wilkinson, 1985; Banner, 1995) and non-equilibrium precipitation. Therefore, the studies of trace element must be used intelligently within diagenetic studies to provide useful information concerning characteristics of the diagenetic environments responsible for cementation, dolomitisation, recrystallisation, etc ...

Two different techniques have been used to characterise the successive cements in composition: i.e. electron microprobe analyses and Atomic Absorption Spectroscopy (AAS). Both techniques are useful but also complementary. AAS allows a geochemical characterisation of a cement, whereas microprobe is more appropriate to analyse crystals, since this technique works at a micron-scale level. In this project, the cements were firstly sampled for AAS. However, as many brecciated fragments and diagenetic minerals often occur as minute phases, microprobe analyses were used in order to characterise them independently.

4.6.3.1- Absorption Atomic Spectroscopy (AAS)

AAS is the first technique used for determining the major (Mg, Ca) and trace element content (Na, Sr, Fe, Mn, K) of the carbonates. It uses the absorption of light to measure the concentration of gas-phase atoms. When samples are liquids or solids, the atoms or ions must be vaporized in a flame or graphite furnace. The atoms absorb ultraviolet or visible light. They make transitions

to higher electronic energy levels. The studied concentration is determined from the amount of absorption. Applying the Beer-Lambert law directly in AAS is difficult due to variations in the atomisation efficiency from the sample matrix, and non-uniformity of concentration and path length of the studied atoms (in graphite furnace AA). Concentration measurements are usually determined from a working curve after calibrating the instrument with standards of known concentration (Magyar, 1982; Welz, 1985; Ingle and Crouch, 1988; Lajunen, 1992).

For this purpose, clean hand-picked carbonate samples were crushed and their powders were dried in an oven at 100°C for one night. 0.5 g of carbonate fraction was digested in 20 mL 1M HCl in order to minimize as much as possible the dissolution of non-carbonate impurities such as clays (Nader, 2003; Nader et al., 2004). Subsequently this solution was evaporated at 60°C. Then, another 10 ml 1M HCl was added and the solution filtered prior to determination of trace elements as well as the HCl-insoluble residue (IR) content.

4.6.3.2- Microprobe analysis

The main interest of the electron microprobe is its ability to provide quantitative geochemical analyses of areas as small as 3-4 μm^2 on a polished thin section. Electron microprobe analyses offer high spatial resolution and low detection limit for many elements in carbonate. The analyses were carried out by using a CAMEBAX SX50 facility, at the University of Louvain-La-Neuve (Belgium), operating at 15 kV, with a gun current of 20 nA and 10 μm beam width. Samples were first polished and then coated with silver to make the surface conductive.

Calcite, dolomite and other minerals (i.e. barite, celestite, apatite), occurring in calcite veins and host-rock have been quantitatively analyzed for Si, S, Ba, K, Na, Sr, Ca, Al, Fe, Mg and Mn. All results are obtained in weight percentage and then converted in ppm. The used standards are: Siderite (Fe); Rhodocrosite (Mn); Calcite (Ca); Oligoclase (Na); Leucite (K); Barite (S); Barite (Ba); Wollastonite (Si); Saphir (Al); Strontianite (Sr); Magnesite (Mg). Detection limits down to tens of parts per million (by weight) can be attained. However it is generally accepted that errors increase close to the detection limits (i.e. <50 μm).

4.7- Microthermometry

Fluid inclusions (FI) are tiny quantities of liquid, gas, or mixtures of these phases, trapped as impurities within minerals. They also may contain minute solid impurities. Their sizes range from microscopic up to several hundred micrometers in diameter (1 to 10 μm in this study). Microscopic observations allow to distinguish inclusions that formed during the crystal growth ("primary inclusions") from those formed after mineral growth and that occur in microcracks or are aligned along twin and cleavage surfaces ("secondary or pseudo-secondary inclusions", Goldstein, 2001). Unfortunately, the distinction between these three types of fluid inclusions is often ambiguous, especially in carbonate minerals where fluid inclusions are often smaller than in quartz and growth zones are not well developed. The technique consists in noticing phase transitions during heating and cooling in these inclusions to have information on the trapping conditions (P, T) and type of fluid (X). In fact, numerous evidences suggest that many primary inclusions preserve the chemical and physical properties of the original fluids from which they formed. Secondary inclusions have also an interest, especially to give data about recrystallisation or maximum burial temperature.

The analytical study of FI is called microthermometry and requires at least biphasic fluid inclusions (gas and liquid). Once the different generations of FI are recognized, microthermometry consists of measuring the temperature at which phase-transitions occur in the FI. Heating studies are used to determine temperatures of homogenization T_h of the FI that corresponds to the disappearance of one of the two phases (i.e. gas or liquid) in the inclusion. It represents the crossing of the liquid-vapour curve of the studied fluid system, where the density has

a major role. It represents the minimum temperature of FI trapping.

At the opposite, after freezing the FI till -180°C , the first melt temperature (T_{fm}) occurs during the reheating and gives an indication of the type of the fluid system. In the case of aqueous system, the freezing experiments can be done also for monophasic inclusions after artificial stretching. The last phase transition corresponds to the last melting of ice (T_m), which allows to calculate the salinity of the fluid (Bodnar, 1993). Single phase inclusions can be artificially stretched by repeated heating and cooling in order to be able to obtain valid measurements of T_{fm} and T_m .

Unfortunately, calcite is an easily cleaved, recrystallised and deformable mineral, so continued heating during burial, above those of the initial precipitation, can cause stretching and leakage. It is important to recognise these processes since they can give misleading microthermometric temperatures and salinities.

Double polished thin sections (100 μm thick), called wafers, were prepared for microthermometric analyses following the procedure of Shepherd et al. (1985) and Roedder (1984). The measurements were performed on a Linkam THMSG 600 heating-cooling stage. Synthetic fluid inclusions are used to calibrate the thermocouples, resulting in measurement accuracies to within ± 0.2 degrees at temperatures below 100°C , and ± 0.8 degrees at higher temperatures.

4.8- Conclusion

It is by a combination of field data, petrography, geochemical and microthermometric characterisation of individual diagenetic phases that the paragenetic sequence in the different studied areas is precisely established.

CHAPTER 5- DIAGENESIS AND FRACTURING IN THE BERATI BELT: CASE STUDY OF THE KELCYRA OUTCROP

In this chapter, results from a structural analysis, as well as petrographical and geochemical investigations in the Kelçyra area will be presented. These analyses have been performed on cemented fractures in Paleocene-Eocene carbonate rocks. The results will be placed into the deformation history of the area in order to unravel the different fluid circulation episodes in relation to the geological evolution of the studied area. Particular attention will be paid to the early and late diagenetic processes since petrographical and geochemical data indicate that several of these processes could operate in disequilibrium with the host rock (e.g. meteoric cementation, dolomitisation, secondary porosity development, interaction with evaporites, ...). Moreover, complex water-rock interactions have been determined. The latter diagenetic alterations may have an important impact on present-day reservoir characteristics, especially by their effect on dual matrix/fracture porosities. In addition, this study may allow to improve the knowledge on preferential fluid migration pathways during FTB development.

The Berati anticlinal belt (Figure 5.1, Figure 5.2) represents the eastern-most anticlinal belt of the Ionian Zone and belongs to the external Ionian sub-zone. It has been developed as an out-of-sequence structure of the Kurveleshi Belt (see Chapter 8: Fluid flow modelling) after deposition of the Upper Miocene sediments (Nieuwland et al., 2001). Geological positioning of this belt near known oil fields, such as Marinza and Kucova, makes the Berati belt among the most interesting regions for hydrocarbon exploration. Nevertheless, no hydrocarbon occurrences are observed at the studied location. A specific structural feature of the Berati belt is the occurrence of diapirs, which are emplaced either at the intersection of longitudinal NW-SE thrusting faults with transversal NE-SW ones or located in local structures, such as in the core of anticlines (Velaj, 2001).

The studied locality of Kelçyra is located near the hanging wall of the Berati thrust belt (location: N40°18'29.35"N latitude;

N20°11'9.10"E longitude; right side of the (B) thrust fault in the Figure 5.1). The outcrop is a quarry of 70 m in height and about 120 m long. According to the work of Vranaj et al. (1997), the Eocene carbonate strata were overlain by approximately 3 km of Oligocene flysch before the thrusting of the Berati unit. Pelagic carbonates are intercalated with thin debris flows and constitute the Late Paleocene-Eocene interval that is up to 410 m thick in the study area. This lithological interval received more attention since it represents a surface analogue of the Paleocene-Eocene carbonate petroleum reservoirs of the Ionian zone. During the fold-and-thrust belt (FTB) evolution, this area has been subjected to several fracturing events along which fluid migration occurred.

A likely geological NE-SW transect is proposed in the Figure 5.2, where the Kelçyra outcrop is indicated. The transect shows the Memaliaj synclinal belt, overthrust by two major thrust faults, i.e. the Berati anticlinal unit in the east (C) and a backthrust fault in the west (B). In the Memaliaj belt, the Neogene sediments are deposited unconformably over the Oligocene flysch. The (B) fault allows also the mobilisation of the Triassic evaporites till the surface as it is indicated in the Figure 5.1.

5.1- Sedimentology

The sedimentology is based on field observations, which subsequently were refined by studying polished samples and thin sections. All the samples have been collected in the same quarry (Figure 5.3), where Late Paleocene-Eocene carbonates crop out. In total, 23 thin sections from the Kelçyra area have been studied and 10 samples have been simultaneously analysed with regard to their "horizontal air permeability" and "Ambient Helium porosity" (Table 5.1 and Figure 5.5).

5.1.1- Macroscopic observations

In the quarry, well-bedded and highly fractured carbonated rocks, oriented N140°32N, occur.

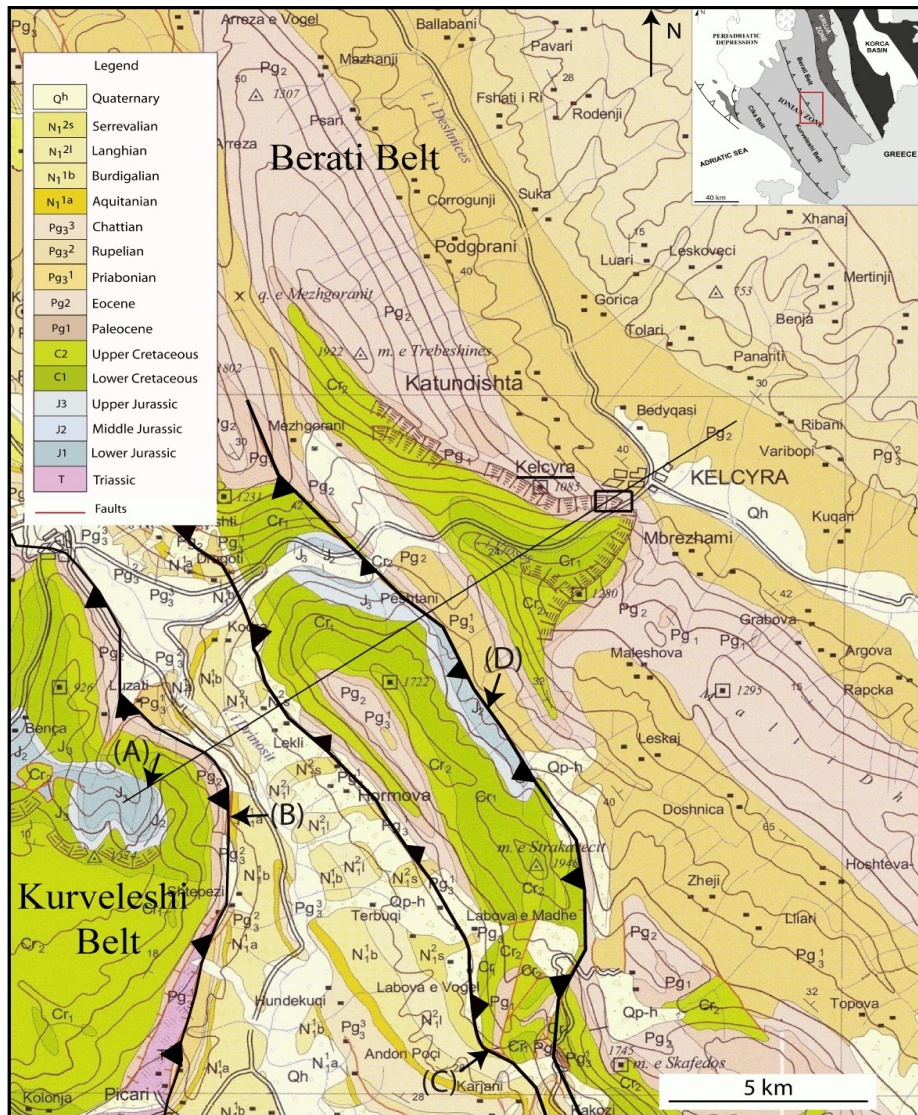


Figure 5.1. Geological map (from the Geological survey of Albania) of the central part of the Berati belt, showing the hanging wall and the footwall of the main thrust fault. The letters from (A) to (D) refer to the position of the main faults, which are described on the NE-SW geological cross-section in Figure 5.2 (black line). The black square indicates the location of the studied quarry.

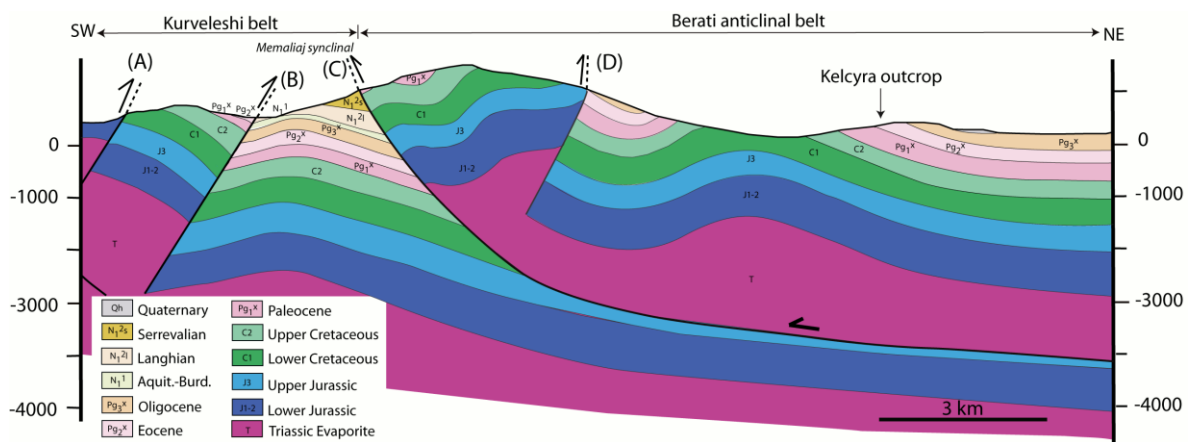


Figure 5.2. NE-SW cross-section through the Berati unit. The location of this transect is shown on Figure 5.1. The main faults are designed by a letter from (A) to (D). The main (C) fault is thrusting the Neogene deposits and borders the western part of the Berati belt. The (B) backthrust fault, occurring in the Kurveleshi belt, is also thrusting the Neogene deposits.

Individual bed thickness varies between 35 and 50 cm. These carbonates consist of dominantly light-beige fine-grained limestones with 2 to 3 % of bioclasts (e.g. mainly benthic foraminifera). Some thinned bioclastic intervals (i.e. packstones) are present but their occurrence is relatively limited. Some intervals contain also elongated silica nodules (i.e. cherts), which are aligned parallel to the stratification.

5.1.2- Microscopic observations

Two distinct stratigraphic assemblages (see Figure 5.4) have been differentiated:

- Microfacies 1, which makes up the most abundant facies (around 70 %), is composed of mud- (M) to wackestone (W) with mainly planktonic foraminiferal and some bivalve and

gastropod fragments (Figure 5.4 A, B, C & F). The micrite contains often less than 8 % of fauna, but locally their content can be up to 14 %. This facies points towards a deep marine environment with low-energy sedimentation. Moreover, most shells are dissolved and filled mainly with calcite and barite. This facies has a very low porosity ranging from 0.2 to 1.2 % and a low permeability varying between 0.001 to 0.08 mD. Locally, porosity and permeability can increase in relation to the occurrence of stylolites or open fractures and reach respectively 2.1 % and 1.36 mD. However, the fractures located in the area are nearly all cemented by calcite, unlike the stylolites. Microfacies 1 is also characterised by the presence of siliceous diagenetic accumulations (e.g. chert nodules), which occur parallel to the stratification (Figure 5.4 D).



Figure 5.3. Satellite image of the studied area; the quarry is indicated by a blue square (from Google Earth 4.3, 2007). The scale of the quarry is of 70m in height and about 120m long.

- Microfacies 2 (Figure 5.4 E) consists of a foraminiferal packstone (P), made up of 60 to 70 % of shell debris. These grain-supported carbonates represent only 30 % of the studied interval and are characterised by thin intervals of about 3 to 9 cm in thickness. Porosity values amount to around 1.7 % and permeability is situated around 0.67 mD. These values increase up to respectively 5.3 % and 1.75 mD, when tectonic stylolites occur. Although porosity is

higher, the pores are not connected principally due to the few number of interparticular porosity or open fractures in the system. Only the presence of stylolites can improve the permeability. This lithology, interpreted as debris flow, indicates a somewhat higher energy environment, likely related to the onset of the compression, which occurs in the hinterland, or could simply due to higher storm frequency, and slope instability due to increased sedimentation.

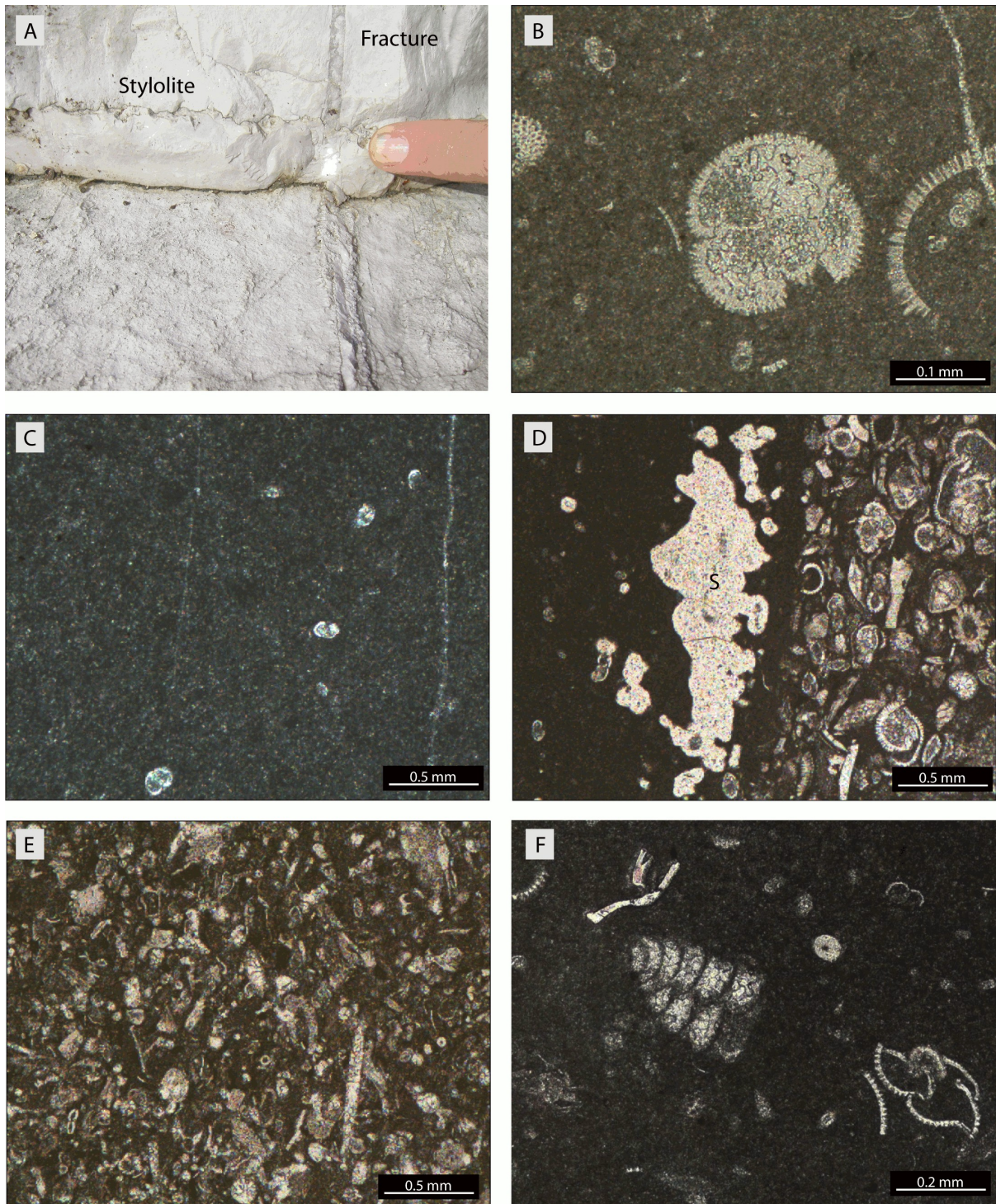


Figure 5.4. Outcrop and petrographic features of the Upper Paleocene-Eocene limestones in the Kelcyra quarry: (A) Macroscopic view of a fractured Upper Paleocene-Eocene mudstone with stylolite. (B) Transmitted light view of wackestone with planktonic foraminifera. (C) Transmitted light view of mudstone with dispersed planktonic foraminifera. (D) Transmitted light view of fine-grained limestone with silica (S), overlain by foraminiferal packstone. The top is towards the right. (E) Transmitted light view of planktonic foraminiferal packstone. (F) Transmitted light view of wackestone with foraminifera.

	Type	Selected	Porosity %	Permeability mD
KI-1	P	X	4.1	0.145
KI-2	P		-	-
KI-3	M		-	-
KI-4	W	X	1.2	0.014
KI-5	M		-	-
KI-6	W		-	-
KI-7	M		-	-
KI-8	M	X	0.2	0.001
KI-9	M		-	-
KI-10	W	X	2.3	0.083
KI-11	M		-	-
KI-12	M		-	-
KI-13	M-TS	X	2.1	1.356
KI-14	P-TS	X	5.3	0.89
KI-15	P-BPS		-	-
KI-16	M		-	-
KI-17	W		-	-
KI-18	M		-	-
KI-19	M		-	-
KI-20	P	X	1.7	0.672
KI-21	M-veins	X	0.3	0.013
KI-22	M		-	-
KI-23	W		-	-
KI-24	M-TS	X	0.4	0.882
KI-25	M		-	-
KI-26	W		-	-
KI-27	P	X	4.2	1.755
KI-28	M-P		-	-

Table 5.1. Porosity and permeability data. Only samples where some porosity could be seen macroscopically were analysed (see column "Selected samples"). M = Mudstone; W = Wackestone; P = Packstone; LPS = Layer Parallel Shortening; BPS = Bedding Parallel Stylolites.

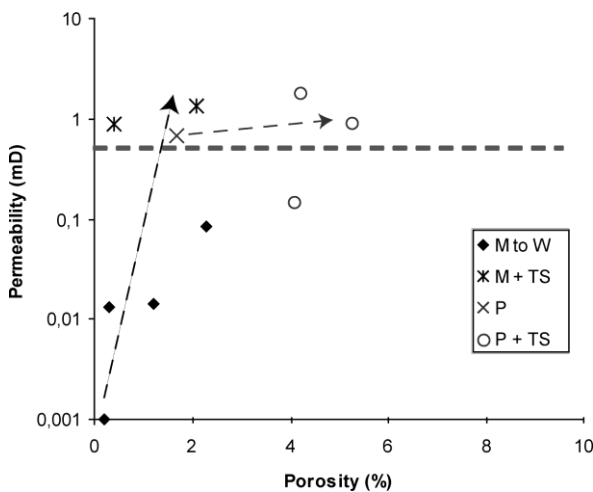


Figure 5.5. Crossplot between porosity and log (permeability) with data for various lithologies. (M = mudstone, W = wackestone, P = packstone with or without TS = Tectonic stylolites). The arrows indicate the increase of the K-Phi properties with the occurrence of tectonic stylolites.

debris flows, making up around 30% of the succession, reflects instabilities during sedimentation of the basin and neighbouring platform, which is, in that case, the Kruja platform. Moreover, major submarine erosions take place in the Ionian zone from the Paleocene onward, which are associated to the onset of the deformational stage, implying debris flow deposition (Swennen et al., 1998, 2000).

Although the porosity can reach up to 5 %, permeability is relatively low with maximum values lower than 2mD, reflecting a weakly connected pore system. However, samples were taken in outcrop conditions, implying the possibility of (sub)recent cementation of fractures and vugs by meteoric fluid, and/or surface alteration. The evaluation of the porosity-permeability distribution with respect to lithology, as illustrated in Figure 5.5, displays the following features: Mud- (M) to wackestone (W) possess the lowest porosity-permeability values (< 2.1 % porosity and permeability < 1.36 mD). Packstone (P) possesses slightly higher values, especially if they are affected by burial or tectonic stylolites (+ TS). Whatever the

Thus, the Paleocene-Eocene limestones of the Kelcyra quarry point towards deep marine depositional conditions. The occurrence of some

lithology, the occurrence of tectonic stylolites, or partially or non-cemented fractures account for higher permeabilities.

For example, a mudstone that is crosscut by tectonic stylolites increases its permeability by more than 100 times. However, the K-Phi analyses were made for a very limited dataset.

5.2- Structural analyses

In petroleum exploration and production, fractures and stylolites are especially common in carbonates and important geological structures, as they often control reservoir fluid flow (Bradbury & Woodwell, 1987; Travé et al., 1998; Swennen et al., 2000; Salvini & Sorti, 2004; Roure et al., 2005; Breesch et al., 2007; Vilasi et al., 2009).

During the Albanides FTB development, the carbonates of the Ionian Zone have been subjected to several stylolitisation phases and fracturing events, being subsequently filled by various calcite cements. During the field campaign, structural characterisation of stylolites and fractures was realised based on cross-cutting relationships between fractures and stylolites, orientations (i.e. azimuth and dip) and density measurements.

5.2.1- Stylolites

One generation of bedding parallel stylolitic planes, i.e. BPS, and two generations of tectonic stylolitic planes, i.e. TS, related to the kinematic evolution of the FTB, have been identified in this quarry. Stereonet projections of raw and backtilted data are detailed in the Figure 5.6 and Table 5.2 summarises the present day data, i.e. the raw data.

BPS planes (i.e. blue line on the stereonet projection) form parallel to the depositional fabric (i.e. bedding). Their amplitudes are millimetric and they sometimes are filled with insoluble residues less than 1 mm in thickness. They thus formed during the burial stage before thrusting. They are synchronous to the first generation of fracture (FRACT1) and are cross cutted by all the other fracture generations. Based on Swennen et al. (2000), the BPS planes are considered to be Lower to Middle Oligocene in age coeval with the flexural episode in the foreland when the overlying flysch sequence reached 1-2 km of thickness. Moreover, the BPS developed previous to the Burdigalian

compression, affecting the Ionian Basin. Consequently they should form at a maximum depth of 2km that represents the thickness of the Pre-Burdigalian sediments (i.e. Oligocene flysch) according to the work of Barrier et al. (2003).

The tectonic stylolites (TS), which are not abundant in the Kelcyra area, are oblique to the bedding and also characterised by high amplitudes. Two sets orthogonal to each other (Figure 5.6), pointing to two distinct directions of main principal stress σ_1 , respectively trending about N70° (i.e. TS1 set) and N160° (i.e. TS2 set) after rotation, have been recognised. The chronologic order between both phases of TS development is unknown, since no crosscutting relationship was observed.

The N°70 oriented σ_1 , defined as the TS1 set (Figure 5.6), is consistent with the main compression developing the NNW-SSE frontal thrusts and folding structures in the Albanides. Regarding to their distributions, TS planes record a syn- to post-deformation stage, since they are roughly orthogonal to the direction of maximum stress and mostly parallel to the fold axes. They attest of the westward migration of the thrust fronts. These stylolites are believed to have formed during layer-parallel-shortening (LPS) when tectonic compression affected the carbonates (Ramsey & Huber, 1983).

The second recorded maximum stress (i.e. TS2) shows either a pre-folding NNW-SSE (N°160) compression or a post-folding NW-SE (N°130) compression. This change in the orientation of the maximum stress attests of the occurrence of a second main tectonic phase, which predates or postdates the development of TS1.

5.2.2- Fracture development

As mentioned above, the Albanian carbonate reservoirs have been subjected to several fracturing events during the FTB development. Four main periods of fracturing have been identified in the Paleocene-Eocene carbonates, individualised principally by their orientations and cross-cutting relationships. When no cross-cutting relationship with stylolites occurs, the necessity of rotating the data is defined by the dip of the fractures or stylolites. In fact, the main stresses are assumed to be sub-horizontal, implying the development of sub-orthogonal fractures in monoclinical structures.

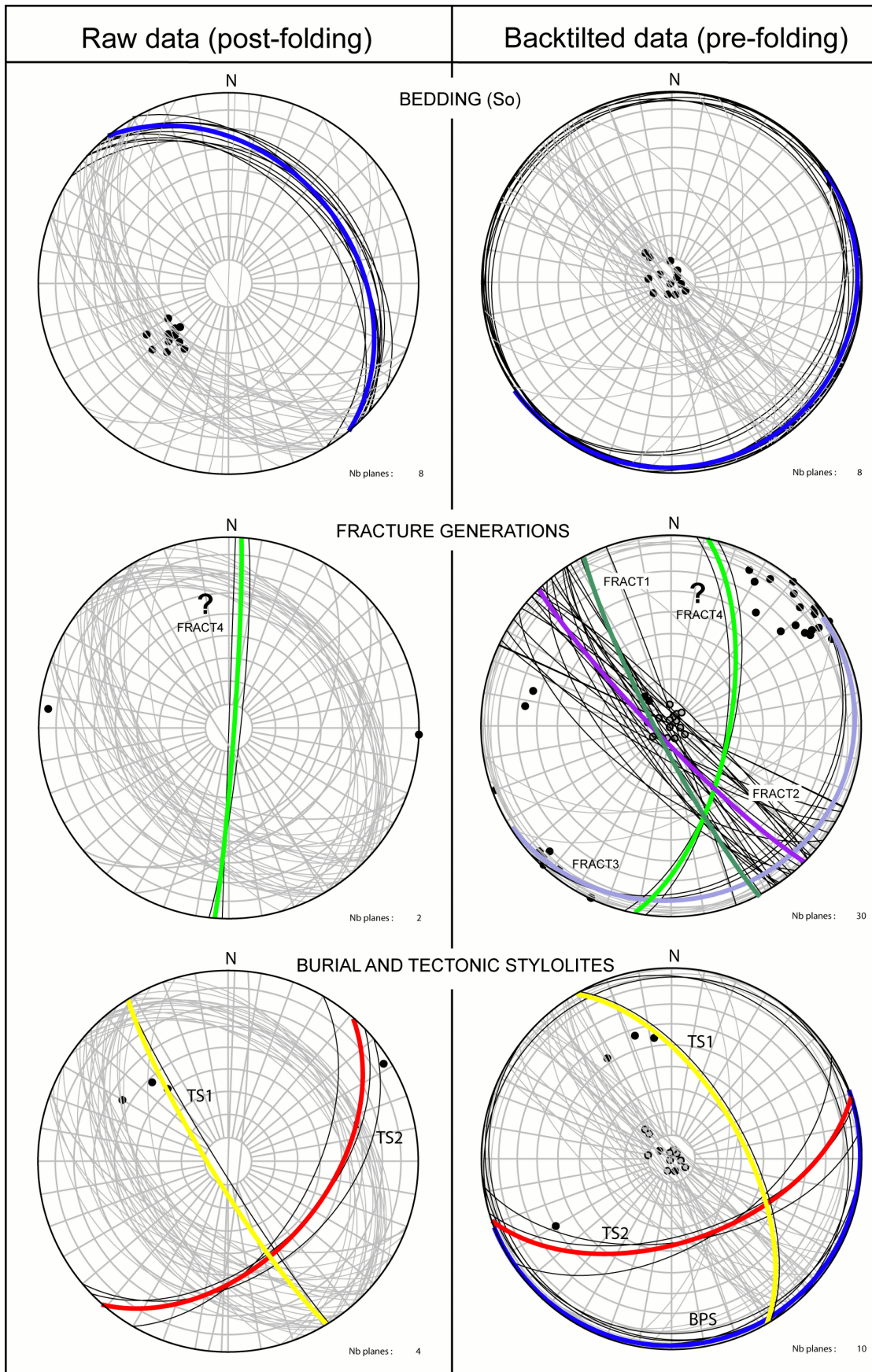


Figure 5.6. Lower hemisphere stereonet projections of raw and backtilted data: bedding (So), fracture generations and stylolites (i.e. burial and tectonic). The colored planes represent a mean of each fracture set.

<i>Identification</i>	<i>Orientation</i>			<i>Identification</i>	<i>Orientation</i>		
So	136	32	N	FRACT2	150	48	S
So	140	32	N	FRACT2	149	55	S
So	140	34	N	FRACT2	152	42	S
So	136	36	N	FRACT2	156	52	S
So	124	34	N	FRACT2	111	58	S
So	132	40	N	FRACT2	138	46	S
So	130	33	N	FRACT2	151	54	S
So	148	42	N	FRACT2	150	40	S
BPS	140	30	N	FRACT2	150	44	S
BPS	138	28	N	FRACT2	134	64	S
BPS	128	38	N	FRACT2	134	59	S
BPS	139	44	N	FRACT2	132	56	S
BPS	146	40	N	FRACT2	142	30	S
BPS	150	30	N	FRACT2	144	50	S
plan - TS1	148	86	S	FRACT2	144	38	S
plan - TS2	50	41	S	FRACT2	142	52	S
plan - TS2	30	54	S	FRACT2	132	49	S
plan - TS2	46	48	S	FRACT2	129	54	S
FRACT1	126	60	S	FRACT2	120	48	S
FRACT1	113	43	S	FRACT2	119	29	S
FRACT1	136	60	S	FRACT3	164	38	N
FRACT1	111	58	S	FRACT3	160	37	N
FRACT2	164	60	S	FRACT4	2	90	N
FRACT3	110	48	S	FRACT4	6	85	N

Table 5.2. Raw data of bedding, stylolites and fractures of the Kelcyra quarry (present day orientations, *raw data*).

The first fracturing stage FRACT1 is characterised by a N°150 orientation with subvertical dip (i.e. unfolded data, Figure 5.6) and is considered synchronous to the compactional stylolites (BPS), based on the fact that they cut and are also crosscutted by BPS. They characterise the pre-folding stage and likely developed simultaneously with the regional flexuring of the foreland.

The second generation FRACT2 trends about N°138 with subvertical dip (i.e. backtilted data, Figure 5.6). They also postdate Bedding Parallel Stylolitic (BPS) planes and predate the tectonic stylolites (i.e. TS). These fractures are interpreted as pre-folding and represent quantitatively the most important fracturing stage during the Albanides FTB development in the studied area. They are likely to develop contemporarily with the maximum burial in the basin under high vertical pressure.

A third generation FRACT3 is represented by sub-horizontal fracturing, parallel to the BPS after rotation of the data (i.e. backtilted data, Figure 5.6). They characterise the syn-folding stage with a displacement along the bedding. This generation is not abundant (n=2) if compared to the previous fracturing generations. Moreover, the BPS are in some samples filled with calcite cement, insoluble residues, and Fe-oxides. The re-opening of Bedding Parallel Stylolites and the development of the FRACT3 generation may be linked to the development of the sub-horizontal stress regime. This observation possibly reflects a decrease of the lithostatic pressure (e.g. the onset of the folding).

The last fracture generation, i.e. FRACT4, has a N-S orientation with subvertical dip. Unfortunately the relationship with stylolites is not known. In the case of a pre-folding origin (cf. backtilted data), the folded data displays also a N-S orientation but with a slightly dipping

attitude, i.e. mainly 70-65°, towards the east. However if these fractures have a syn to post-deformational origin (cf. raw data), they may be linked either to an E-W compression, or they developed during a second burial stage, characterised by a N-S extension.

These fracture generations record a complex deformation history. Based on the data, three main phases of deformation can be preliminarily pointed out:

(1) A westward migration of a deformation front through the foreland basin, causing a lithospheric flexure induced by thrust sheet loading in front of the fold belt. This depression is subsequently filled with turbidites, constituting the Oligocene flysch. During this important subsidence, the FRACT1 generation as well as the FRACT2 generation likely formed under high (close to lithostatic) pore-fluid pressure regime. According to field observations, FRACT1 are synchronous and FRACT2 postdates the BPS development. Both generations predate the formation of tectonic stylolites.

(2) The second phase corresponds to the folding stage and the out-of-sequence development of the Berati unit, which is thrust over the Kurveleshi unit. This phase occurs from the Middle Miocene onward (Nieuwland et al., 2001) and can be linked with the FRACT3 generation and the TS1, which are parallel to the frontal thrusts.

(3) Concerning the generation FRACT4 and the second set of TS (i.e. unfolded planes oriented N70°), several uncertainties remain. However, based on the work of Mantovani et al. (2002), the Ionian Zone undergoes a SE-NW compression during the Middle Miocene, subsequently followed by an E-W compression during the Late Miocene. This evolution of the main stress, pointing to the active tectonics at the trench between the African and Eurasian plate (Le Pichon and Angelier, 1979), may have developed the second set of tectonic stylolites (i.e. folded TS2 oriented N50°86S; raw data) and the generation FRACT4 by folding. Under this regime, the NE faults would act as transfer zones with dominant dextral strike-slip motion and subsidiary normal displacement.

5.3- Paleofluid characterisation

In petroleum exploration, many geologists carried out detailed research to obtain a precise

paragenesis (i.e. successive generations of diagenetic phases) as well as to determine the nature/origin of the fluids and water-rock interactions. As mentioned in the methodology chapter, it requires an integration of a wide range of different techniques, including field studies, accurate petrographical and geochemical studies and other techniques such as microthermometry. However, reconstructing the paragenetic sequence is rather difficult since not always crosscutting relations exist, fractures might have reactivated, the development of a fracture is not necessarily succeeded by cementation, and replacive phases and recrystallisation phenomena have been observed. Often petrographical and geochemical signatures have been reset by later water-rock interactions. Experience learns that especially in carbonates, it is very often difficult to address the primary nature of the diagenetic products and their related fluids. With regard to the interpretation below this should be kept in mind. Based on a critical evaluation of the former aspects, 8 major stages of fluid cementations have been distinguished. A relative timing of different vein types compared to stylolites, i.e. bedding parallel stylolites and tectonic stylolites, is represented in Table 5.3.

5.3.1- Petrography and structural data

5.3.1.1- Cal-1 cement

The first vein generation Cal-1 crosscuts and is crosscutted by burial stylolites (BPS), indicating that they are synchronous. Its infill consists of calcite cement, characterised by dull-luminescent blocky calcite crystals (Figure 5.7). The structural orientation of Cal-1 veins corresponds to FRACT1 (Figure 5.6). Since the FRACT1, which is characterised by an average direction of N138°, has a subvertical dip (backtilted data) and is crosscut by TS, it has been interpreted as pre-folding.

5.3.1.2- Cal-2a cement

In samples where stylolites are present, the calcite cement Cal-2a is interpreted to have developed after pressure-solution based on the fact that they crosscut the BPS and are affected by TS (Figure 5.7 A). These veins are mainly 0.5 cm wide. Their structural orientations are represented on stereonet in Figure 5.6 (i.e. FRACT1). Their mean strike is N150° with subvertical dip, which is similar to the structural orientation of the previous vein generation Cal-1

Vein type	Cement generation	Fracture generation	Relative timing
Pre-deformational veins	Cal-1; Cal-2	FRACT1	Syn- and post-BPS veins
Breccia veins	Cal-3 / Dol-2	Reopened FRACT1 - FRACT2	Pre-tectonic stylolites
Shear veins	Cal-4	FRACT3	Syn-folding
Crack-seal veins	Cal-5; Cal-6/ Dol-2	New-phase of FRACT2 Undefined fracture generation for Cal-6	Post-tectonic stylolites
Dolomite veins	Dol-1 / Dol-3	-	Post-tectonic stylolites
Late veins	Cal-7	Reopened FRACT2 – FRACT4	Post-tectonic stylolites

Table 5.3. Relative timing of the different vein types compared to stylolites and fracture generations, principally based on crosscutting relationships.

Cal-2a veins consist of blocky and highly twinned calcite crystals ranging in size from 10 to 500 μm (Figure 5.7B & C). The crystals likely possess a minor content of iron, attested by the purple coloration of the calcite (Figure 5.7F). Under cathodoluminescence, a minor sector zoning occurs with dull to bright luminescence (Figure 5.7D). In most cases, this cement precipitates at the border of the fractures with an increase of the crystal size towards the centre of the vein. This cement occurs also in enlarged vugs of dissolved aragonite components. In this cement, few percents of transported quartz and barite crystals, up to 25 μm wide, occur, which are usually fractured, angular to subrounded and surrounded by clay minerals.

5.3.1.3- Cal-2b cement and Dol-1 dolomite

➤ Calcite cement

The next vein postdating the BPS and predating the TS consists of Cal-2b cement. These veins occur in fractures that are oriented N 150° with subvertical dip (i.e. FRACT1). They are 0.4 to 0.5 cm wide. Cal-2b precipitates either in newly created fractures or is crystallising upon Cal-2a cement. No crosscutting relationships with Cal-2a cement have been observed, neither an irregular contact pointing to a stop in the cementation between both generations. Only a change in crystal habit and geochemistry differentiates both generations (see Figure 5.7C & D).

Petrographically, Cal-2b is characterised by non-transparent, large and blocky non-ferroan calcite crystals (Figure 5.7F), with a size up to 800 μm . The crystals show strong development of twinning planes (e.g. simple and double twins). Under CL, a sector-zoned calcite occurs with dull to orange luminescence, which becomes

brighter where the crystals are non-transparent. On Figure 5.8G & H, a relic of a zoned Cal-2a calcite is recognisable in the Cal-2b cement, which proves that some of the Cal-2a cements have been intensely recrystallised. In some fractures, the occurrence of a dissolved area can be noticed, as it is shown on Figure 5.8 E.

➤ Dol-1 crystals

Some micrometric dolomite crystals (Dol-1) are scattered in the central part of the Cal-2b vein, usually close to dissolved areas. These dolomite crystals have a preferential orientation, since they precipitate parallel to twinning planes. The crystals are sub- to euhedral with a size varying between 5 to 100 μm (Figure 5.8 F). They display uniform red-dull luminescence and are often surrounded by homogeneous dull luminescent calcite. They make up to 10 % of the Cal-2b vein (Figure 5.8B).

However some dolomite crystals are partly corroded on the SEM photomicrographs partially due to the polishing and to the use of dilute HCl during the coloration. Based on these observations, Dol-1 crystals likely precipitated in places, where secondary porosity developed at the vicinity of longitudinal dissolved areas in the Cal-2b cement (Figure 5.8 E).

➤ Other minerals

Cal-2b vein is also characterised by the occurrence of around 1-2 % of strontianite (SrCO_3) which are determined on the one hand since they remain not stained with Alizarin red-S (Figure 5.9A & B) and on the other hand by microprobe analyses. These crystals consist of clear (i.e. transparent), spiky and minute crystals, characterised by thin and nearly acicular shapes with a size varying between 6 and 80 μm long and 1.5 and 10 μm wide. As for the dolomite

crystals, the strontianite precipitates along the calcite twinning planes. It is important to note that their small size contributes to minimize their representative occurrence, because they are detected with difficulties. Consequently the geochemical results, e.g. Sr-content from the AAS analyses can be misinterpreted.

Small barite crystals (BaSO_4), up to 10 μm in size, are also scattered in the Cal-2b cement. The distinction between barite and strontianite (Figure 5.9C) is made on the one hand by using Scanning Electron Microscopy coupled with X-ray microanalysis and on the other hand by using microprobe analyses.

Few small brecciated fragments occur also in Cal-2b cement and contain transported minerals such as apatite, barite, strontianite and fibrous celestite (SrSO_4), associated with detrital phyllosilicates (Figure 5.9D). Many iron oxide/hydroxides, which are defined by opaque and prismatic crystals, also occur and likely relate to weathering products.

5.3.1.4- Cal-3 cement

Cal-3 represents the most heterogeneous cement of the Kelcyra area due to a number of large brecciated fragments (Figure 5.11 E & F) that are included in the cement. This fluid precipitates in NW-SE (FRACT2) or in re-opened veins (FRACT1) and displays usually many brecciated wall-rock fragments, especially in the central part of the veins. These veins are up to 2 cm wide and the brecciated fragments can reach a

size of 1 mm. The timing of this generation is uncertain since no crosscutting relationship with preceding veins is observed. The Cal-3 cement, which contains brecciated fragments, is called Cal-3b.

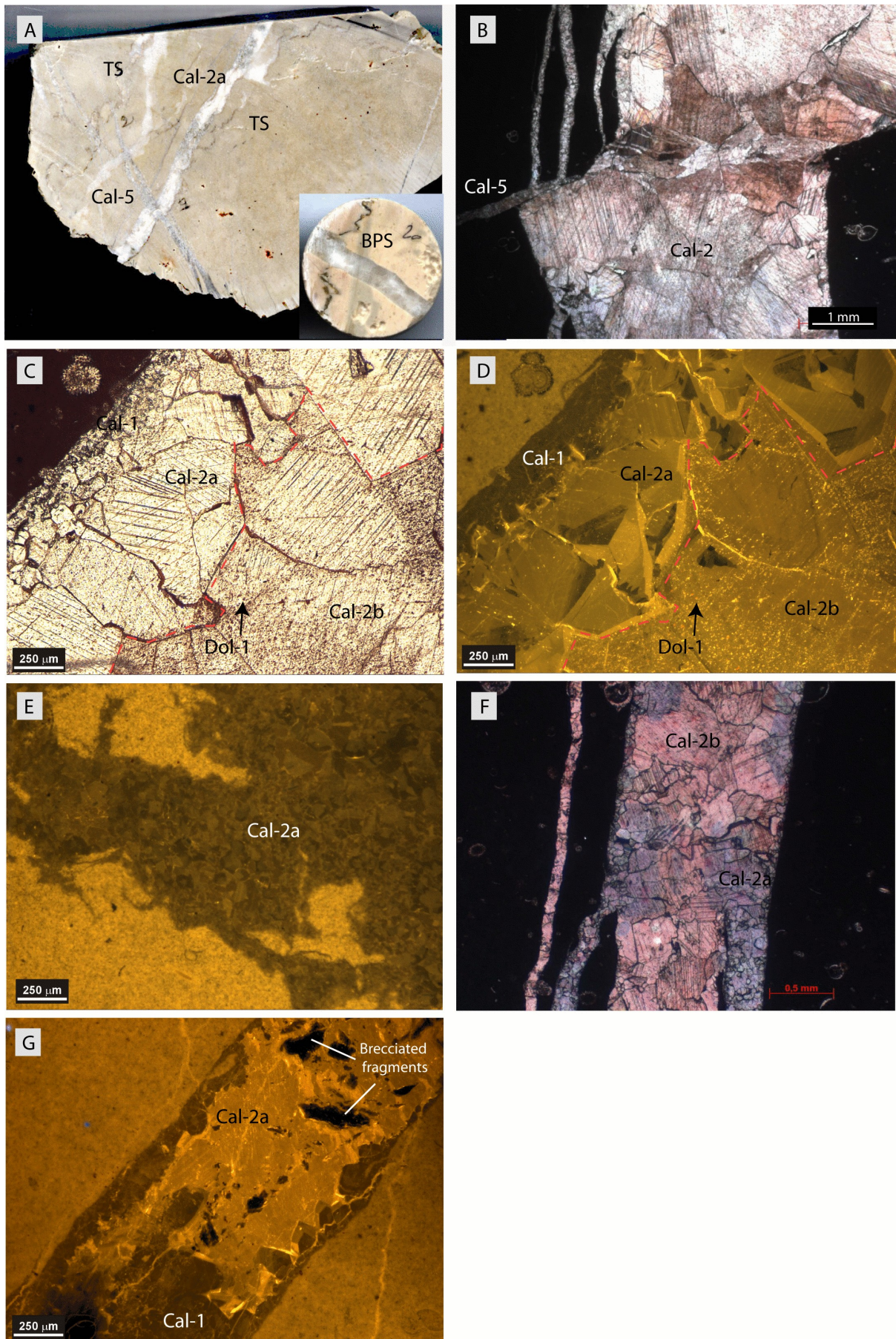
➤ Calcite cement

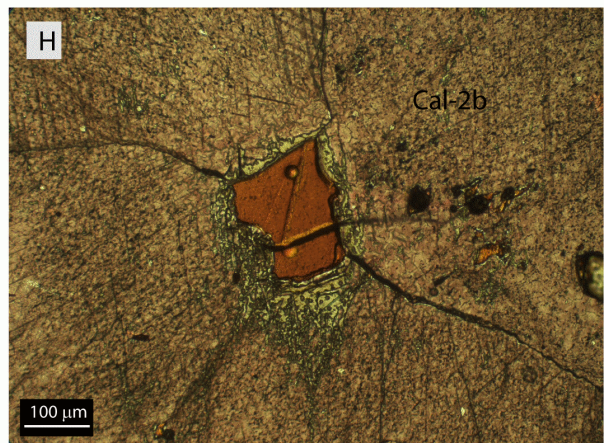
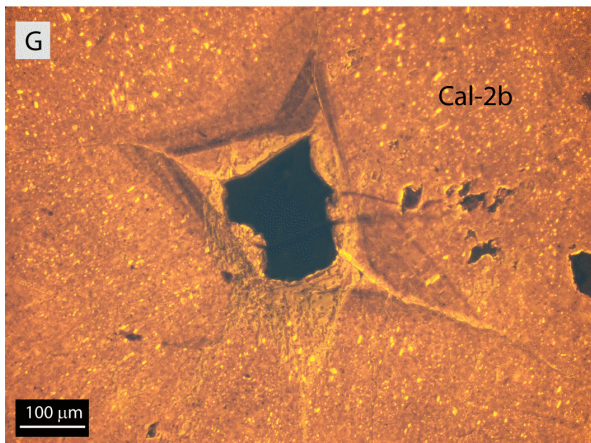
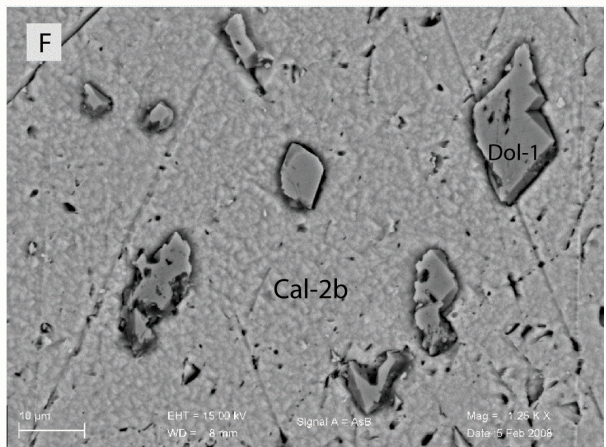
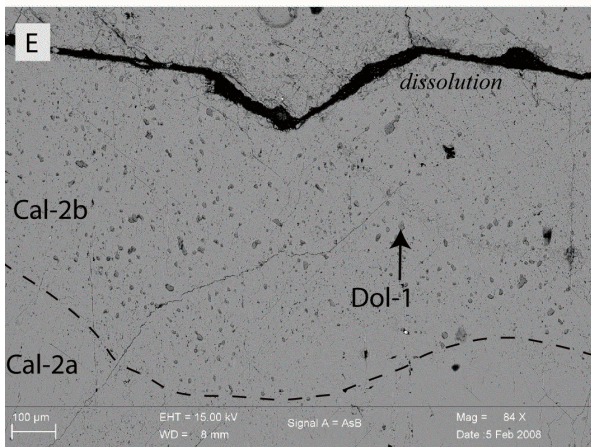
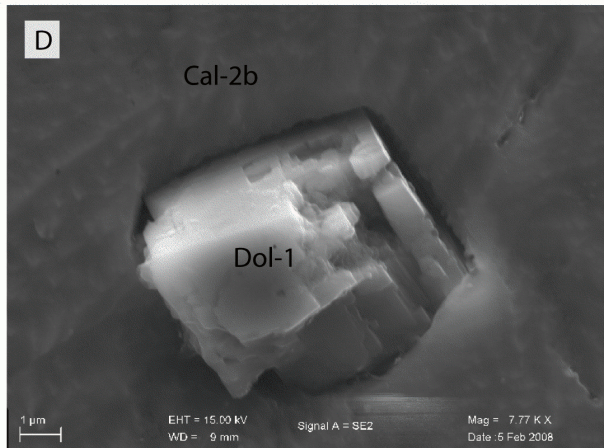
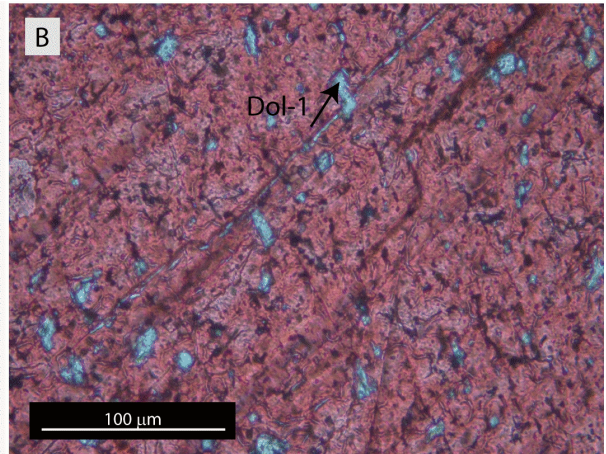
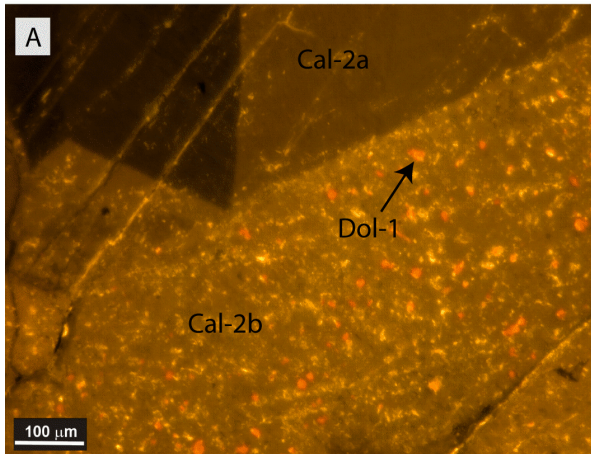
The calcite crystals are large blocky to elongated and usually non-transparent with abundant scattered dolomite inclusions (Dol-1, Figure 5.11C & D). The calcite is non-ferroan and displays a recrystallised pattern under CL but locally exhibits also the original dull to bright sector zoned luminescence (Figure 5.11 C & D). In some places, these crystals are crosscut by a dull luminescent calcite vein but this crosscutting is only evident in CL. Moreover, the twinning, which postdates this calcite cementation, is not disturbed by the reopening and develops a continuous pattern that crosscuts the fractures (Figure 5.10A).

This development of double twins indicates that the fluid, which precipitates the dull luminescent calcite, crystallised in crystallographic continuity with the host crystal phases, i.e. Cal-3b, along fractures, forming a crack-seal texture (Figure 5.10; Laubach et al., 2004). This type of fracturing attest of a high pressure regime and the change of the cathodoluminescence reflects an evolution in precipitation conditions between early and late cements in the growth of the fracture.

Figure 5.7. (A) Photograph of crosscutting relationship between vein generations and tectonic stylolites (TS). Here, TS are cutting a Cal-2 vein and predate a Cal-5 vein. (B) Photomicrograph of Cal-5 vein crosscutting Cal-2 vein. (C) Transmitted light view of Cal-2a and Cal-2b vein generations, showing highly twinned calcite crystals. Note the continuity between both phases and the occurrence of Dol-1 inclusions. (D) CL view of picture (C). A distinction between Cal-2a and Cal-2b can be made. Cal-2a cement displays a sector zoning, whereas Cal-2b is recrystallised as attested by the varying CL characteristics. It contains many scattered red luminescent dolomite crystals. (E) CL microscopic view of Cal-2a cement, which has precipitated in a vug. (F) Transmitted light view of Cal-2a and Cal-2b cements, stained with Alizarin Red-S and K-ferricyanide. Cal-2a is relatively more enriched in Fe than Cal-2b, attested by the blue coloration of the calcite crystals. (G) CL view of Cal-2a cement, which precipitated in a reused Cal-1 vein. Cal-2a cement displays undefined brecciated fragments.

Figure 5.8. (A) CL view of a contact between Cal-2a and Cal-2b with red-dull dolomite crystals (Dol-1) precipitated into Cal-2b calcite cement. (B) Transmitted light view of unstained dolomite crystals scattered into pink-coloured calcite crystals (Cal-2b cement). (C) and (D) SEM views of euhedral dolomite crystals. The crystals are partially corroded due to the polishing and the etching by HCl in the Alizarin Red-S stain. (E) & (F) Backscattered Electron (BSE) images of Dol-1 crystals, which have precipitated parallel to the twinning planes. In (E), it is clear that the dolomite precipitates close to the dissolved area of the Cal-2b vein. (G) & (H) CL and transmitted light views respectively of a rest of sector-zoned luminescent calcite into the Cal-2b cement. Notice that this sector zoned luminescent calcite part remains more transparent on normal view.





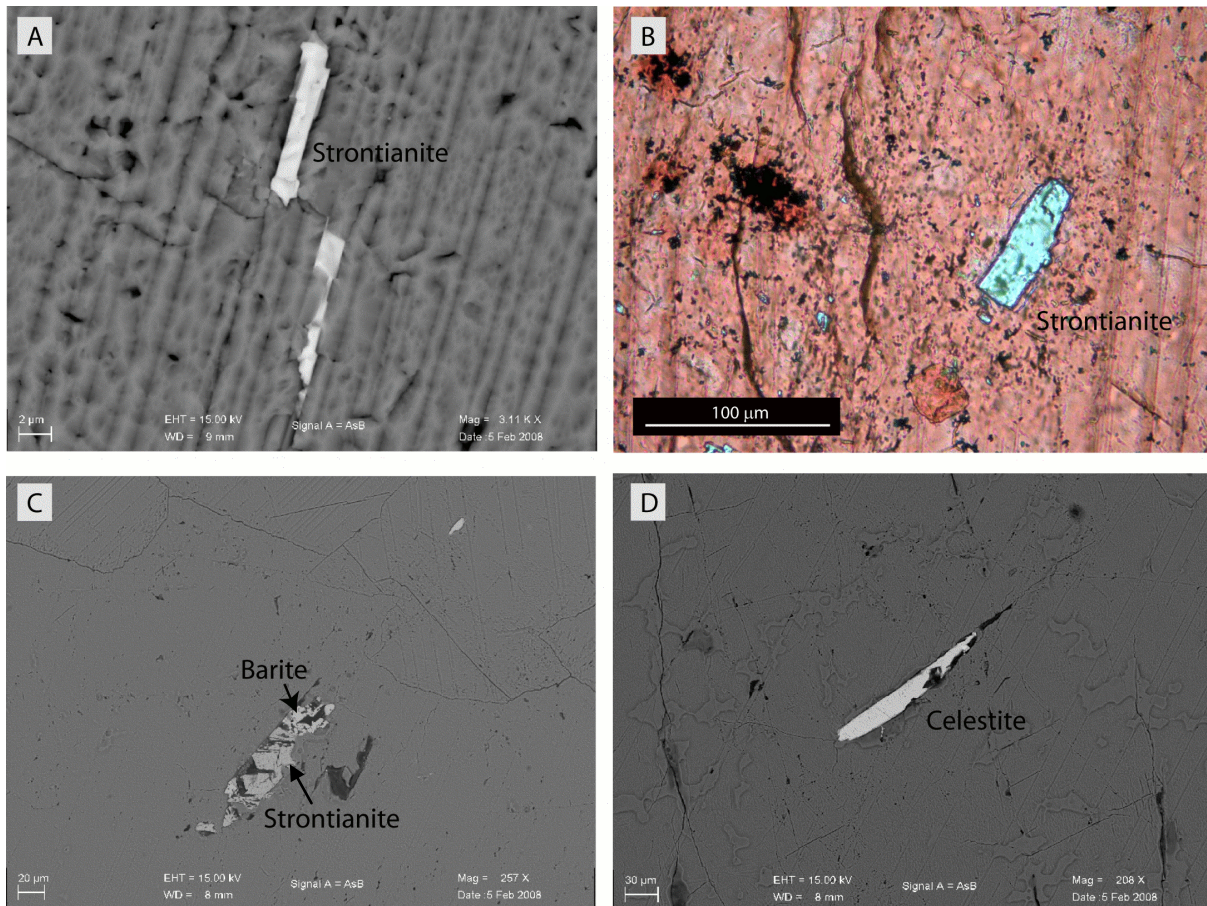


Figure 5.9. (A) Backscattered electron (BSE) image of acicular strontianite, which has precipitated along calcite twins in Cal-2b cement. (B) Photomicrograph of strontianite in Cal-2b cement. Strontianite remains uncoloured after Alizarin Red-S staining. (C) BSE image of strontianite crystal associated with barite in Cal-2b cement. (D) BSE image of celestite.

➤ Dol-1 crystals

These dolomite crystals have a size varying between 10 and 100 μm, similar to the ones observed in Cal-2b veins. The dolomitic phases are sub- to euhedral, not deformed and display a red-dull luminescence. These dolomites occur especially in non-transparent calcite crystals, which may attest of a recrystallisation process affecting the latter calcite phases. In Figure 5.11A & B, dissolution features are visible in the centre of the Cal-3 vein and may relate to the interaction with a later fluid.

➤ Strontianite

SEM-EDS analysis allowed to identify strontianite crystals that occur along calcite twins. These oriented prismatic crystals are up to 10 μm long. Based on their euhedral shape and orientation, these crystals likely precipitated in place and thus postdate or they formed simultaneously with Cal-3 cement.

Their total content is more difficult to assess since only micrometric crystals exist. Moreover, up to 5% of vuggy pore space have oriented and elongated shapes, with a size similar to the strontianite crystals.

Consequently it is not unlikely that some of the strontianite has been dissolved or detached during the polishing and this phenomenon should be taken into account when assessing their real strontianite content.

➤ Brecciated fragments

The brecciated fragments, which are very abundant in this cement generation, are up to 1 mm large and contain principally transported grains in the fragments as dolomite (Dol-2) and barite, phyllosilicates, quartz, some feldspar grains, micrometric apatite and associated Fe-oxides (Figure 5.15B).

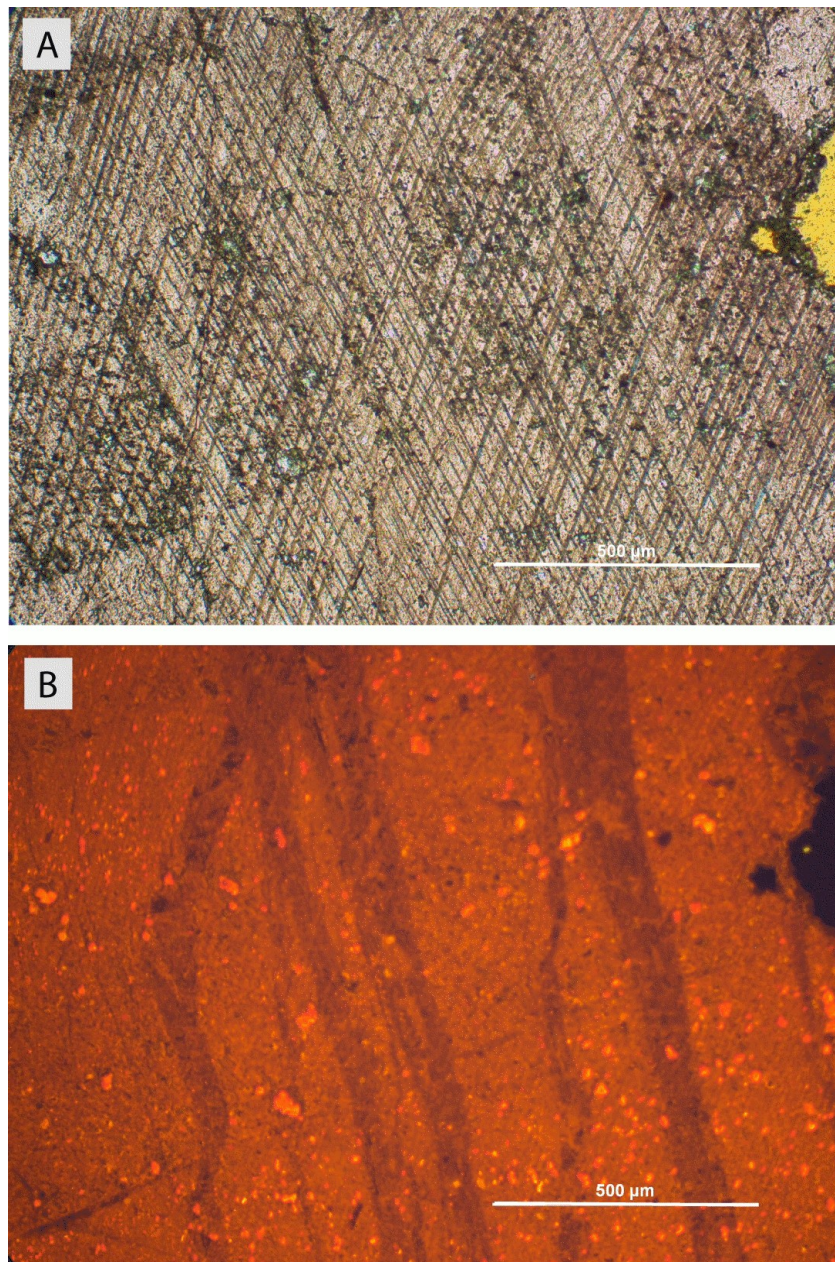


Figure 5.10. Transmitted light (A) and CL (B) views of a crack seal texture in the Cal-3b cement. Notice the fracture opening, characterised by a dull luminescent calcite cement, into the Cal-3b filling. On picture A, the twinning is continuous through the orange and the dull luminescent cements. It demonstrates that the fluid has nucleated in crystallographic continuity with host phases along the fracture wall as a crack-seal texture. Notice also that the Dol-1, i.e. the micrometric red-dull luminescent dolomites, occur only in the orange luminescent calcite (i.e. early growth), whereas they do not occur in the dull luminescent calcite, i.e. late growth phases.

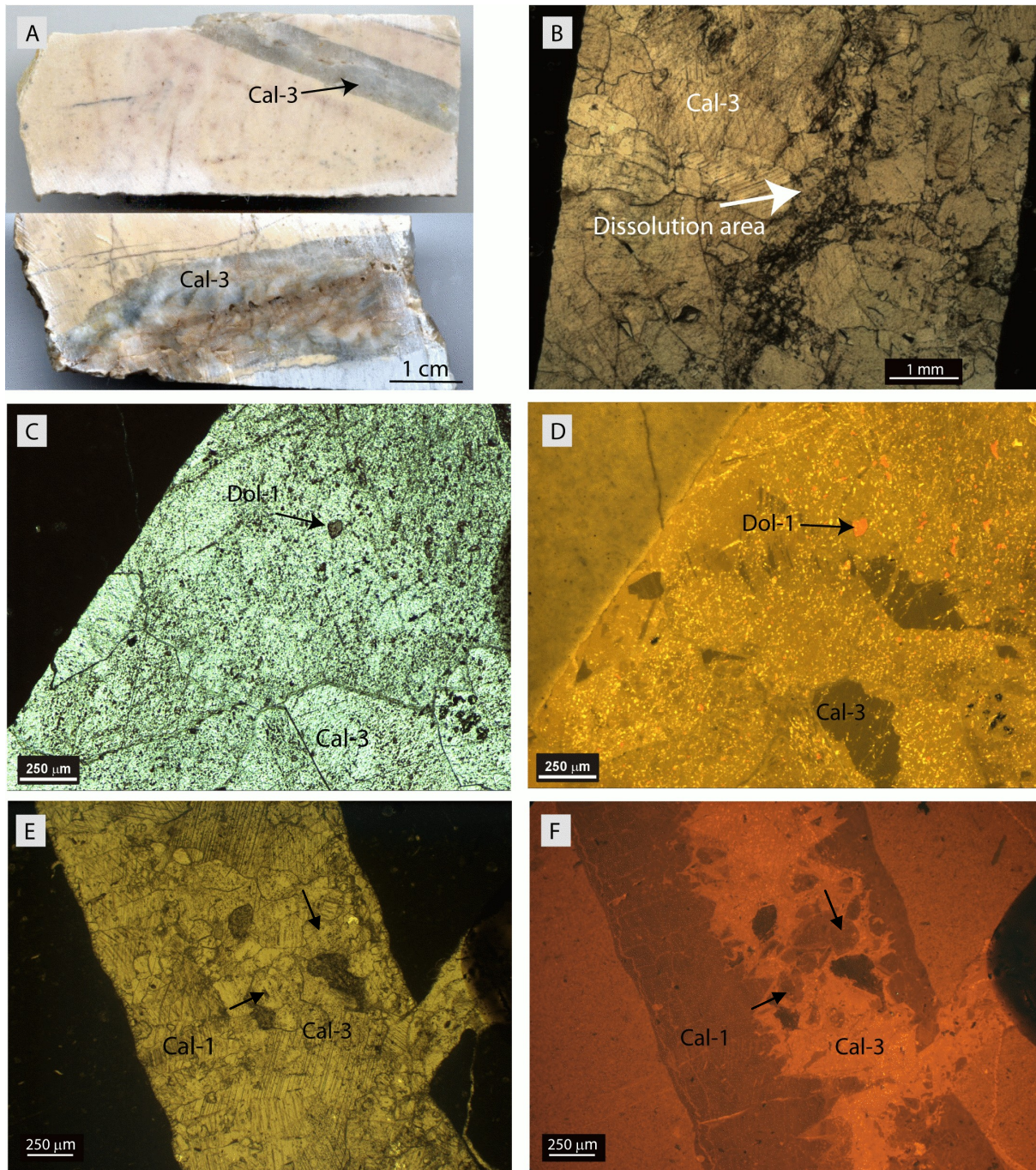


Figure 5.11. Images of Cal-3 cement. (A) Photograph of Cal-3 cement on polished sections. The vein is up to 2 cm wide. (B) Photomicrograph of Cal-3 cement, displaying highly twinned calcite crystals. The centre of the vein is characterised by longitudinal dissolution features, giving rise to a grainy texture. (C) & (D) Respectively transmitted light and CL views of dolomite crystals (Dol-1), scattered in Cal-3 calcite cement. Notice the presence of a relict texture of sector zoned calcite. (E) & (F) Respectively transmitted light and CL views of Cal-1 cement (dull luminescence) re-used by Cal-3 cement (yellow luminescence) that contains many brecciated Cal-1 vein fragments (shown with arrows).

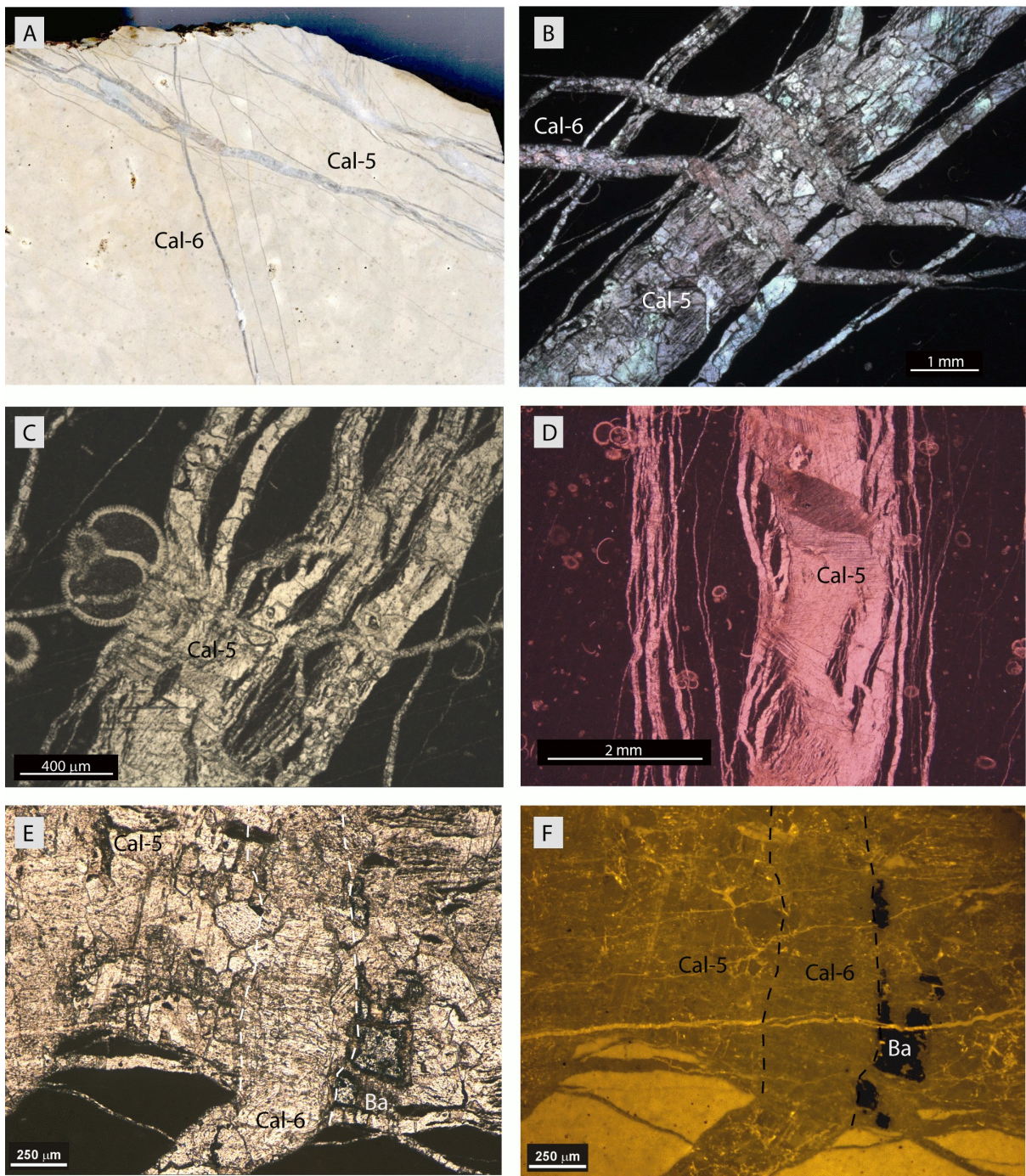


Figure 5.12. Cal-5 and Cal-6 veins. (A) Photograph of a vein filled by Cal-5 cement crosscutted by a vein with Cal-6 cement. (B) Transmitted light view of Cal-5 vein crosscutted by Cal-6 veins. (C) Transmitted light view of Cal-5 vein, showing many host-rock fragments, which are parallel to the fracture opening. (D) Transmitted light view of stained Cal-5 vein. The pink colour of the calcite crystals reflects a low Fe-content. (E) and (F) respectively transmitted light and CL views of Cal-6 vein postdating Cal-5 vein. Notice the occurrence of barite (Ba) in Cal-5 cement (i.e. non-luminescent crystal in F) adjacent to the Cal-6 vein.

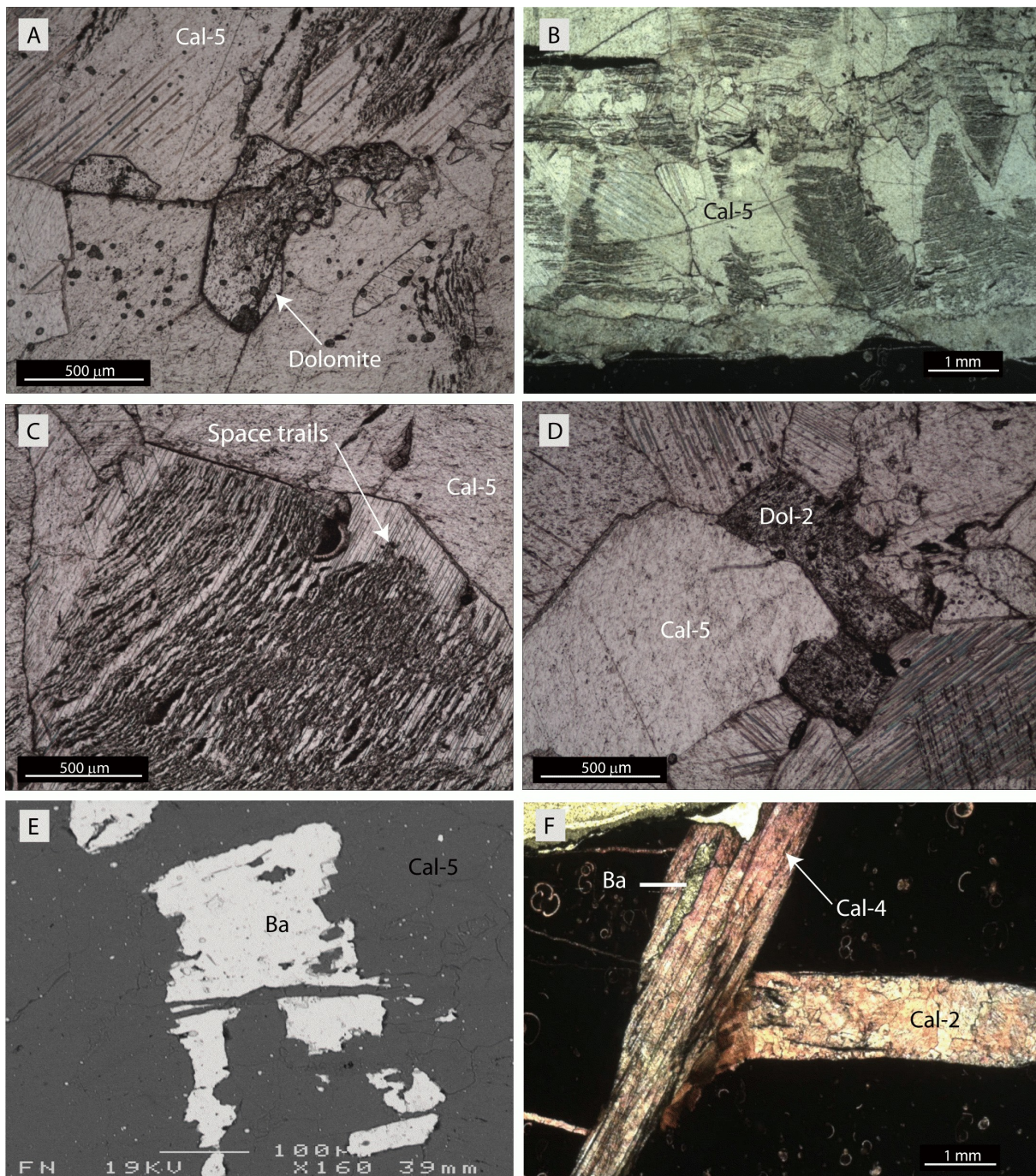


Figure 5.13. (A) Transmitted light view of Cal-5 cement, surrounding subhedral dolomite crystals. (B) Transmitted light view of the fibrous antitaxial texture of the Cal-5 cement, showing many trails of pieces of wall-rock. (C) Enlargement of regularly trails of pieces of wall-rock in Cal-5 cement. (D) Transmitted light view of Dol-2 crystals emplaced into Cal-5 cement. The dolomite is non-transparent and possesses a subhedral shape. The calcite cement is highly twinned. (E) Backscattered electron (BSE) image of barite, located in Cal-5 cement. (F) Photomicrograph of stained Cal-2 cement cut by Cal-4 vein. The latter displays fibrous and elongated non-ferrous calcite crystals and contains some barite phases.

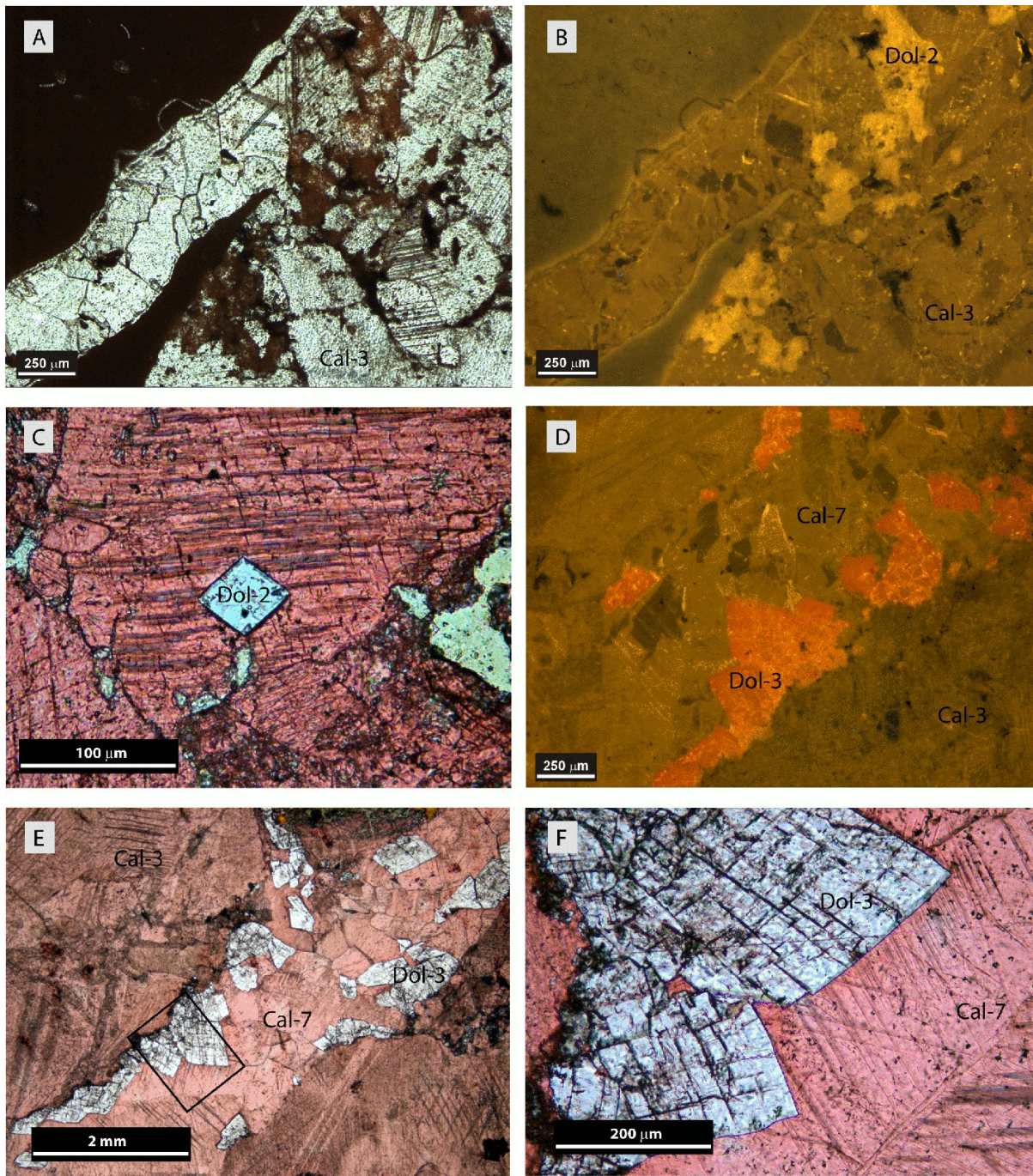


Figure 5.14. (A) & (B) Respectively transmitted light and CL views of Cal-3 cement, displaying brecciated fragments in a dull luminescent calcite cement. Here the fragments are composed of dolomite crystals, which are partially dedolomitised (bright luminescent calcite). (C) Transmitted light view of pink-stained Cal-5 cement with an unstained euhedral dolomite crystal (Dol-2). (D) & (E) Respectively CL and transmitted light views of Dol-3 cement, which precipitates in a re-activated fracture. The unstained dolomite crystals are subhedral, and display a red dull luminescence. This generation predates Cal-7, which consists of dull sector zoned calcite crystals. In picture (E), the unstained dolomite (Dol-3) is clearly visible. (F) Detail of twinned and partially dedolomitised Dol-3 in contact with Cal-7.

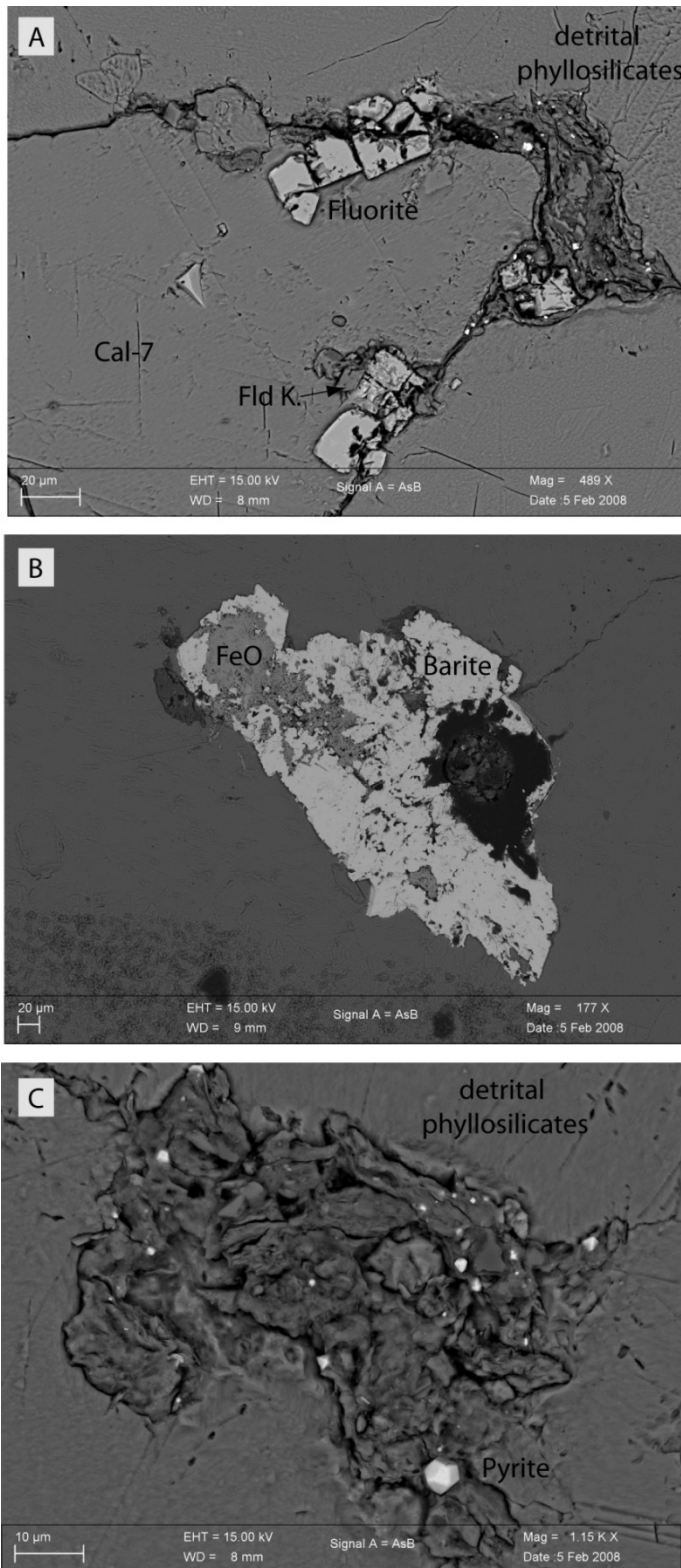


Figure 5.15. Backscattered Electron (BSE) images. (A) Occurrence of altered cubic fluorite and feldspath phases (Fld K.) associated with detrital phyllosilicates at the grain boundaries in Cal-7 cement. (B) Corroded barite crystals associated with oxy/hydroxides (FeO). (C) Detrital phyllosilicates associated with euhedral pyrite.

They are defined by subhedral and partially eroded shapes and determined based on SEM examination, since their small size compromises clear observations when using classical microscopy. The occurrence of fragments, composed of non-transparent crystals and

phyllosilicates in the veins, likely points to a transported origin of these grains and fragments. Dol-2 crystals, which are the most abundant component in the brecciated fragments, have a rhombohedral shape up to 300 μm long and are surrounded by clay or argillaceous phases (Figure

5.14 A & B). At present day, these rhombohedral phases are partially calcitised, a feature that becomes clearly visible by the bright yellow luminescent calcite zone that is associated with the red-dull luminescent dolomite. Under transmitted microscopy, Dol-2 crystals are non-transparent and characterised by a brownish colour, which is in agreement with the proposed dedolomitisation process.

5.3.1.5- Cal-4 cement

Cal-4 veins cement FRACT3. They consist of a dull luminescent calcite, similar to the host-rock. The cement consists of fibrous or elongated calcite crystals, sub-parallel to oblique with respect with the shear plane (i.e. sub-parallel to the bedding). Their long axes have a low angle with the vein wall, describing slicken-fibres (Figure 5.13 F). The veins are up to 2 mm large and displace the already described Cal-2 veins by a dextral movement. At the contact with the host-rock and between stacked zones of differently oriented fibres, pressure solution seams may develop. No crosscutting relationship with Cal-3 has been observed. It is important to note the presence of barite and pyrite crystals, which precipitate in the Cal-4 cement and within adjacent tectonic stylolitic planes.

5.3.1.6- Cal-5 cement

Cal-5 cement, which crosscuts tectonic stylolites TS1 (Figure 5.7A), precipitates in fractures oriented mainly N 138° with subvertical dip (unfolded data, new fracturing phase of FRACT 2).

These calcite-filled fractures, with a size varying up to 1 cm large, possess a crack-seal fabric, as inferred by the existence of micro-structural indicators such as regularly spaced trails of pieces of wall-rock (i.e. mudstone) and elongated calcite crystals. Many pieces of wall-rock, i.e. inclusion bands, and fossils fragments are parallel to the vein wall and spaced in the order of 10 µm (Figure 5.13 B & C). These bands have undulatory shapes and are mainly parallel to one another and to the adjacent vein wall.

The elongated to blocky dull luminescent calcite vein infill has often a fibrous antitaxial texture (Figure 5.13B). The crystals are deformed, twinned and display undulose extinction under crossed polars. Some barite (Figure 5.13E), rhombohedral dolomite (Dol-2 generation, Figure 5.13A & D) and pyrite with a size smaller

than 1 mm, surrounded by phyllosilicates, are also present in Cal-5 vein.

5.3.1.7- Cal-6 cement

Cal-6 vein (Figure 5.12 E & F) predates the second generation of tectonic stylolites TS2. They are 400 and 800 µm wide. Crystal size increases from the border to the centre, from respectively 100 to 300 µm in diameter. This calcite has a low Fe-content and displays a dull luminescence with the same intensity as Cal-5. The calcite crystals have a blocky shape and slight undulose extinction under crossed polars. The crystals possess simple and double twins. Several minerals, such as pyrite and quartz, that are characterised by eroded or dissolved surfaces, occur in Cal-6. Their outlines likely do not suggest a precipitation in place.

5.3.1.8- Dol-3 cement

The next diagenetic phase consists of red-dull luminescent dolomites that are transparent and characterised by coarse subhedral crystals (Figure 5.14 D to F). These crystals have a size of 200 to 800 µm and border some fractures. This generation is observed only a few times. Based on their precipitation along the border of re-activated fractures and their euhedral shapes, dolomite cement precipitates subsequently to the opening of Cal-3 vein (Figure 5.14 D & E) in the created space. Dolomite crystals exhibit characteristic slightly curved crystal surfaces (Figure 5.14 D, E & F) and weak sweeping extinction. The crystals possess also double twinning planes. Small inclusions of barite occur in the dolomite crystals that can be observed under the SEM. This red-dull luminescent dolomite displays bright luminescent calcite areas that point to a partial dedolomitisation (less than 5 % of the total volume).

The only difference between Dol-1 and Dol-3 generations is the way of precipitation, which occurs respectively as dolomite inclusions in calcite cement and as euhedral dolomite crystals in open fractures.

5.3.1.9- Cal-7 cement

The last vein related calcite cement, determined in the Kelcyra outcrop, is characterised by dull sector zoned luminescence (Figure 5.14 D). The size of the veins varies between 0.5 and 1 cm in width. In comparison to many previous calcite cement types, these veins do not contain any dolomite, neither barite inclusions. The calcite

crystals are transparent and show thin double twinning planes. Some transported minerals such as partially calcitised dolomite crystals, feldspar and phyllosilicates (Figure 5.15C) are present in Cal-7. Moreover few small cubic fluorite crystals, i.e. $< 20\mu\text{m}$ in diameter (Figure 5.15 A), characterised by altered and fractured surfaces, have been found along crystal boundaries.

5.3.2- Stables isotopes

Figure 5.16 displays a stable isotope crossplot of $\delta^{18}\text{O}$ and $\delta^{13}\text{C}$ values of the Upper Paleocene to

Eocene limestones of the Kelcyra outcrop and of the differentiated diagenetic phases. Marine values for the Upper Paleocene-Eocene display $\delta^{18}\text{O}$ values varying between -2 and +0.1 ‰ V-PDB and $\delta^{13}\text{C}$ from +0.5 and +4 ‰ V-PDB (Veizer et al., 1999). The studied host rocks of the Kelcyra outcrop have $\delta^{18}\text{O}$ values comprised between -1.84 and -0.31 ‰ V-PDB and $\delta^{13}\text{C}$ ranging from +1.53 to +1.88 ‰ V-PDB, consistent with the marine signature.

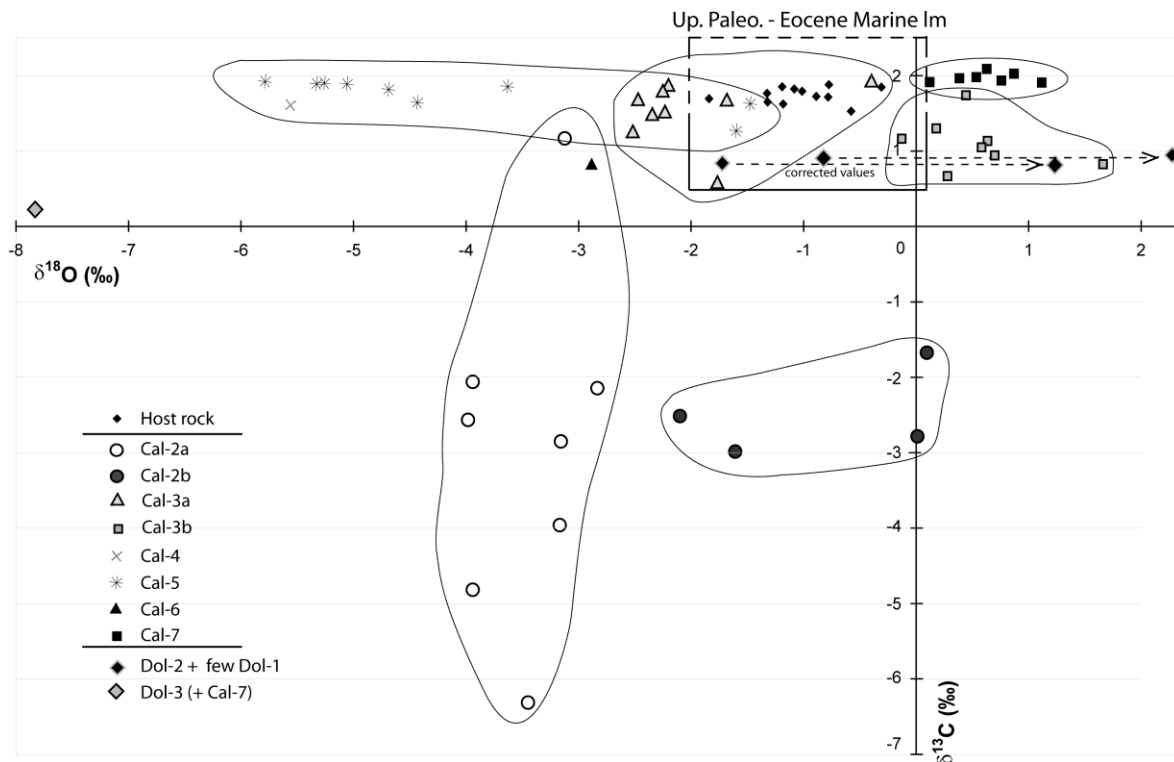


Figure 5.16. Carbon and oxygen isotopic crossplot with compositions of the Upper Paleocene-Eocene limestones (Im, Veizer et al., 1999) from the Kelcyra outcrop and their diagenetic products. Notice that the isotopic data for the dolomite phases have not been corrected with the fractionation factor of the dolomites of about 3 ‰ (Land, 1980).

With the exception of Cal-1 cement, due to its small size, nearly all vein generations have been sampled separately and therefore all these individual diagenetic phases were isotopically characterised. However it was not possible to avoid dolomitic and host-rock inclusions during sampling. The isotopic signature of the second fracture-filling stage (i.e. Cal-2a cement) plots in a very narrow range with $\delta^{18}\text{O}$ from -3.98 to -2.82 ‰ V-PDB, and exhibits a large spread in $\delta^{13}\text{C}$ between -6.32 to +1.18 ‰ V-PDB. Concerning the Cal-2b cement, the data shows a complex signature, characterised by $\delta^{18}\text{O}$

between -2.10 and +0.1 ‰ V-PDB and $\delta^{13}\text{C}$ ranging from -1.68 to -3.0 ‰ V-PDB. Notice however that these results reflect a mixed signature, the isotopic signature of the calcite cement being mixed with an average of 10 % of scattered dolomite inclusions (i.e. Dol-1 generation), determined petrographically. Due to the small size of the dolomite crystals, it has been impossible to separate the two phases, i.e. Dol-1 and Cal-2b. Notice that Cal-2a and Cal-2b are the only cement phases in the Kelcyra paragenesis, characterised by a depleted carbon signature.

Filling stage		Mg (ppm)	Ca (ppm)	Mn (ppm)	Sr (ppm)	Si (ppm)	Fe (ppm)
Cal-2a	Minimum	420	379460	< dl	< dl	160	< dl
	Maximum	2540	415390	1470	13190	1320	2840
	Average (n=13)	1010	401118	488	3678	654	523
	Average AAS	286	371764	511	1559	-	440
Cal-2b	Minimum	930	397960	< dl	470	170	< dl
	Maximum	4960	406620	790	6960	860	< dl
	Average (n=6)	3263	402335	132	2238	412	< dl
	Average AAS	3420	390218	390	742	-	69
Cal-3a	Minimum	1010	399550	< dl	30	160	<dl
	Maximum	4080	403260	100	1780	270	740
	Average (n=4)	2775	401768	25	653	213	185
	Average AAS	2177	368115	380	662	-	500
Cal-3b	Minimum	1500	404750	< dl	120	< dl	< dl
	Maximum	2740	405790	<dl	1030	120	<dl
	Average (n=3)	2237	405420	<dl	623	40	0
	Average AAS	2159	373487	378	1231	-	108
Cal-4	Minimum	260	401840	< dl	< dl	< dl	< dl
	Maximum	640	409860	620	1190	780	1030
	Average (n=3)	440	406223	207	597	260	597
Cal-5	Minimum	550	394910	400	2900	120	880
	Maximum	2120	399740	1010	4870	740	3100
	Average (n=3)	1550	396920	783	3573	487	2193
	Average AAS	1133	371820	573	1321	-	1365
Cal-6	Minimum	1530	396930	< dl	< dl	600	< dl
	Maximum	3320	405300	520	510	690	< dl
	Average (n=2)	2425	401115	260	255	645	< dl
Cal-7	Minimum	1730	399390	< dl	< dl	< dl	< dl
	Maximum	4350	408110	460	380	250	< dl
	Average (n=7)	3466	404441	127	54	67	< dl
	Average AAS	2943	381973	409	291	-	46

Table 5.4. Minimum, maximum and average data for the major and trace elements in ppm based on microprobe analysis of the main diagenetic phases in the Kelcyra area. Values below detection limit are indicated with "< dl" (about <10 ppm). The sign "-" means the lack of analytical results. Additionally, 14 samples of diagenetic phases have also been analysed by using AAS. Their average measurements are given in Average AAS. In the case of data below the detection limit, <dl has been replaced by 10 ppm, consisting of the average lowest limit, to calculate the average value.

The isotopic signature of the brecciated veins (i.e. Cal-3 cement) plots into two clusters (i.e. Cal-3a and Cal-3b), according to the occurrence of brecciated fragments, which "contaminate" the isotopic signature of the calcite cement, and

perhaps also the large amount of Dol-1 in the centre of the vein interferes. Cal-3a, without brecciated fragments and Dol-1, displays $\delta^{18}\text{O}$ and $\delta^{13}\text{C}$ values between -2.52 to -0.4 ‰ V-PDB and +0.56 to +1.92 ‰ V-PDB respectively, that

is practically similar to those of the host-rock. The Cal-3b cluster, representing the calcite cement with brecciated fragments (i.e. mainly dolomite crystals, Dol-2 generation), is enriched in $\delta^{18}\text{O}$ with respect to the host-rock and the marine reference, showing $\delta^{18}\text{O}$ values between -0.13 to +1.66 ‰ V-PDB and $\delta^{13}\text{C}$ varying between +0.67 to +1.74 ‰ V-PDB. Only one analysis could be realised in Cal-4 cement due to the small thickness of this vein type. It shows a depleted $\delta^{18}\text{O}$ -signature of -5.57 ‰ V-PDB and a $\delta^{13}\text{C}$ of +1.61 ‰ V-PDB. The stable isotopes for the crack-seal Cal-5 veins exhibit a large spread in $\delta^{18}\text{O}$, displaying depleted values varying from -5.78 to -1.48 ‰ V-PDB and $\delta^{13}\text{C}$ signatures between +1.28 to +1.92 ‰ V-PDB. For Cal-6 cement, only one sample was analysed. It possesses a value of -2.88 ‰ V-PDB for $\delta^{18}\text{O}$ and of +0.82 ‰ V-PDB for $\delta^{13}\text{C}$. The last studied calcite cement, i.e. Cal-7, which also is characterised by the occurrence of transported mineral phases, exhibits positive oxygen and carbon signatures. They have a $\delta^{18}\text{O}$ signature varying from +0.12 to +1.12 ‰ V-PDB and $\delta^{13}\text{C}$ between +1.91 to +2.09 ‰ V-PDB.

Since the dolomite phases could not be sampled separately, a chemical separation of dolomite and calcite was carried out prior to the isotope analysis (cf. Nader et al., 2008). The results of the dolomite phase show $\delta^{18}\text{O}$ and $\delta^{13}\text{C}$ ranging from respectively -0.12 to +0.73 ‰ V-PDB and from +0.82 to +0.94 ‰ V-PDB. They consist of a mixture of Dol-1 and Dol-2 generations (predominantly). If the fractionation factor is applied for dolomite reported by Land (1980), $\delta^{18}\text{O}$ values vary from +1.25 to +2.20 ‰ V-PDB. Notice that the dolomite crystals possess the same isotopic signature as the Cal-3b cement. Therefore, it is questionable whether the separation was successful. However, no classical geochemical technique allows to separate both mineralogies, except the use of a microdrill, laser or the nanosims.

Only one isotopic analysis of Dol-3 was realised and displays a $\delta^{18}\text{O}$ of -7.87 ‰ V-PDB and a $\delta^{13}\text{C}$ of +0.26 ‰ V-PDB. However, this oxygen isotopic ratio has not been corrected by using the fractionation factor for the dolomite given by Land (1980). Consequently, a shift of 3‰ should be taken into consideration when interpreting the Dol-3 signature. Moreover, due to the small size

of the vein, this isotopic ratio has been likely contaminated by a limited amount of Cal-7 cement.

5.3.3- Elemental geochemistry

The major and trace element content of the carbonate phases is listed in the Table 5.4, Table 5.5 and Table 5.6. On the Table 5.4, minimum, maximum and average values of the successive fracture-filling phases correspond to measurements realised by microprobe analyses, whereas also the average values measured by AAS (i.e. Average AAS) are also mentioned.

Table 5.5 and Table 5.6 list all the major and trace element data, obtained respectively with microprobe and AAS. It is important to notice that both techniques provide sometimes different element contents for the same vein-filling. This is principally due to a differentiation in the sampling way and in the sample quantity to analyse. In the description below, only the data from the microprobe will be used to characterise the cements since this sampling technique allows to differentiate the different phases, calcite from dolomite phases as well as the uncommon minerals, such as strontianite and barite. The sampling used for the AAS analyses also involves the incorporation of minerals such as fluorite, phyllosilicates, barite and dolomites. Moreover, not all vein generations have been geochemically analysed with AAS. Only the most important phases, determined by petrography, have been studied.

5.3.3.1- Calcite cements

Due to the small size of Cal-1 vein and its homogeneous calcitic content, this cement has not been analysed for trace and minor elements.

Cal-2a phase is characterised by high Sr-contents (Figure 5.17), with values up to 13190 ppm and an average of 3678 ppm and variable content of Fe, Si and Mg (e.g. Mg-content varying from 420 to 2540 ppm). Cal-2b has a relative high Mg-content, reaching up to 4960 ppm, but Sr values are relatively low and vary from 470 to 2820 ppm. Noteworthy is that Cal-2b normally has Mn and Fe contents that remain below the detection limit (i.e. below 10 ppm), a feature that is very uncommon in calcite cements. This phase is characterised by intense recrystallisation and by the occurrence of dolomite and strontianite inclusions.

Stage	Mg (ppm)	Ca (ppm)	Fe (ppm)	Mn (ppm)	S (ppm)	Si (ppm)	Sr (ppm)
Cal-2a (n=13)	420	402640	< dl	< dl	< dl	720	2980
	500	406370	< dl	< dl	< dl	650	4640
	640	406880	< dl	< dl	< dl	160	< dl
	660	400090	< dl	< dl	< dl	840	5900
	740	400430	< dl	< dl	< dl	690	2250
	860	400470	< dl	530	600	720	1280
	880	389490	2840	< dl	1350	910	4680
	1020	407330	< dl	860	< dl	160	300
	1050	405570	< dl	1060	< dl	190	8400
	1060	400950	< dl	1470	< dl	770	540
	1190	415390	1760	830	< dl	720	1780
	1570	379460	< dl	570	1820	1320	13190
	2540	399470	2200	1030	< dl	650	1880
Cal-2b (n=6)	930	401130	< dl	790	< dl	710	6960
	1240	401720	< dl	< dl	< dl	860	2820
	3260	406620	< dl	< dl	< dl	220	1600
	4240	397960	< dl	< dl	< dl	320	640
	4950	405770	< dl	< dl	< dl	190	470
	4960	400810	< dl	< dl	< dl	170	940
Cal-3a (n=4)	1010	399550	740	< dl	< dl	170	1780
	2290	402050	< dl	100	< dl	250	810
	3720	403260	< dl	< dl	< dl	160	< dl
	4080	402210	< dl	< dl	< dl	270	20
Cal-3b (n=3)	1500	405720	< dl	< dl	< dl	< dl	1030
	2470	404750	< dl	< dl	< dl	< dl	720
	2740	405790	< dl	< dl	< dl	120	120
Cal-4 (n=3)	260	406970	760	< dl	< dl	< dl	< dl
	420	401840	1030	620	< dl	780	600
	640	409860	< dl	< dl	370	< dl	1190
Cal-5 (n=3)	550	396110	880	400	< dl	600	4870
	1980	399740	3100	1010	< dl	120	2900
	2120	394910	2600	940	< dl	740	2950
Cal-6 (n=2)	1530	405300	< dl	520	< dl	600	< dl
	3320	396930	< dl	< dl	< dl	690	510
Cal-7 (n=7)	1730	404700	< dl	< dl	< dl	< dl	< dl
	3420	402560	< dl	< dl	< dl	250	< dl
	3590	407240	< dl	< dl	< dl	< dl	380
	3610	402540	< dl	460	< dl	< dl	< dl
	3740	408110	< dl	430	< dl	< dl	< dl
	3820	406550	< dl	< dl	< dl	< dl	< dl
	4350	399390	< dl	< dl	< dl	220	< dl

Table 5.5. Major and trace element data in ppm (microprobe data) of diagenetic phases of Kelcyra area. Values below detection limit are indicated with "<dl".

Stage	Ca	Al	Sr	Mg	Fe	Mn	K
Cal-2b	373 079	438	1752	1403	527	594	99
	390 218	238	742	3420	69	390	49
	370 448	134	1366	2087	352	427	104
Cal-3a	359 751	250	703	1154	1065	448	84
	381 826	189	1271	1741	143	373	61
Cal-3a + Cal-3b + Dol	366 581	206	637	2904	208	345	87
	378 012	231	645	2473	226	348	63
	365 147	219	1191	2577	72	383	70
Cal-5	371 820	113	1321	1133	1365	573	87
Cal-7	378 866	171	252	3196	53	432	143
	385 079	62	329	2689	38	386	62

Table 5.6. Major and trace element data in ppm (AAS analyses) of major diagenetic phases of Kelcyra area.

Cal-3 cement displays a large variation in geochemistry especially in relation to the absence or occurrence of brecciated fragments in the cement, i.e. Cal-3a and Cal-3b respectively. Cal-3a cement, which is characterised by dolomite inclusions, possesses a low Mn-content and relatively low Fe and Sr contents, when compared to Cal-2 cement. Mg-content is variable and reaches values up to 4080 ppm. This Mg-composition is very close to that of Cal-2b cement. Notice that Cal-3b cements contain brecciated fragments of dolomites (Dol-2 generation) and clays. Cal-3b has a Sr-content with an average of 623 ppm. However this cement phase is low in Fe, Si, and Mn, whereas its Mg-content averages 2237 ppm. Cal-4 cement is characterised by very low Mg-contents with an average of 440 ppm, variable Sr values with an average of 597 ppm and higher Fe content (up to 1030 ppm).

Cal-5 cement is characterised like many previous calcite cements by a high Sr-content, with more than 2900 ppm. This generation of cement has the highest Fe-content and possesses variable Mn- and Si-contents. From stage Cal-6 onwards, the Sr content is much lower and the cements possess in general low contents of minor and trace elements (i.e. Mn, Fe, Si). Cal-6 cement has Sr-values varying around 255 ppm and Mn- and Fe-contents below the detection limit, possibly reflecting oxidising conditions. Finally, Cal-7 cement is characterised by very low Sr-contents. It is also poor in Mn, Si and Fe, with all data below the detection limit of the microprobe.

However its Mg content is comparable with the previous Cal-6 cement, with a mean of 3466 ppm

5.3.3.2- Dolomite and barite phases

The three generations of dolomite, as well as associated barite crystals, have been analysed with the microprobe. Their geochemical compositions are summarised in Table 5.7, Figure 5.18 and Figure 5.19.

Dol-1 generation, i.e. the micrometric dolomite inclusions as observed in Cal-2 cement, possess a high strontium content with values up to 3390 ppm. Its Si- and Al-contents are low (Table 5.7). Its Mn-content is not important but still higher than those of the other dolomite generations. One analysis displays a high Fe-content with a value of 35100 ppm. This value can be explained either by a possible interference with Fe-oxide adjacent to the dolomite, since the electron beam penetration depth is around 3 μm or by the occurrence of ankerite. In the same way, the high content in Sr likely reflects an overestimation due to the resolution area of the electron beam and in this way, part of the measured Sr-content may indeed be derived from the Cal-2b cement or from minute non-identified inclusions of strontianite.

Dolomites located in brecciated fragments, i.e. Dol-2 generation, are low in Fe and contain less Sr than Dol-1 with values up to 1270 ppm. However, this is still relatively high for dolomite. This generation of dolomite furthermore shows around 450 ppm of Si and 200 ppm of Al.

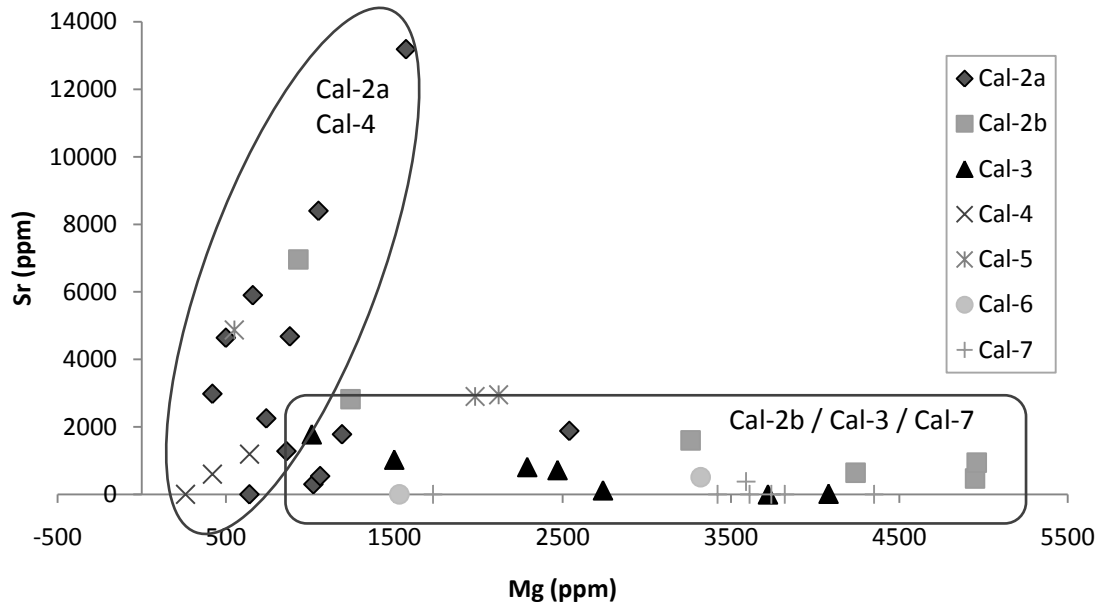


Figure 5.17. Elemental composition in magnesium versus strontium of the successive vein filling calcite generations.

Generation	Mg	Ca	Fe	Mn	S	Ba	Si	Al	Sr
Barite	<dl	1980	<dl	<dl	139700	581540	1210	2980	10160
	<dl	480	<dl	<dl	142430	535530	1180	2750	40970
	<dl	1000	<dl	<dl	139300	561530	1360	2780	34620
	<dl	<dl	<dl	<dl	139500	555140	230	2790	34850
	<dl	900	<dl	<dl	140200	576870	600	3190	21210
	<dl	3130	<dl	<dl	137440	581900	560	3000	6500
	<dl	380	<dl	<dl	138180	584360	<dl	3150	13130
Dol-1	108050	223230	35100	2180	<dl	<dl	<dl	<dl	2270
	113280	261680	<dl	860	<dl	<dl	<dl	<dl	3390
	110150	256790	<dl	860	<dl	<dl	<dl	<dl	3230
Dol-2	111560	249520	<dl	<dl	280	<dl	480	260	1270
	124810	234180	<dl	560	<dl	<dl	660	170	950
	124870	227200	3730	690	<dl	<dl	210	<dl	240
	113820	247790	<dl	640	<dl	<dl	320	100	830
Dol-3	110430	266370	<dl	750	<dl	<dl	250	<dl	<dl
	117110	246720	<dl	<dl	<dl	<dl	150	150	<dl

Table 5.7. Major and trace element data (in ppm) of barite and dolomite (Dol) crystals in the Kelcyra area. Values below the detection limit are indicated with "<dl" (about <10 ppm).

The last dolomite generation, i.e. Dol-3, corresponding to coarse subhedral dolomites, possesses a low Sr-content with values below the detection limit (i.e. lower than 10 ppm), as well as low Al and Si values. Its Mn content fluctuates from below the detection limit to 750

ppm. However, it should be noted that only two analyses have been carried out.

The barite crystals have variable Sr-content with values varying from 6500 to 40970 ppm and low Al-contents varying around 3000 ppm.

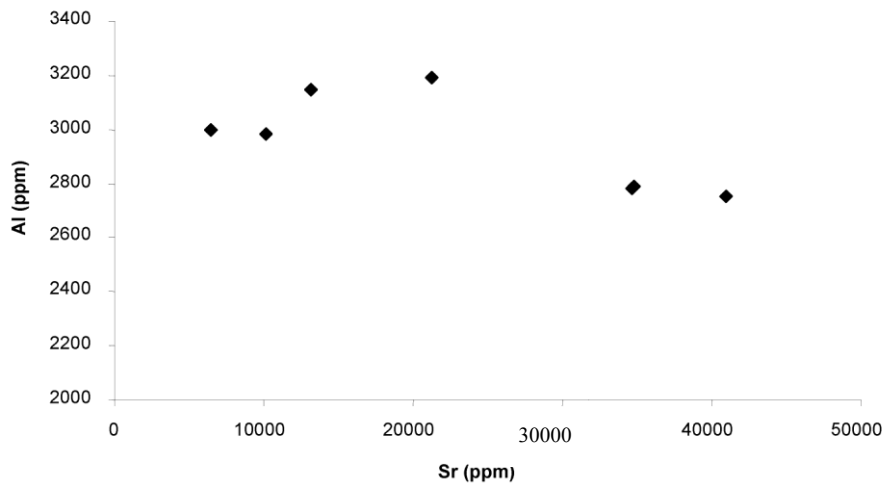


Figure 5.18. Elemental composition in strontium versus aluminium of the barite crystals.

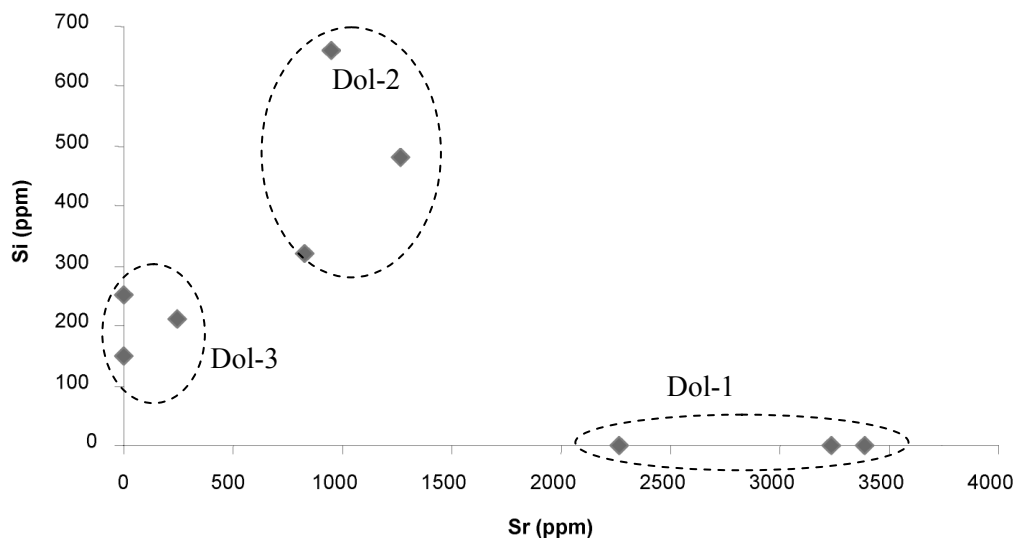


Figure 5.19. Elemental composition in strontium versus silica of the dolomite crystals.

Other data:

In order to determine whether the dolomitic phases can have a Triassic origin, a summary of a previous study realised on the Triassic dolomites is given below.

During the Albanian Subtrap project, a limited number of samples was analysed to infer the trace element content of the Triassic dolomites (Swennen et al., 1998). The data are given in Table 5.8. The Triassic dolomites possess a rather uniform Sr-content, which varies around 91 ppm, while their Fe-content fluctuates from low values, i.e. lower than 2000 ppm, in the dolomite/evaporite section, to very high concentration up to 18276 ppm in the clay/dolomite section. Also Mn is very high with values ranging between 1380-1640 ppm.

5.3.4- Strontium isotopes

In order to define possible fluid-rock interactions, 5 samples (i.e. 2 host-rocks and 3 calcite cements) were analysed for their Sr^{87} / Sr^{86} ratio. The data are given in Table 5.9. These results are plotted in Figure 5.20, where the secular trend in Sr^{87} / Sr^{86} signature against time is given as a reference curve.

Based on the work of McArthur and Howarth (2004), the Late Paleocene-Eocene marine water is characterised by an increasing Sr^{87} / Sr^{86} signature varying from 0.70770 to 0.70782 (Table 5.9). The Sr^{87} / Sr^{86} ratio of the Cal-2b vein and its surrounded matrix (i.e. Late Paleocene) display values of 0.707770 and 0.707756 respectively. The Cal-3b cement, characterised by many brecciated fragments of

especially rhombohedral dolomite, has a Sr^{87} / Sr^{86} value of 0.70782, which is similar to the signature of its surrounded host-rock, having a value of 0.70782.

The Sr^{87} / Sr^{86} signature of the Cal-7 cement, characterised by low Sr-content, is 0.70804. It is important to notice that the surrounded limestone of the sampled veins, except for Cal-7 where no data are available, possesses a similar Sr^{87} / Sr^{86} ratio, which reflects a possible host-rock buffering of the fluids. Possible matrix contamination should also be taken into account because of the small size of the veins.

Cal-2b and Cal-3 cements display a similar signature to respectively Late Eocene-Early Oligocene marine water (McArthur and Howarth (2004), Figure 5.20 b) and to the Triassic evaporites and dolomites (Swennen et al. (1998); Figure 5.20 c), located in the southern part of the Ionian Zone along the décollement level

(Swennen et al., 1998). Therefore their Sr-signatures support a host-rock buffering either by the Late Eocene-Early Oligocene marine carbonates or by the Triassic evaporites (Figure 5.20 b & c). Based on these results, it is not possible to differentiate whether these fluids have interacted with the Triassic evaporites or with the Late Eocene-Early Oligocene lithologies, since both origins possess the same Sr-signature.

However, the high Sr-trace element content of the Cal-2b and Cal-3 veins point towards fluids that interacted with evaporites. Two evaporite-bearing units are recognised in the Albanides: the Triassic interval, which is located along the décollement level or in diapirs (Chapter 2), and the Late Messinian interval, which relates to the Mediterranean salinity crisis.

Sample	IR %	Fe	Mn	Na	Sr
Dolomite 161	8.6	15862	1636	324	86
Dolomite 167	16.8	18276	1380	354	105
Dolomite 102	2.6	1908	64	366	109
Dolomite 113	3.9	755	9	358	78

Table 5.8. AAS trace element geochemical data from dolomites from southern Albania (Mali Gjere section, Swennen et al., 1998). IR = Insoluble Residue in %; all trace element concentrations in ppm.

Samples	Sr^{87} / Sr^{86}	std Error
Host limestone (Late Paleocene) Cal-2b	0.707756	0.000015
Host limestone (Late Paleocene) Cal-3	0.707822	0.000012
Cal-2b vein	0.707770	0.000015
Cal-3b vein	0.707823	0.000017
Cal-7 vein	0.708039	0.000014
Late Paleocene – Eocene carbonates (McArthur and Howarth, 2004)	0.707700 to 0.707815	-
Triassic Evaporites (Swennen et al., 1998)	0.707777	0.000020
Triassic Dolomites (Swennen et al., 1998)	0.708010	0.000067
Triassic Dolomites (Swennen et al., 1998)	0.709498	0.000024

Table 5.9. Sr^{87} / Sr^{86} ratio of limestone (mudstone) and some vein-filling calcite samples from the Kelcyra outcrop (Upper Paleocene to Eocene age). For reference also the Late Paleocene-Eocene marine water values are given (McArthur and Howarth, 2004) as well as measured for Triassic dolomite and evaporites from the south of Albania (Swennen et al., 1998).

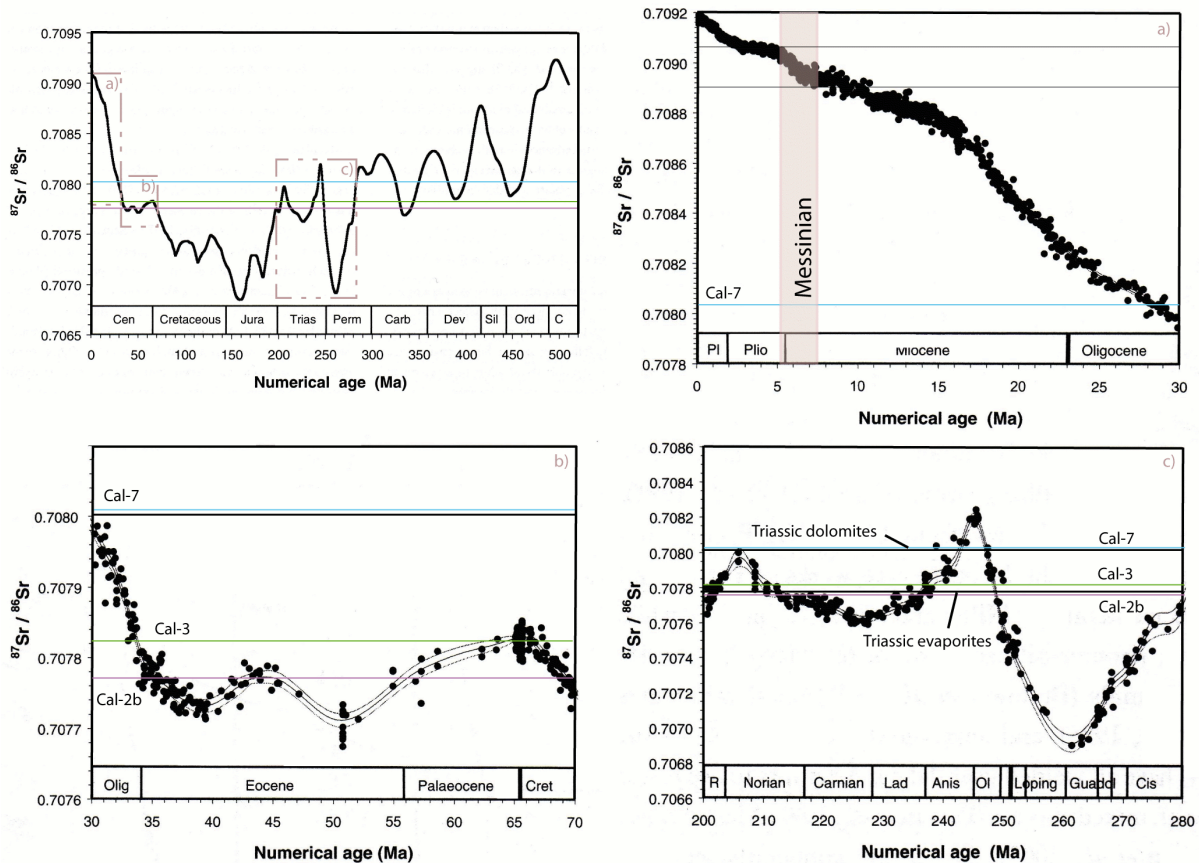


Figure 5.20. Plots of Sr^{87} / Sr^{86} secular variation, compiled after McArthur and Howarth (2004) with enlargement of specific time intervals, i.e. a), b), and c), with indication of measured Sr-isotopic composition of Triassic dolomites and evaporites (Swennen et al., 1998), and of the three main vein-filling (i.e. Cal-2b, Cal-3 and Cal-7 cements).

In the Figure 5.20a, the signature of the Messinian marine water and thus also of the rocks formed in equilibrium with this water is plotted and displays an increasing Sr^{87}/Sr^{86} ratio through time from 0.70892 to 0.70906 (McArthur and Howarth, 2004). The Messinian water signature is higher than the Sr^{87}/Sr^{86} ratios of different cements studied, which excludes the possible involvement of ascending evaporate brines. This interpretation has an important impact in the diagenetic study, especially with regard to the origin of the high Sr-content of the calcite cements.

The Sr^{87}/Sr^{86} signature of the Cal-7 cement is different to the Late Paleocene-Eocene marine water signature, i.e. the host limestone. However the Sr-signature of the Cal-7 is similar to the Middle Oligocene marine water signature, determined by McArthur and Howarth (2004), and to the Triassic dolomites signature (Figure

5.20c), with values ranging from 0.707943 to 0.709522 (Swennen et al., 1998).

5.3.5- Fluid inclusions

Fluid inclusions could only be studied in a limited number of samples (i.e. 4 usable wafers) due to the intense deformation of most veins and the small size of the fluid inclusions, causing a bad reliability of the measurements.

5.3.5.1- Results of Cal-2b vein

Only one wafer of Cal-2b cement was suitable for microthermometric analyses. Here, the inclusions are mainly rectangular (Figure 5.21) with a size varying from 1 to 2.4 μm . Two generations of fluid inclusions, i.e. F1 and F2, occur together in Cal-2b. They are principally located in the centre of the vein, where the calcite crystals display many solid inclusions and a recrystallised CL-pattern.

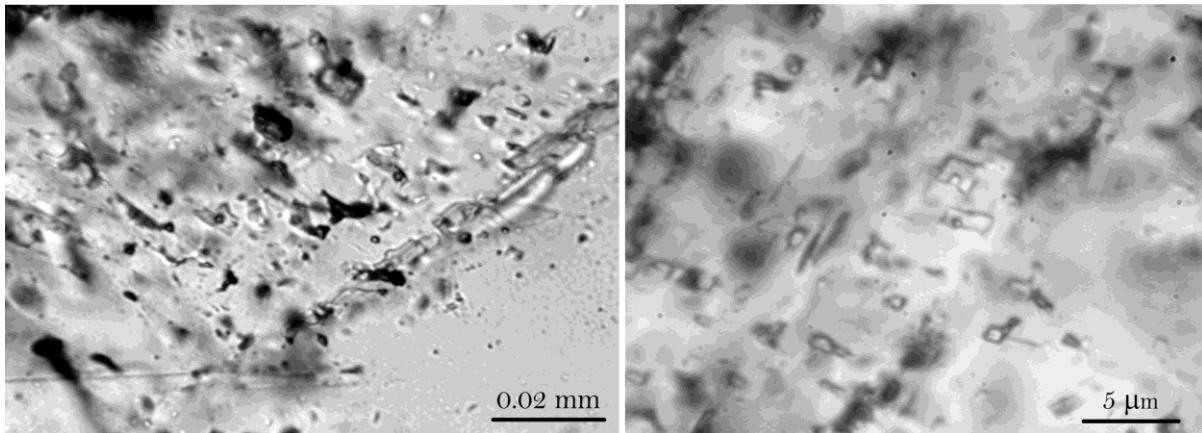


Figure 5.21. Photomicrograph of primary inclusions into Cal-2b cement.

The F1 generation consists of monophasic inclusions, which are located along growth zones in the crystal parts bordering the Cal-2b vein in the centre. The F1 fluid inclusions represent 70 % of the inclusions and are assumed to be primary in origin. They display final ice melting temperature (T_m) varying from -19 to -38°C . Based on the equation described by Bodnar (1993), such values can be related to a fluid with high salinity, with 21.9 to 35 eq. wt.% NaCl. The presence of non metastable one-phase fluid inclusions can point to an entrapment below about 80°C from a homogeneous liquid system (Goldstein, 2001). This entrapment temperature can also sometimes be higher than 80°C when the size of the fluid inclusion is lower than $2.4\mu\text{m}$.

Measured data for F2 fluid inclusions, which are essentially located along growth zones of recrystallised calcite crystals, are given in the Figure 5.22. They have homogenisation temperatures (T_h) varying from 95 to 142°C and variable T_m from 0°C to -5.4°C , representing a variation in salinity from 0 to 8.40 eq. wt.% NaCl (Bodnar, 1993). The gas/liquid ratio for the F2 inclusions varies around 25%. These inclusions likely relate to a H_2O -NaCl fluid, which has precipitated at high temperature. By assuming that the entrapment occurred under thermal equilibrium conditions and by using a surface temperature of 15°C and a geothermal gradient of $21^\circ\text{C}/\text{km}$ (see the Chapter: Fluid flow modelling for more explanation about the geothermal gradients), the F2 fluid inclusions could have been formed at a depth of 6 km.

5.3.5.2- Results of Cal-3 vein

Two wafers were prepared to study this cement generation, which is characterised by many

brecciated fragments, containing dolomite crystals (Dol-2 generation). The fluid inclusions are rectangular with clear edges and are located along growth zones. These inclusions are mainly located in calcite crystals, characterised by numerous twinning planes and recrystallised-CL pattern. Therefore the results should be interpreted with care. The data are shown on Figure 5.23. The inclusions are essentially biphasic, where the gas phase averages 20% of the total volume of the inclusion.

A first generation of solitary fluid inclusions has T_h -values varying between 34 and 60°C . The T_m values describe a spread from -32 to -14°C , corresponding to salinities of 19 to 30 eq. wt.% NaCl.

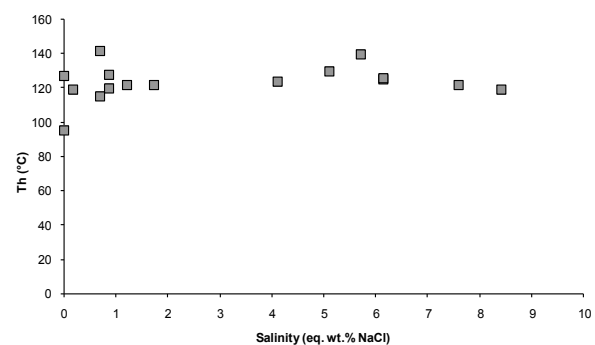


Figure 5.22. T_h ($^\circ\text{C}$) versus salinity (eq. wt.%NaCl) diagram of F2 fluid inclusions in Cal-2b.

The second generation of fluid inclusions, which also developed along growth zones, displays T_m from -10 to -22°C and T_h from 120 to 142°C . They relate to a high saline fluid (14 up to 24.4 eq. wt.% NaCl), with a higher temperature. In the case of entrapment under thermal equilibrium conditions with the host-rock, the precipitation might have occurred at a depth of 6 km, by using

a surface temperature of 15°C and a geothermal gradient of 21°C/km. This depth is likely the maximum burial depth of this system. This fluid signature, as it relates to a second generation of fluid inclusions, cannot be associated precisely to a cement but could reflect the recrystallisation of the Cal-3 cement.

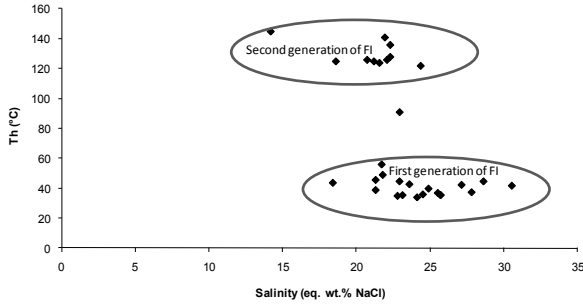


Figure 5.23. T_h (°C) versus salinity (eq. wt.% NaCl) diagram of the two generations of fluid inclusions. Note the 2 clusters attesting of a variation in salinity.

5.3.5.3- Results of Cal-7 vein

The last suitable sample analysed for microthermometry corresponds to Cal-7 cement. No fluid inclusions occur along growth zones. These solitary inclusions are rectangular shaped and not numerous.

T_m has values ranging from -5 to -22°C and T_h from 45 to 156°C (Figure 5.24). These values correspond to salinities ranging from 7.9 to 24 eq. wt.% NaCl. The T_h values are highly variable (Figure 5.25), which likely reflects variable entrapment temperatures, necking down and/or recrystallisation/resetting. The acquired results are difficult to interpret since they do not cluster together. Nevertheless, the Cal-7 cement does not display a recrystallisation pattern under CL. Consequently, these measurements either relate to an heterogeneous entrapment, i.e. immiscibility, at elevated temperature or a necking down after a phase change.

5.4- Interpretation

In the following paragraphs, the origin of the main fluid migration stages, responsible for each generation of vein filling, will be discussed based on an integration of the available petrographic and geochemical data. The data are summarised in the Table 5.10. First evidences of fluid flow

that interacted with evaporites will be discussed. Subsequently the paragenesis and the fluid evolution, which is described in the Figure 5.26, and Figure 5.27 will be addressed.

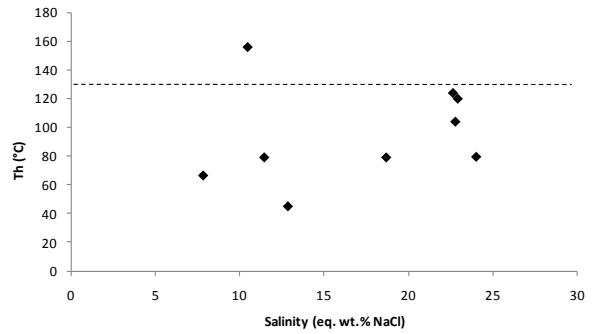


Figure 5.24. T_h (°C) versus salinity (eq. wt.% NaCl) diagram of solitary fluid inclusions of Cal-7.

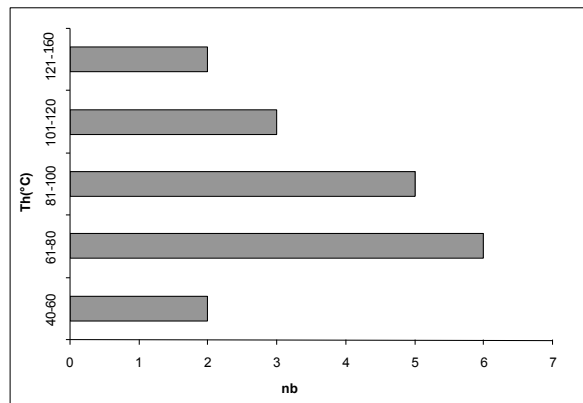


Figure 5.25. Histogram of fluid inclusion homogenisation temperatures of Cal-7 cement.

5.4.1- Evidences of evaporitic interactions

Many geochemical and petrographical features described above, like the Sr-content of calcite crystals, occurrence of strontianite associated with barite, occurrence of transported celestite in calcite cement and the presence of high salinity fluid inclusions, with a salinity up to 35 eq. wt.% NaCl, point to involvement of highly saline brines, likely derived from evaporites.

Only two evaporitic intervals crop out in the Albanides FTB, i.e. the Triassic and the late Messinian evaporite-bearing units (Rouchy, 1982). The evaporites of the Triassic occur along the basal décollement level and also in diapirs, whereas the late Messinian interval is only located in the Peri-Adriatic depression (cf. molasse sequence).

Cements	Fracture generation	Petrographic characteristics			Geochemical characteristics					Th (°C)	Salinity (wt.% NaCl)	
		Classical microscope	CL	Twinning	Other minerals	$\delta^{18}\text{O} - \delta^{13}\text{C}$ (‰)	$\text{Sr}^{87} / \text{Sr}^{86}$	Sr (ppm)	Mg (ppm)			Fe (ppm)
Cal-1	FRACT 1	Blocky calcite	Dull	Important								
Cal-2a	FRACT 1	Blocky calcite	Minor sector-zoning, from dull to bright CL	Important	Strontianite, quartz and barite	$\delta^{13}\text{C} = +1.18$ to -6.32 $\delta^{18}\text{O} = -3.98$ to -2.82	0.707770	3678	1010	523	< 80	21.9 to 35
Cal-2b	FRACT 1	Non-transparent, large and blocky calcite crystals	Light sector zoning from dull to orange CL, partially recrystallised	Important	Dol-1 (10%), barite, celestite and strontianite	$\delta^{13}\text{C} = -1.68$ to -3.00 $\delta^{18}\text{O} = -2.10$ to $+0.10$		2238	3263	< dl	95 to 142 (Recrystallisation)	0 to 8.4 (Recrystallisation)
Cal-3a	FRACT 1 and 2	Non-transparent, large and blocky to elongated calcite crystals	Recrystallised	Important	Dol-1 (10%)	$\delta^{13}\text{C} = +0.56$ to $+1.92$ $\delta^{18}\text{O} = -2.52$ to -0.40	0.707823	653	2775	185	34 to 60 Recrystallisation or heterogeneous entrapment	19 to 30 Recrystallisation or heterogeneous entrapment
Cal-3b	FRACT 1 and 2	Blocky to elongated	Recrystallised	Important	Dol-2, barite, Fe-oxides, strontianite and quartz	$\delta^{13}\text{C} = 0.67$ to 1.74 $\delta^{18}\text{O} = -0.13$ to $+1.66$		623	2237	< dl	120 to 140 (Recrystallisation ?)	14 to 24.4 (Recrystallisation ?)
Cal-4	FRACT 3	Fibrous to elongated calcite crystals	Dull	Important	Pyrite and barite	$\delta^{13}\text{C} = 1.61$ $\delta^{18}\text{O} = -5.57$		597	440	597		
Cal-5	New-FRACT 2	Elongated to blocky calcite crystals with regularly spaced trails of pieces of wall rocks	Dull	Important	Pyrite, quartz and barite, Dol-2	$\delta^{13}\text{C} = 1.28$ to 1.92 $\delta^{18}\text{O} = -5.78$ to -1.48		3573	1550	2193		
Cal-6	-	Blocky calcite	Dull	Important	Pyrite and quartz	$\delta^{13}\text{C} = 0.82$ $\delta^{18}\text{O} = -2.88$		255	2425	< dl		
Cal-7	FRACT 2 (reused) FRACT 4	Blocky calcite	Dull sector zoned	Thin twins	Fluorite, feldspath, Dol-2 (partially calcified)	$\delta^{13}\text{C} = 1.91$ to 2.09 $\delta^{18}\text{O} = 0.12$ to 1.12	0.708039	54	3466	< dl	45 to 156 Necking down or heterogeneous entrapment	7.9 to 24 Necking down or heterogeneous entrapment
Cements	Fracture	Classical microscope	CL	Twinning	Other minerals	$\delta^{18}\text{O} - \delta^{13}\text{C}$ (‰)	Fe (ppm)	Sr (ppm)	Si (ppm)	Mn (ppm)		
Dol-1	-	Micrometric sub- to euhedral crystals	Red-dull	no visible	Strontianite (2%), barite		11700	2963	< dl	1300		
Dol-2	Cal-3b	Non-transparent rhombohedral crystals	Red-dull partially calcified (bright CL)	no	Phyllosilicates, quartz, Barite	$\delta^{13}\text{C} = 0.82$ to 0.94 $\delta^{18}\text{O} = -1.25$ to 2.20	1243	822	450	472		
Dol-3	Fract 2 and 4	Coarse subhedral and transparent crystals; exhibit slightly curved surfaces	Red-dull	Thin double twins	Barite	$\delta^{13}\text{C} = 0.26$ $\delta^{18}\text{O} = -7.58$	< dl	< dl	200	375		

Table 5.10. Summary of the petrographic, cathodoluminescence, geochemical, isotopic data and fluid inclusion for calcite and dolomite cements.

The latter relates to the abrupt 'salinity crisis', which occurred all over the Mediterranean region. The calcite cements, which are characterised by high to very high Sr-content, have Sr-isotopic values similar to those of Triassic marine carbonates and evaporites as well as Oligocene marine carbonates. These values are lower than the Messinian marine water Sr-isotope signature. The latter has a $\text{Sr}^{87}/\text{Sr}^{86}$ average value of 0.70898 (Matano et al., 2005). This indicates that the fluids, rich in Sr, are not in equilibrium with Messinian marine water or lithologies.

Moreover, according to the structural analysis, many cement types are related to the pre- to syn-folding stages. Consequently, they are dated as Langhian-Serravalian (cf. Chapter 6: Ceres Modelling), which corresponds to the timing of the main thrust phase in the Ionian Basin (Nieuwland et al., 2001). The Berati unit has been thrust by an out-of-sequence process on the top of the Kurveleshi unit. This event is dated as post-Tortonian, since Tortonian sediments have been folded in the Memaliaj synclinal belt. Thus this event occurs prior to the Messinian.

Therefore, in the following paragraphs, the fluids, which display evidences of evaporitic interactions, are linked to the fluid circulation along the Triassic evaporites, especially those that are dated as pre-thrusting.

5.4.2- Early marine process

During the early diagenetic stage, cementation affecting the deep marine carbonates reflects a marine setting. This period is characterised by dissolution of unstable platform-derived sedimentary components, deposited in basinal environments and testifies of recrystallisation/cementation by marine fluids (compare with Melim et al., 2002; Dewever et al., 2007).

5.4.3- Compaction and fracturing

Subsequently these pelagic mudstones underwent physical compaction that is characterised by a major loss in porosity. At this stage, burial stylolites (BPS) developed. Porosity decreases to very low values as a result of physical and chemical compaction.

This period was also characterised by the first set of fractures oriented N 150° (FRACT1) and likely predating folding. It corresponds to a N30°-directed extension (Vilasi et al., 2009),

which is responsible of the early Cal-1 vein development. This set is interpreted to reflect early extension prior to folding, in relation to the flexure of the foreland contemporary of the burial in the basin in front of advancing units and under a high pore fluid pressure regime. The dull luminescent calcite Cal-1 likely precipitated from reducing waters during increasing burial.

5.4.4- Early meteoric fluid

The pre-deformational stage is further characterised by the occurrence of meteoric-derived fluids (Vilasi et al., 2006), which also precipitated during an extensional phase in N150° oriented fractures (i.e. FRACT1). The signature of this early fluid has been mainly buffered by interactions either with the rock matrix along its migration pathways or has been geochemically affected during reopening of the former veins by late fluid migration. Due to these interactions, it is difficult to trace its initial origin and migration pathways, which are essentially based on the presence of some remnants of former cements.

➤ Cal-2a cement

Cal-2a that has precipitated in FRACT1 is characterised under cathodoluminescence by sector-zoned calcite crystals (Figure 5.7). This cement precipitated during the burial stage from meteoric-derived fluids as attested by the isotopic data. Values (i.e. Figure 5.16) are plotting on the meteoric water line (Krajcar-Bronić et al., 1998; Surić et al., 2005) with rather constant $\delta^{18}\text{O}$, varying around -3.2 ‰ V-PDB and negative $\delta^{13}\text{C}$, with values from -2 to -6.25 ‰ V-PDB. The $\delta^{13}\text{C}$ -values are interpreted in terms of varying degrees of incorporation of isotopically light carbon from soil- CO_2 .

These results are also consistent with the occurrence of non metastable one-phase primary fluid inclusions, which can point to an entrapment below about 80°C or even higher (Goldstein, 2001), corresponding to a maximum depth of 3 km. Cal-2a is also characterised, according to microthermometric analyses, by salinities varying from 21.9 to 35 eq. wt.% NaCl. Consequently this meteoric fluid should have intensely interacted with evaporite-bearing units, that is in line with the high Sr-content with values averaging 3678 ppm and by the occurrence of transported strontianite (SrCO_3) phases that are enclosed in the cement (Figure 5.9C).

Based on the Sr-isotopic analyses and geodynamic context, the high Sr-content of the Cal-2a cement likely originate from a rock-fluid interaction with Triassic evaporites, since they display a similar $\text{Sr}^{87}/\text{Sr}^{86}$ signature. Moreover, the Neogene flexural sequence is deposited on average 2 to 3 km above the Triassic interval (Swennen et al., 1998), supporting an interaction with Triassic evaporites located in diapirs (Figure 5.27A). This meteoric cement likely points to a topography-driven fluid from the uplifted surrounding area.

➤ Cal-2b cement

The precipitation of Cal-2 ends with the widespread cementation of Cal-2b cement, characterised by high Mg-content, with values up to 4960 ppm and by strontium concentration slightly lower than Cal-2a with a maximum content of 6960 ppm (Table 5.4). This change in the Mg composition points either to an interaction with a later Mg-rich fluid or to a progressive enrichment of the fluid during its precipitation. At present, the main part of the cement consists of a dull-orange luminescent calcite with some bright yellow spots without any specific arrangement under CL, which suggests that this cement has been recrystallised. Cal-2b is the recrystallised equivalent of Cal-2a. This recrystallisation, where only few relics of the original zoned calcite crystals survived (Figure 5.8 G), supports the hypothesis of an interaction with a Mg-rich fluid post-dating cementation. The latter likely relates to the development of Dol-1 cement. Moreover a dissolution occurs along the central part of the veins (Figure 5.8 E), which attests of the migration of a post-Cal-2b corrosive fluid, causing diagenetic alteration, secondary porosity development and possibly recrystallisation of Cal-2 cement.

Concerning the O- and C-isotopic signatures, $\delta^{18}\text{O}$ values plot between -2.1 to +0.1 ‰ V-PDB with negative $\delta^{13}\text{C}$ from -1.68 to -3 ‰ V-PDB (Figure 5.16), that can be interpreted as a mixture between two end-members. The difficulty here is to differentiate whether the signature is original, relates to recrystallised Cal-2b cement, or whether it should be interpreted in terms of a mixture of two fluid types or crystalline phases, of which the original Cal-2b fluid is one of the end members. In fact, Dol-1 occurs with Cal-2b and thus likely has also an influence on the bulk isotopic signature. This spread in isotopic values

could relate to a minimum of 10 % contribution of the Dol-1 phase, but the rest of the $\delta^{18}\text{O}$ signature likely reflects an important resetting in $\delta^{18}\text{O}$ due to recrystallisation. The first end-member likely corresponds to the first meteoric cement, i.e. Cal-2a original cement, the second end-member to the signature of the Dol-1 cement. This recrystallisation did not reset the $\delta^{13}\text{C}$, which mainly reflects the carbon isotopic composition of the precursor calcite cement, i.e. Cal-2a. This suggests that the fluid responsible for the recrystallisation was, in this case, host-rock buffered by the enclosing limestone (Nielsen et al., 1994). Alteration of the original trace and minor elements, i.e. Sr- and Mg-contents, and O-isotopic signature of the Cal-2b cement relates to the recrystallisation, where the spread in $\delta^{18}\text{O}$ values demonstrates different degrees of recrystallisation.

As described for Cal-2a cement, monophasic primary F1-fluid inclusions occur in Cal-2 cement, pointing to relatively low formation temperatures and salinities higher than 21.9 eq. wt.% NaCl. The latter is interpreted to be related to intense fluid interaction with Triassic evaporites localised in diapirs. The second generation of fluid inclusions, i.e. F2, is located along growth zones of recrystallised calcite crystals. These inclusions have been trapped at elevated temperature varying from 95 to 142°C and are characterised by varying salinities from 0 to 8.4 eq. wt.% NaCl, demonstrating different degrees of interaction with salt bearing layers or mixing of a salt-derived fluid with a second less saline type of fluid. According to their variation in salinity and their location in recrystallised calcite crystals, these inclusions are assigned to the fluid responsible of the recrystallisation of Cal-2a.

Finally, the Sr- and Mg-content of the Cal-2b cement may be explained by an intense interaction of a meteoric fluid with Triassic evaporite-dolomite strata, located in diapirs and likely by a mixing with the fluid related to Dol-1. The interaction with diapirs and not with a deeper evaporitic layer is suggested first: (i) by the low precipitation temperature below 80°C, determined with monophasic fluid inclusions in Cal-2 cement and also (ii) by the depth of the Triassic interval during the pre-deformational stage, which does not likely allow meteoric fluid migration so deep.

➤ **Dolomite inclusions (Dol-1) in the Cal-2b cement**

The dolomite inclusions in the Cal-2b cement precipitated in the secondary porosity that mainly developed along calcite twins (Figure 5.8). The dolomite crystals are rhombohedral, without corrosion or dissolution and enriched in Sr, with an average content of 2963 ppm (Figure 5.17). The dolomite crystals are usually associated with barite (BaSO₄) and acicular subhedral strontianite crystals (SrCO₃).

One of the possible and even likely events for secondary porosity development relates to the fluid interaction causing Cal-2b recrystallisation. At least at that period a “reactive fluid” existed.

Assuming that the development of the secondary inclusions, i.e. F2 fluid inclusions, was generated during this recrystallisation event, the T_h from 95 to 142°C could reflect the temperature of the recrystallisation. Considering a geothermal gradient of 21°C/km (see CHAPTER 8), a surface temperature of 15°C and assuming thermal equilibrium with the host-rock during precipitation, this recrystallisation/precipitation might have occurred at a depth of approximately 6 km. Based on the T_m values, the fluid is characterised by variable salinity, displaying a range from 0 to 8.40 eq. wt.% NaCl. This variation demonstrates different degrees of interaction with salt bearing layers.

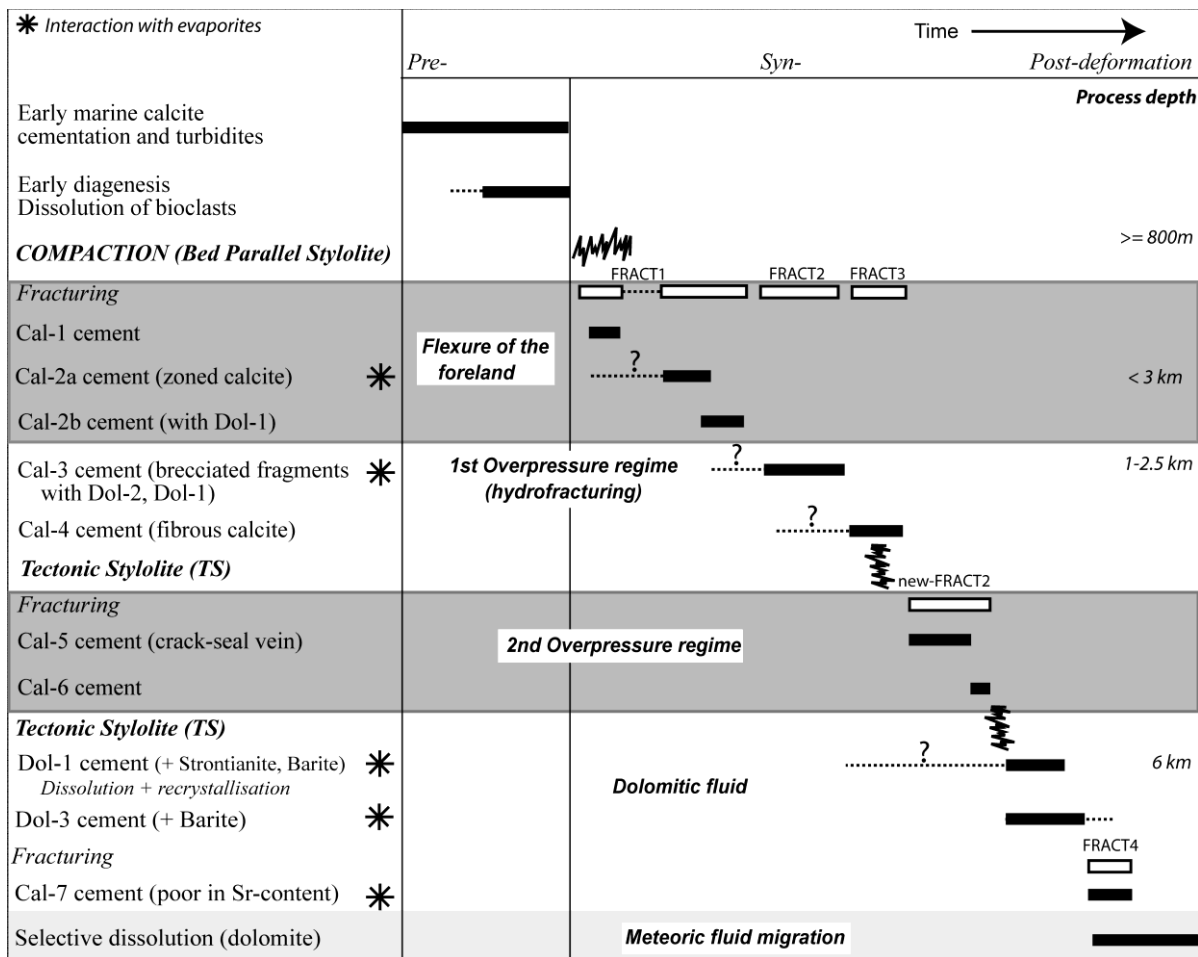


Figure 5.26. Paragenesis of Late Paleocene – Eocene deep marine carbonates in the Kelcyra area.

The dolomitising fluid, which precipitated dolomite, barite and strontianite, should be partially aggressive with respect to the calcite. This interpretation is explained first by the large amount of dolomite, strontianite and barite close to the central dissolution in Cal-2b cement (see

Figure 5.8 E) and by the recrystallisation of the former calcite Cal-2a cement. All these data likely suggest that this fluid, derived from a SO₄²⁻, Sr²⁺, Ba²⁺ and Mg²⁺ -rich bearing unit, characterised with normal δ¹³C and positive

$\delta^{18}\text{O}$, like Triassic evaporites, interacted with Cal-2a.

5.4.5- First main compressive stress

Cal-3, which is the next cement generation (Figure 5.11), precipitates in fractures oriented NW-SE (FRACT2) or in re-opened veins (FRACT1). It usually is characterised by the incorporation of numerous brecciated wall-rock fragments, which differ from the immediate neighbouring vein wall. That suggests that the Cal-3 vein formed by hydraulic fracturing during the syndeformational stage. This is in agreement with the occurrence of N 150° oriented veins. The brecciated fragments contain imported minerals such as phyllosilicates, strontianite, apatite, barite, calcite, dolomite crystals ... (Figure 5.15 B and C).

However, the exact timing of this fracture-fill generation is uncertain since no cross-cutting relationship with preceding veins has been observed. It has been placed in the syndeformational stage in the paragenesis according to fluid inclusion data, and also the relationship with later cements. However, these veins, which precipitated in fractures perpendicular to the bedding, are interpreted to predate the folding stage. This is in agreement with other studies, such as Ferket (2004), where hydraulic fractures also were dated as syndeformational. Consequently Cal-3 veins have formed in response to some combination of regional tectonic loading and/or burial and pore-pressure changes (Nelson, 1985).

Cal-3b cement is also highly recrystallised and characterised by the presence of many scattered dolomite crystals (Dol-1), characterised by a red-dull luminescence, and barite. The dolomitising fluid, i.e. Dol-1, is rich in SO_4^{2-} , Sr^{2+} , Ba^{2+} and Mg^{2+} . This Dol-1 has the same petrographic and geochemical characteristics as those mineral phases identified in the Cal-2b cement. They also precipitated close to the central part of the vein with evidences of dissolution in relation to post-Cal-3 aggressive fluid migration.

Based on assumed primary fluid inclusion analyses, located in and outside recrystallised parts, this calcite cement has a T_h from 34 to 60°C and T_m varying between -14 and -32°C , corresponding to elevated salinities with values from 19 to 30 eq. wt.% NaCl.

Two hypotheses can be proposed in order to interpret this T_h spread: the first one suggests

various temperature of precipitation, whereas a second hypothesis relates this spread to a partial resetting during the recrystallisation of the Cal-3b calcite (Nielsen et al., 1994). Anyhow, the fluid inclusions have been trapped at low temperature, i.e. lower than 60°C . The variation in salinity can be explained by water, which underwent intense water-rock interaction with evaporite/salty layers during its migration.

The second generation of fluid inclusions, which developed along growth zones of recrystallised calcite crystals, reflects higher precipitation temperatures with values varying from 120 to 140°C and salinities in the range of 14 to 25 eq. wt.% NaCl. According to their location, they likely reflect characteristics of the fluid that accounts for the recrystallisation of the Cal-3 cement. It is postulated that this recrystallisation occurred by a corrosive fluid rich in Mg^{2+} and SO_4^{2-} , causing the crystallisation of Dol-1 and associated mineral phases. Under this hypothesis, the second generation of fluid inclusions possibly indicates the entrapment conditions of Dol-1. According to the measured T_h , the recrystallisation could have occurred at a maximum depth of about 6 km, by using a geothermal gradient of $21^\circ\text{C}/\text{km}$ and a surface temperature of 15°C . It is important to note that these recrystallisation conditions are in agreement with those obtained from the recrystallised Cal-2b cement, pointing to a similar fluid interaction event.

Geochemically, Cal-3 cement is rich in strontium, with values up to 4080 ppm and has on average a Mg-content of 2500 ppm (Table 5.4). Its composition in trace and minor elements is very close to that of the Cal-2b cement, most likely also influenced by the occurrence of Dol-1 and associated phases. A possible interaction with a fluid that initially interacted with Triassic evaporite is proposed in order to explain the quantity of Sr and the similarity of their Sr-isotope signature (i.e. $\text{Sr}^{87}/\text{Sr}^{86}$ ratios of 0.70782 for Cal-3 and 0.70800 for the Triassic evaporites; Swennen et al., 1998).

Based on the C- and O- isotope results, Cal-3a cement displays a $\delta^{13}\text{C}$ signature, buffered by the host-rock with values between $+0.56$ and $+1.92\text{‰}$ V-PDB and more depleted $\delta^{18}\text{O}$, with values ranging from -2.52 to -0.40‰ V-PDB (Figure 5.16). The depleted $\delta^{18}\text{O}$ can be explained by the minor contribution of meteoric water or by a precipitation at higher temperature.

However, in vein samples where clear brecciated fragments occur (Cal-3b), the O-isotopic signature is shifted towards somewhat more positive values, between -0.13 and 1.66 ‰ V-PDB, whereas the $\delta^{13}\text{C}$ remains within the range of host-rock buffering. This less depleted to even

positive $\delta^{18}\text{O}$ of the breccias-containing veins is of major interest since they attest of a fluid system either influenced by clay diagenesis (i.e. smectite/illite conversion; Boles and Franks, 1979) or that interacted or originates from Triassic evaporites.

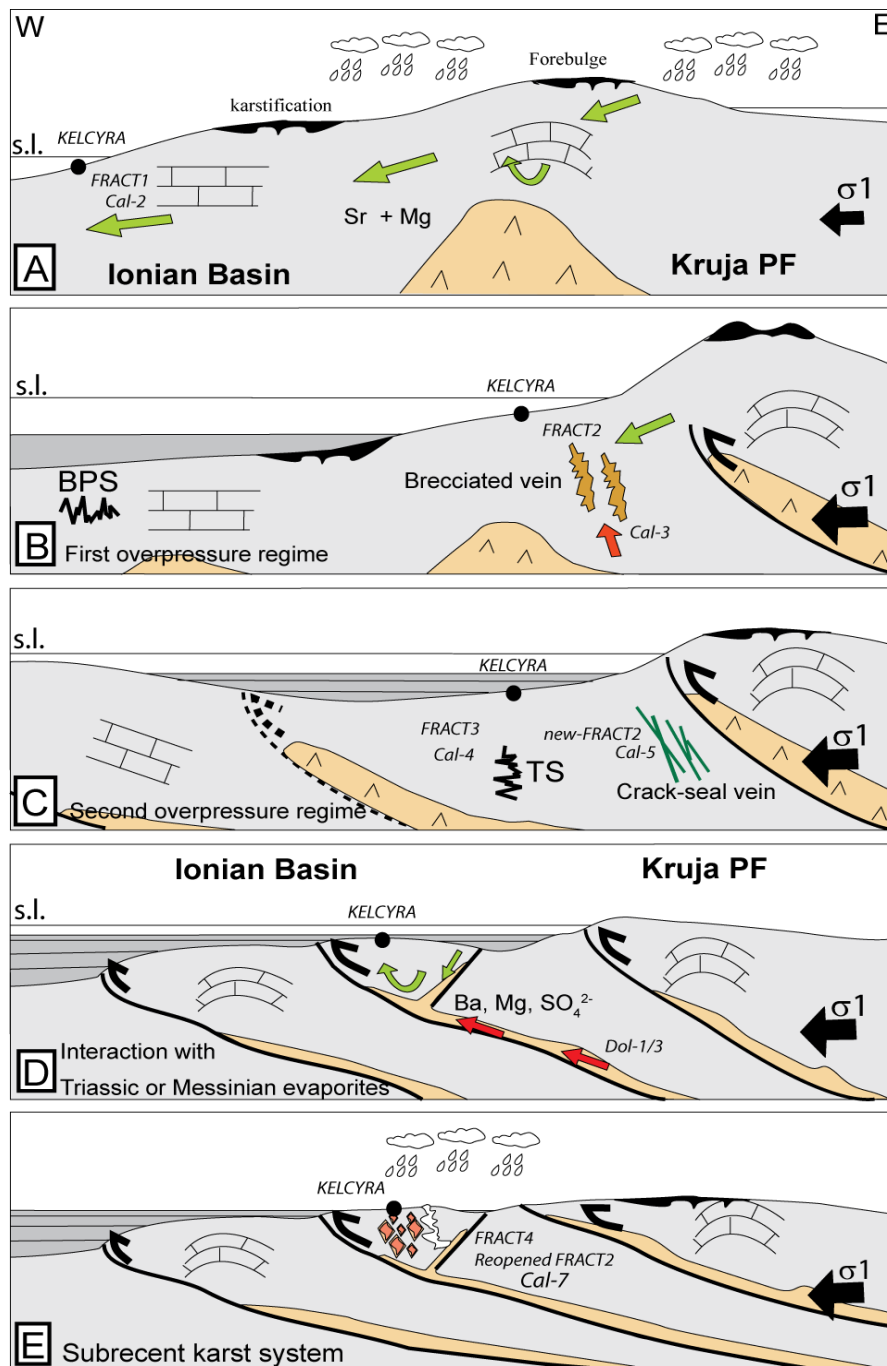


Figure 5.27. Conceptual model for the diagenetic study. (s.l.: sea level). Red and green coloured arrows relate respectively to down- and upward fluid migrations. For explanation see text: the step A corresponds to the pre-deformational period; B and C indicate the onset of thrusting respectively in the hinterland and in the Ionian basin; “D” shows the out-of-sequence development of the Berati belt; “E” corresponds to the uplift of the Berati belt.

➤ Transported fragments (Dol-2)

To determine the origin of the dolomites, which were transported together with the breccias fragments, geochemical analyses were realised on Dol-2 phase. With respect to the Dol-1 cement, Dol-2 phase has a lower Sr-content, with values on average of 822 ppm, and high Si-content.

The Dol-2 crystals likely were transported with a fluid from a dolomitic interval. In the external Albanides, the dolomitic intervals are localised in the Upper Triassic strata of the Ionian Basin and in the Upper Cretaceous dolomitic platform of the Kruja unit. Their long transport over a few kilometres, from their initial location to the studied interval, necessitates a high pressure regime (Laubach, 2004; Ferket, 2006). This interpretation is in agreement with the crack-seal texture attesting of high pore-fluid pressure, observed in Cal-3 cement (Figure 5.10).

Thus, high salinities and precipitation at low temperature under high pressure, with transportation of Triassic dolomite fragments, characterise the Cal-3 cement. It is postulated here that this fluid interacted with the Triassic dolomite / evaporites, located along the décollement level or in diapirs. This explains the high Sr-content of the fluid. This precipitation of Cal-3 likely occurred at a depth of 1-2.5 km (Figure 5.27 B).

Afterwards, this vein infill was affected by a corrosive fluid, rich in Sr^{2+} , Mg^{2+} and SO_4^{2-} . The latter allows to develop a secondary porosity into the Cal-3 cement. It is here that minute dolomite (Dol-1), barite and strontianite crystals formed. This precipitation likely is concomitant with the recrystallisation of the Cal-3b calcite. If the second generation of fluid inclusions effectively relate to the recrystallisation process and if these fluids are in thermal equilibrium with their host-rocks, this diagenetic interaction possibly occurred at a temperature from 120 to 142°C. This is consistent with a depth of at least 6 km.

Dol-1 in Cal-3a displays the same petrographic and geochemical characteristics as Dol-1 in Cal-2b. As a final remark, it is important to note that the Cal-2b and Cal-3b cements are differentiated from each other by their $\delta^{13}\text{C}$ signatures, which are separated by 4-5‰ V-PDB and by the presence of brecciated fragments in Cal-3b.

5.4.6- Evidences of a second overpressure regime

Subsequently, shear veins, i.e. Cal-4, are cemented with calcite cement, displaying a dull luminescence, which is similar to the luminescence of the host rock. These veins displace the previously described fractures by a dextral movement. Therefore, the Cal-4 generation is interpreted as syn-deformational and likely formed during thrust emplacement subsequently to the development of tectonic stylolites.

The subsequent evolution of the fluid results in the precipitation of Cal-5 calcite cement. These elongate-blocky calcite crystals are ferroan, with on average 2193 ppm of Fe, and display a dull luminescence. They have very high Sr-content, with values up to 4870 ppm. Their $\delta^{13}\text{C}$ signatures vary between +1.28 to +1.92‰ V-PDB, which are buffered by the host rock (Figure 5.16). These veins show negative $\delta^{18}\text{O}$ values varying from -1.48 to -5.78‰ V-PDB. This spread in $\delta^{18}\text{O}$ values can be interpreted in terms of precipitation at different elevated temperatures and/or differences in non-equilibrium precipitation temperature between host-rock and fluids or (multi-stage) recrystallisation of the cement.

The characteristic feature of the Cal-5 vein is the presence of inclusion bands, aligned parallel to the vein wall, i.e. new fracturing phase of FRACT2 (Ramsay, 1980; Cox, 1987 and Bons, 2000). These regularly spaced trails are clearly bands of wall-rock detached from the neighboured vein-wall. This is especially pointed out by the occurrence of fossils fragments, associated with the inclusion bands and relate to crack-seal growth (Cal-5 cement, Figure 5.12, Figure 5.13). These spaced solid phase inclusion bands in the antitaxial calcite vein, are explained by growth from solution during cyclic hydrofracturing (Harper and Tartarotti, 1996) followed by sealing due to mineral precipitation at the boundary between vein and wall-rock (Ramsay, 1980). Consequently the spacing of adjacent inclusion bands records the amount of vein, which was added during each crack-seal increment. The latter are often only a few μm thick. Note that the crack-seal process may indicate overpressuring (Figure 5.27 C).

Unfortunately, the origin of this fluid cannot yet be determined with the current data. Only few fluid inclusions, characterised by a size smaller

than 3 μm , were found. The latter were metastable. Moreover the timing of this suggested overpressure episode cannot be further constrained with the actual data. Cal-5 vein postdates the Cal-3 and Cal-4 veins, which reflect the existence of a high pressure regime. Consequently, Cal-5 can originate from a second episode of high pressure or can be developed during the same Cal-3 overpressure regime. However, the change in the cement composition (Sr- and Fe-contents) and geochemistry ($\delta^{18}\text{O}$) from Cal-3 to Cal-5 supports the first hypothesis, assigning the development of Cal-5 to a separate second compression event.

5.4.7- Change of the main tectonic stress

Cal-6 veins are cemented by dull luminescent blocky calcites. According to the fracture study, these veins are syn- to post-deformational and relate to the folding stage or to a second burial stage, reflecting an extensional regime. Here, only a low content of Sr, i.e. on average 255 ppm, and a high Mg-content, i.e. on average of 2425 ppm, characterise these calcite infills. Only one isotopic analysis was realised, displaying $\delta^{18}\text{O}$ and $\delta^{13}\text{C}$ values of -2.88 ‰ V-PDB and +0.82 ‰ V-PDB respectively. The latter value is similar to that of the host rock, which supports a rock buffering system (Figure 5.16) and consequently high water-rock interaction. The origin of this fluid is unknown, since no stable fluid inclusions were found.

5.4.8- Dolomitic fluid, Dol-3

This stage is characterised by the cementation of subhedral dolomite (i.e. Dol-3 phase), characterised by slightly curved surfaces. They precipitate in re-opened veins, as it has been encountered in Cal-3b cemented veins (Figure 5.14 D, E & F). They display double twins, which are possibly due to thin section preparation, and red-dull luminescence. The crystals are actually partially dedolomitised, which is deduced from the yellow bright luminescent calcite areas that especially occur along dolomite twins. Geochemical analyses revealed that these dolomite crystals have low Sr-content, with values below the detection limit, and low Si- and Al-contents. Unfortunately, no fluid inclusions have been encountered in these crystals.

Only one isotopic analysis could be realised in order to characterise the corresponding fluid. But since the vein is surrounded by other vein

generations, which in total measures 1.5 mm wide, its sampling was not very phase selective and therefore Dol-3 phases likely mixed also with Cal-7 cement. A $\delta^{18}\text{O}$ value of -7.58‰ V-PDB (corrected with the fractionation factor of the dolomite (see 5.3.2- Stable isotopes) and a $\delta^{13}\text{C}$ signature of 0.3‰ V-PDB was measured. This result can be interpreted as a precipitation at more elevated temperature (i.e. deep-sourced fluid origin). But no indication, proving or disproving a precipitation in thermal equilibrium with the matrix, was found.

Based on SEM observations, micrometric barite inclusions, with high Sr- and Al-contents, occur scattered in Dol-3 crystals. They could point to the remobilisation of sulphate. Consequently, this fluid likely has interacted with or was expelled from a SO_4^{2-} , Mg^{2+} , Ba^{2+} -rich bearing unit, like the Triassic or Messinian evaporites.

Except their distinct isotopic signature and content in Sr^{2+} , Dol-1 and Dol-3 cements present the same petrographic and geochemical characteristics, likely revealing a similar origin. If this is correct, the initial fluid had a low Sr-content, which is attested by the geochemical analyses realised on Dol-3 cement. Its enrichment, observed in Dol-1 cement, then has to relate to the interaction with Cal-3b or Cal-2b cements (i.e. rich in Sr) before or during Dol-1 precipitation, if Dol-1 is a replacive phase. Otherwise the Sr-content might have been overestimated due to the resolution of the electron beam. However Dol-1 and Dol-3 can also record the migration of two distinct fluids, which possessed clearly different Sr-contents.

To summarise, two scenarios are proposed:

(i) The first scenario describes the migration of a corrosive dolomitic fluid, rich in Mg^{2+} , Ba^{2+} and SO_4^{2-} , derived from an evaporite-bearing layer, along re-opened veins. This diagenetic process occurred at elevated temperature. It caused the development of secondary porosity and induced also a partial recrystallisation of the former calcite cement. These fluids partially dissolved former calcite cements (i.e. Cal-2b, Cal-3b) and precipitated also strontianite and barite in created secondary pores. In the case of a process in thermal equilibrium with the host rock, this recrystallisation occurred at a depth of 6 km (Figure 5.27 D). If no thermal equilibrium was reached, this fluid system could point to a hydrothermal nature, but additional research is

needed to confirm this hypothesis. By fluid/cement interaction in a closed system, the dissolution of high Sr-content calcite cement, i.e. Cal-2 and Cal-3, allows to enrich the fluid in Sr. Or if the dolomite is replacive, it can inherit some of the Sr. However, in an open system, the fluid precipitates as low Sr-content dolomite, i.e. Dol-3. However an overestimation due to the resolution of the microprobe cannot be excluded.

(ii) In the second scenario, Dol-1 and Dol-3 originate from different fluids or formed at different moments. In this case, no thermal constraints can be attributed to the Dol-3 cementation.

At present day, no geochemical analyses allow to validate one of these scenarios. However, the association of barite with Dol-1 and Dol-3 and the similar CL signature of the two generations of dolomite rather support the first hypothesis, which refers to the migration of a single dolomitising fluid.

5.4.9- Late calcite cement

Cal-7 cement postdates the second generation of tectonic stylolites and precipitates in FRACT2 and FRACT4. The cement displays dull sector-zoned luminescence and usually contains brecciated and transported fragments of dolomite (Dol-2). The latter are similar to those in Cal-3b cement, but less numerous and smaller in size. The brecciated fragments represent less than 5% of the total vein infill. In some places, especially along grain boundaries, accumulations of transported fluorite, characterised by blue luminescence under CL, were observed, associated with pyrite and detrital phyllosilicates.

At present-day, fluorite, associated with barite has been documented from WSW-ENE transversal faults (i.e. Scutari-Pec alignment or Elbasan transfer zone). Ferrini et al. (2003) suggests that these minerals were deposited during the migration of fluids that have previously leached from deeply buried magmatic strata. These fluids attest of a circulation along tectonic contacts. Consequently, the fluorite observed in Cal-7 can point to a migration adjacent and through main faults.

The occurrence of brecciated fragments of dolomite points towards the migration within a high pressure regime, since the nature of the clasts is different from that of the immediate neighbouring wall-rock. The Sr-isotope signature of 0.70804 for Cal-7, which is similar to previous

measurements realised on the Triassic dolomites of 0.70801 (Swennen et al., 1998), may support intense interaction with Triassic dolomite interval. However, this Sr^{87}/Sr^{86} ratio also may indicate a Middle Oligocene marine signature.

The positive $\delta^{18}O$ signature of the Cal-7 cement with values varying between +0.12 and +1.12‰ V-PDB can be also explained by intense host-rock buffering with evaporite intervals. Geochemically, Cal-7 cement has low Sr-, Al-, Si- and Fe-contents.

Based on fluid inclusions analyses, the cement is characterised by homogenisation temperatures ranging from 45°C up to 156°C and moderate to high salinities from 7.9 to 24 eq. wt.% NaCl. The variation in T_h likely can be explained by variable entrapment temperatures or necking-down. The large spread in T_m values can be explained by different degrees of fluid interaction with a salt-rich layer or mixing of fluids.

This cement can be associated to a fluid, which underwent intense water-rock interaction with evaporite-bearing strata as well as with Triassic dolomites. The latter is required to explain the occurrence of Dol-2. However, no indication concerning the initial origin of the fluid exists. Consequently, a first hypothesis can be proposed accounting for the migration of a fluid, which finally interacted with the Triassic or the Messinian evaporites. The second hypothesis relates to the migration of a deep-sourced fluid through the Triassic evaporites, located along the basal décollement level or along diapirs. A third possibility suggests a topography driven flow, which interacted with diapirs or the Messinian evaporites. This fluid became mixed with a deeper-source fluid, in order to get such variable homogenisation temperature and salinities.

5.4.10- Selective dissolution stage

The last stage in the diagenesis is characterised by the development of a possibly subrecent karst system (Figure 5.27 E). It caused a selective dissolution of dolomite crystals as testified by the rhombohedral shape of the moldic secondary porosity. Some dolomite crystals however are also partially replaced by bright yellow luminescent calcite, which points to dedolomitisation. This probably occurs in a near-surface setting, in relation to a telogenetic process due to the percolation of meteoric water (Chaftez, 1972; Nader et al., 2008).

5.5- Conclusions

In this chapter, a diagenetic study of a fractured carbonate reservoir analogue is presented, coupling structural, petrographical, geochemical and microthermometric data. The main focus is to improve the knowledge of the petroleum system and predict the exploration risks in the case of complex tectonic systems (overpressures, evaporitic diapirs, important erosions, ...). Here, many diagenetic processes have been encountered, which reflect different episodes in the foreland fold-and-thrust belt development. They are dependent on the fracture

characteristics (orientations, ...) and the fluid flow, e.g. fracture opening, fluid pressure (e.g. hydrofracturing, driven meteoric water), vicinity to main faults with evaporites as décollement level, allowing influx of exotic water with subsequent fluid/rock interactions, ... Once the different diagenetic episodes of a specific reservoir have been identified, basin modelling can help to validate possible scenarios of fluid migrations (Figure 5.27, Figure 5.28). The latter is based on the thermal evolution and faults behaviour, evolving through time, to place the characterised fluids into the kinematic evolution of the FTB (see Chapter: Modelling).

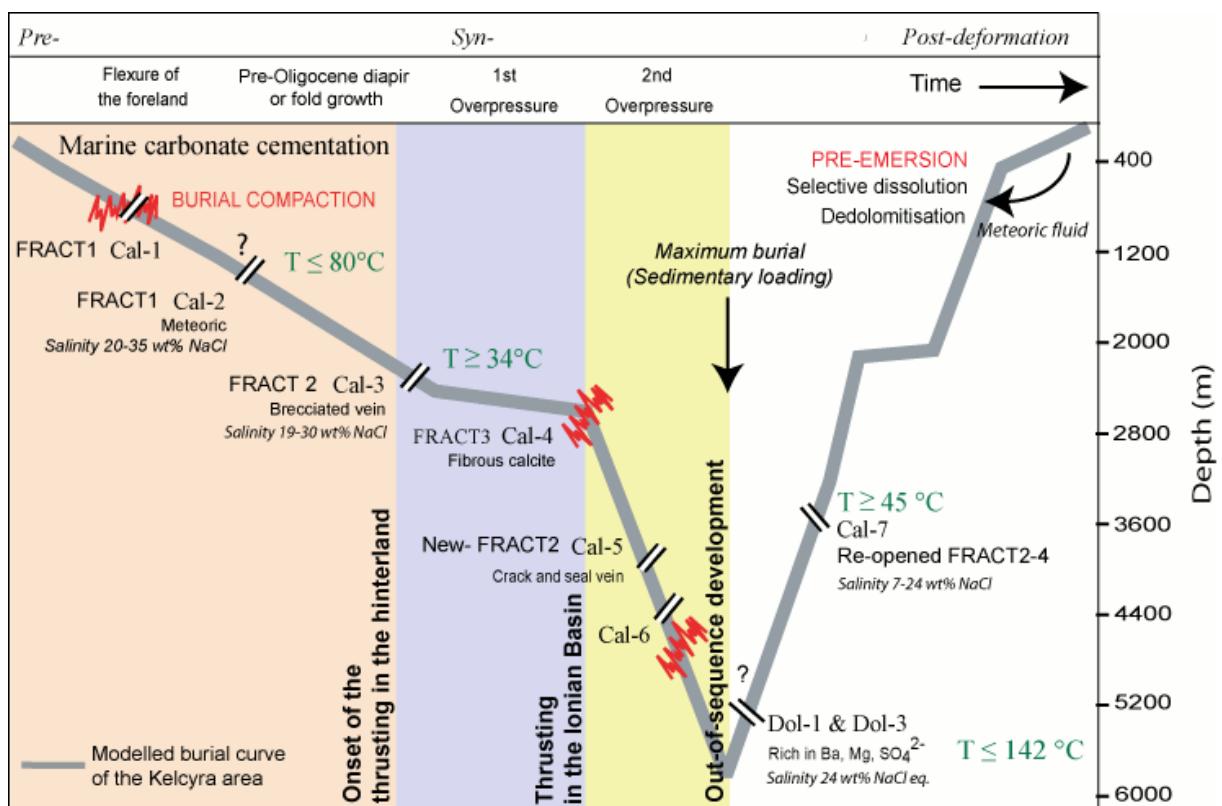


Figure 5.28. Fluid flow evolution versus burial history. The construction of the burial curve is discussed in the chapter on fluid flow modelling. “T” corresponds to homogenisation temperatures, which were measured within fluid inclusions.

5.5.1- Evolution of the fluid flow versus kinematic evolution

In the Kelcyra area, the majority of the fracturing of the reservoir-interval has a pre-folding origin, i.e. sedimentary burial loading. Its first recorded cement infill (Cal-2) has a meteoric origin, implying migration pathways of meteoric water from the surface to the buried Eocene deep marine limestones. This likely happened during the earlier forebulge development or growth

anticline or diapir (Figure 5.27A). This fluid, during its migration, interacted with Triassic evaporites, explaining its enrichment in strontium. Regarding the low temperature of precipitation, reaching a maximum of only 40-50°C, this meteoric fluid must have reacted with evaporitic diapirs at relative shallow depth to finally precipitate at a maximum depth of 1.5 km. In fact, the cementation of the meteoric fluid predates the main compression stage, dated as lower to middle Oligocene time and relates to the

burial phase. At this period, the Triassic evaporites lie at least at 5 km depth in the Ionian basin (Swennen et al., 2002), except where diapirs occurred.

From then onwards, the maximum principal stress becomes horizontal due to tectonic compression. The majority of the fluid generated in the Kelcyra area migrated under influence of a high pressure regime, as attested by veins with brecciated fragments and with Triassic dolomite, crack-seal veins, ... These fluids interacted intensely with the Triassic rocks, located in diapirs or along décollement levels (Figure 5.27B & C). This period is also characterised by two stages of tectonic stylolites development that must be linked to different pulses taking place during the main thrusting phases, in relation to the thrusting of the Kurveleshi belt and the out of sequence development of the Berati unit. The fluids, which transported brecciated fragments, precipitate at low temperature, at on average a depth of 3 km, if a thermal equilibrium occurs with their host-rocks. Afterwards, the tectonic burial increased due to the overthrusting of the Berati unit by the Kurveleshi and Kruja belts, and the temperature of precipitation rapidly increased. This stage is characterised by the development of hydrofracturing and may be linked to the maximum burial of the Berati belt.

With respect to the following stage, a scenario is proposed where sulphate-enriched fluids, giving rise to Dol-3, derived from Triassic migrated along the décollement level, which should act as a conduit for deep sourced fluids (Figure 5.27D) since the dolomites only occur in the Triassic interval. This precipitation, causing diagenetic processes such as the development of secondary porosity and a partial recrystallisation of the former calcite cement, likely occurs at deep burial (~ 6 km). It is not unlikely that the fluid velocity of this saline fluid flow along the décollement level is higher than through the fractures, allowing a precipitation in thermal disequilibrium (Schroenherr et al., 2007). This period corresponds to the beginning of the thrusting in the Ionian Zone, and consequently to the associated tectonic uplift of the Berati belt.

The last stage is likely characterised by the migration of fluids along fractures during erosional unroofing, which results in the formation of a selective dissolution of a part of the euhedral dolomites and a partial dedolomitisation (Figure 5.27E). This fluid may

have a meteoric origin, but more evidences should be determined.

5.5.2- Characterisation of the evaporitic interactions

The Kelcyra reservoir analogue reflects a complex and heterogeneous type of fluid circulation, whereby the main fluids have interacted with evaporite-bearing intervals, i.e. Late Messinian or Triassic layers, in the latter case either due to fluid migration along the décollement level or in diapirs. Three main sources of fluid are inferred from the geochemical data of the calcite cements:

- an early *meteoric* fluid;
- a topography driven fluid;
- a highly saline *deep-sourced* fluid.

However, whatever the fluid generations, they often attest of an interaction with the Triassic intervals (e.g. evaporites and/or dolomites) whereby the evidence of this interaction is demonstrated, either by the occurrence of transported Triassic dolomite fragments, by saline fluid signatures, by the occurrence of high Sr-content and celestite in the cements or by a similar Sr-isotopic signature to the Triassic intervals. Two groups of cements can be distinguished: (1) the first is characterised by an enrichment in Sr and Mg with occurrence of transported barite and/or celestite. A high salinity, characterised by values up to 30 eq. wt.% NaCl, based on Tm values of fluid inclusions, is also observed; (2) the second group displays cements diagenetically enriched in sulphate, magnesium and barium and is characterised by an elevated salinity. Moreover it possesses a positive O-isotope signature and a Sr-isotopic signature similar to Triassic dolomites.

By placing these fluid migration episodes in the geological context and its evolution through time (Figure 5.28), the first group occurs in the pre- to syn-deformational stage in fractures, whereas the second group takes place after the thrusting phase, likely by fluid circulation along a décollement level and/or backthrusts. These two ways of migration imply different fluid velocity and consequently interactions.

CHAPTER 6- DIAGENESIS AND FRACTURING IN THE CIKA BELT: THE SARANDA ANTICLINE CASE STUDY

The purpose of this study is to gain a better understanding of the fracture development and fluid flow through time that occurred in the Upper Cretaceous to Eocene carbonates of the southern external Albanides, i.e. the Cika belt. Based on geological and geochemical data, focusing on vein infillings, different fluid flow systems were determined and placed into the burial history of the Cika belt.

The Saranda anticline is located in the southwest of the Ionian zone (Figure 6.1, Figure 6.2) and belongs to the frontal Cika belt of the Albanides FTB system. It is situated next to the Sazani platform, which corresponds to the western border of the Ionian Basin. At present-day, the anticline is unconformably and partially covered on both flanks by the Oligocene flysch deposits. The highly fractured Upper Cretaceous to Eocene deep marine carbonates of the Saranda anticline were chosen as an outcrop-analogue for the adjacent oil-bearing Delvina reservoir carbonates. The principal interest is to characterise the evolution of the dual porosity system (i.e. matrix and fractures), occurring in the reservoir interval, by determining the agenda of fracture development. In fact, studying surface analogues allows to have a direct access to 3D heterogeneities and fracturing features. However, no hydrocarbon occurrences have been observed in the study area.

The geological SW-NE transect shown in Figure 6.3 shows the Cika unit, which is thrust westward over the flysch and molasse deposits of the Peri-Adriatic Depression and, is underthrust beneath the Kurveleshi unit and partially by the Berati belt. The Saranda anticline constitutes a pop-up fold, bounded by two conjugate opposite major faults, i.e. forethrust and backthrust. Triassic evaporite accounts for the décollement level. The anticline covers an area of 7 by 20 km and represents an asymmetric structure, characterised by a subvertical and a partly overthrust eastern flank. This flank has a steeply dip with an average of 65°NE (Figure 6.4 E & F), whereas the western flank dips less steeply, with an average of 20°SW (Figure 6.4

D). The anticline axis trends towards the south-east, which is sub-parallel to the main thrust fronts of the Ionian Basin.

In the study area, Lower Jurassic - Eocene carbonates occur in the structure (Figure 6.2). However, the diagenetic study will only focus on the Upper Cretaceous to Eocene carbonates. This interval consists principally of fine-grained limestones and is characterised by a large amount of intercalated debris flows and cherty interbeds. Pelagic carbonates from the Jurassic to the Lower Cretaceous outcrop in the core of the anticline. The highly fractured Upper Cretaceous deep marine carbonates, intercalated with debris flow, are well exposed at the topographic top of the anticline (Figure 6.4 C) and demonstrate an important alteration phase (i.e. surface processes) with meteoric phreatic diagenesis. The overlying part of the succession consists of Paleocene to Eocene deep marine carbonates, which are intercalated with debris flow and slumping horizons (i.e. Paleocene interval). They occur in the eastern and western flanks of the Saranda anticline and reflect the instabilities of the neighboured platform, which developed at the onset of the compression in the hinterland.

Subsequently, a siliciclastic overburden, consisting of the Oligocene to Early Miocene flysch sequence, gradually changes to pre-molasse and is overlain by coarse-grained porous Miocene molasse. This succession reflects the overthrusting that prograded from the east to the west of the Ionian basin. Field pictures of the main studied outcrops as well as satellite images of the Saranda anticline are illustrated in the Figure 6.4.

In this chapter, results from structural analyses, petrographical and geochemical investigations will be presented. According to the work realised by Muska (2002), this anticline has not been deeply buried during the FTB development, allowing the infiltration of heterogeneous fluids (e.g. marine and meteoric) into the studied sedimentary intervals. Special attention will be paid to characterise the successive fracturing stages in order to integrate them into the

deformation history of the area. Here, the fractures and the paleofluids were difficult to characterise due to the intense recrystallisation and deformational twinning of the cements and the few crosscutting relationships between veins that have been recognised.

6.1- General characteristics

The sedimentology was made first on field observations and then subsequently refined by studying polished samples and thin sections. After a precise mapping of the totality of the Saranda anticline, eight study areas, located on the Figure 6.2, were selected for sampling. They are mainly situated along the flanks of the

anticline, where the Upper Cretaceous to Eocene carbonates crop out in quarries. In total, 97 samples were taken, 25 thin sections were studied and 7 samples have been simultaneously analysed with regard to their "horizontal air permeability" and "ambient porosity (Helium)".

6.1.1- Description of the studied areas (macroscopic observations)

Sedimentological analyses in quarries allow to overcome the present-day surficial erosion and to work in the three dimensions. The eight selected studied areas, indicated in the Figure 6.2, are numbered from 1 to 8:

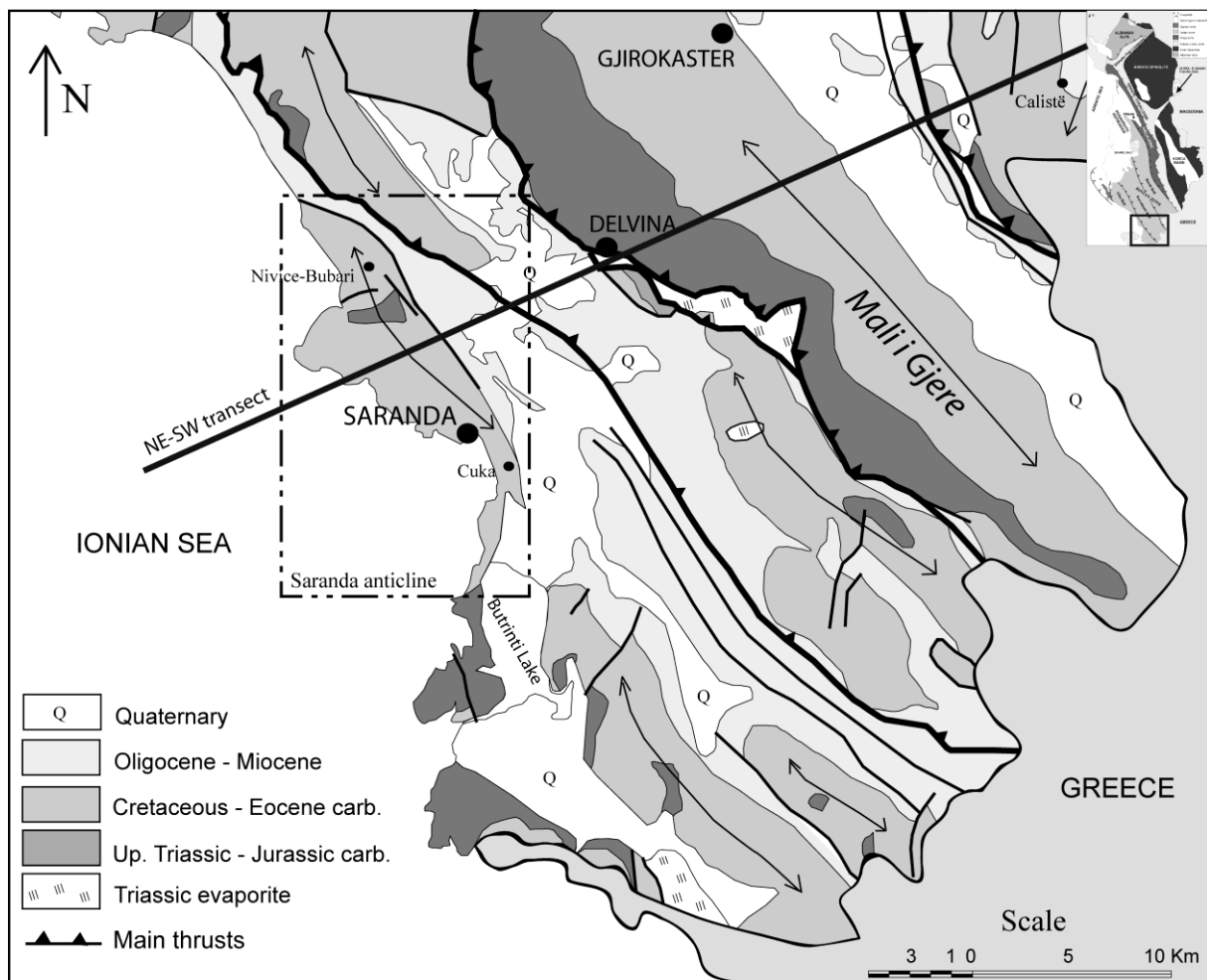


Figure 6.1. Simplified structural map of the southern part of the Ionian zone (based on the geological map of Albania, 2002). The Saranda anticline is indicated by a dashed square. The indicated NE-SW transect is shown in the Figure 6.3.

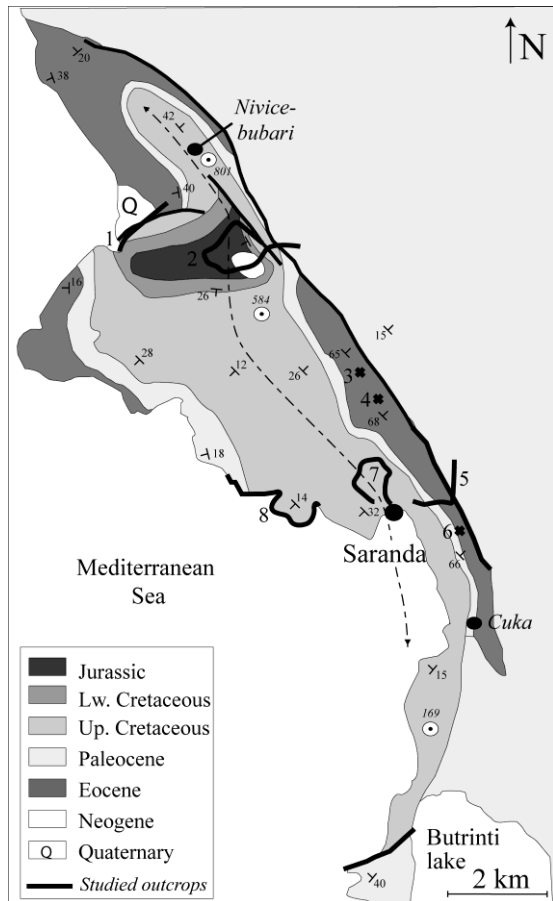


Figure 6.2. Detailed geological map of the Saranda anticline. The studied outcrops are indicated on the map and identified by numbers 1 to 8.

- *Location 1*, situated in the Kakomere Bay (Figure 6.4 D), was chosen to study the Upper Cretaceous interval. This outcrop presents well-bedded and highly fractured carbonates, which are mainly oriented $N45^{\circ}23N$. These Upper Cretaceous carbonates consist dominantly of light fine-grained mudstones with 5 to 10% of fauna (i.e. foraminifera), intercalated with fine-grained laminated turbidites and some debris flow (Swennen et al., 2000; Van Geet et al., 2002). The Male I Gjere section, i.e. Figure 3.4, represents the best outcrop in the Ionian Zone, showing the turbiditic intervals of the Upper Cretaceous intervals. The turbidites present a typical sequence, including basal coarser grained intervals overlain by parallel laminated fine-grained wacke- to mudstones. Their basis shows often scour marks, pointing to the erosive character of the turbidity flow. The debris flows have a fine grained matrix with a significant content of clay-sized material. No sorting nor internal bedding occur. Individual bed thicknesses of the fine-grained limestones and the debris flow vary respectively from 10 to 35 cm and 40 to 55 cm. The total thickness of the Upper Cretaceous interval averages 200 m. The lower part of the section makes the transition with the Albian "phosphatic horizon".

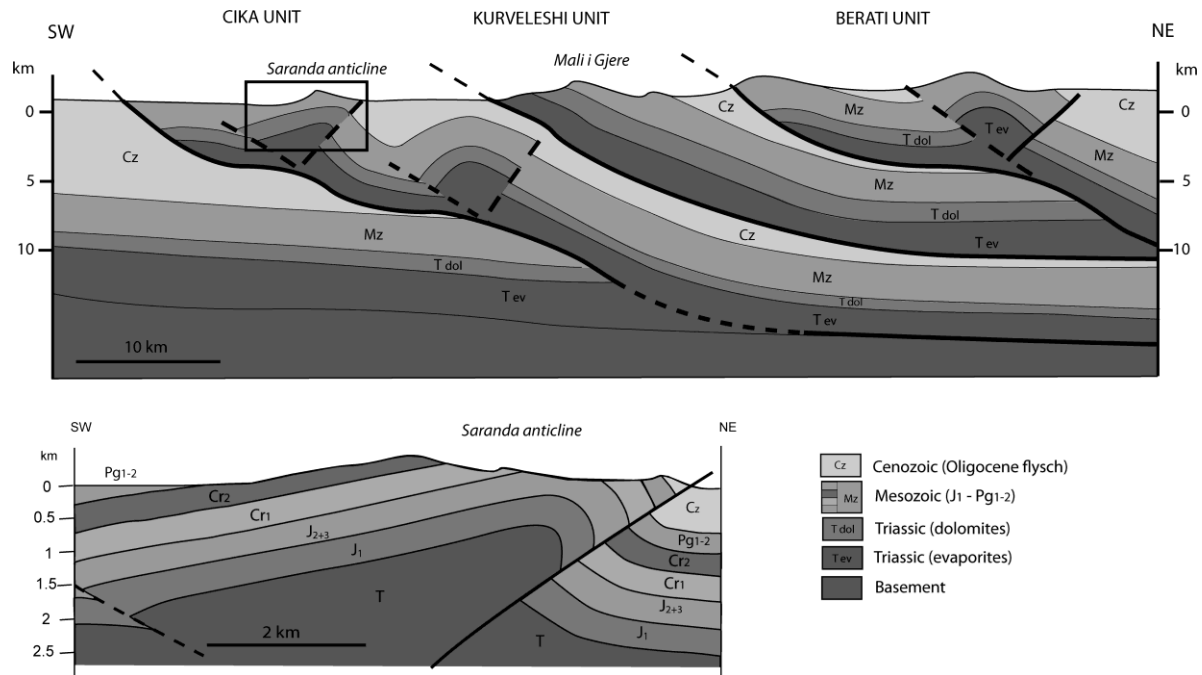


Figure 6.3. SW-NE geological transect (modified from Roure et al., 1995) of the southern part of the Ionian Zone, which is located on the Figure 6.1. A detailed zone of the Saranda anticline, showing its asymmetric structure, is also given in the lower part.

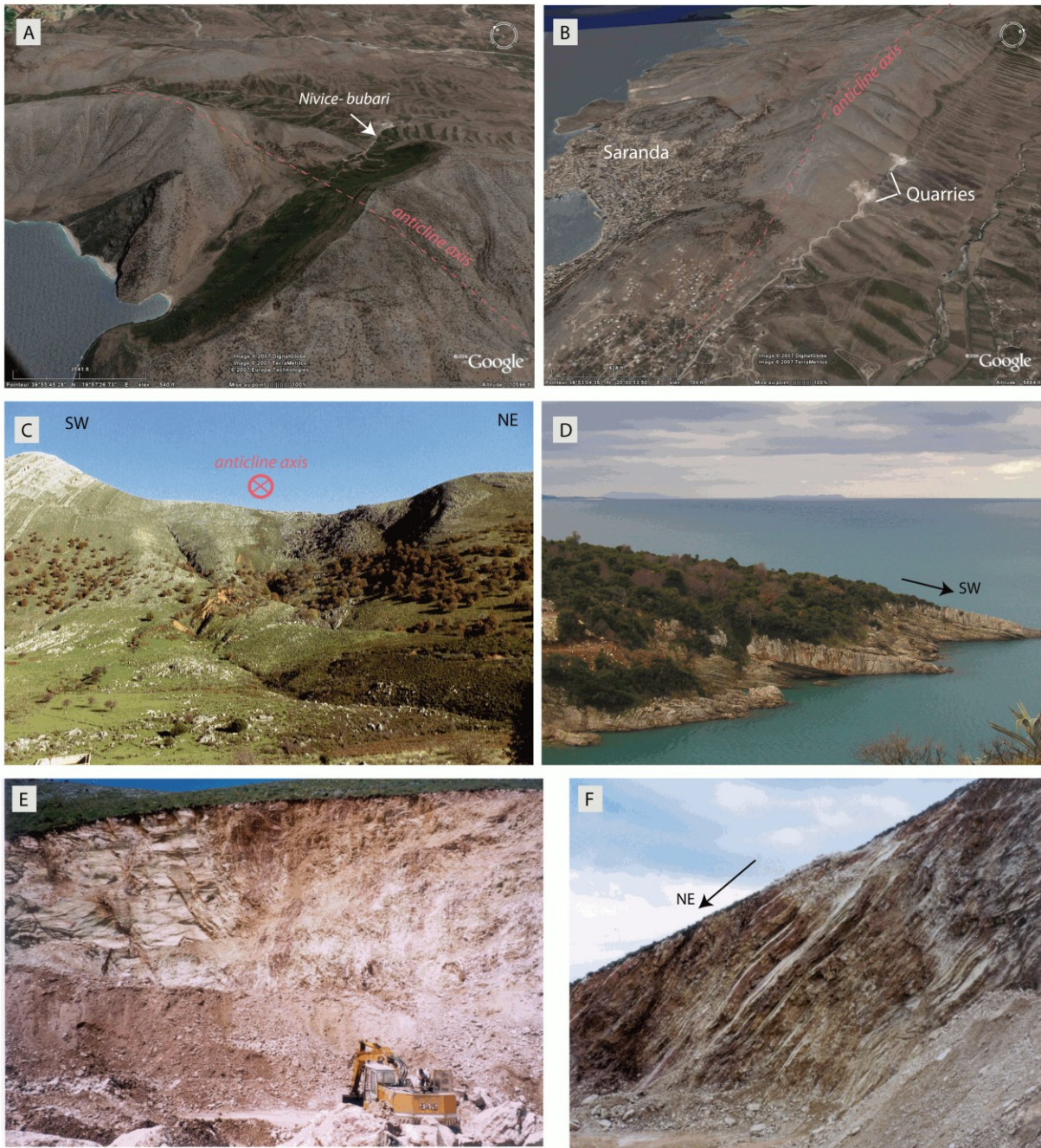


Figure 6.4. Overview of the study areas in the Saranda anticline: Satellite image of the northern (A), central and southern (B) parts of the Saranda anticline (Google Earth 4.3, 2007); (C) Field picture of the Upper Cretaceous carbonates, which are located in the central part of the anticline (location 7, Figure 6.2). (D) Outcrop located in the western side (location 1), where the Upper Cretaceous to Paleocene fine-grained limestones and debris flow are characterised by beds slightly dipping towards the SW. (E) Overview of a studied quarry (location 3), where Eocene limestones are cropping out. The limestones display a pinkish colour. (F) Quarry of well-bedded Eocene carbonates (location 4), consisting of pink to white limestones and characterised by steeply dipping beds towards the NE.

This section is characterised by the occurrence of silica chert nodules and horizons. The top of the Upper Cretaceous interval is better characterised by the presence of fine-laminated limestone turbidites, intercalated with grainflows, averaging 1 m thick. This interval is also characterised by the development of burial

stylolites and thin cemented fractures, principally in the fine-grained limestones. Their repartition is not homogeneous, since no stylolites and only few thin and cemented fractures occur in the debris flow. At present, this interval has been subjected to meteoric alteration, which is indicated by the intense dissolution of siliceous

nodules and the recrystallisation of the carbonate matrix.

- *Location 2* has been selected to study the Neogene deposit. However, the Neogene deposits, indicated on the geological map, have been removed within the last two years. Thus these deposits have not been studied, preventing a precise timing of the syn- to post-folding diagenetic processes.

- In *locations 3, 4 and 6*, well-bedded and highly fractured Eocene carbonates occur in exploited quarries (Figure 6.4 E & F), allowing a good and precise sampling. These quarries are situated in the eastern flank of the anticline, where the beds are mainly oriented N140°68E. The Eocene interval is on average 150 m thick and individual bed thickness varies from 10 to 20 cm. Eocene carbonates consist of white and fine-grained limestones with few foraminifers. No siliceous accumulation occurs. The limestones at the base of the interval are more pinkish, indicating the transition to the Paleocene interval.

- *Location 5* represents an E-W track across the southern part of the anticline and allows to study the Paleocene interval. Here, well-bedded and pinkish limestones, mainly oriented N162°50E, are intercalated with debris- and grainflow strata (i.e. slumping horizons). These slumping horizons have a regional spread and increase largely the matrix porosity of the reservoirs in Albania. Figure 3.4 shows an overview of the famous Male I Gjere section, i.e. Kurveleshi unit, demonstrating the Upper Cretaceous to Paleocene carbonate succession, intercalated with two main slumping horizons. Some fine-grained intervals contain cherts parallel to the bedding. The Paleocene interval is approximately 55 m thick and the bed thickness of the micritic beds varies from 10 to 20 cm. Here, the Paleocene carbonates are altered and highly recrystallised, due to meteoric alteration. That is in agreement with the occurrence of red-coloured and partially dissolved silica nodules.

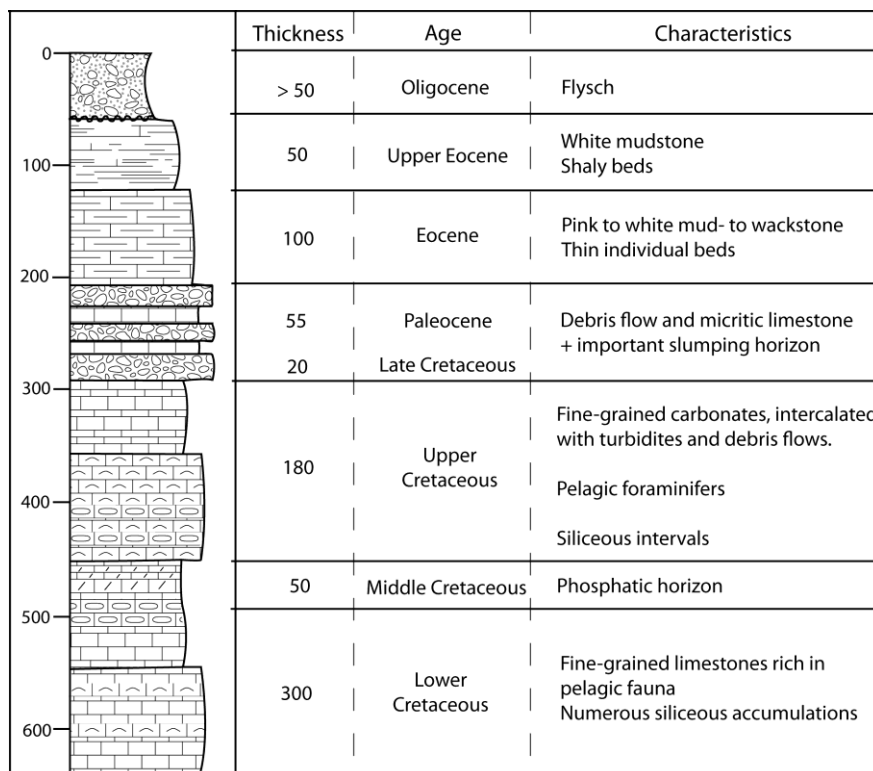


Figure 6.5. Schematic sedimentary log based on own data of the Saranda anticline.

- *Location 7* occurs in the surrounding of Saranda city and is of interest since it is situated on the fold hinge. Unfortunately, the Upper

Cretaceous limestones are highly recrystallised and partially eroded. The layers are mainly oriented N145°30NE on the eastern part of the

fold hinge and N135°45SW on the western part (Figure 6.4 C).

- The last studied area is located in the western side of the anticline (i.e. *location 8*) characterised by a low dip orientation. Here, well-bedded Upper Cretaceous to Paleocene carbonates, oriented mainly N138°12S, occur.

6.1.2- Microscopic observations

The Upper Cretaceous to Eocene carbonates of the Saranda anticline consist mainly of pelagic limestones. A schematic lithostratigraphic column of the Saranda area is illustrated in the Figure 6.5.

The Upper Cretaceous strata consist of white micritic limestones, intercalated with fine-laminated clastic turbidites and packstone (i.e. debris flow). They commonly contain 10% of planktonic foraminifers (i.e. *Globotruncana gansseri*; *Globotruncana fornicate*; *Abathomphalus mayaroensis*; *Rotalipora*) and gastropods, which are at present recrystallised. The bioclasts are usually micritised and show intraparticle porosity. The typical pelagic foraminiferal character of the Upper Cretaceous points towards deep marine depositional conditions. The occurrence of silica beds and nodules, which often have a length of about 50 cm, decreases from the base to the top of the succession. The top of the succession is characterised by the presence of regional slumping horizons (i.e. grainstone), intercalated with debris flow (i.e. packstone, Figure 6.6A) and fine-grained limestone.

The well-bedded and highly fractured Paleocene carbonates consist of pinkish mud- to wackestone (Figure 6.6 B). This section displays also some intercalations of grainstone (Figure 6.6 C & D), which attest of the occurrence of mass movements, as it is the case for the Late Cretaceous interval.

Paleocene limestones are made up to 15% of pelagic to benthic foraminifers (i.e. *G. Spinulosa*) and display often red-colour siliceous diagenetic accumulations (i.e. cherts).

The highly fractured Eocene limestones, which represent the upper part of the oil-producing intervals in the Delvina field, evolve from pink (at the base) to white mud- to wackestone (Figure 6.6 E & F), intercalated with rare packstone. In this formation, no silica lense

occurs. The top of the Eocene carbonates is marked by the presence of shaly beds, which characterise the transition to the Oligocene flysch.

Thus, these Upper Cretaceous to Eocene fine-grained carbonates reflect predominantly deep basinal depositional conditions, according to the presence of fine-grained calciturbidites and pelagic mudstones. The occurrence of debris flow and important slumping horizons should reflect instabilities of the neighboured Sazani platform.

6.1.3- Porosity versus permeability

Figure 6.7 illustrates the porosity-permeability (K-Phi) distribution for some lithologies. In addition, samples, such as mudstone, where no porosity could be seen macroscopically have not been studied. The dataset is very small and is only meant as a reconnaissance dataset. The diagram shows that wackestone (W) facies possess the lowest porosity-permeability values of respectively <1.5% and < 0.5mD. But it should be noted here that the presence of fractures or burial stylolites (i.e. BPS) concurs with higher permeabilities up to 1mD.

Late Cretaceous and Paleocene intervals, which are characterised by fine-grained limestones, numerous debris flow (i.e. packstone "P") and slumping horizons (i.e. grainstone "G") possess interesting porosity-permeability characteristics, especially when they display a dual porosity, i.e. fractures and/or stylolites apart from matrix porosity.

The grainstone facies has porosity values averaging 1.6% and permeabilities ranging from 1.2 to 1.6 mD. The packstone facies, characterised by a dual porosity, has higher porosity-permeability values of respectively up to 2.5% and of 3.4mD. However, in the Saranda anticline, these K-Phi values are in general very low, but the presence of open fractures or non-cemented stylolites improves largely the reservoir permeability up to 100 times.

However, the most interesting interval with regard to the porosity-permeability values consists of the Upper Cretaceous to Paleocene section, where many grainstone (slumping horizons) and packstone (debris flow) facies occur.

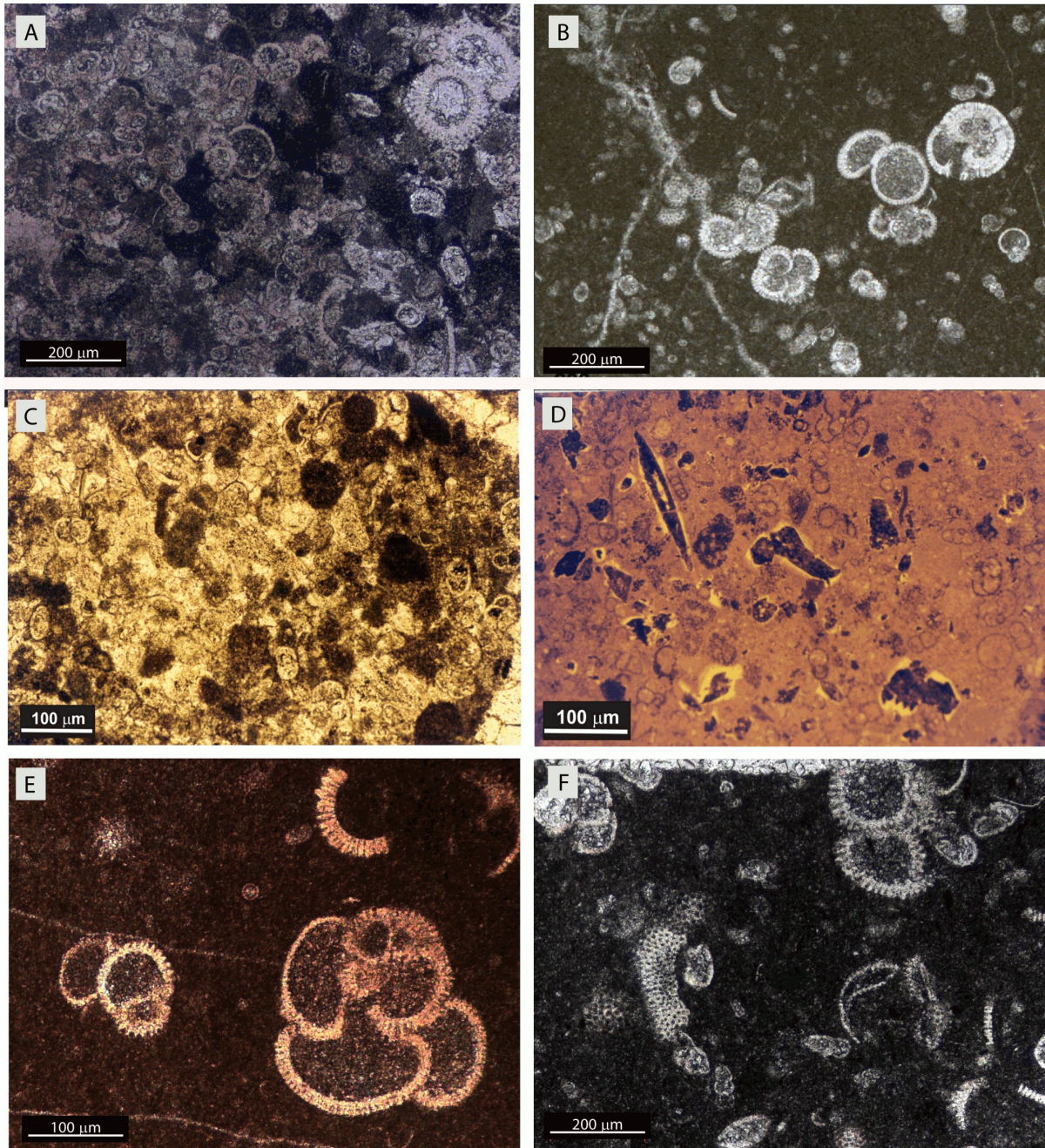


Figure 6.6. Petrographic characteristics of Upper Cretaceous to Eocene limestones in the Saranda area: (A) Transmitted light view of planktonic foraminiferal Upper Cretaceous packstone; (B) Transmitted light view of Paleocene wackestone and recrystallised foraminifera; (C) and (D) Respectively transmitted light and cathodoluminescence (CL) views of Paleocene grainstone (i.e. debris flow); (E) and (F) Transmitted light views of Eocene mud- to wackestone with benthic and planktonic foraminifera.

They have permeabilities higher than 1 mD, reaching up to 3 mD when dual porosity occurs. The Eocene limestones, consisting of mudstone (not analysed, since they do not contain macroscopic porosity) and wackestone, display very low matrix porosity but can possess some reservoir porosity, in relation to the occurrence of numerous non-cemented fractures and stylolites.

6.2- Structural analyses

During the FTB development, the Saranda anticline has been subjected to numerous stylolitisation and fracturing episodes, being successively filled by calcite cements, which indicate the circulation of several fluids into the basin. These fractures together with the presence of stylolites (i.e. burial and tectonic stylolites)

help to reconstruct the diagenetic evolution of the reservoir analogue.

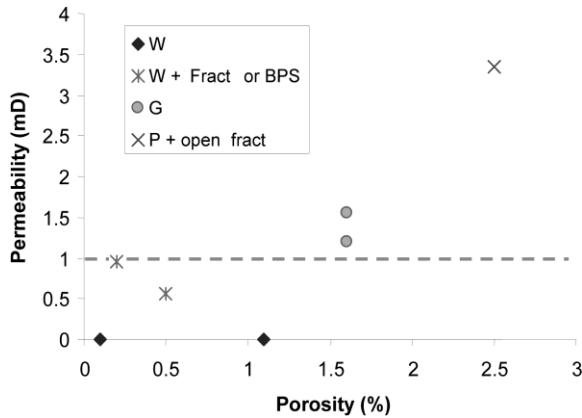


Figure 6.7. Crossplot of the porosity versus permeability for various lithologies (W = Wackestone; G = Grainstone; P = Packstone; BPS = Bedding Parallel Stylolites; open fract = open fractures).

Their structural characterisation is principally based on cross-cutting relationships between

fractures (i.e. veins) with stylolites and their orientations (i.e. raw or backtilted data). In this study, the main difficulty consists in determining a precise chronology of the fracturing stages, and placing them into the deformation history of the Saranda anticline, i.e. inferring if they are pre-, syn- and post-folding. For that, the assumption is made that fractures were initially created sub-vertically or parallel to the bedding. The latter is of importance since the fractures or stylolites dated as pre-folding necessitate to be backtilted with regard to the actual bedding attitude. In fact, the main stresses are assumed to be sub-vertical (burial phase) or sub-horizontal (during the main compressive phase), implying the development of sub-orthogonal fractures in monoclinical structures, as the Saranda structure.

In this part, a tentative timing of the fracturing will be given. Then, this timing will be precised, by incorporating first the petrographic observations and then the geochemical analyses, such as stable and strontium isotopes, element geochemistry and calcite twin analysis.

Samples	Type	Porosity (%)	Permeability (mD)
S18	W	0.1	0.001
S01	W	1.1	0.001
S04	W, open fracture	0.2	0.953
S16	W, BPS	0.5	0.558
S07	G	1.6	1.204
S09	G	1.6	1.545
S14	P, open fracture	2.5	3.339

Table 6.1. Porosity and permeability data (W= Wackestone; BPS= Bedding Parallel Stylolites; G= grainstone; P= Packstone).

6.2.1- Stylolites

In the Saranda anticline, the compactional stylolites (i.e. BPS), which are associated to the burial evolution of the Ionian basin, are generally better developed than the tectonic stylolites (i.e. TS). Based on stylolite orientations, one generation of BPS and four stages of TS, related to the kinematic evolution of the Albanides FTB, have been identified.

The BPS forms mainly parallel to the depositional fabric (i.e. bedding), whatever their location in the anticline. Sometimes, they are reopened and filled with green-coloured clayey material. These burial stylolites are mostly

developed along the fine-grained limestones interbeds. Consequently, they are likely formed during the burial stage of the area, which is Lower to Middle Oligocene in age (Nieuwland et al., 2001) and thus predate the folding.

The tectonic stylolites (TS), which are characterised by higher amplitude indentations than the burial stylolites, are not abundant in the studied strata. The Figure 6.8 summarises the different generations of tectonic stylolites, which are interpreted either as pre- to syn- (i.e. backtilted data, TS1) or as post-folding (i.e. raw data, TS2). Notice that in each diagram, two sets of stylolitic planes are conjugated, likely characterising a similar origin.

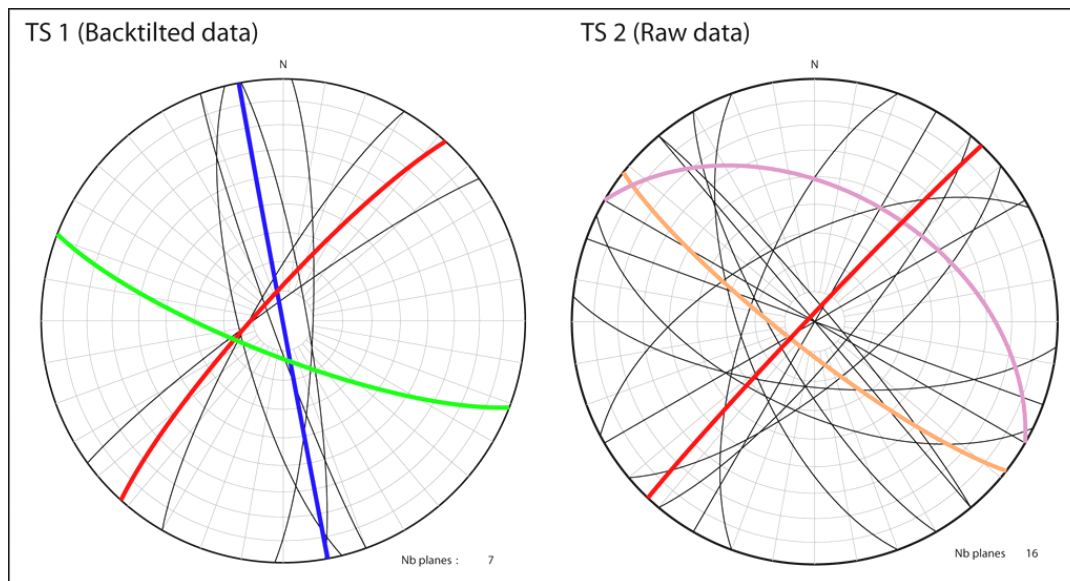


Figure 6.8. Lower hemisphere stereonet projections of the pre- (TS 1, backtilted data) and post-folding (i.e. TS2, raw data) tectonic stylolites. The coloured-planes identify the mean tectonic stylolite orientations. The black planes show the orientations of the recorded tectonic stylolitic planes.

The pre- to syn-folding stage, i.e. TS 1 generation, displays three main sets of tectonic stylolites, pointing to two directions of maximum principal stress σ_1 , trending about N55° and N120° with subvertical dips (i.e. backtilted data). Concerning the TS 2, which have been dated as post-folding stage, two sub-orthogonal sets point to two directions of σ_1 , trending about N45° and N130°. However, no timing between the generations of TS is indicated since no cross-cutting relationship has been observed. Whatever the generation of TS, a homogeneous evolution occurs during the deformational stage, and is characterised by the co-evolution of N50° ±5 and N130° oriented maximum stresses σ_1 . However, the post-folding stage is also characterised by tectonic stylolitic planes, oriented N120° (i.e. purple and orange planes TS2), dipping towards the NE.

A first maximum stress, oriented on average N50°, occurred during the pre- to post-folding stage. This orientation is consistent with the main compression developing the NNW-SSE frontal thrusts and folding structures in the Albanides, which are roughly orthogonal to the maximum stress (N65°) and mostly parallel to the fold axis.

The second recorded maximum stress is oriented N130° and occurred during the pre- to post-folding stage. This orientation is in agreement with the development of a NW-SE compression, described by Mantovani et al. (2002), dated during the Middle Miocene. This evolution

points to the active tectonics at the trench between the African and Eurasian plate (Le Pichon and Angelier, 1979).

The third recorded σ_1 , oriented N30°, which developed also N120° oriented fractures, corresponds to the orientation of the main NE-SW compression, developing the NW-SE frontal thrusts in the Albanides. However, this σ_1 is characterised by an important dip, which likely suggests a relation to the folding stage. Consequently, this TS generation likely developed as pressure-solution cleavage in the inner arc region and expressed the deformation feature of the anticline (Ramsay and Huber, 1987).

The change in the orientation, with regard to the N50°-oriented compression can either demonstrate a rotation of the maximum stress through time or a late rotation of the studied area due to activation of transversal faults. This event is not well understood but could be related to the presence of transform faults, such as the Vlora-Elbasan lineament. On Figure 6.1, the frontal thrusts are not exactly straight and present locally some changes of azimuths. Such change occurs also in the southern part of the Saranda anticline, where the anticline hinge clearly shows a N-S orientation (Figure 6.2). Then a late reactivation of the structures, especially close to possible transfer zones, likely relates to this NE-SW compression.

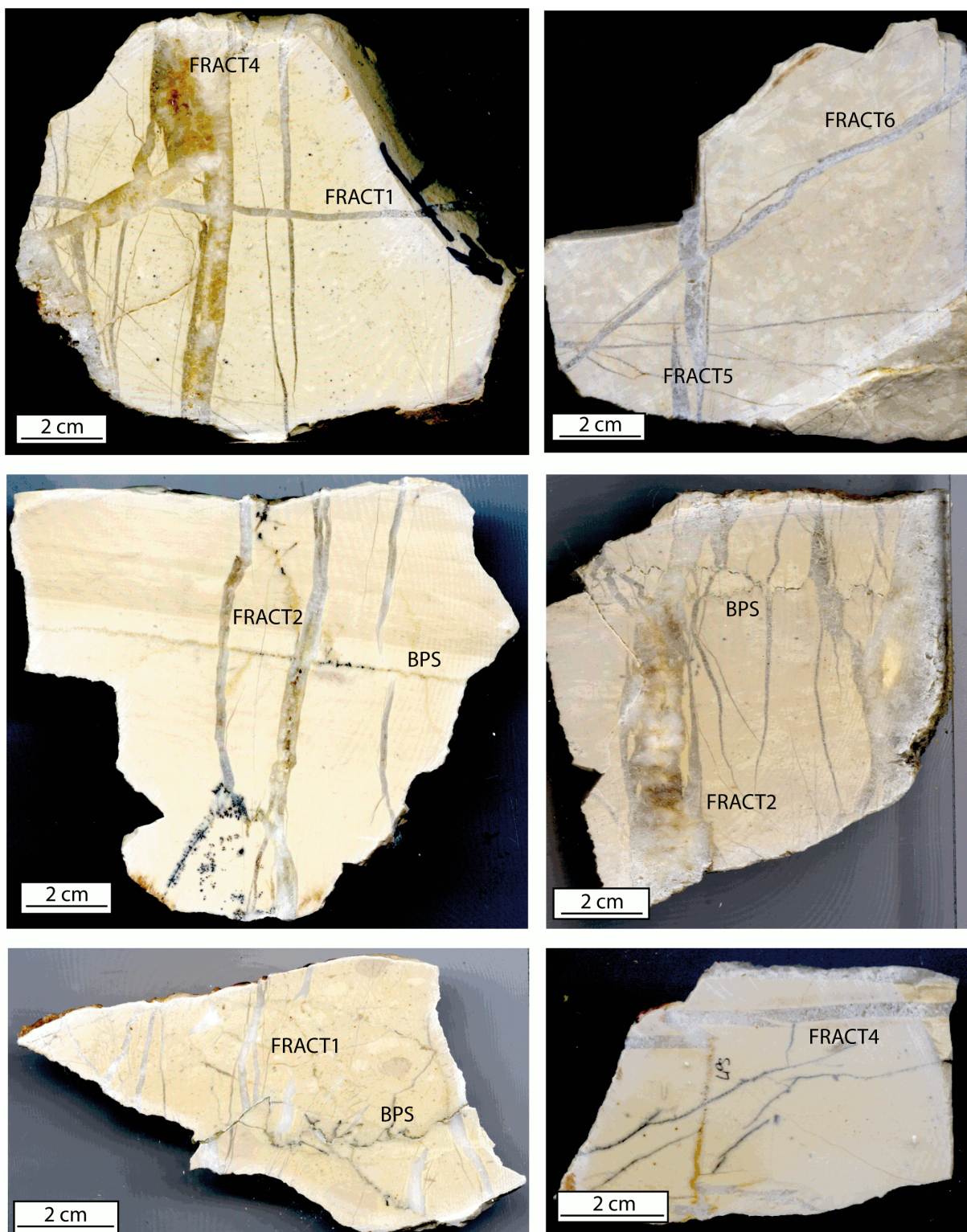


Figure 6.9. Macroscopic observations of cross-cutting relationships between fractures and with stylolites.

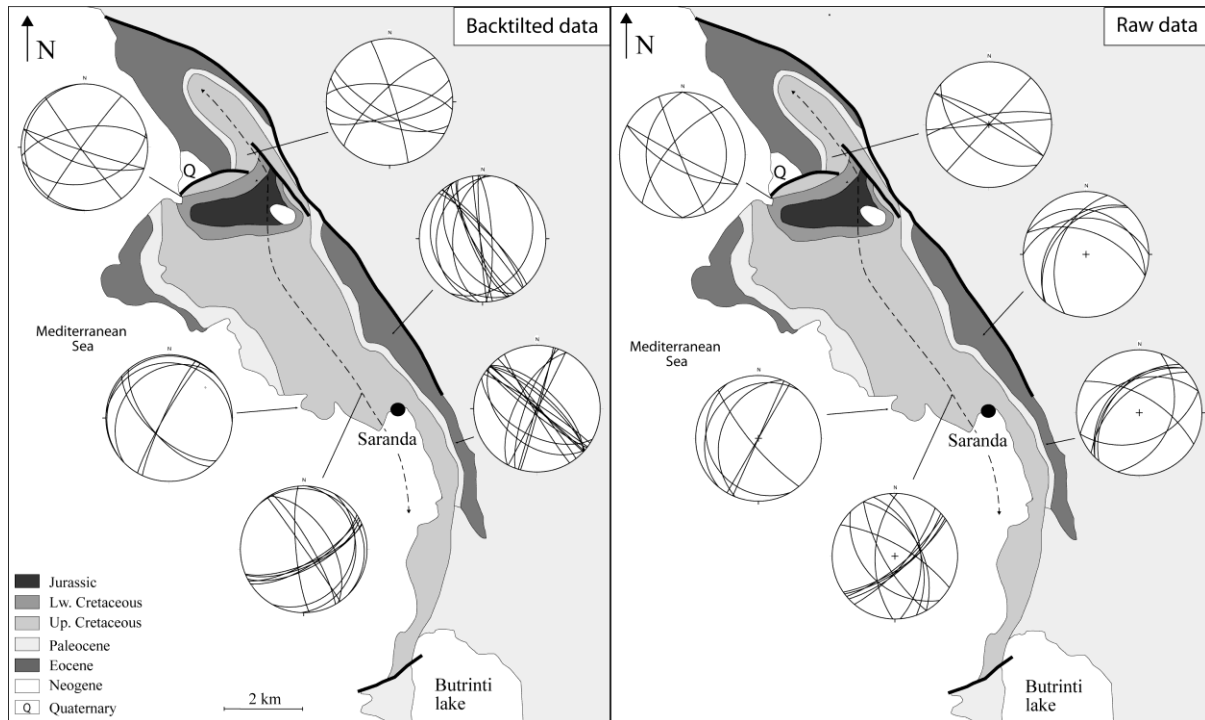


Figure 6.10. Raw and backtilted data of the recorded fractures.

6.2.2- Joint and fracture development

As mentioned before, the Saranda anticline has been subjected to numerous fracturing events during the Neogene Alpine deformation. The highest density of fractures occurs at the top and in the eastern flank of the anticline and shows a clear relationship with lithology. The density of fractures is higher in the fine-grained limestones than in the debris flow carbonates.

Six main sets of fracturing, occurring during the pre- to syn-folding stage and one set, dated as post-folding, were encountered. They have been relatively dated based on the cross-cutting relationships between veins (i.e. fracture fillings, Figure 6.9) and with stylolites. The relative timing of the fracture generations with regard to the tectonic evolution of the Saranda anticline was established based on the fractures dip. In fact, the assumption is made that fractures were initially created sub-vertically or parallel to the bedding. Based on this assumption, all fractures, which are not vertical or horizontal, have been unfolded with regard to the actual bedding. Raw and backtilted fracture orientations are presented on the Figure 6.10 and a synthesis of the fracture characterisation is illustrated in Figure 6.11.

The first recorded fracture orientation, i.e. FRACT1, characterises the pre-folding stage and trends about N165° with a subvertical dip (i.e.

green planes on the Figure 6.11). They crosscut and are cut by burial stylolites. Consequently, FRACT1 likely developed simultaneously with the regional flexuring of the foreland (Vilasi et al., 2009). This generation is followed by a second set of fractures, i.e. FRACT2, which is oriented N140° with subvertical dip. Since this fracture generation has a subvertical dip, it is interpreted as pre-folding. These fractures are parallel to the fold hinge and developed either to accommodate the folding or due to the occurrence of a NW-SE compression, which also developed N40° oriented tectonic stylolites.

FRACT3, represented by blue planes on the Figure 6.11, are oriented sub-parallel to the bedding. Also, they have been formed during the prefolding stage, likely during the increase of the vertical and lateral compression. Due to their orientation, FRACT3 will help lateral fluid flow migration.

Subsequently, FRACT4 to FRACT6 formed during the pre- to syn-folding stage (Figure 6.12). FRACT4 (i.e. red planes in Figure 6.11) trends about N65° with subvertical dip and is oriented sub-perpendicular to the fold hinge. They constitute a vein system that formed in response to the regional compressional stress responsible for folding, because FRACT4 orientation is similar to the main compression stress occurring in the Ionian Zone. FRACT5

(i.e. yellow planes in Figure 6.11) is defined by N105°-oriented fractures, with subvertical dip angle and FRACT6, i.e. orange-coloured planes in Figure 6.11, shows a N35° orientation and subvertical dip. FRACT5 and FRACT6 are oblique to the fold hinge. These generations of fractures are consistent with the main compressional stress in the Albanides and are attributed to the folding process.

As syn- to post-folding deformation feature, FRACT7 has been encountered with orientations varying from N90° and N130° with almost subvertical dips. This fracture set relates to a late deformational stage in the folding, since they have been formed along the subvertical and overthrust eastern flank. Consequently FRACT7 should be linked to a reactivation of a compressive event, developing also new faults, such as backthrusts.

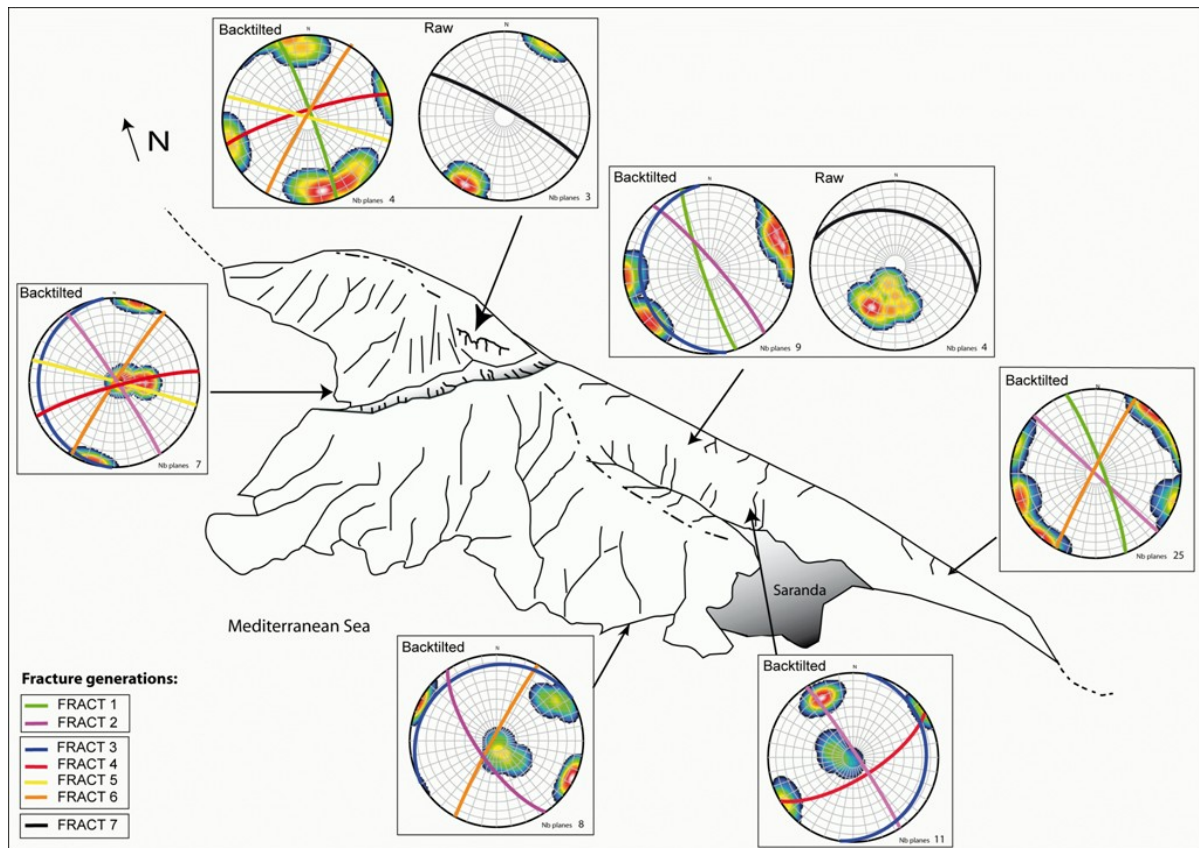


Figure 6.11. Synthesis of the successive sets of fractures in relation to its position in the Saranda anticline.

These successive fracture sets record a complex deformation history. These sets can be grouped into three main deformational stages, namely in: the *early foreland flexure*, the *folding* and the *overthrusting stages*:

(1) Tectonic loading applied by the hinterland and westward thrusting in the eastern parts of the Albanides induced the progressive development of a wide flexural basin. This depression was subsequently filled with turbidites and breccias, constituting the Oligocene flysch. During this flexuring event, compactional stylolites (i.e. BPS) and FRACT1 developed possibly under high pore fluid pressure regime. They likely date

back to the Oligocene. Afterwards, a NW-SE compression occurred, developing likely N40° oriented TS and FRACT2 during the Miocene (Mantovani et al., 2002). Under this regime, the NE faults would act as transfer zones with dominant dextral strike-slip motion and subsidiary normal displacement.

(2) The onset of the folding corresponds to the second recorded deformational phase, which likely began during the Middle Miocene (i.e. Burdigalian, Nieuwland et al., 2001). This period postdates the development of tectonic stylolites, oriented N170°. The depositional fabric associated with cylindrical folding consists of

structural elements trending almost perpendicular, i.e. FRACT4, and parallel to the fold hinge. The latter may consist of reactivation of FRACT1 and FRACT2 sets.

The next fracture set consists of hinge-perpendicular conjugate shear fractures, i.e. FRACT5 and FRACT6. They are synchronous to the development of N110°-oriented TS, and are believed to accommodate the folding (Figure 6.12), as described in the model of Stearns and

Friedman (1972). Cooper et al. (2006) demonstrates that this type of model is especially appropriate to fault propagation and fault-bend folds in foothills, which are characterised by thin-skinned thrusting (Cooper, 1992). This period is also characterised by the development of pressure-solution cleavage in the inner arc region, oriented N120°, 45NE (i.e. TS2, raw data; Figure 6.8).

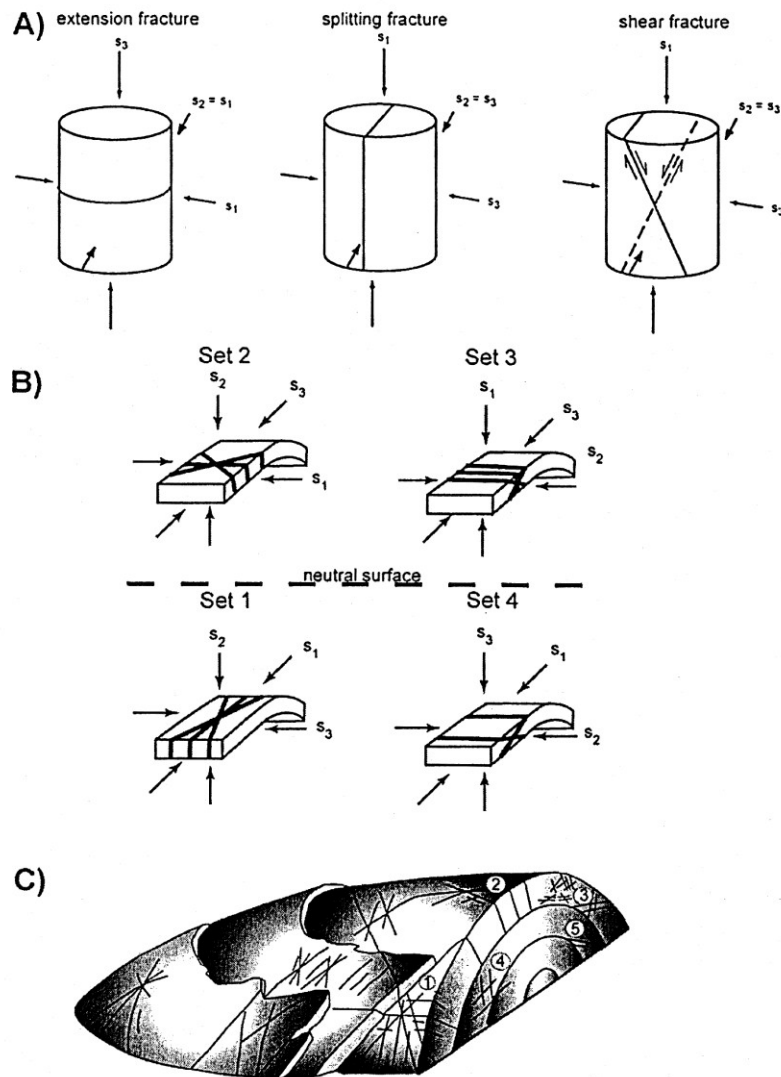


Figure 6.12. Models of fracture sets associated with folding: (A) Summary taken from Griggs and Handin (1960) based on laboratory rock mechanical testing of cylindrical samples; (B) Stearns (1968) model of primary fracture sets during folding. The maximum and minimum principal stresses lie within the bedding. (C) Spatial relationship of fractures and fold of the Stearns (1968) model (modified from Bergbauer and Pollard, 2004).

Raw data (fractures)	Location	So	Backtilted fractures	TS 2 (Raw data)	TS1 (Backtilted)
0 30 W	1	45 60 N	77 42 SE	140 90	
0 30 W	1	62 72 S	36 87 NW		
40 64 N	1	45 60 N	176 6 SW		
0 20 E	1	62 72 S	82 64 NW	26 14 W	54 84 NW
118 63 S	1	45 60 N	103 90 SW		
158 86 S	1	45 60 N	143 68 SW		
118 68 S	1	45 60 N	108 87 NE		
90 30 S	3-4	144 74 E	120 88 NE	60 70 S	75 90
130 45 N	3-4	138 65 N	154 21 SW		
80 40 N	3-4	138 65 N	3 51 NW		
110 50 N	3-4	138 65 N	8 28 NW		
110 20 N	3-4	138 65 N	150 48 SW		
40 30 N	3-4	142 80 N	171 87 SW		
42 35 N	3-4	142 80 N	176 87 SW		
20 41 N	3-4	142 80 N	177 78 NE		
145 12 SE	3-4	140 80 N	141 88 NE		
130 20 SE	3-4	140 80 N	136 80 NE		
141 21 SE	3-4	140 80 N	140 79 NE		
65 10 N	3-4	140 80 N	150 78 SW		
63 15 N	3-4	140 80 N	155 77 SW		
70 18 N	3-4	140 80 N	157 74 SW		
85 90	2	20 60 W	97 68 NE		
120 90 N	2	160 40 W	112 60 SW		
120 75 N	2	160 40 SW	120 74 SW		
42 90	2	160 40 SW	48 72 NW		
80 76 S	2	160 34 SW	70 73 SE	160 60 E	160 86 SW
130 40 S	2	20 80 E	163 85 NE		
80 72 N	2	20 80 E	85 65 SE	120 90	
134 30 S	5-6	120 60 N	127 89 SW		
125 35 S	5-6	120 60 N	123 85 NE		
20 35 S	5-6	162 68 E	131 43 SW	120 45 N	28 41 NW
106 36 S	5-6	162 68 E	133 90 NE		
40 40 N	5-6	162 68 E	15 88 SE		
120 48 S	5-6	162 68 E	131 75 NE		
45 40 N	5-6	162 68 E	17 89 NW		
124 50 S	5-6	162 68 E	132 71 NE	62 62 N	42 88 NW
126 22 S	5-6	162 68 E	149 86 SW		
50 50 N	5-6	162 68 E	27 89 SE		
130 56 S	5-6	162 68 E	133 64 NE		
45 36 N	5-6	170 50 E	20 75 NW	140 85 E	
120 54 S	5-6	170 50 E	132 89 NE	6 50 W	2 80 SE
70 40 S	5-6	170 50 E	119 55 SW	170 48 W	170 82 NE
110 50 S	5-6	170 50 E	128 83 SW		
108 42 S	5-6	170 50 E	132 76 SW		
70 34 N	5-6	170 50 E	28 63 NW		
68 38 N	5-6	170 50 E	31 66 NW		
140 34 W	5-6	170 62 E	154 88 NE	62 42 N	30 80 NW
160 34 W	5-6	170 62 E	164 84 NE	20 68 W	23 58 SE
165 35 W	5-6	170 62 E	167 83 NE	116 60 S	124 78 NE
160 35 W	5-6	170 62 E	164 83 NE	160 65 W	159 54 NE
160 45 W	5-6	170 62 E	163 74 NE	96 68 S	107 87 NE
70 34 N	5-6	170 50 E	28 63 NW	160 25 W	166 75 SW
132 50 S	5-6	170 50 E	142 87 NE	90 58 S	111 78 SW
150 70 W	7	144 30 E	150 80 NE		
120 70 E	7	60 50 N	147 55 NE		
150 45 E	7	135 45 W	145 89 NE	150 76 S	
	7	135 42 S		40 78 S	
150 45 E	7	135 45 W	145 89 NE		
135 38 S	7	135 45 W	135 7 NE		
160 46 N	7	145 30 NE	2 19 SE		
2 55 n	7	145 30 NE	175 80 SW		
175 45 N	7	145 30 NE	29 24 SE		
55 67 S	7	145 30 NE	67 71 SE		
45 70 S	7	145 30 NE	57 68 SE		
50 72 S	7	145 30 NE	60 72 SE		
47 65 S	7	145 30 NE	62 65 SE		
53 65 S	7	145 30 NE	66 68 SE		
40 12 NE	8	130 12 S	94 14 NE	110 90	
30 90 N	8	130 12 S	30 84 NW	120 90	
150 12 S	8	138 12 S	54 3 NW		
150 90 S	8	138 12 S	150 78 SW		
140 76 S	8	138 12 S	140 64 SW		
22 28 W	8	138 12 S	46 25 NW		
24 90 NE	8	138 12 S	25 83 NW		
24 90 NE	8	138 12 S	50 90 NW		
	8	142 14 S		30 90	
	8	142 14 S		60 90	
	8	142 14 S		50 70 S	

Table 6.2. Raw and backtilted data of bedding (So), tectonic stylolites (TS) and fractures, according to their locations (i.e. from 1 to 8, Figure 6.2). Yellow-highlighted raw data corresponds to the post-folding fractures; green-highlighted data consists of TS 1 interpreted as pre- to syn-folding. The blue colour data shows TS, interpreted as post-folding but where the timing is not constrained. They probably reflect a syn-folding development.

During the late stage, the anticline developed an asymmetric structure (Figure 6.3), characterised by a subvertical and partly overthrust eastern flank. FRACT7 likely developed along this main fault to accommodate the folding.

6.3- Paleofluid characterisation

Several generations of calcite cements have been identified in the anticline. However, a precise chronology of the pre-folding stage could not be

established due to the lack of cross-cutting relationships between cements. Consequently, an attempt was made to resolve this problem by using other parameters, such as geochemical data, e.g. Sr-isotopes, and deformation features (e.g. calcite twins).

According to these methods, five different cement types have been distinguished. A relative timing of the different vein types and fractures compared to the tectonic evolution of the Saranda anticline is given in the Table 6.3.

Generation	Fracture generation	Timing	
Cal-1	FRACT1; FRACT2	Pre-folding	Flexure
Cal-2	FRACT1; FRACT2; FRACT4	Pre- to syn-folding	Onset of the folding or/and NW-SE compression
Cal-3	FRACT2; FRACT5; FRACT6	Syn-folding	Accommodation of the folding
Cal-4; Cal-5	FRACT1; FRACT2; FRACT4; FRACT5; FRACT6	Syn- to post-folding	

Table 6.3. Relative timing of the different vein generations compared to fracture sets, principally based on cross-cutting relationships.

6.3.1- Petrography and structural data

6.3.1.1- Cal-1 cement

The first vein generation, henceforth called Cal-1, precipitates in subvertical NNW-SSE oriented-fractures, i.e. FRACT1 and FRACT2. The veins are on average 0.2 to 1.5 cm wide. They crosscut and are sometimes cut by compactional stylolites, implying their synchronous development.

Cal-1 cement consists of blocky to elongated calcite crystals, ranging in size from 50 to 600 μm (Figure 6.13H). Calcite crystals are characterised by a minor content of iron, attested by the blue staining. They also are characterised by a strong development of twins (Figure 6.13F to H). Two sets of twins, which are classified as type I (Burkhard, 1993; Ferrill et al., 2004), have been distinguished in Cal-1 crystals: a first set is characterised by few thick twins (Figure 6.13H), whereas the second set demonstrates thinner and numerous twins, as shown in Figure 6.13G. Cal-1 displays a typical pattern of recrystallisation under CL, characterised by disorganised dull to non-luminescent areas (Figure 6.13C and D). Where the crystals are not recrystallised, they exhibit a non-contrasted zoning from dull to orange luminescence, which likely corresponds to the initial texture of the Cal-1 crystals (Figure 6.13A and B, E).

6.3.1.2- Cal-2 cement

Cal-2 cement occurs in FRACT1, FRACT2 and FRACT4 and postdates the N170°-oriented

tectonic stylolites (pre-folding TS). Usually the veins have a size varying from 0.3 to 1.2 cm and calcite crystals range in diameter from 80 to 500 μm . This cement generation has been encountered in both flanks of the anticline, but not along its hinge. Cal-2 cement is characterised by elongated to blocky calcite crystals (Figure 6.14 A & B). These crystals are highly deformed, a feature that is pointed out by the occurrence of non-transparent calcite crystals, intense twinning planes of type I (Burkhard, 1993; Ferrill et al., 2004) and existence of many solid inclusions.

Nevertheless, this cement has similar petrographical characteristics than Cal-1 and is differentiated from the latter only by its CL characteristics. In fact, the centre of Cal-2 calcite crystals is recrystallised, while their borders possess a dull zoning. The recrystallised zone is characterised by a dull luminescence, with many scattered bright spots (Figure 6.14 C to F). Cal-2 vein contains also some barite crystals (BaSO_4 ; Figure 6.14 C & D), characterised by non-euhedral and non-luminescent crystals and quartz. According to these petrographical observations, Cal-1 and Cal-2 either correspond to two distinct cement generations, implying different timing, or they form a single cement generation, which has been subjected to different diagenetic processes (e.g. meteoric alteration, ...).

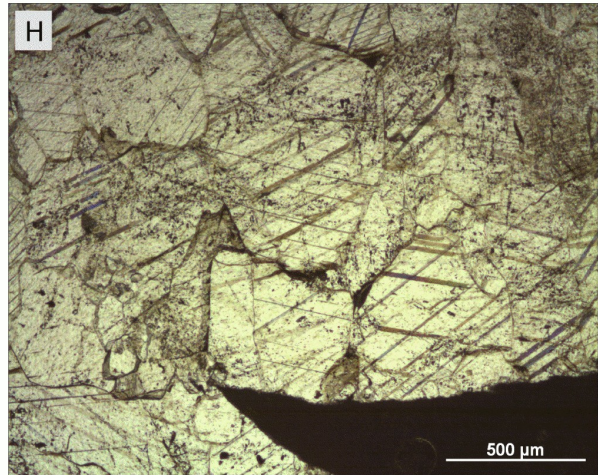
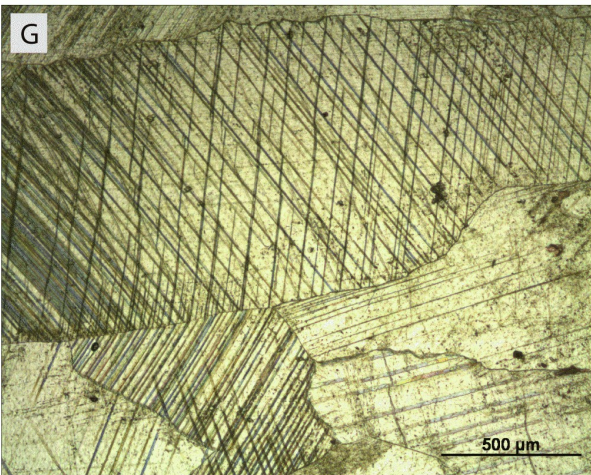
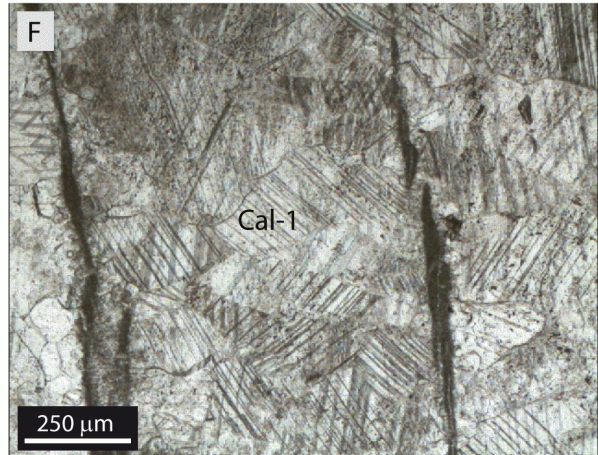
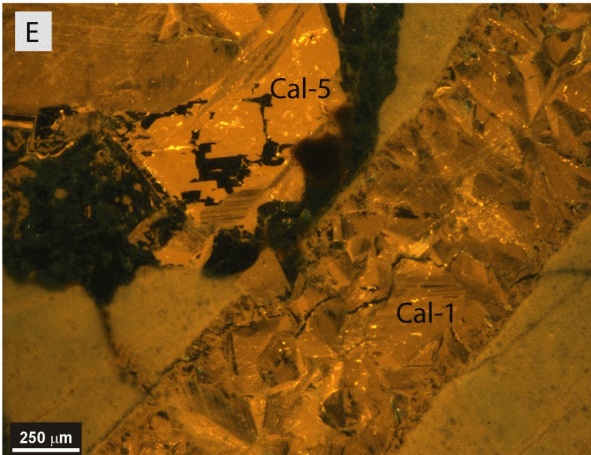
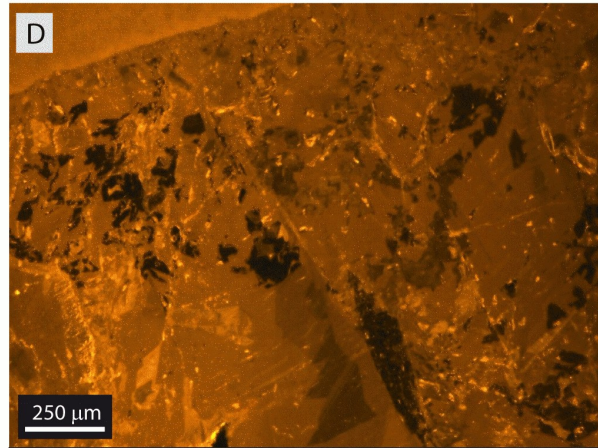
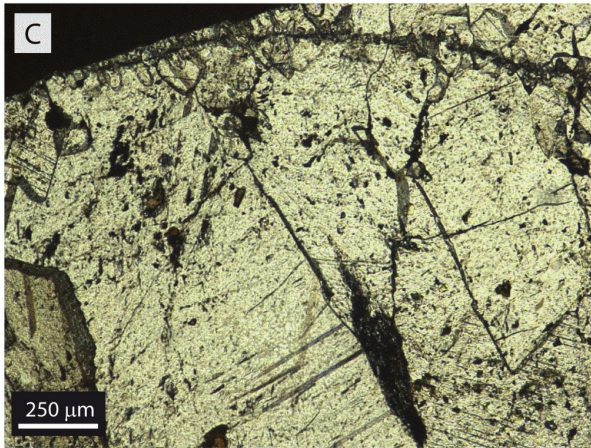
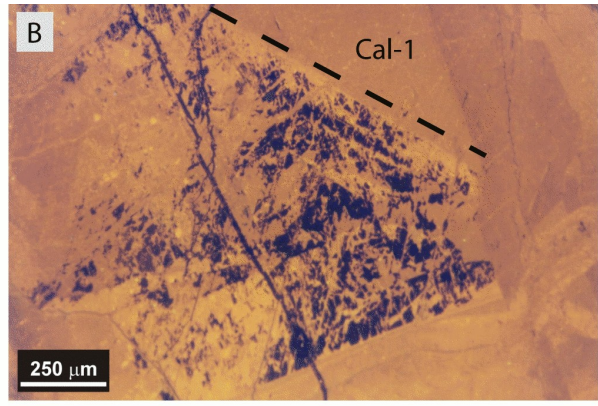
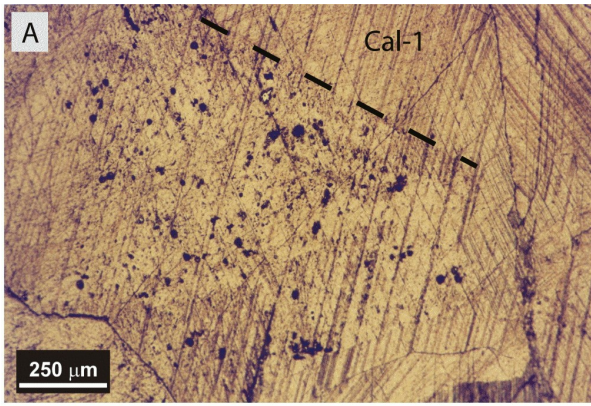


Figure 6.13. Photomicrographs of the Cal-1 cement: (A) and (B) Respectively transmitted light and CL views of recrystallised calcite crystals. Note the presence of a relic of zoned calcite pattern under CL. The twinning planes partially disappear in the recrystallised calcite, showing that recrystallisation likely postdates the twinning. (C) - (D) Respectively transmitted light and CL views of a typical recrystallised pattern of Cal-1 cement. (E) CL view of zoned-calcite with bright to dull luminescence; (F) Transmitted light view of highly twinned and deformed calcite crystals. The twins are closely spaced; (G) Detailed area, showing two sets of thin twinning planes in Cal-1; (H) Transmitted light view of calcite, displaying thicker and less numerous twins.

6.3.1.3- Cal-3 cement

Cal-3 has been exclusively detected in the Eocene interval located in the southern part of the anticline (i.e. location 6 on Figure 6.2). This cement occurs in FRACT2 (new fracturing stage) and oblique fractures, oriented NE-SW and NW - SE (i.e. FRACT5 and FRACT6) with respect to the hinge of the anticline. Cal-3 generation consists of thick veins, which have a size varying from 0.5 to 2 cm wide. These veins crosscut bedding parallel stylolites and are synchronous to N110°-oriented TS (Figure 6.15 E), based on their mutual crosscutting relationships.

Cal-3 cement consists of blocky to elongated calcite crystals. Compared to the previous cement generations, calcite crystals are transparent and display thin and closely spaced type I twinning planes as shown in the Figure 6.15 A & B. Locally, some crystals, which are located along stylolites or fractures, are more deformed, displaying thicker twins. Under CL, Cal-3 shows a dull to orange zoning, where the luminescence decreases towards the centre of the crystals (Figure 6.15 C & D). Cal-3 cement also encloses non-euhedral non luminescent barite crystals, which can make up 2% of the crystals.

6.3.1.4- Cal-4 cement

Cal-4 cement has been identified in all studied locations, but is more abundant along the anticline hinge. This cement is characterised by concentric bright to non-luminescent zoned calcites (Figure 6.16 C). Cal-4 precipitates in non-cemented fractures or upon Cal-1 (Figure 6.17 E) and Cal-2 cements, i.e. in reactivated fractures.

However, no irregular contact pointing to a stop in the cementation between Cal-1/Cal-2 and Cal-4 has been observed in transmitted light views (Figure 6.16 A-B & C-D). On scanning electron microscope, acicular calcite crystals of Cal-4 are growing on Cal-1 (Figure 6.18 B and C), suggesting an overgrowth precipitation.

6.3.1.5- Cal-5 cement

The last recorded vein generation corresponds to Cal-5 cements. As for Cal-4, Cal-5 cement has been identified in all studied locations. Cal-5 crystallises upon Cal-4 cement and consists of transparent and non-luminescent calcite crystals (Figure 6.16 E & F). In the Figure 6.18 B and C, the acicular and micrometric calcite crystals that precipitated upon Cal-1 and Cal-2 cements, are defined as being Cal-4 and Cal-5 cements. In detail, two sets of twinning are observed in Cal-4 and Cal-5 (see Figure 6.17 C-D (1st set) and A-B (2nd set)). The first set occurs in Cal-1 and Cal-4 cements and is not present in Cal-5 cement, which assumes a twinning predating the cementation of Cal-5 (i.e. the non-luminescent calcite). The second generation of twins displays thin and numerous twinning planes and occurs even in the Cal-5 cement, suggesting that it postdates the Cal-5 cementation. These observations point to a stop in the cementation between Cal-4 and Cal-5. Consequently, two twinning episodes, which relate to two tectonic deformation (i.e. the evolution of the folding episode), are recorded during the growth of the calcite crystals, as far as the second twin generation is not created by making the thin-sections.

Based on petrographical observations, five main cement generations have been identified in the Saranda anticline. Nevertheless, Cal-1 and Cal-2 likely can only be distinguished based on their state of recrystallisation and consequently likely correspond to a single cement generation. A second important point is the straight contact between Cal-1/Cal-2 and Cal-4/Cal-5 cements, suggesting a chemical evolution of the cement through time or two episodes of growth stages without existence of a corrosive episode. Moreover this evolution records the tectonic deformation from the twinning sets. Consequently, the chemical variations are likely governed by the evolution of the folding.

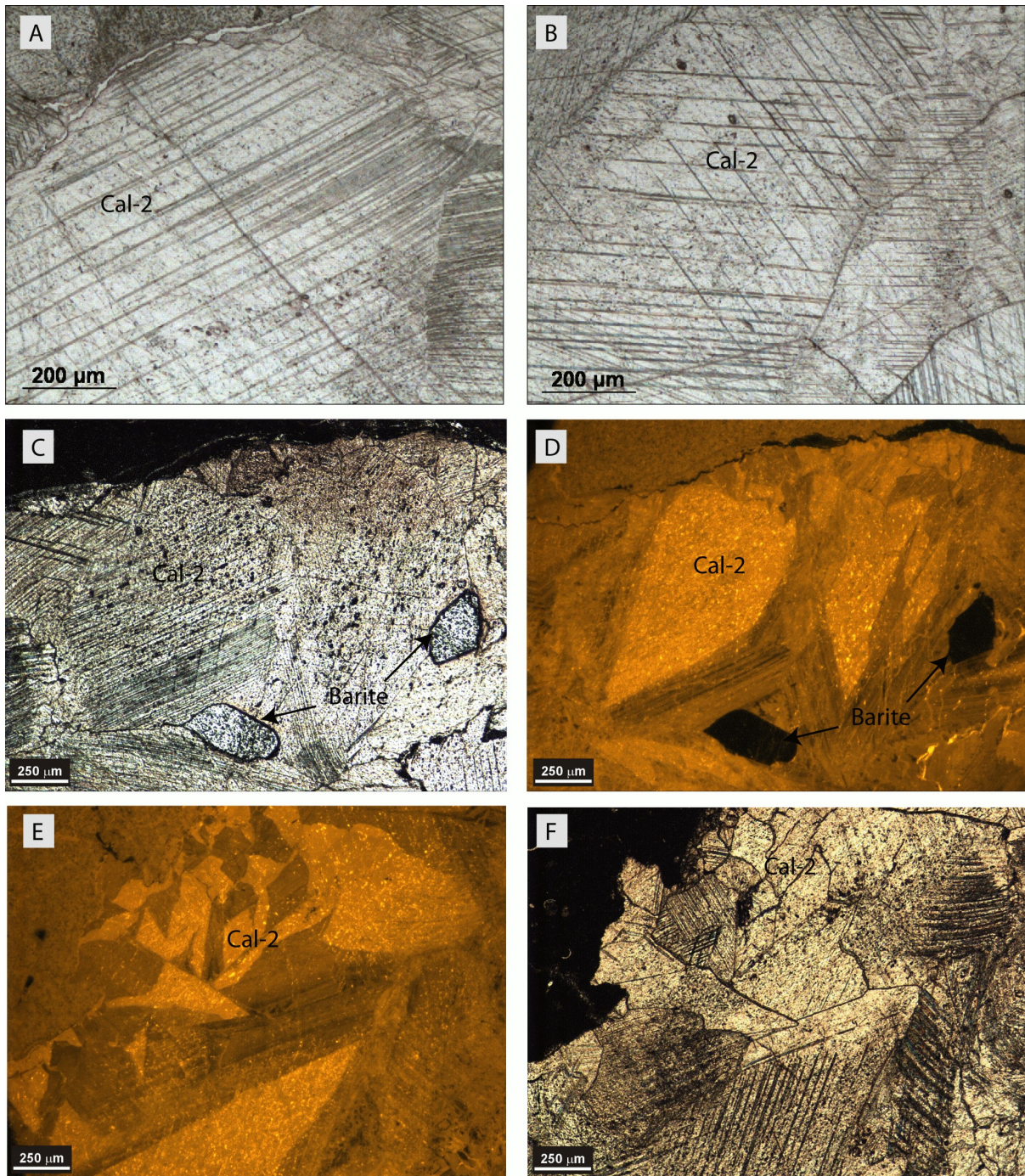


Figure 6.14. Photomicrographs of the Cal-2 cement: (A) and (B) Transmitted light views showing thin and numerous twinning planes in the calcite crystals; (C) and (D) Respectively transmitted light and CL views of the recrystallised Cal-2 cement. Notice that the centre of the crystals are more recrystallised than the border, which likely relates to differences in the initial composition; (E) and (F) Respectively CL and transmitted light views of Cal-2 cement, displaying a sector zoned pattern under CL. On the right side, the cement is more twinned along a reopening zone in Cal-2. The same observation has been encountered along tectonic stylolites. This process occurs due to pressure building afterwards.

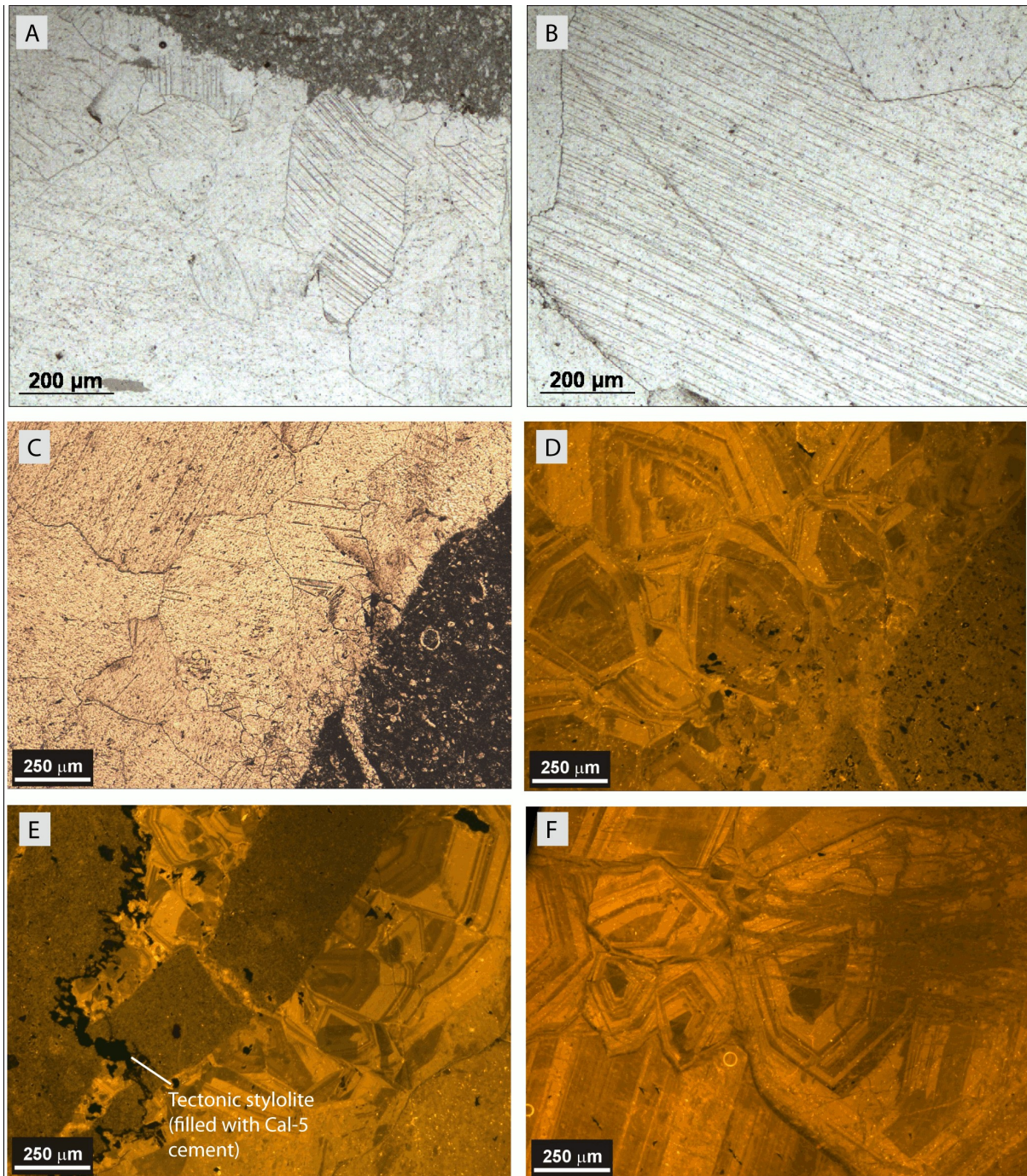


Figure 6.15. Photomicrographs of Cal-3 cement: (A) and (B) Transmitted light views of transparent calcite crystals, characterised by thin twinning planes; (C) and (D) Respectively transmitted light and CL views of Cal-3 cement, showing a characteristic dull to orange zoning. Notice that Cal-3 crystals are not or only weakly recrystallised; (E) CL view of N110° oriented tectonic stylolitic planes, filled with Cal-5 cement, crosscutting Cal-3 cement; (F) CL view of Cal-3 predating undefined dull luminescent calcite vein.

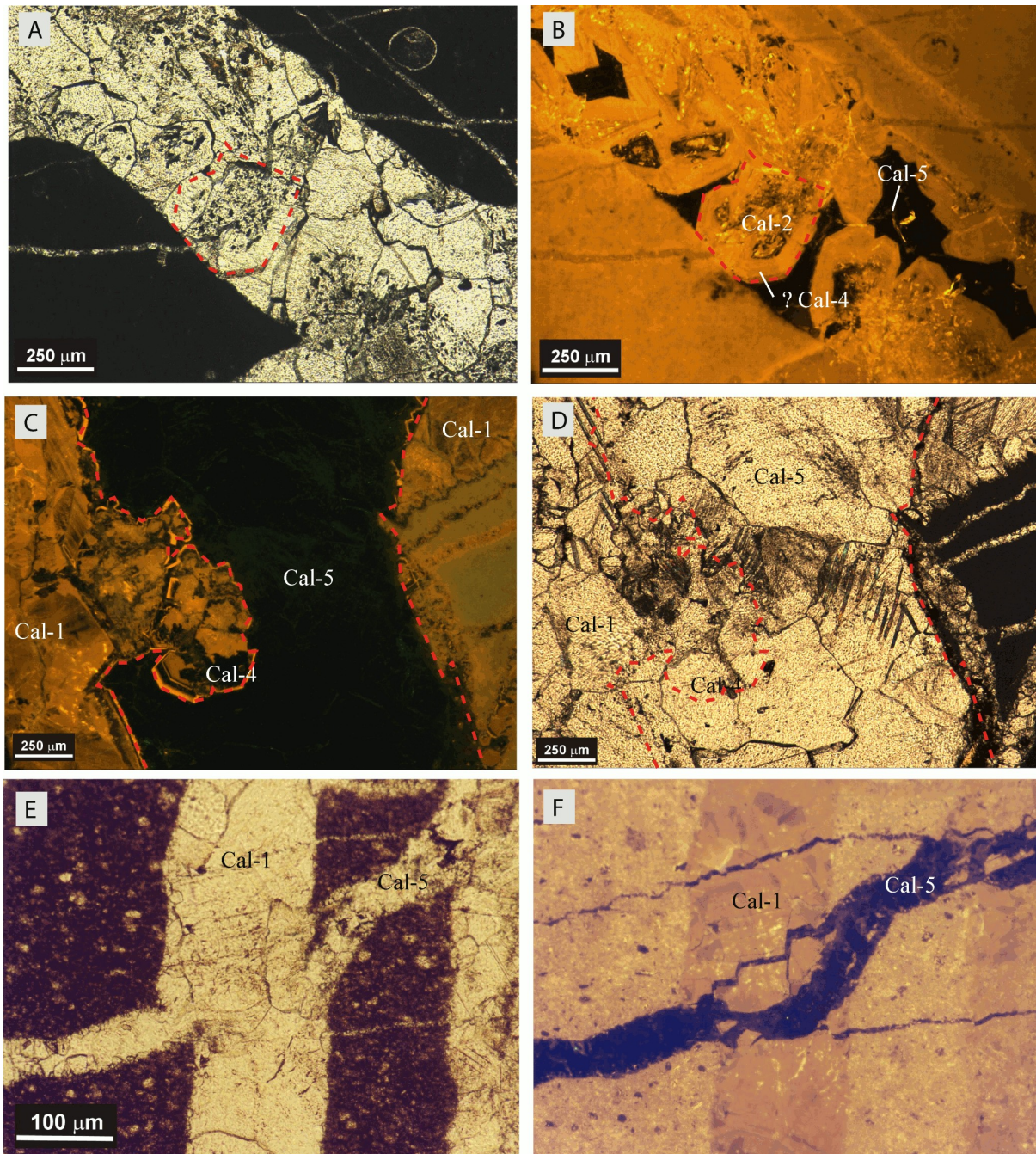


Figure 6.16. Photomicrographs of Cal-4 and Cal-5 cements: (A) and (B) Transmitted light and CL views of a continuous precipitation from Cal-2, overgrown by Cal-4 and Cal-5, without any corrosive contact between these cement generations. Cal-2 is highly recrystallised compared to the later cements. (C) and (D) Respectively CL and transmitted light views of Cal-4, precipitating upon Cal-1. Here, Cal-1 is highly recrystallised. (E) and (F) Respectively CL view of Cal-5 vein crosscutting Cal-1 vein. Both cements occur in different oriented fractures, i.e. in FRACT2 (Cal-1) and FRACT6 (Cal-5).

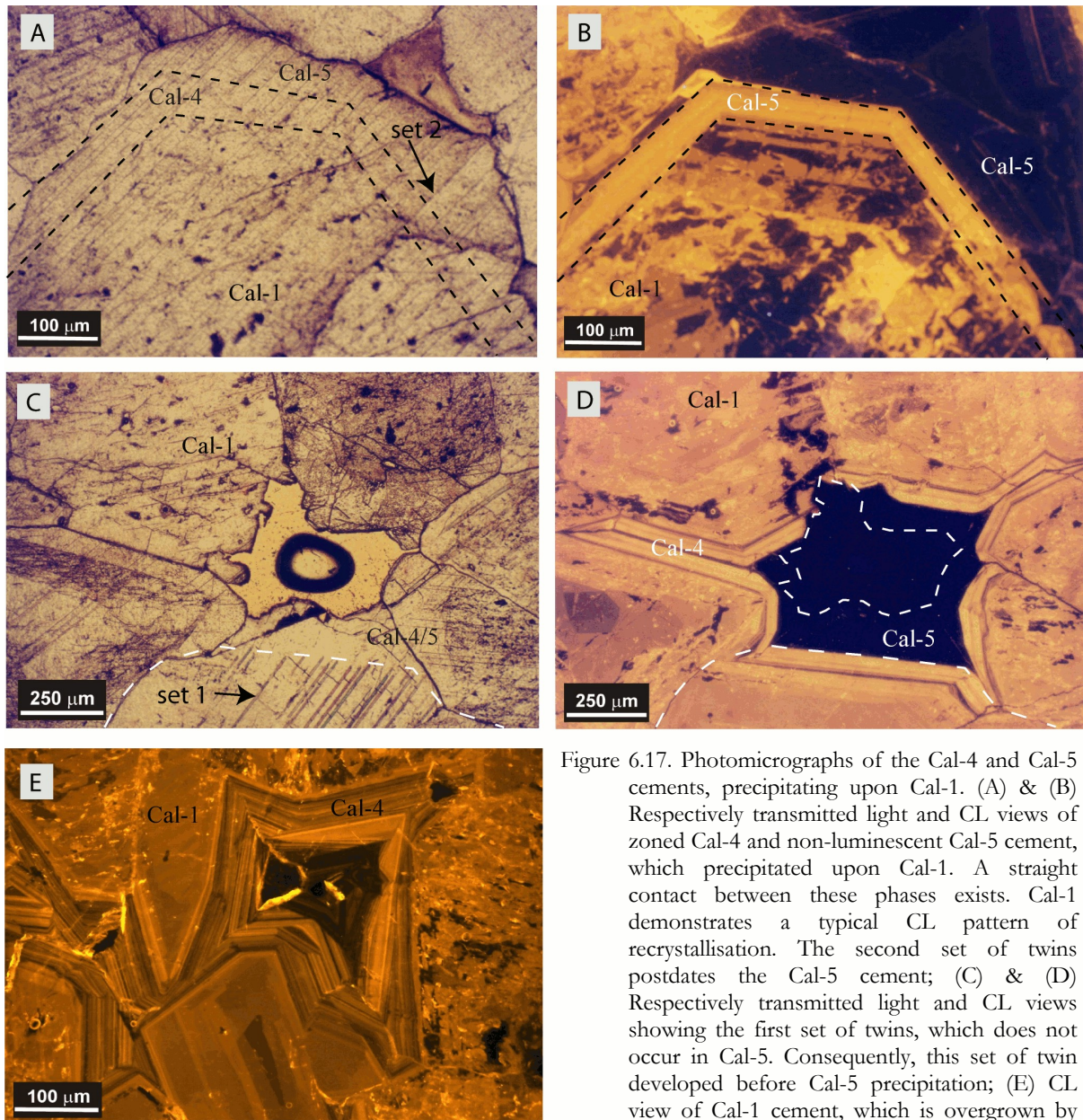


Figure 6.17. Photomicrographs of the Cal-4 and Cal-5 cements, precipitating upon Cal-1. (A) & (B) Respectively transmitted light and CL views of zoned Cal-4 and non-luminescent Cal-5 cement, which precipitated upon Cal-1. A straight contact between these phases exists. Cal-1 demonstrates a typical CL pattern of recrystallisation. The second set of twins postdates the Cal-5 cement; (C) & (D) Respectively transmitted light and CL views showing the first set of twins, which does not occur in Cal-5. Consequently, this set of twin developed before Cal-5 precipitation; (E) CL view of Cal-1 cement, which is overgrown by Cal-5 cement.

6.3.2- Stables isotopes

In the Figure 6.19, the carbon and oxygen isotope values of the Upper Cretaceous to Eocene limestones and of the different diagenetic phases previously described are given. According to Veizer et al. (1999), marine values for the Upper Cretaceous to Eocene display $\delta^{18}\text{O}$ between -2 and +0.1‰ V-PDB and $\delta^{13}\text{C}$ from +0.5 and +3‰ V-PDB. The studied Upper Cretaceous to Eocene host-rocks in the Saranda anticline have $\delta^{18}\text{O}$ values varying between -2.28 and -0.88 ‰ V-PDB and $\delta^{13}\text{C}$ ranging from +1.60 and +2.82 ‰ V-PDB, which is consistent with the marine signature, described by Veizer et al. (1999). Only one sample, characterised by a

highly recrystallised matrix (i.e. Upper Cretaceous carbonates located in the topographic top of the anticline), plots outside the marine signature.

The first generation of cement has been subdivided into two groups, i.e. Cal-1.1 and Cal-1.2, according to their geographical locations in the anticline. Cal-1.1 was sampled in Kakomere and along the fold hinge (location 1 and 7, Figure 6.2) and Cal-1.2 in the quarries, i.e. locations 3 and 4 (Figure 6.2).

The isotopic signature of the Cal-1.1 cement displays $\delta^{18}\text{O}$ and $\delta^{13}\text{C}$ varying respectively between -3.23 to -1.48 ‰ V-PDB and from +0.94 to +2.19‰ V-PDB. $\delta^{13}\text{C}$ values are similar

to those of the host-rock, suggesting a likely host-rock buffering. The $\delta^{18}\text{O}$ signature is slightly lower than the signature of the host-rock. The second group, i.e. Cal-1.2, exhibits a large spread in $\delta^{18}\text{O}$, displaying values from -5.75 to -1.48‰ V-PDB and $\delta^{13}\text{C}$ values, plotting from +0.82 to +2.15 ‰ V-PDB. Cal-2 cement possesses much lower $\delta^{18}\text{O}$ values from -10.90‰

to -7.40‰ V-PDB and still homogeneous $\delta^{13}\text{C}$ values varying between -0.16‰ and +2.47‰ V-PDB, which are similar to those of the host-rock. That suggests likely host-rock buffering. The next cement, i.e. Cal-3, shows the most negative $\delta^{18}\text{O}$ values varying from -13.08 to -10.21‰ V-PDB and still uniform $\delta^{13}\text{C}$ -values, varying between +1.28 and +2.85 ‰ V-PDB.

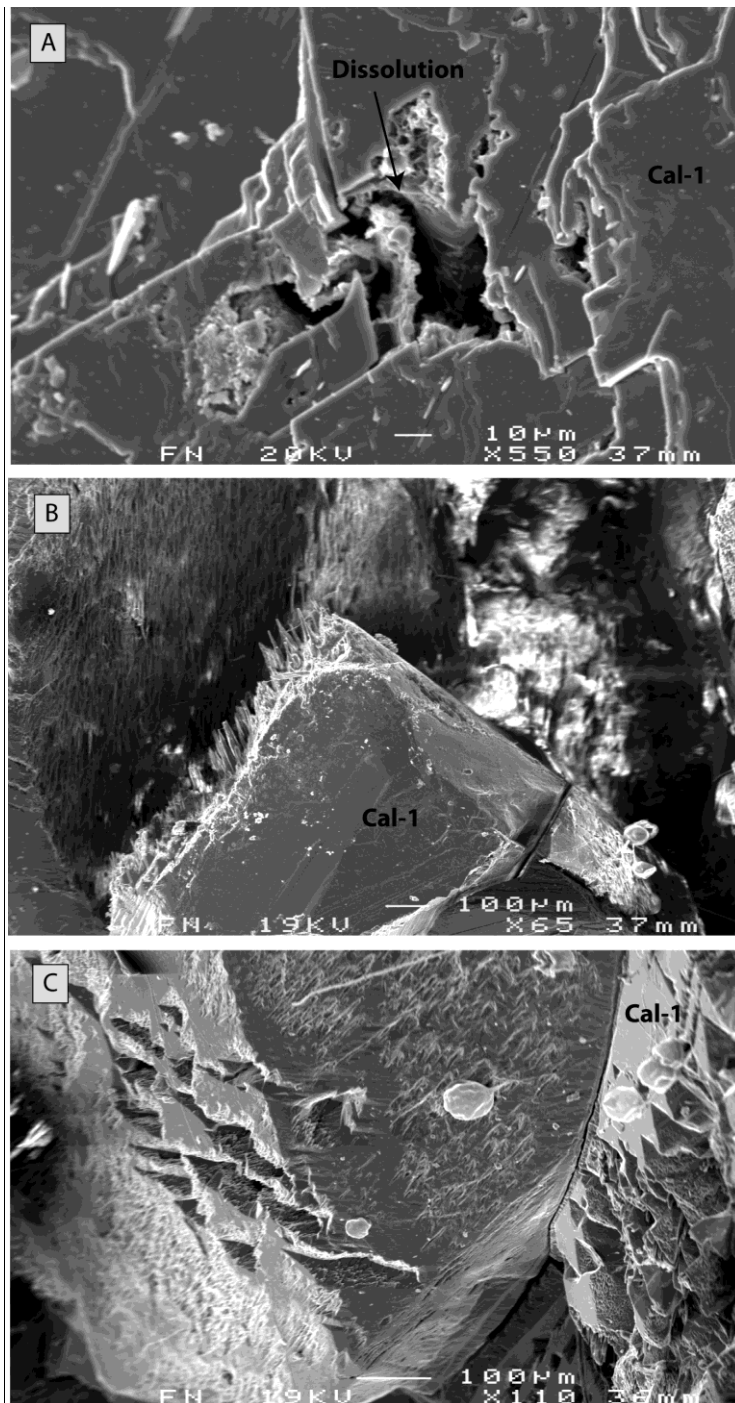


Figure 6.18. Backscattered electron images of the Cal-4 and Cal-5 cements, which precipitate upon Cal-1 and Cal-2 cements: (A) Partial dissolution of the Cal-1 cement; (B) – (C) Acicular and micrometric calcite crystals (likely Cal-5 cement), which precipitate upon Cal-1 calcite crystals.

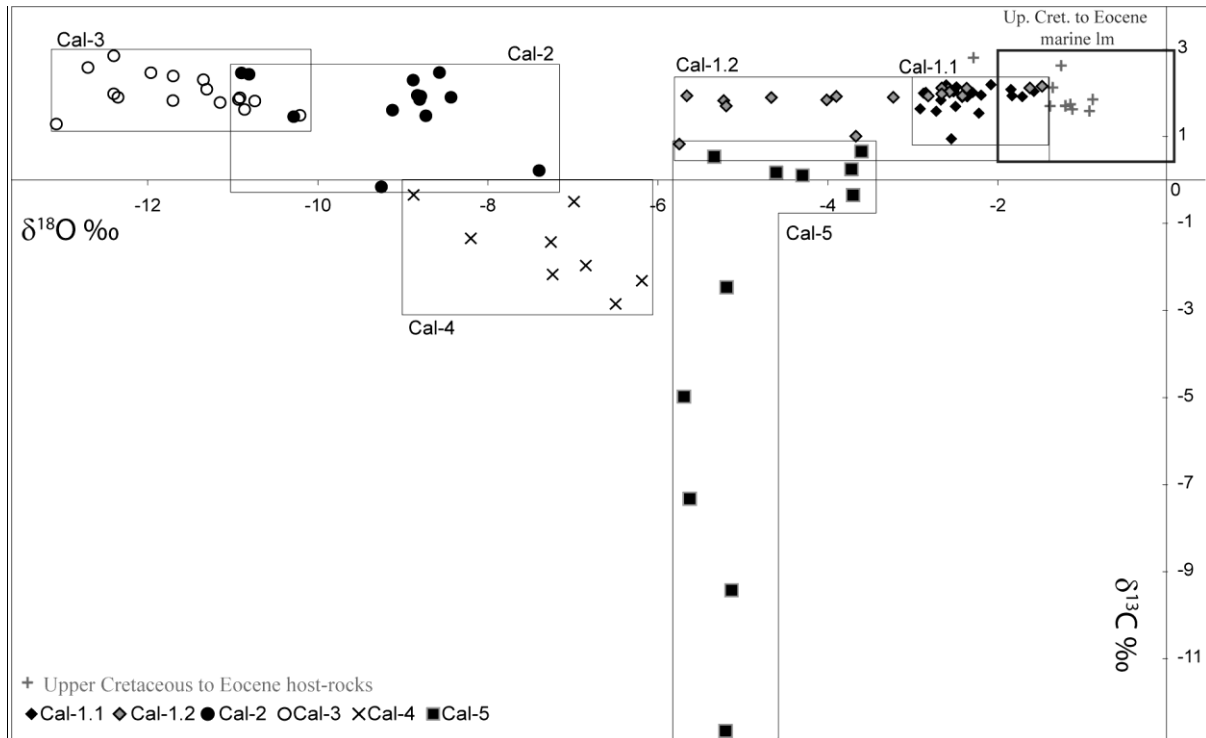


Figure 6.19. Carbon and oxygen isotopic crossplot with compositions of the Upper Cretaceous-Eocene limestones and their diagenetic products from the Saranda anticline study area.

In contrast to the above mentioned cements, Cal-4 and Cal-5 display principally negative $\delta^{13}\text{C}$ values. Cal-4 possesses $\delta^{13}\text{C}$ signatures from -2.85 to -0.35‰ V-PDB and depleted $\delta^{18}\text{O}$, varying between -8.87 and -6.19‰ V-PDB. The last cement, i.e. Cal-5, displays the most negative and large trend in $\delta^{13}\text{C}$, characterised by values from -12.66 to +0.66‰ V-PDB. The $\delta^{18}\text{O}$ signature plots in a relatively narrow range from -5.69 to -3.61‰ V-PDB.

6.3.3- Elemental geochemistry

The content of major and minor elements of the vein-fillings was determined by using the microprobe and by Absorption Atomic Spectroscopy (AAS). In Table 6.4, the maximum, minimum and average values of the studied cements correspond to measurements realised with the microprobe. The totality of the measurements, derived from microprobe or AAS analyses, are listed in ppm respectively in the Table 6.5 and able 6.6.

Since the veins contain mostly calcite crystals, no significant difference exists between the results acquired by both techniques, i.e. AAS and microprobe. Consequently, AAS data will be used to determine the composition of the main veins, whereas microprobe analyses will help to

study Cal-4 and Cal-5, since they usually occur scattered in small areas.

Cal-1 is characterised by variable to high-content in Mg with values up to 1638 ppm (cf. AAS analyses) and an average of 1497 ppm (cf. AAS analyses). The Sr-content is on average 364 ppm. The Fe-content averages 337 ppm (cf. AAS). In detail, Cal-1.1 and Cal-1.2 are distinguished by their Fe-, Sr- and Mn-contents. Cal-1.1 has higher Fe-, Sr- and Mn-contents, with values respectively up to 1620, 1420 and 600 ppm, whereas Cal-1.2 shows only values below the detection limit. On the contrary, Cal-1.2 is more rich in S, with values up to 310 ppm.

The elemental composition of Cal-2 is similar to that of Cal-1 with a Mg-content varying around 1540 ppm, variable Fe-content between 57 to 317 ppm, but locally values up to 1850 ppm have been measured. Only the Sr-content allows to some extent to distinguish Cal-1 to Cal-2. Sr-content of Cal-2 varies from 333 ppm to 1549 ppm (cf. AAS), but can reach locally up to 6140 ppm. The Cal-3 cement is characterised by high Mg-content generally up to 1729ppm and relatively high Sr-content, which can reach up to 1128 ppm (cf. AAS analyses). This cement displays also a Fe-content that is characterised by

values between 216 to 524 ppm and higher Mn values varying around 420 ± 20 ppm.

The two last cements, i.e. Cal-4 and Cal-5, geochemically differ from the previously analysed cements, especially with regard to their Mg- and Fe-contents. Only microprobe measurements will be interpreted for these two cements. Cal-4 has variable Mg-content, with values below the detection limit in non-luminescent (NL) areas and up to 2790 ppm in bright luminescent zones. Fe-content varies from below the detection limit, in bright luminescent calcite, up to 6260 ppm in NL calcite. Si-content is high with values varying from below the detection limit to 1690 ppm. Cal-5, which consists of non-luminescent calcite, has the same characteristics than the non-luminescent areas in

Cal-4. It is characterised by low Mg-content, with a maximum of 450 ppm, and Fe-, Mn- and Sr-contents below the detection limit. Cal-5 possesses a Si-content of ~220 ppm.

6.3.4- Strontium isotopes

To determine the timing of marine cementation or to define possible fluid interactions with surrounding carbonates or exotic rocks, 7 samples of calcite cements were analysed for their $\text{Sr}^{87}/\text{Sr}^{86}$ ratio. The data are given in the Table 6.7.

The Sr-signatures are indicated in the Figure 6.20, where the $\text{Sr}^{87}/\text{Sr}^{86}$ secular trend, compiled from McArthur and Howarth (2004), is plotted against time.

Filling stage		Mg	Ca	Fe	Mn	S	Si	Sr
Cal-1.1	Min	510	401470	< dl				
	Max	3990	418550	1620	600	< dl	210	1420
	Average	2183	411849	511	94	< dl	112	142
Cal-1.2	Min	370	405620	< dl				
	Max	3330	408140	< dl	< dl	310	310	< dl
	Average	1537	407377	< dl	< dl	103	170	< dl
Cal-2	Min	1250	400180	< dl				
	Max	2620	400970	1850	< dl	< dl	200	6140
	Average	1935	400575	925	< dl	< dl	100	3070
Cal-3	Min	800	402970	< dl				
	Max	3220	410330	1150	340	< dl	210	< dl
	Average	2258	406617	342	57	< dl	78	< dl
Cal-4	Min	< dl	388580	< dl				
	Max	2790	431000	6260	1130	930	1690	< dl
	Average	1083	412585	888	171	186	284	< dl
Cal-5	Min	< dl	404220	< dl	< dl	< dl	50	< dl
	Max	450	420860	< dl	< dl	< dl	660	< dl
	Average	140	412572	< dl	< dl	< dl	220	< dl

Table 6.4. Minimum, maximum and average data for the major, minor and trace elements in ppm based on microprobe analysis of the main diagenetic phases in the Saranda anticline. Values below the detection limit are indicated with <dl.

Stage	Mg (ppm)	Ca (ppm)	Fe (ppm)	Mn (ppm)	S (ppm)	Si (ppm)	Sr (ppm)
Cal-1.1 (n=10)	510	417530	<dl	<dl	<dl	170	<dl
	950	413310	940	<dl	<dl	160	<dl
	1340	414150	<dl	340	<dl	210	1420
	1470	418550	580	<dl	<dl	110	<dl
	1870	405160	<dl	<dl	<dl	200	<dl
	2160	413970	<dl	<dl	<dl	160	<dl
	3020	412410	1450	<dl	<dl	<dl	<dl
	3230	409600	1620	<dl	<dl	50	<dl
	3290	401470	520	<dl	<dl	<dl	<dl
	3990	412340	<dl	600	<dl	60	<dl
Cal-1.2 (n=3)	370	408140	<dl	<dl	<dl	300	<dl
	910	408370	<dl	<dl	310	<dl	<dl
	3330	405620	<dl	<dl	<dl	210	<dl
Cal-2 (n=2)	1250	400180	<dl	<dl	<dl	<dl	6140
	2620	400970	1850	<dl	<dl	200	<dl
Cal-3 (n=6)	800	408710	<dl	<dl	<dl	<dl	<dl
	1870	406170	<dl	<dl	<dl	<dl	<dl
	2190	410330	900	<dl	<dl	<dl	<dl
	2270	405020	<dl	<dl	<dl	180	<dl
	3200	402970	1150	<dl	<dl	80	<dl
	3220	406500	<dl	340	<dl	210	<dl
Cal-4 (n=15)	2790	388580	5040	650	930	1690	<dl
	2640	393800	6260	780	790	580	<dl
	2920	403700	490	<dl	<dl	310	<dl
	2120	409820	<dl	1130	<dl	270	<dl
	1770	413100	<dl	<dl	460	<dl	<dl
	1140	415150	1530	<dl	610	<dl	<dl
	1040	409380	<dl	<dl	<dl	280	<dl
	670	414600	<dl	<dl	<dl	330	<dl
	470	425320	<dl	<dl	<dl	200	<dl
	370	408260	<dl	<dl	<dl	50	<dl
	210	414610	<dl	<dl	<dl	270	<dl
	110	431000	<dl	<dl	<dl	120	<dl
	<dl	426230	<dl	<dl	<dl	60	<dl
	<dl	424470	<dl	<dl	<dl	100	<dl
	<dl	410760	<dl	<dl	<dl	<dl	<dl
Cal-5 (n=6)	<dl	420860	<dl	<dl	<dl	90	<dl
	<dl	408980	<dl	<dl	<dl	50	<dl
	<dl	404220	<dl	<dl	<dl	660	<dl
	<dl	416340	<dl	<dl	<dl	140	<dl
	390	416220	<dl	<dl	<dl	200	<dl
	450	408810	<dl	<dl	<dl	180	<dl

Table 6.5. Major, minor and trace element data in ppm, measured with microprobe. Values below the detection limit are indicated with "<dl".

Stages	Ca	Al	Sr	Mg	Fe	Mn	K
Cal-1	387 841	150	206	1638	408	293	94
	371 658	132	523	1356	265	475	40
+Cal-5	380 448	128	154	548	350	218	36
Cal-2	373 696	151	333	918	317	280	49
	381 416	119	1549	1253	57	294	77
Cal-3	331 560	137	1128	1218	524	415	54
	385 388	149	325	1729	216	427	58
Cal-4/5	371 066	178	259	1377	393	262	93
	372 903	205	331	1132	248	232	62
Recrystallised matrix	247 693	330	337	1697	255	524	84

Table 6.6. Major, minor and trace element data in ppm of the main recorded cement generations, based on AAS analyses.

The Sr^{87}/Sr^{86} ratio of the Cal-1.1 cement, which occurs in the Upper Cretaceous interval, possesses values from 0.707773 to 0.707814. Cal-1.2 cement, which precipitates in the Eocene interval, displays lower Sr^{87}/Sr^{86} ratios, averaging 0.707758. Cal-2 cement, sampled in the Upper Cretaceous interval, is characterised by a Sr^{87}/Sr^{86} value, reaching 0.707851. Finally, Cal-3 is also coming from the Eocene interval and displays a Sr^{87}/Sr^{86} ratio of 0.707801.

The Sr^{87}/Sr^{86} signature of the Upper Cretaceous to Eocene marine water and related carbonates precipitates fluctuates through time within the same range, hampering the interpretation of the vein-filling Sr-signatures. According to Swennen et al. (1998), the syn-deformational period in the Ionian zone is dated as post-Oligocene onward, thus some of the cements could reflect a marine post-Oligocene composition.

Samples	Sr^{87}/Sr^{86}	Standard error
Cal-1.1	0.707773	0.000014
	0.707791	0.000015
	0.707814	0.000021
Cal-1.2	0.707759	0.000011
Cal-1.2 + Cal-4 + Cal-5	0.707757	0.000013
Cal-2 + Cal-4 + Cal-5	0.707851	0.000014
Cal-3	0.707801	0.000012

Table 6.7. Sr^{87}/Sr^{86} ratio of some vein-filling cements from the Saranda anticline.

The Sr^{87}/Sr^{86} signatures of the calcite cements plot in the Upper Cretaceous – Early Oligocene marine interval (Figure 6.20), attesting either of a cementation during the pre-deformational stage or a possible host-rock buffering of the fluids.

Cal-1.1, Cal-1.2 and Cal-3 cements possess a Sr-signature similar to the Upper Cretaceous - Eocene marine water (McArthur and Howarth, 2004). Cal-2 displays a higher ratio, fitting with the Late Cretaceous and the Early Oligocene

marine water or with a fluid, which had a higher radiogenic contribution.

However, all these vein-fillings display a rather similar Sr-signature than their surrounding rock matrix, accounting for a host-rock buffering of the fluids: Cal-1.1 and Cal-2 have a similar Sr^{87}/Sr^{86} signature than Upper Cretaceous marine carbonates; Cal-1.2 and Cal-3 cements display more the Sr^{87}/Sr^{86} signature of the Eocene marine carbonates.

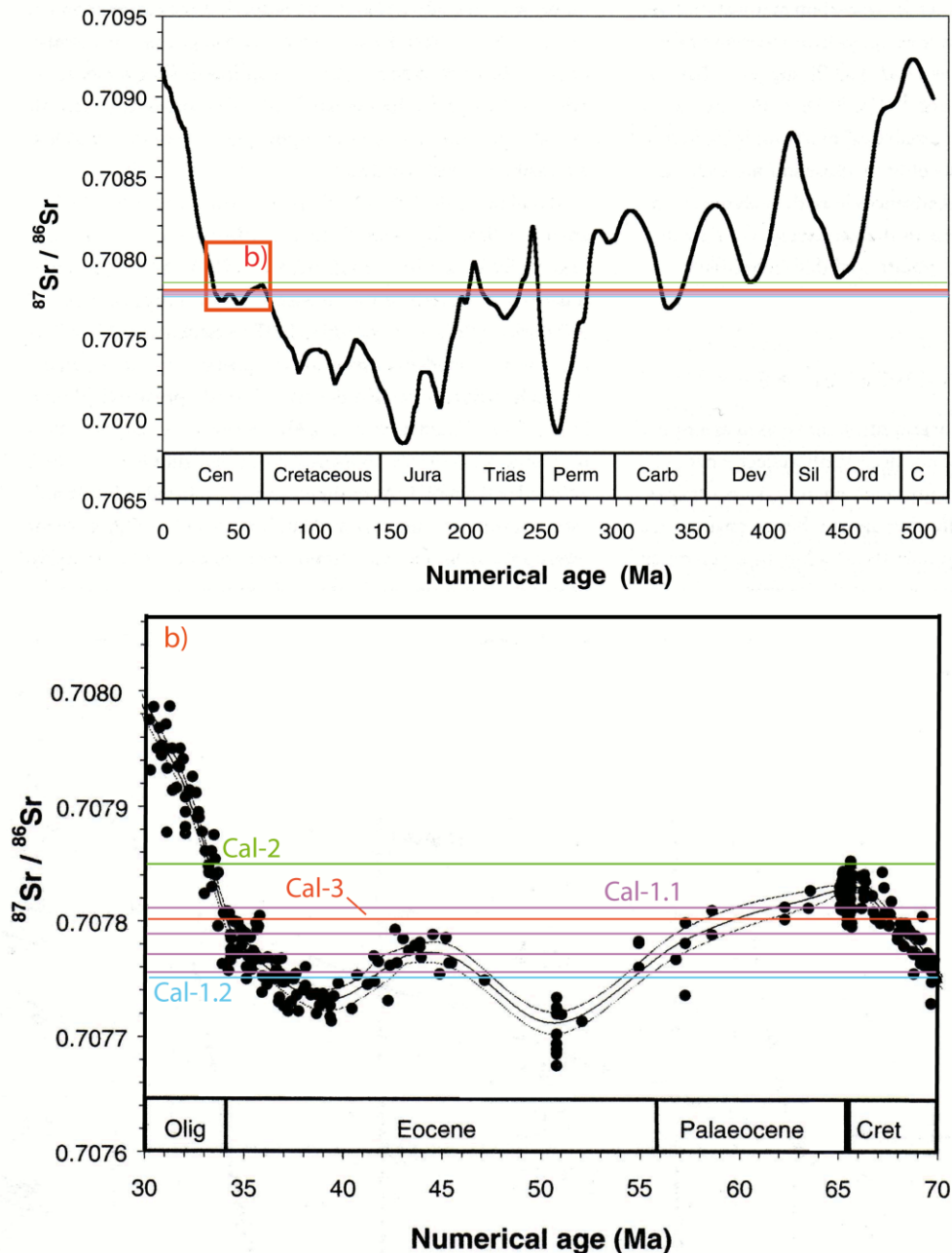


Figure 6.20. Plots of $\text{Sr}^{87}/\text{Sr}^{86}$ secular variation and Sr-isotopic composition of the vein infillings (i.e. Cal-1.1; Cal-1.2; Cal-2 and Cal-3). The secular trend is compiled after McArthur and Howarth (2004).

6.3.5- Fluid inclusions

In the case of the Saranda anticline, the fluid inclusion study was not successful, since the calcite cements are almost totally recrystallised. Only five FI, which were located in the recrystallised part of the Cal-1 and Cal-2 cements, could be analysed. Partial results are shown on the Table 6.8. In this case study, T_h measurements were stopped at 150°C , since the Saranda area has not been buried deeper than 2 km (Muska, 2002).

The measured fluid inclusions, situated along growth zones, have a rectangular shape and a size lower than $4\ \mu\text{m}$. T_h values vary principally from 128 to 141°C . However, 70% of the fluid inclusions were not analysed since no phase transition occurred below 150°C .

T_m values are very low and range from -1.1 to -0.2°C . According to the equation described by Bodnar (1993), these T_m -values correspond to salinities varying from 0.35 to 1.9 eq. wt.% NaCl. According to the FI location along growth zones, FI likely reflect the recrystallisation

conditions of the Cal-1 and Cal-2 cements. Moreover, that is in agreement with the various measured T_h , ranging from 128°C to 141°C, suggesting a necking down after a phase change.

These inclusions likely relate to a H₂O-(NaCl) fluid, characterised by low salinity.

Samples	T _m (°C)	T _h (°C)	Salinity (eq. wt.% NaCl)
SA04	-0.2	141	0.35
SA43	-1.1	135	1.9
SA08	-0.6	128	1.05
SA64	-0.3	-	0.53

Table 6.8. Melting temperature (T_m) and homogenisation temperature (T_h) in °C measured in Cal-1 and Cal-2 cements. The salinity, expressed in eq. wt.% NaCl, was calculated based on the equation described by Bodnar (1993).

6.4- Discussion

In the discussion, all petrographic and geochemical data are combined in order to characterise the fluids responsible for the successive cement generations. These results are summarised in the Table 6.9. A special attention will be paid to determine the timing of the diagenetic processes (Figure 6.21), since the successive generation of cement are likely associated to the folding evolution.

6.4.1- Paleofluid characterisation

6.4.1.1- Cal-1.1 cement

Cal-1.1 vein cemented N(N)W-S(S)E fractures, i.e. FRACT1 and FRACT2, is synchronously with the development of burial stylolites during the pre-folding stage. As Cal-1.1 occurs in FRACT1, this cement likely suggests precipitation during the regional flexuring of the foreland. Cal-1.1 is at present day almost totally recrystallised, as indicated by a typical recrystallised CL pattern of the calcite crystals.

The recrystallisation of the calcite crystals is in agreement with the spread of the T_h values, varying from 128 to 145°C. This trend possibly reflects partial decrepitation (stretching) of the inclusions either during heating (Bodnar and Bethke, 1984) or due to high pressure, developed during the folding stage or during uplift. This calcite is characterised by an intense twinning of the calcite crystals. According to calcite twin analysis, Cal-1.1 is associated to a N30° directed extension, which is likely responsible for the opening of the early FRACT1 and FRACT2. The

formation of these pre-folding veins can be attributed to overburden stress associated to the burial stage.

Concerning the C- and O-isotopic results, Cal-1.1 displays a $\delta^{13}C$ signature (+0.94 and +2.19‰ V-PDB), reflecting host-rock buffering. This host-rock buffering is in agreement with the Sr-isotopic signature of the Cal-1.1, which indicates also a fluid-rock interaction with the surrounding matrix. The depleted $\delta^{18}O$, with values ranging from -3.23 to -1.48‰ V-PDB, can be explained by a minor contribution of meteoric water or by a precipitation at higher temperature. Since no salinity data from fluid inclusions were gathered, a differentiation between both possibilities is not possible.

Geochemically, Cal-1.1 is characterised by an average 364 ppm of Sr and 1497 ppm of Mg, which possibly suggests a marine origin or fluid-rock interaction with marine sediments.

6.4.1.2- Cal-1.2 cement

Cal-1.2 precipitated in FRACT1 and FRACT2 during or after an extensive regime that was determined based on the calcite twins study (i.e. vertical maximum stress σ_1 and σ_3 perpendicular to the vein aperture; Lacombe et al., 2009).

Cal-1.2 formed synchronously to the development of burial stylolites, suggesting a cementation at a minimum depth averaging 500-700 m (Lind, 1993; Railsback, 1993; Nicolaides and Wallace, 1997; Drivet and Mountjoy, 1997; Duggan et al., 2001) and a maximum depth of 2 km during the pre-deformational stage.

Cements	Fracture generation	Petrographic characteristics				Geochemical characteristics						
		Classical microscope	CL	Twinning	Other minerals	$\delta^{18}\text{O} - \delta^{13}\text{C}$ (‰)	$\text{Sr}^{87} / \text{Sr}^{86}$	Mg (ppm)	Fe (ppm)	Mn (ppm)	Si (ppm)	Sr (ppm)
Cal-1.1	FRACT1-2	Elongated to blocky Fe-calcite crystals, many solid inclusions in recrystallised zones, small fluid inclusions	Recrystallised pattern and light zoning from orange to dull luminescence	Important Simple and double twin planes		$\delta^{13}\text{C} = 0.94$ to 2.19	0.707773 - 0.707814	548 - 1638	265 - 408	218 - 475	112 - 170	154 - 523
Cal-1.2						$\delta^{18}\text{O} = -1.48$ to -3.23						
Cal-2	FRACT1-2.4	Elongated to blocky non transparent calcite crystals, deformed and partially recrystallised (solid inclusions), small fluid inclusions	Recrystallised pattern (crystal centre) + light dull zoning	Important thin twins	Quartz, barite	$\delta^{13}\text{C} = -0.16$ to 2.47	0.707851	918 - 1253	57 - 317	280 - 294	100	333 - 1549
Cal-3	FRACT2-5.6	Elongated to blocky calcite crystals, important size, not deformed, no solid inclusions and few fluid inclusions	Zoning from dull to orange luminescence	Numerous thin twins	Barite	$\delta^{13}\text{C} = 1.28$ to 2.85	0.707801	1218 - 1729	216 - 524	415 - 427	78	325 - 1128
Cal-4	FRACT2-4-5-6	Blocky and transparent calcite crystals	Zoning from non- to bright- luminescence	Few thin twins; 2 different sets		$\delta^{13}\text{C} = -0.35$ to -2.85		1083	888	171	284	259 - 337
Cal-5		Block calcite crystals, transparent and few fluid inclusions	Non-luminescent	only one set of twin		$\delta^{18}\text{O} = -6.19$ to -8.87	$\delta^{13}\text{C} = 0.66$ to -12.66		0-450	< dl	< dl	220

Table 6.9. Summary of the petrographic, cathodoluminescence (CL) and geochemical data for the successive calcite cements. Minimum and maximum contents for Cal-1.1, Cal-1.2, Cal-2 and Cal-3 are measured by AAS. Measurements for Cal-4 and Cal-5 cements were made with microprobe.

The maximum depth is defined by the thickness of the pre-folding and post-Eocene deposits, which is of about 1.5-2 km in this area (Barrier et al., 2003). Cal-1.2 has only been determined in exploited quarries (i.e. locations 3 and 4) along the eastern border of the Saranda anticline.

Cal-1.2 has the same petrographical characteristics than Cal-1.1, but displays a distinct isotopic signature. Cal-1.2 exhibits a large spread in $\delta^{18}O$ with values ranging from -5.75 to -1.48‰ V-PDB. This spread in oxygen is either explained by the involvement of meteoric water, with possibly minor interaction with the host-rock or by a precipitation at higher temperature. $\delta^{13}C$ varies from +0.82 to +2.15‰ V-PDB, which is practically similar than the $\delta^{13}C$ of the surrounding carbonate matrix, thus also reflecting rock-buffering.

Geochemically, Cal-1.2 displays very low Sr-, Fe- and Mn-contents, with values below the detection limit, suggesting a possible meteoric origin. The Sr-content should come either from the recrystallisation process or from fluid interaction with marine sediments such as shaly beds, covering the Upper Cretaceous-Eocene intervals, i.e. the Oligocene flysch and Neogene molasse. This cement has also a low S-content, averaging 103 ppm and relatively high Mg-content of 1537 ppm. Cal-1.2 should have either a meteoric origin or could relate to a meteoric recrystallisation of marine cement.

Further to the previous description, no data allows separation of Cal-1.1 and Cal-1.2 in two different phases, since it is obvious that the precipitation temperature can vary for the same cement generation.

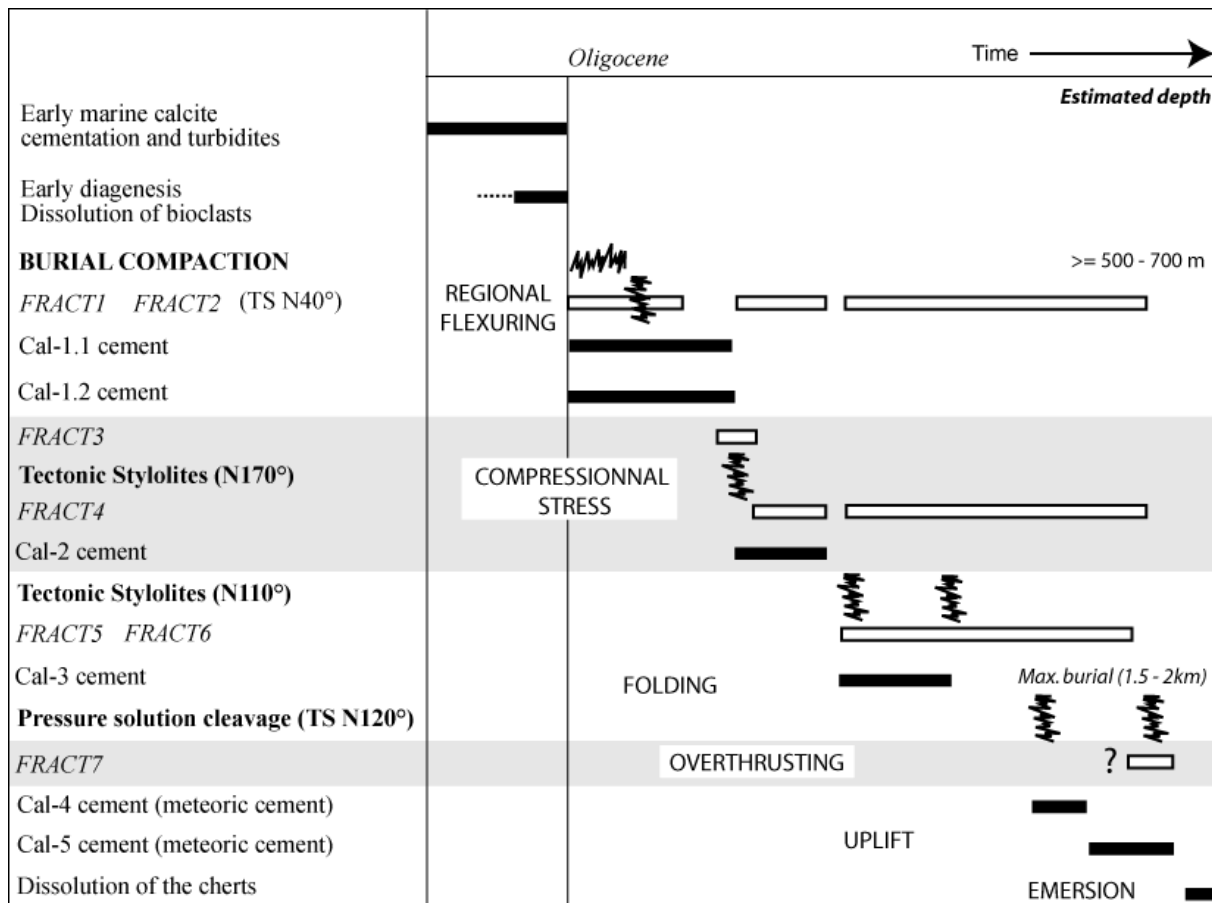


Figure 6.21. Paragenesis of the Upper Cretaceous-Eocene deep marine carbonates in the Saranda area. The depth for the maximum burial has been estimated based on the analysis of calcite twins. See text for explanation.

6.4.1.3- Cal-2 cement

Cal-2 precipitated in fractures parallel, i.e. FRACT1 and FRACT2, and perpendicular, i.e.

FRACT4, to the fold hinge during the pre- to syn-deformational stage (cf. backtilted data). This cement has been determined in the SW and the NE part of the anticline, i.e. locations 2 and

8. Cal-2 postdates the development of tectonic stylolites, oriented N170°, which point to the onset of the main compressive stress in the Ionian zone developing folds and thrusts.

Cal-2 is characterised by highly twinned and a recrystallised central part of the calcite crystals. Few barite crystals are associated with this calcite. The non-luminescent barite crystals are deformed and not euhedral, which suggests a transported origin. This likely points out a fluid migration pathway through the Neogene molasse, which reworked the barite crystals from the clay intervals. Based on the calcite twin study (Lacombe et al., 2008), it has been demonstrated that FRACT4 developed within a compressive regime, where the main stress σ_1 is oriented N80°. This tectonic event consists of the main NE-SW compression, which develops the NNW-SSE frontal thrusts and folding structures in the Albanides.

Concerning the isotopic signatures, Cal-2 displays a $\delta^{13}\text{C}$ signature varying between -0.16 and +2.47‰ and more depleted $\delta^{18}\text{O}$, with values ranging from -7.40 to -10.90‰ V-PDB. The $\delta^{13}\text{C}$ displays a similar signature than that of the surrounding carbonates, suggesting a host-rock buffering. The depleted O-signature likely reflects precipitation at a higher temperature. Regarding their elemental composition, Cal-1 and Cal-2 are practically similar, but diverge in their Sr-content. Cal-2 has high Sr-values, up to 1549 ppm (AAS analysis), suggesting a possible interaction with evaporitic layers, such as the Messinian or Triassic evaporitic interval or fluids that interacted with Sr-rich marine limestones.

Based on the reference data reported by McArthur and Howarth (2004), Cal-2 cement displays a nearly similar Sr-isotopic signature than the Upper Cretaceous and the Late Eocene marine waters (Figure 6.20). Since Cal-2 precipitated in FRACT4, developed during the deformational stage, i.e. post-Oligocene age, this signature could originate from a fluid interaction with one of both intervals, i.e. Upper Cretaceous and Late Eocene, or with a fluid, which had a higher radiogenic contribution, such as the Messinian interval, characterised by higher $\text{Sr}^{87}/\text{Sr}^{86}$ varying from 0.70885 to 0.7091 (i.e. Figure 5.20). This interaction may explain the relatively high Sr-content of the Cal-2 cement.

At present, no petrographical or geochemical data allow to determine the initial origin of the fluid, which precipitated Cal-2. However, if the

scenario implying an interaction with the Messinian interval is correct, Cal-2 should be dated as syn- or post-Pliocene. The other hypothesis, involving an interaction with the Triassic evaporites, is not yet proved, since no fluid-rock interaction with this interval has been evidenced, such as for example a buffering of the O- and Sr-isotopic signatures.

6.4.1.4- Cal-3 cement

The next cement, i.e. Cal-3, occurs in fractures developed parallel to the fold hinge, i.e. FRACT2, and oblique fractures, i.e. FRACT5 and FRACT6. It is therefore concluded that Cal-3 cementation formed during the folding stage. Notice that Cal-3 was only determined in the south-eastern part of the anticline, i.e. in location 5.

The Cal-3 vein formed synchronously with the N110°-oriented tectonic stylolites that developed during the syn-folding stage (6.2.2. Joint and fracture development). This is in agreement with the NE-SW compression and NE-SW extension recorded in FRACT4, as deduced from the calcite twin analyses (Lacombe et al., 2008). Here, the NE-SW compression relates to the main compression developing the thrusts and the folding in the Albanides. The NE-SW extension likely reflects the outer-rim extension during fold development. As a consequence, these fractures developed during the syn-deformational stage to accommodate the folding, as described in the model of Stearns and Friedman (1972).

Petrographically, Cal-3 cement is characterised by elongated to blocky non-recrystallised calcite crystals. Under CL, a dull to orange zoning occurs. The calcite crystals display also thin and numerous closely spaced type 1 twinning planes.

Cal-3 possesses the lowest $\delta^{18}\text{O}$ values, ranging from -10.21 to -13.08‰ V-PDB and a $\delta^{13}\text{C}$ signature, slightly higher than those of the surrounding matrix, varying from +1.28 to +2.85‰. This depleted $\delta^{18}\text{O}$ signature suggests an increase of the precipitation temperature and can be linked to the maximum burial, i.e. sedimentary and possible tectonic loadings.

Geochemically, Cal-3 cement has a Sr-content between 325 and 1128 ppm and a Mn-content between 415 and 427 ppm. At present, no data allows to precise this cement origin. Finally, this cement likely precipitated at a deeper level than the previous recorded cements, during the syn-

folding stage, likely due to the increase of the sedimentary and tectonic loading.

6.4.1.5- Cal-4 cement

Cal-4, which is encountered in all previous fractures, precipitated upon Cal-1 and Cal-2. A straight contact under CL occurs between Cal-1/Cal-2 and Cal-4, suggesting an overgrowth cement. These acicular calcite crystals (Figure 6.18 B and C) represent well-crystallised calcite aggregates that grew in open spaces, in the central part of some thick veins and in some cavities inside the veins.

Cal-4 is characterised by an intensely zoned luminescence pattern, with bright yellow and non-luminescent zones. The CL pattern is often interpreted as meteoric cements, which formed at shallow depth and low temperatures (Meyers, 1974, 1978; Grover and Read, 1983). The bright yellow luminescent zones could then reflect precipitation in a suboxic environment and the non-luminescent zone could have formed under oxic environment (Suchy et al., 2000). This suggests that the Saranda anticline has been uplifted and likely eroded before cementation took place.

Isotopically, Cal-4 displays a depleted $\delta^{13}\text{C}$ signature, varying from -2.85 to -0.35‰ V-PDB, and a negative $\delta^{18}\text{O}$ signature, ranging between -8.87 and -6.19‰ V-PDB. However, a minor part of this signature also might correspond to the Cal-1 or Cal-2 cements, since these phases are difficult to separate from Cal-4. Here, the isotopic signature of Cal-4 likely supports the involvement of meteoric water, with a meteoric water line characterised by a $\delta^{18}\text{O}$ between -6 and -8‰ V-PDB. The depleted $\delta^{13}\text{C}$ likely attests of a slight soil CO_2 component.

Geochemically, the non-luminescent calcite zones of the Cal-4 cement are characterised by Fe-, Mn-, S-, Mg- and Sr-concentrations below the detection limit. In the bright luminescent zones, Fe-, Mn-, S- and Mg-contents reach respectively 6260, 1130, 930 and 2790 ppm. The elementary composition is consistent with a meteoric fluid derived in a phreatic environment.

6.4.1.6- Cal-5 cement

Cal-5 represents the younger cement, encountered in all previous cemented fractures and continuously precipitated upon Cal-4. It displays large non-luminescent calcite phases (Figure 6.16 C & D), which reflect precipitation

under oxic environment (Suchy et al., 2000). Isotopically, Cal-5 cement is characterised by a trend in $\delta^{13}\text{C}$, varying from very depleted values of -12.66 up to +0.66‰. This trend is likely caused by the incorporation of ^{12}C from soil-gas CO_2 into the calcite lattice. Cal-5 is also defined by $\delta^{18}\text{O}$ plotting in a very narrow range from -5.69 to -3.61‰ V-PDB, which likely characterise the $\delta^{18}\text{O}$ of the meteoric water during the cementation. Cal-5 reflects the same element concentrations than the non-luminescent zones of Cal-4, characterised by Fe- Mn- Sr- and S-contents below the detection limit. Moreover, this cement displays low Mg-concentration with on average 140 ppm, supporting the meteoric origin.

Two different sets of twinning planes were identified in Cal-4 and Cal-5 cements. The first one occurs in Cal-1 and Cal-4, whereas the second set is developed after Cal-5 (Figure 6.17). These petrographic observations suggest that the first twin set developed after the cementation of Cal-4 and predates the cementation of Cal-5, whereas the second set postdates the Cal-5 cement. Consequently, Cal-4 and Cal-5 record the tectonic deformation during the crystal growth. This tectonic deformation likely relates to the folding stage, characterised by fracture development in the outer arc region. This interpretation is supported by the calcite twin study (Lacombe et al., 2008), which recorded an E-W extension, i.e. FRACT5, sub-perpendicular to the local NNW-SSE trend of the Saranda anticline.

Petrographical features and the stable isotopic composition of the Cal-4 and Cal-5 stages suggest that calcite crystals precipitated under conditions that were different from those of the previous stages, i.e. Cal-1 to Cal-3. Cal-4 is likely derived from meteoric water, reflecting the phreatic environment at low temperature, oxic/suboxic setting. Afterwards, Cal-5 points to the evolution of the environment, characterised by the migration of meteoric fluid, which could correspond to the emersion of the studied area.

6.4.2- Origin and relative timing of the vein formation

In the Saranda anticline, the major difficulty in working out a paragenetic sequence relates to the insufficient number of crosscutting relationships between diagenetic phases. If the late meteoric fluid cementations (i.e. Cal-4 and Cal-5) are not

taken in account, all other vein generations present very similar petrographic and geochemical characteristics as well as recrystallisation process. In this study, they have been principally individualised by using CL characteristics, the O-isotopic signature, and their deformation features (i.e. twins), without data on fluid inclusion. Then, the cements were placed into the deformation history of the Saranda anticline, according to the fracture paragenesis; i.e. FRACT1 to FRACT7. In fact, each fracture generation characterises a precise step of the tectonic deformation, such as the flexure, the compression and the folding.

Moreover, identifying the successive vein-fillings, regarding to their state of deformation or to the O-isotopic signature, is not very accurate. In fact, the $\delta^{18}\text{O}$ signature depends mainly on the isotopic composition and the temperature of the host-fluid. Consequently, this parameter in the calcite can vary largely for a same cement generation in function of temperature and the recrystallisation. The state of deformation of a crystal can also depend to many local processes, such as the stylolitisation, the reactivation of fractures, the folding....

To place the vein-fillings into the tectonic history and to understand the lack of cross-cutting relationship between veins, special attention was paid to in the geographical repartition of the cements and their isotopic signatures in the anticline. In Figure 6.22, the geographical repartition of the C- and O- isotopic signatures, obtained from the vein-fillings is shown. It is clear that each studied location can be individualised by one isotopic cluster, which likely reflects one dominant cement generation.

Moreover, in Figure 6.23, a geographical repartition of the vein-fillings, associated to the fracture generations is given. Each studied area is characterised by the precipitation of an unique calcite cement. Assuming that cementation immediately followed fracture development, the vein-filling should reflect the evolution of the deformation history of the Saranda area.

This leads to the following interpretation (Figure 6.24):

- FRACT1 and FRACT2, likely developed synchronously to the development of burial stylolites. The latter relate to the burial of the basin. The calcite infill is characterised by isotopic signatures buffered by the host-rock. Cal-1 precipitated during the pre-folding stage, i.e. stage 1, and therefore can be dated as Lower to Middle Oligocene (Nieuwland et al., 2001). This stage is associated to sedimentary loading in the Ionian basin.

- This period is followed by the onset of the main compression, i.e. stage 2, affecting the Ionian basin and developing possibly FRACT3 and FRACT4. At this time, the main stress σ_1 is horizontal and the fluids, i.e. Cal-2, are still buffered by the host-rock. Moreover, the precipitation temperature of the fluids increased, likely due to the increase of the sedimentary loading. This period can be dated as Lower Miocene (Nieuwland et al., 2001). Stage 2 is also characterised by the development of a first generation of tectonic stylolites, which have planes perpendicular to the main stress.

- In stage 3, which corresponds to the folding, shear fractures, i.e. FRACT5-6, developed and a conjugated system of tectonic stylolites also formed in order to accommodate the folding. Here, the still depleted $\delta^{18}\text{O}$ signature of the Cal-3 possibly reflects the increased depth of the studied area until the maximum burial. However, Cal-3 could also reflect ascending fluids, but at present, no data allows to precise this scenario.

According to the work of Swennen et al. (1998) and Nieuwland et al. (2001), the folding period is dated as Langhian/Serravalian.

- The last stage is characterised by the cementation of Cal-4 and Cal-5 cements in re-opened fractures during folding or tectonic reactivation. This process occurs after the uplift and points to the erosion of the overlying flysch and molasse sediments. This is demonstrated by the occurrence of meteoric derived cements into the system.

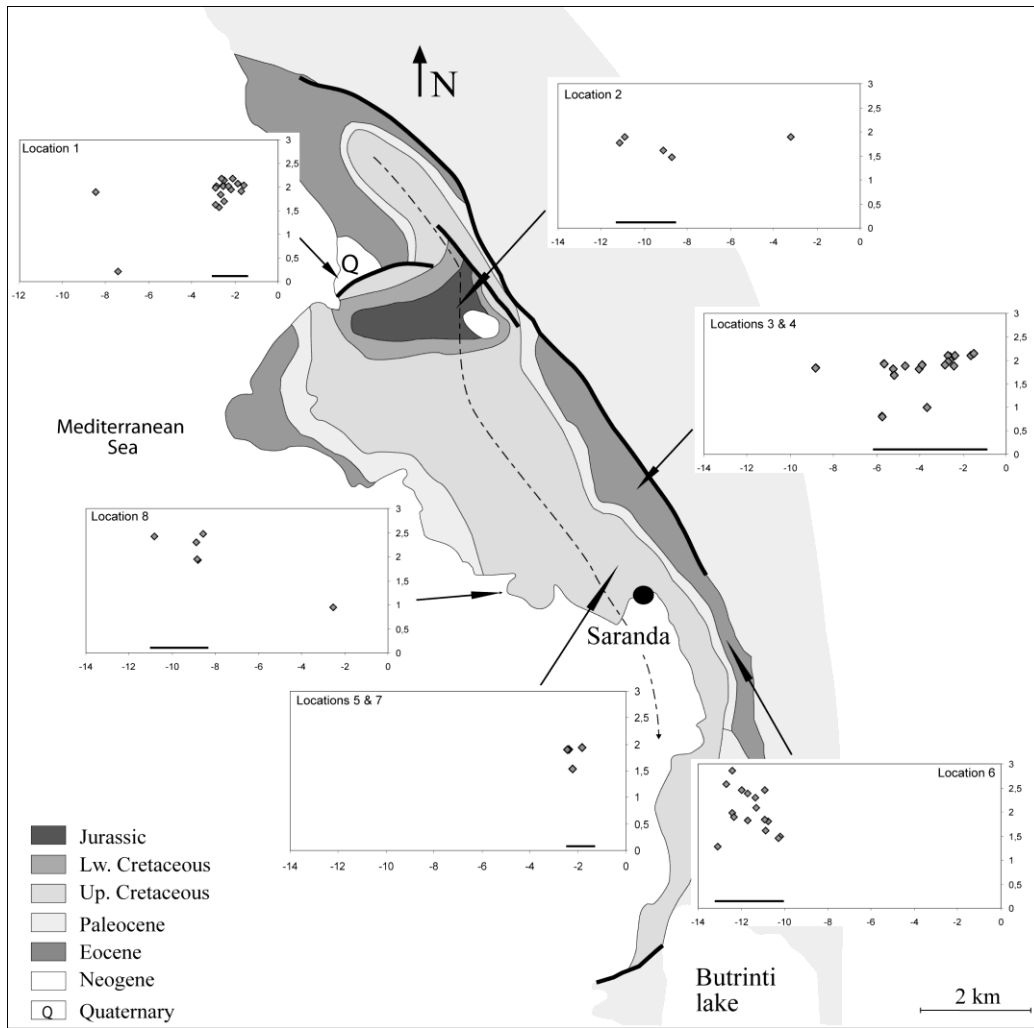


Figure 6.22. Geographical repartition of the C- and O-isotopic results of the successive vein-fillings. Notice that each studied location is characterised by a similar isotopic trend.

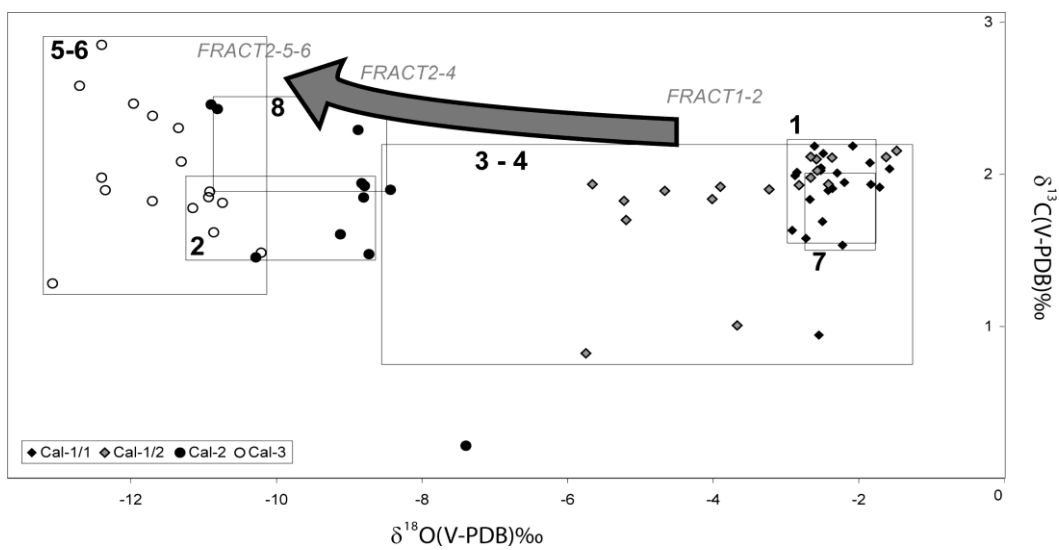


Figure 6.23. C- and O-isotopic signature of the different vein-fillings, regrouped according to the studied areas (bold numbers) and associated to the fracturing stages. The arrow suggests a parallel evolution of the fracture generations with the burial of the Saranda anticline.

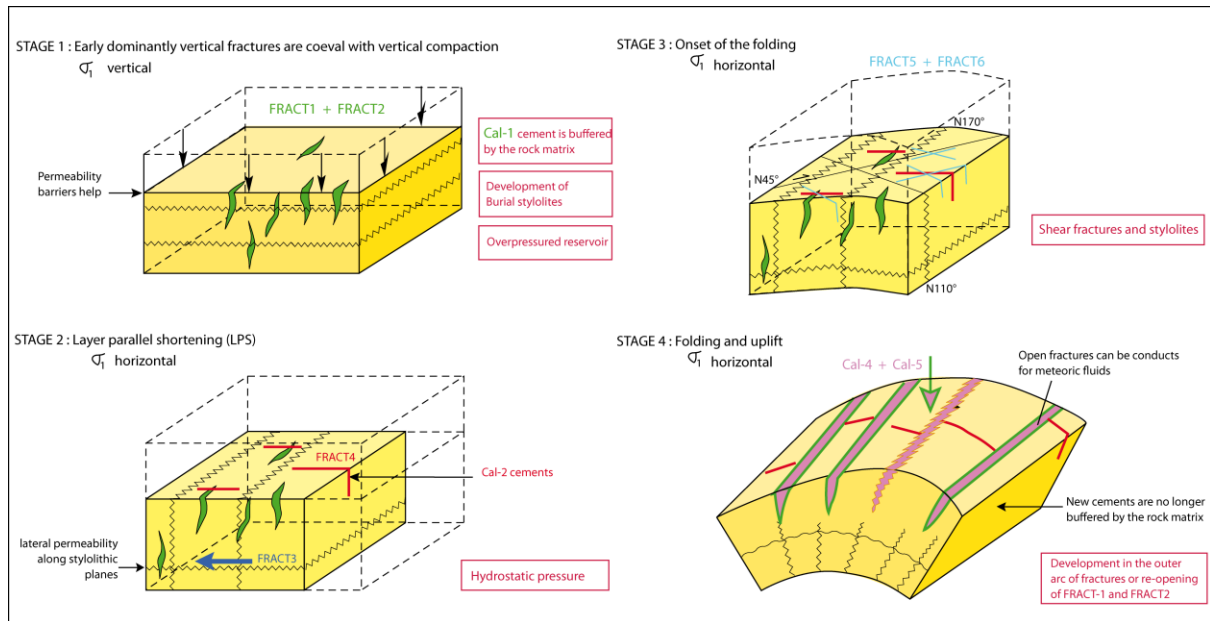


Figure 6.24. Summary of the deformation history, which characterised the Saranda area. The successive steps are described in the text.

CHAPTER 7- DIAGENESIS AND FRACTURING IN THE KURVELESHI BELT: THE KREMENARA ANTICLINE CASE STUDY

The Kremenara anticline (Figure 7.1), which has a size of 5 by 8 km, is located in the northern part of the Kurveleshi belt. This anticlinal structure constitutes a reservoir analogue for nearby and underlying hydrocarbon reservoirs, such as Selenica and Selishta, which occur in duplex structures below and adjacent to Kremenara (Figure 7.2). This anticline is located in the vicinity of the Vlora-Elbasan transfer zone, which probably originally formed as a deep seated basement fault (Roure et al., 1995). The transfer zone accommodates a strike-slip motion within the Triassic/Jurassic, which functioned in the early plate tectonic history of the Albanides as a trajectory along which the Ionian series in the south were moved westward with respect to the Peri-Adriatic Depression (Nieuwland and al., 2001).

Since 1992, the Kremenara anticline has been widely studied especially by IFP in collaboration with the geology section of the K.U.Leuven in the framework of the SUBTRAP consortium, to unravel the diagenetic history of the Upper Cretaceous to Eocene carbonates and to determine the effects of diagenetic processes on reservoir properties (Swennen et al., 1998; Van Geet et al., 2002; Graham-Wall et al., 2006; Breesch et al., 2007; Dewever et al., 2007). Recent reconnaissance surveys, inspecting several outcrops, have shown that oil staining occurs in a dual matrix-fracture porosity and that major stratigraphic variations and structural elements (Figure 7.3A & C), such as fractures and stylolites, play a major role in the evolution of the petroleum system. Oil seeps are not restricted to fractures, but also occur in matrix porosity of carbonate turbidites (Figure 7.3A & B) and debris flows (Van Geet et al., 2002; Dewever et al., 2007). The nearly ideal exposure conditions of the Kremenara anticline, with topographical differences of about 600 m, allow to study these variations in 3-dimensions. Moreover, several exploration wells have been drilled in the central part of the anticline and in the alluvial deposits of its western flank, providing information about the deepest structures.

The Kremenara anticline (Figure 7.1) has a main axis trending about N°40-45 NE, oblique to the main thrust fronts located in the Ionian Zone. Pelagic carbonates of the Tithonian crop out in the core of the anticline, whereas Upper Cretaceous to Eocene fractured carbonates and debris flows, i.e. the reservoir strata, are well exposed in the flanks (Figure 7.4A) and in the northern closure. These Mesozoic and Paleogene series are unconformably covered by Serravalian deposits (Figure 7.4B & C). Three major tear faults, oriented NW-SE to NNW-SSE, cut the Kremenara anticline into four distinct compartments (Figure 7.1).

Based on well data and scientific discussions with Albanian geologists, two NW-SE cross-sections were realised (Figure 7.5 and Figure 7.6). On the 4-4' cross-section (Figure 7.5), located in the central part of the anticline, the compartment 2 (Figure 7.1) is folded and thrust over the compartment 3 (Figure 7.1). Both compartments are moving towards the south-west on the compartment 4 (Figure 7.1). A similar tectonic evolution is observed in the 5-5' cross-section (Figure 7.6). Notice that the Serravalian interval was deposited unconformably on the already folded sediments of the Mesozoic-Paleogene series. The evolution of NW-SE tear faults developed successive duplexes. The latter allow the compartmentalisation of the reservoir interval, developing interesting reservoir capacities in the buried intervals.

In order to complete the previous studies, this chapter will be essentially focussed on the microtectonic study of the Kremenara anticline and the characterisation of the fracture fillings. A first paragenesis of the successive fracture sets and vein generations was established, especially by unravelling the crosscutting relationship between vein types, and with tectonic and burial stylolites. Another essential aspect has been to understand the tectonic deformation of this complex area, of which the fold hinge does not record the main NE-SW compression, and to

place each stage of fracturing into the overall kinematic evolution of this thrust unit.

7.1- General characteristics

The sedimentary evolution of the Kremenara area is based on field observations, which subsequently were refined by studying polished samples and thin sections. The samples have been collected at different places within the anticline, where the Upper Cretaceous-Eocene carbonates crop out. Two sedimentary logs, which characterise the northern part of the anticline, i.e. Greshica, and the eastern flank, i.e. Fratari log, are given in the Figure 7.8. and

Figure 7.7., respectively based on wells, log and my own field data.

7.1.1- Lithologies of the Upper Cretaceous-Eocene interval

Exposed Cretaceous to Eocene limestone turbidites constitute reservoir analogues for the deep water carbonate reservoir interval of the entire Adriatic domain (Albpetrol, 1993). They are equivalent to the Scaglia carbonate formation in Italy (Cazzola and Soudet, 1993). They have been studied in the Kremenara anticline (northern part of the Ionian Zone), which has the specificity to host oil seeps in a dual matrix-fracture porosity.

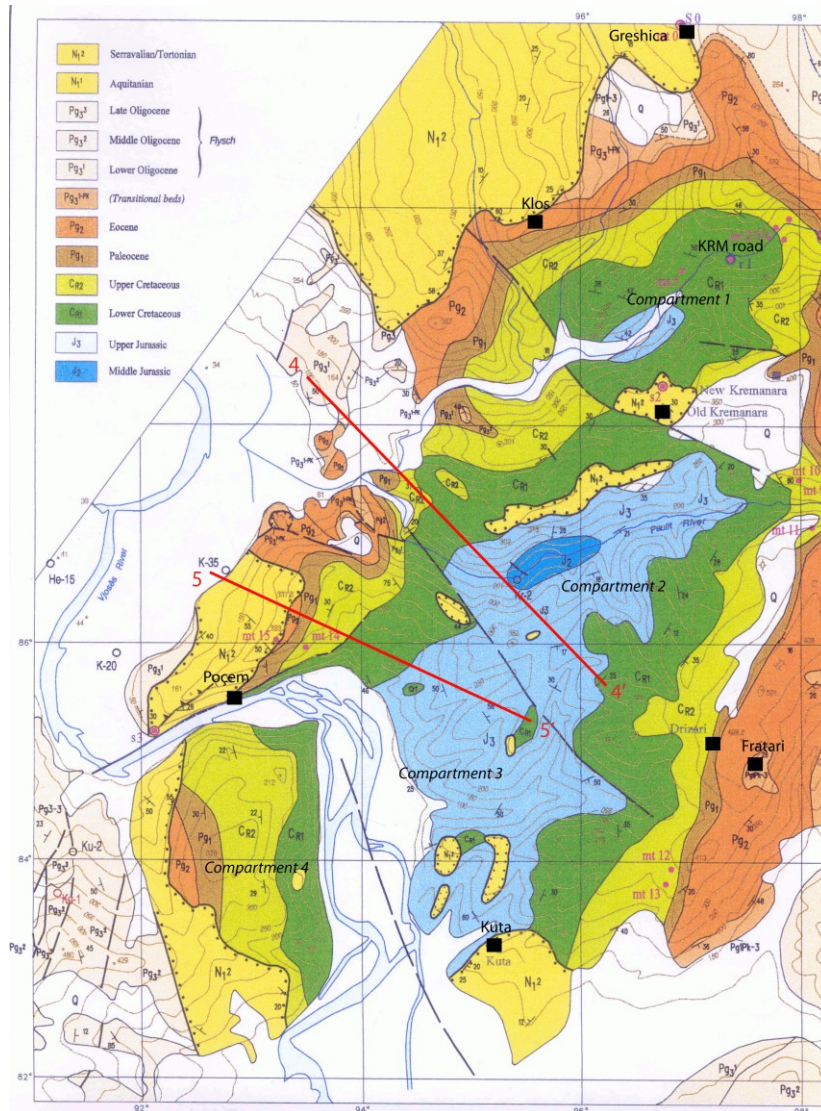


Figure 7.1. Geological map of the Kremenara anticline (from Swennen et al., 1998). Profiles 4-4' and 5-5', described in Figure 7.5 and Figure 7.6, are indicated by red-lines on the map. Note the three NW-SE faults, which compartmentalise the anticline into four compartments.

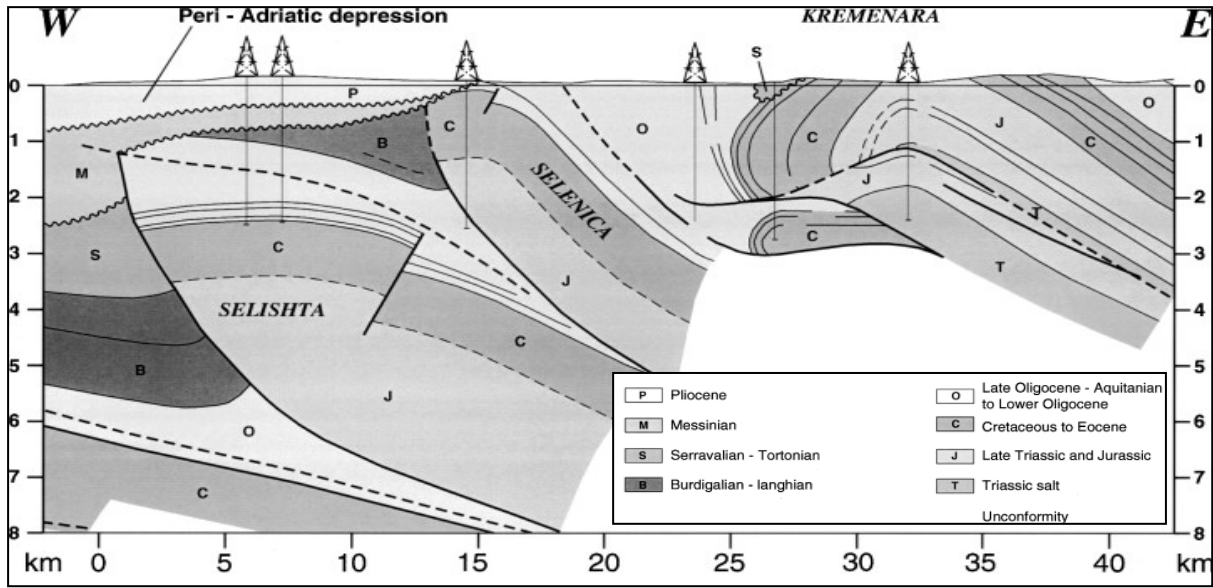


Figure 7.2. W-E geological profile through the Kremenara anticline (Swennen et al., 1998).

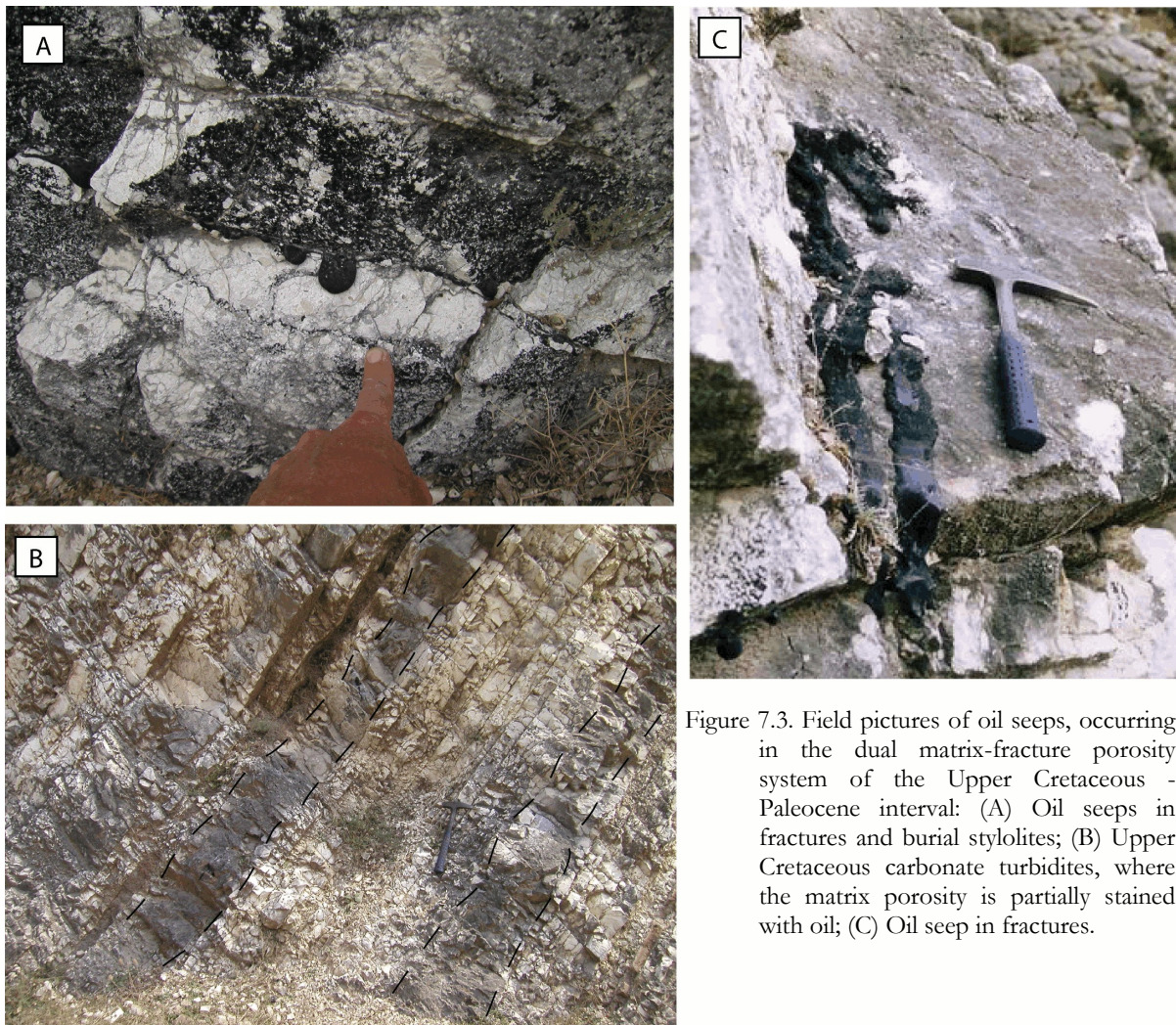


Figure 7.3. Field pictures of oil seeps, occurring in the dual matrix-fracture porosity system of the Upper Cretaceous - Paleocene interval: (A) Oil seeps in fractures and burial stylolites; (B) Upper Cretaceous carbonate turbidites, where the matrix porosity is partially stained with oil; (C) Oil seep in fractures.

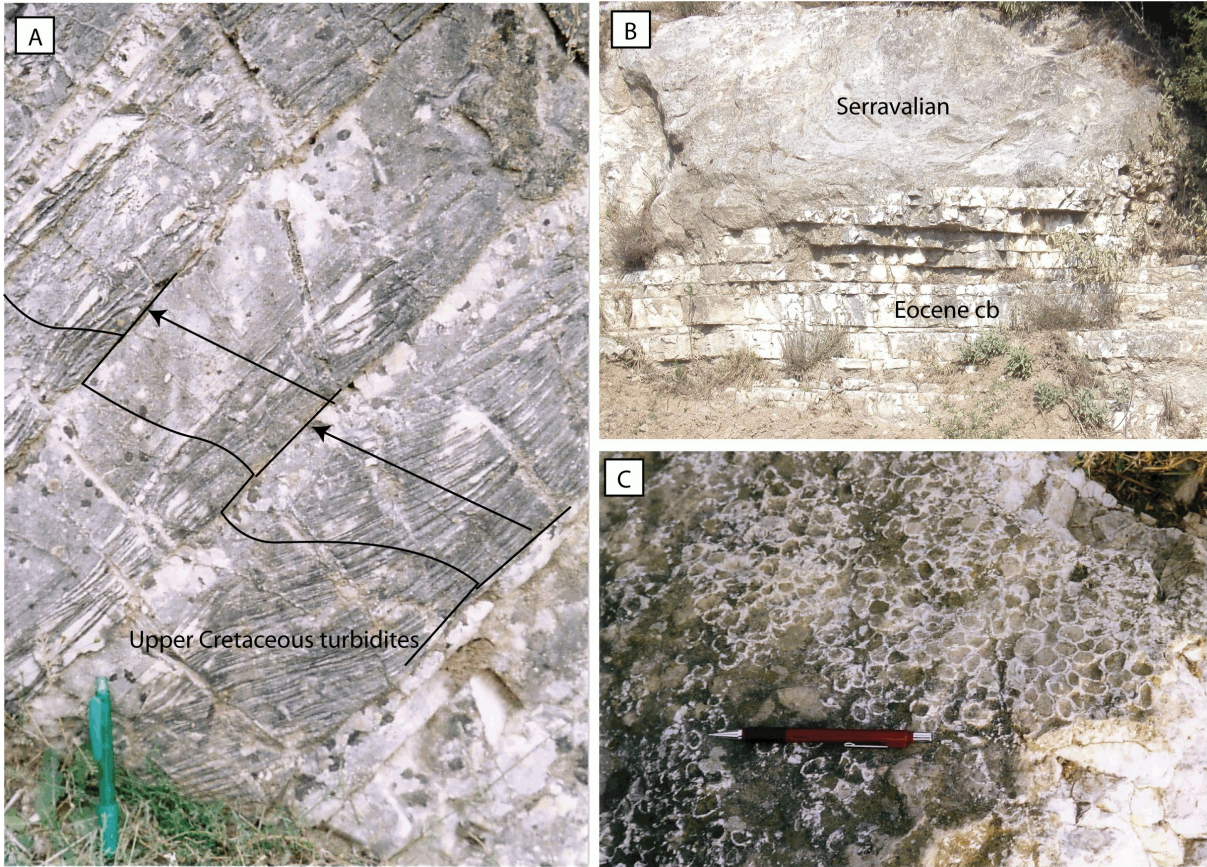


Figure 7.4. Field pictures of (A) Upper Cretaceous carbonate turbidites, characterised by the development of Bouma sequences (Deweever et al., 2007); (B) Unconformable draping of the Serravalian deposits on the Eocene carbonates (cb); and (C) Barnacle assemblages in the Serravalian sandstone, which covers unconformably the Lower Cretaceous carbonates.

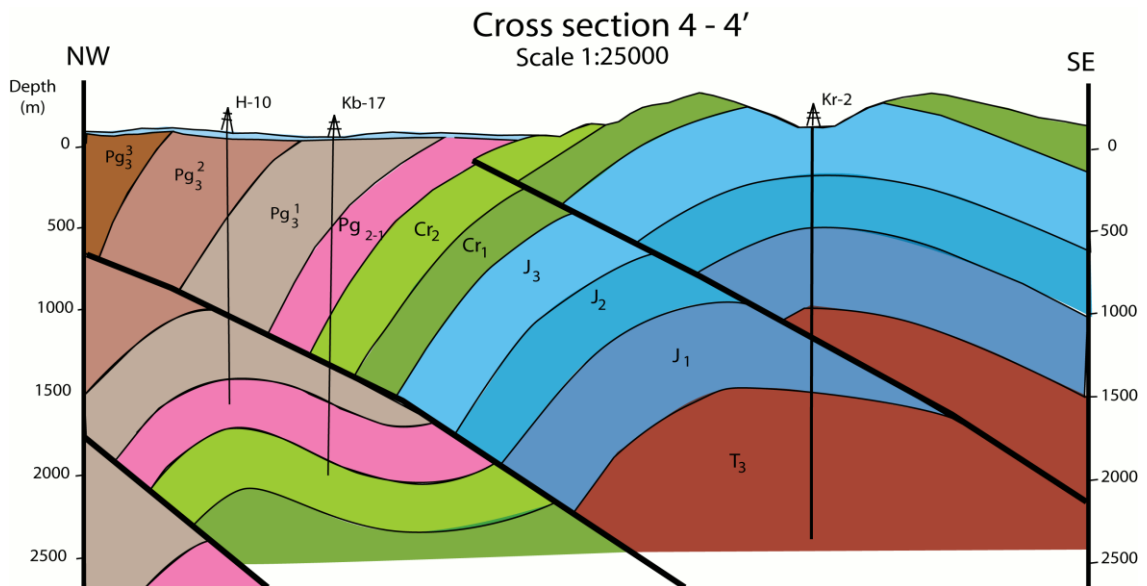


Figure 7.5. NW-SE geological transect of the central part of the Kremenara anticline, i.e. compartment 2 (Figure 7.1). The location of the 4-4\' transect is given in the Figure 7.1. (based on own and wells data).

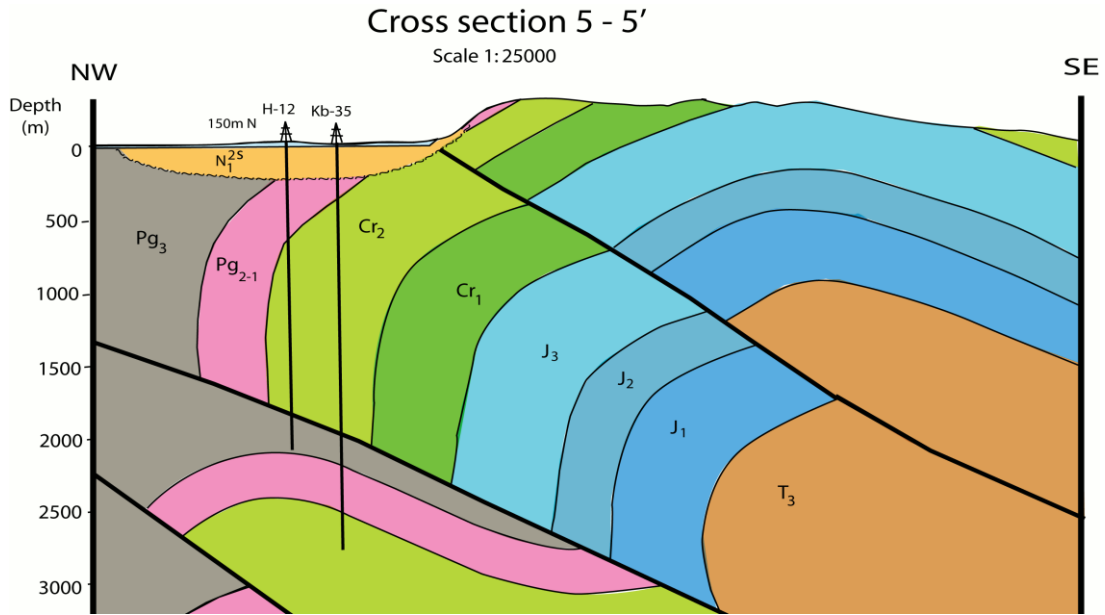


Figure 7.6. NE-SW geological transect of the central part of the Kremenara anticline, located in the Figure 7.1. , i.e. compartment 3 (based on own and well data).

Age	Lithology	Depth (m)	Description						Thickness (m)	Facies Description
			Marls	Mudstone	Wackestone	Packstone	Grainstone	Bounstone		
OLIG.		0-10	[Marls pattern]						10	Flysch
EOCENE	Lutetian	10-50	[Limestone pattern]						145	Micritic limestone and carbonate turbidites intercalated with cherty limestone <i>Nummulites sp.</i> <i>Disocyclus sp.</i> <i>Alveolina</i> <i>Aragoensis sp.</i>
	Ypresian	50-150	[Limestone pattern]							
PALEO.	Thanetian - Danian	150-200	[Limestone pattern]						66	Carbonate turbidites with slumps <i>Miscellanea miscell.</i> , <i>Miscellina</i> <i>Globorotalia sp.</i> , <i>Ethelia alba.</i>
		200-250	[Limestone pattern]							
UPPER CRETACEOUS	Maastrichtian	250-350	[Limestone pattern]						196	Carbonate turbidites with slumps <i>Globotruncana sp.</i> <i>G. Lapparenti</i> <i>G. Stuarti-conica</i> <i>Stomosphaera sp.</i> <i>Sulcaperulina sp.</i> <i>Rudistae miliolidae</i>
	Cenomanian	350-400	[Limestone pattern]							
		400-410	[Cross-hatched pattern]							Phosphatic horizon

Figure 7.7. Sedimentary log of the Fratari area (eastern flank), based on well data and own field observations.

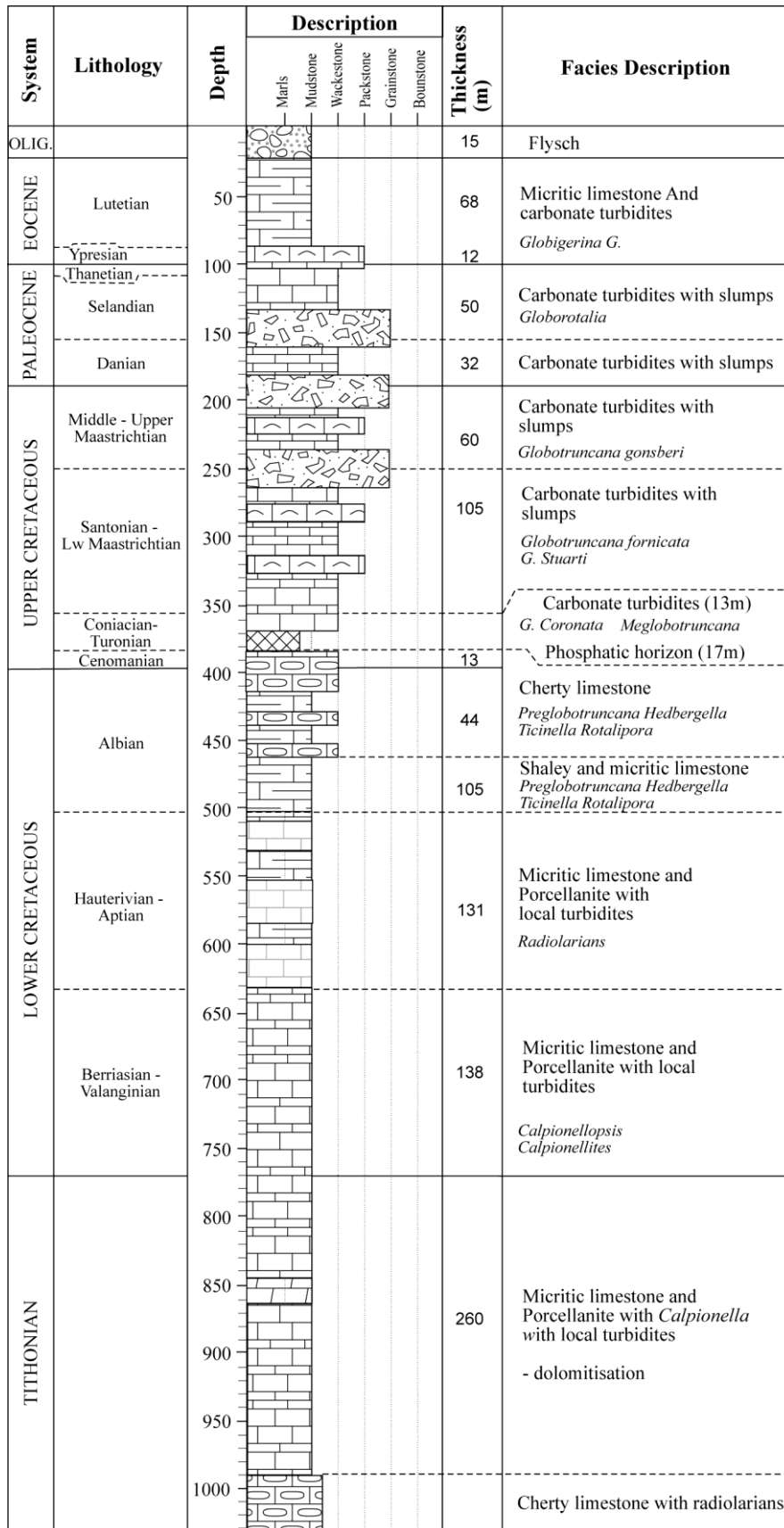


Figure 7.8. Sedimentary log of the Greshica area, in the northern part of the Kremenara anticline (based on well data and own observations).

The Upper Cretaceous interval is 160-185 m thick and consists of carbonate turbidites, associated with many debris flow intercalations. The carbonates are highly fractured, especially in the micritic/pelagic limestones. The top of the interval is characterised by a major slumping horizon, which marks the transition with the Paleocene strata. In the northern compartment of the Kremenara anticline, i.e. compartment 1 (Figure 7.1), the Upper Cretaceous carbonates display numerous oil seeps, distributed in some beds (Figure 7.10 A to C), fracture sets and stylolites.

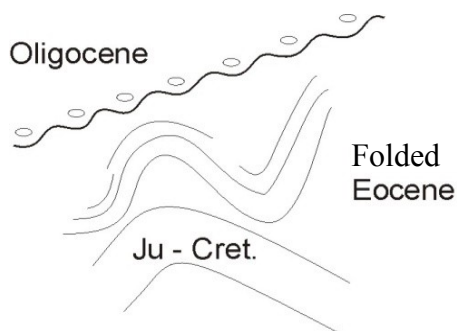


Figure 7.9. Schematic drawing of the present-day situation of the carbonate series in the Kremenara area, covered unconformably by the Oligocene flysch.

The Paleocene interval is made up of similar lithologies (Figure 7.10 D to F) as the Upper Cretaceous interval, with two main slumping horizons (Figure 3.4). The Eocene carbonates evolve from white micritic (Figure 7.11 A), present in lower part, towards bioclastic limestones (Figure 7.11 B), existing in the upper part. Some chert lenses occur parallel to the bedding. The top of the Eocene interval is characterised by a mudstone interval rich in foraminifers, such as *Nummulites* sp., *Disocyclus* sp. and *Alveolina*, which have a size up to 1.5 cm (Figure 7.11 C to F). These Eocene carbonates are highly folded (Figure 7.9) and fractured, and shows a very low matrix porosity. It is also important to note that the Eocene interval has a thickness varying largely from place to place, possibly reflecting the onset of the deformation and folding. Based on well data, a thickening of 65m is recorded from the north (less thick) to the south. The transition with the Oligocene flysch, Rupelian in age, consists of an intercalation of yellow-brown shaly interbeds within beige sandy limestones.

The Serravalian deposits cover unconformably the Oligocene flysch, as well as older sediments.

The latter consist of argillaceous sediments, with few lithothamium reefal carbonates, i.e. red algae, which evolve progressively into sandstones, pointing to a transgressive episode (Breesch et al., 2007).

7.1.2- Previous work: Matrix porosity of carbonate turbidites

The study of the matrix porosity represents a major interest for carbonate reservoir characterisation, since active tectonic deformation can generate a succession of diagenetic processes due to important fluid migrations. Determining the evolution of the porosity is a complicated task and requires good and precise sampling and petrographical examination.

The fractured Upper Cretaceous to Paleocene carbonate turbidites of the Ionian Basin, which are made up of classical turbidites or Bouma sequences (Bouma, 1962), constitute an excellent rock-type to study the dual matrix and fracture porosity characteristics and thus the overall reservoir evolution. Carbonate turbidites of the Ionian Zone display important matrix deformation due to the successive diagenetic processes. Van Geet et al. (2002) and Dewever et al. (2007) described precisely these lithological intervals and the different diagenetic processes controlling the matrix porosity evolution (i.e. creation and/or destruction). A summary of their work is given below. Petrography and porosity measurements demonstrate that the actual porosity and permeability distributions are principally controlled by initial sedimentological contrasts (fabric, mineralogy) and the eogenetic dissolution/precipitation, which occurred since the onset of the burial history. Turbidite beds, which are thicker than 35 cm, i.e. B to C horizons of the Bouma sequences, still possess some primary matrix porosity over one third of the bed thickness. The occurrence of diagenetic processes such as dissolution, cementation, neomorphism and compaction, operating shortly after the deposition, modified the primary porosity characteristics and distribution. Today, the matrix porosity is only preserved in the bioclastic grain- to packstones (middle part of the turbidite beds), where syntaxial cementation around rudist and crinoid fragments (ideal substrates for calcite cementation) stabilised the framework (Swennen et al., 2000; Dewever et al., 2007).

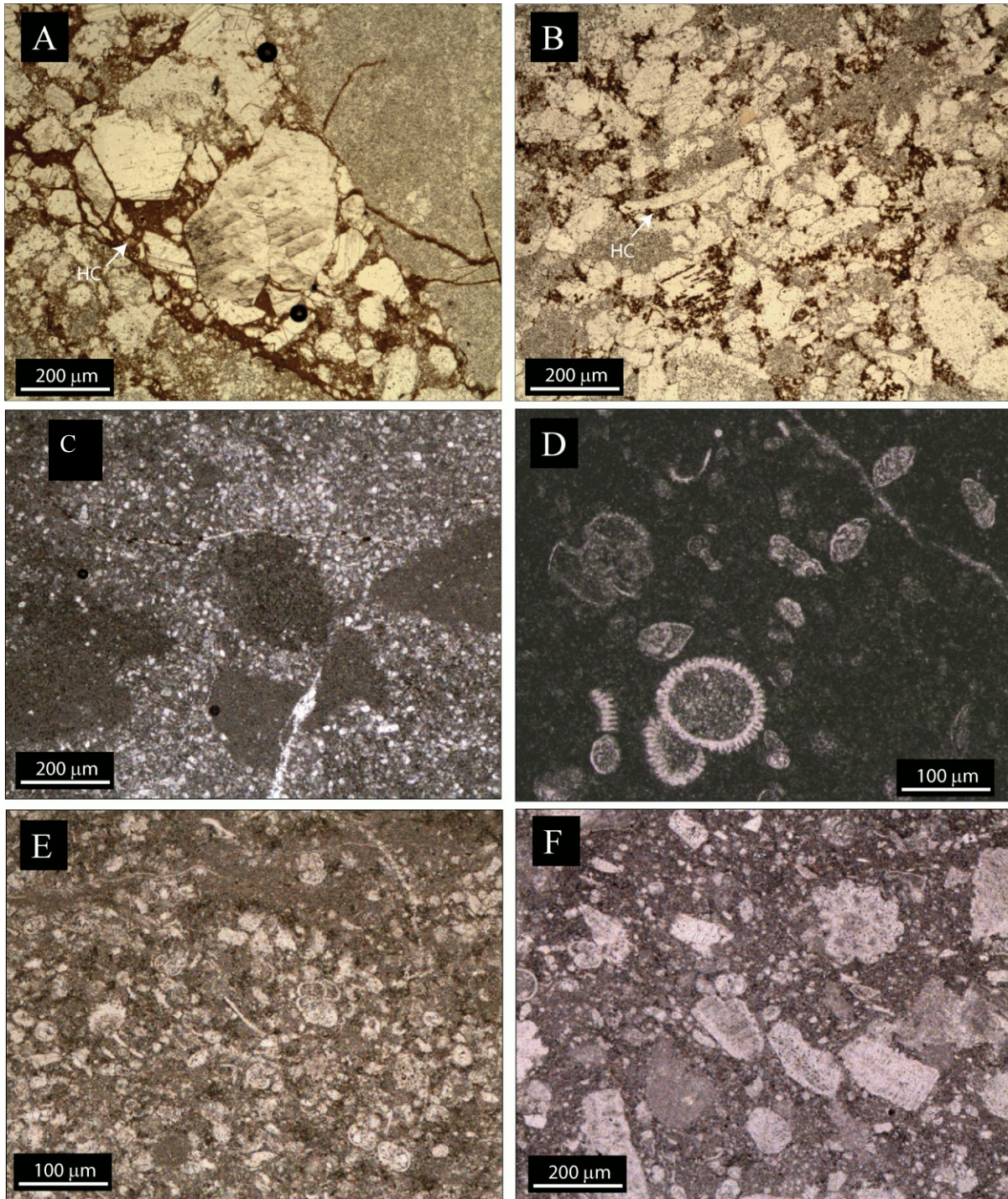


Figure 7.10. Photomicrographs in transmitted light view of the Upper Cretaceous and Paleocene limestones from the Kremenara anticline: (A) and (B) Basal part of the turbidites with matrix supported wackestone, stained with hydrocarbon (HC); (C) Wackestone to mudstone from the upper part of the turbiditic interval; (D) Paleocene mudstone/wackestone lithology with foraminifers; (E) Oil impregnated packstone with hydrocarbon in the Paleocene interval; (F) Packstone located in the Paleocene interval.

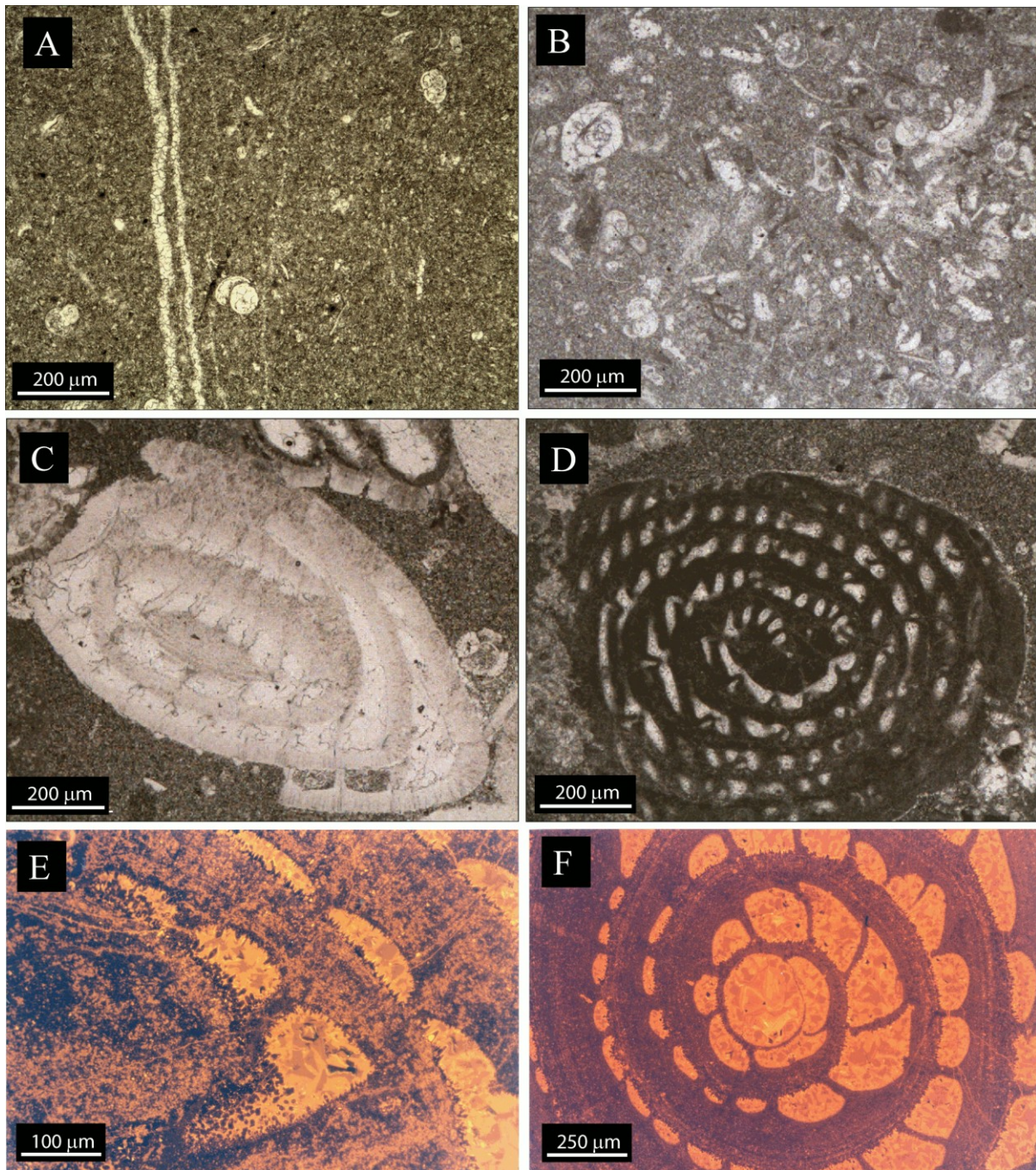


Figure 7.11. Photomicrographs of the Eocene limestones: (A) Eocene mudstone lithology with foraminifers; (B) Eocene wackestone with foraminifers, such as *Nummulites* sp.; (C)-(D) and (E)-(F) Respectively transmitted light and CL views of *Nummulites* with intraparticle porosity cemented with calcite.

Here, the dissolution of aragonite components plays a major role in the reservoir characteristics. Its dissolution increases the matrix porosity and saturates the expelled fluid in HCO_3^- and Ca^{2+} , thus allowing to stabilise the pore network by inducing a rapid framework stabilising cementation, wherever nucleation sites occurred (e.g. Halley et al., 1984; Hendry et al., 1996). However, when no substrate for cementation occurs, or where the distribution of potential

substrates does not allow to develop a stabilising framework (i.e. in wackestone), the porosity is lost by compaction. This is the case for the A and D horizons, which are characterised by high matrix micrite content. Consequently, even if the lithology displays good initial porosity, the reservoir characteristics evolve drastically according to the diagenetic events like aragonite dissolution, burial compaction, and stabilisation of the pore network.

7.2- Structural Analyses

As explained in the preceding chapters, the carbonates of the Ionian Zone have been subjected to several stylolitisation and fracturing events, being subsequently filled by various calcite cement generations. In the case of the Kremenara anticline as well as of some other locations at the vicinity of the Vlora-Elbasan transfer zone, many fractures and stylolites are impregnated by oil due to a late reactivation of the structures (Roure et al., 2004).

In this part, a tentative timing of the stylolitisation and fracturing will be worked out. Additional data, such as fracture fillings and their stable isotopes, will later help to refine this paragenesis.

7.2.1- Stylolites

7.2.1.1- Burial stylolites

One major episode of development of burial stylolites in the Upper Cretaceous to Eocene carbonates has been identified. These stylolitic planes generally formed parallel to the depositional fabric (i.e. bedding) and are well developed throughout the studied area. They likely formed during the burial stage before thrusting, which according to Nieuwland et al. (2001) occurred during the Lower to Middle Oligocene. These stylolites are rarely filled with cements, implying that they did not act as pathways for fluid migration.

A second set of BPS, which crosscuts the first one, was determined in the south-western part of the Kremenara anticline in post-Eocene conglomerates, according to Breesch et al. (2007). This second generation is interpreted to be post-folding and is related to a second post-Miocene burial phase. During this project, where the focus was on the reservoir interval, this second generation of burial stylolites was not encountered. Nevertheless, this stage will be taken into account in the final paragenesis.

7.2.1.2- Tectonic stylolites

Tectonic stylolites (TS) are well-developed, preferably in the micritic intervals. In Figure 7.12 and Figure 7.13, a summary of the different generations of TS, which previously have been interpreted either as pre- to syn-folding (i.e. backtilted data) or as post-folding (i.e. raw data), are presented. To determine which TS planes

must be backtilted, the TS planes have been supposed initially to develop sub-vertically. In the figures, each fracture generation is characterised by a mean plane, represented by a different colour in the stereograms. The locations of the studied areas, indicated in the stereograms, are shown in the geological map (Figure 7.1).

The pre- to syn-folding stage, shown in Figure 7.12, displays four main sets of tectonic stylolites, which are each individualised by a mean plane, recording two maximum principal stresses σ_1 .

The stylolite generations, represented by the blue and green planes, are observed throughout the study area and point to the same maximum principal stress σ_1 , trending about $N40^\circ \pm 5^\circ$.

The two other generations of TS oriented NE-SW with subvertical dip, i.e. orange and yellow planes, record a second maximum principal stress, oriented $N140^\circ$.

It is important to notice that the main stress oriented $N40^\circ/90$ is perpendicular to the orientation of the three faults, which compartmentalise the anticline, and are mainly parallel to the NE-SW compression developing the frontal thrusts in the Ionian Zone. The second recorded stress, oriented $N140^\circ$, is slightly perpendicular to the fold hinge (Figure 7.1). It likely records the folding stage. However, no cross-cutting relationship between these two TS generations has been observed.

Concerning the post-folding stage, the TS sets (Figure 7.13) are distributed according to the areas studied (Figure 7.1) and split up into three lines, corresponding to the different compartments, separated by the previously mentioned NW-SE faults. Four dominant directions of the main principal stress σ_1 were determined, trending respectively about $N40-60^\circ$ (green plane), which is roughly orthogonal to the NW-SE faults and to the frontal thrusts, $N110^\circ$ (blue plane) and $N135^\circ$, perpendicular to the fold hinge, and the last maximum principal stress oriented NS (yellow plane).

According to cross-cutting relationships, the $N40-60^\circ$ oriented σ_1 , likely developing concomitant with the frontal thrusts and the NW-SE faults, predates the $N110^\circ$ oriented σ_1 , which is slightly perpendicular to the Kremenara fold hinge.

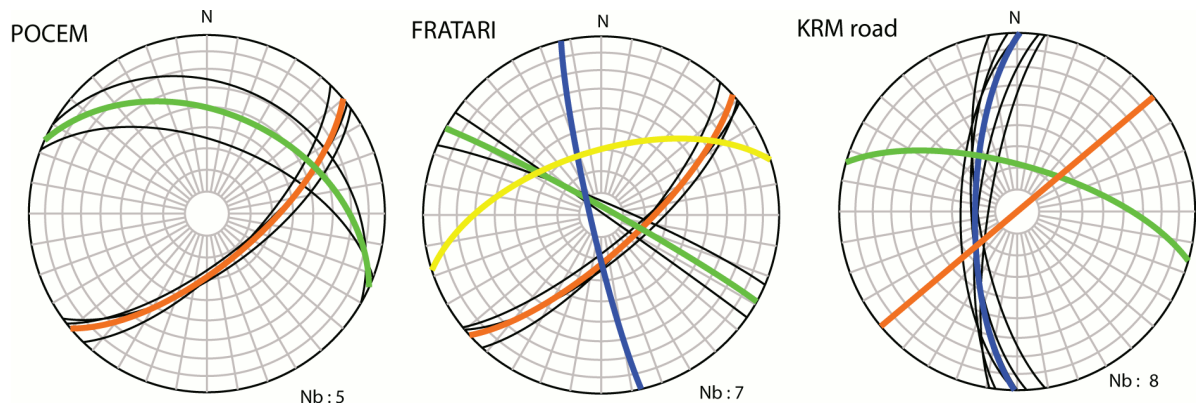


Figure 7.12. Backtilted data of the recorded tectonic stylolites, which have been previously assumed to be pre-folding.

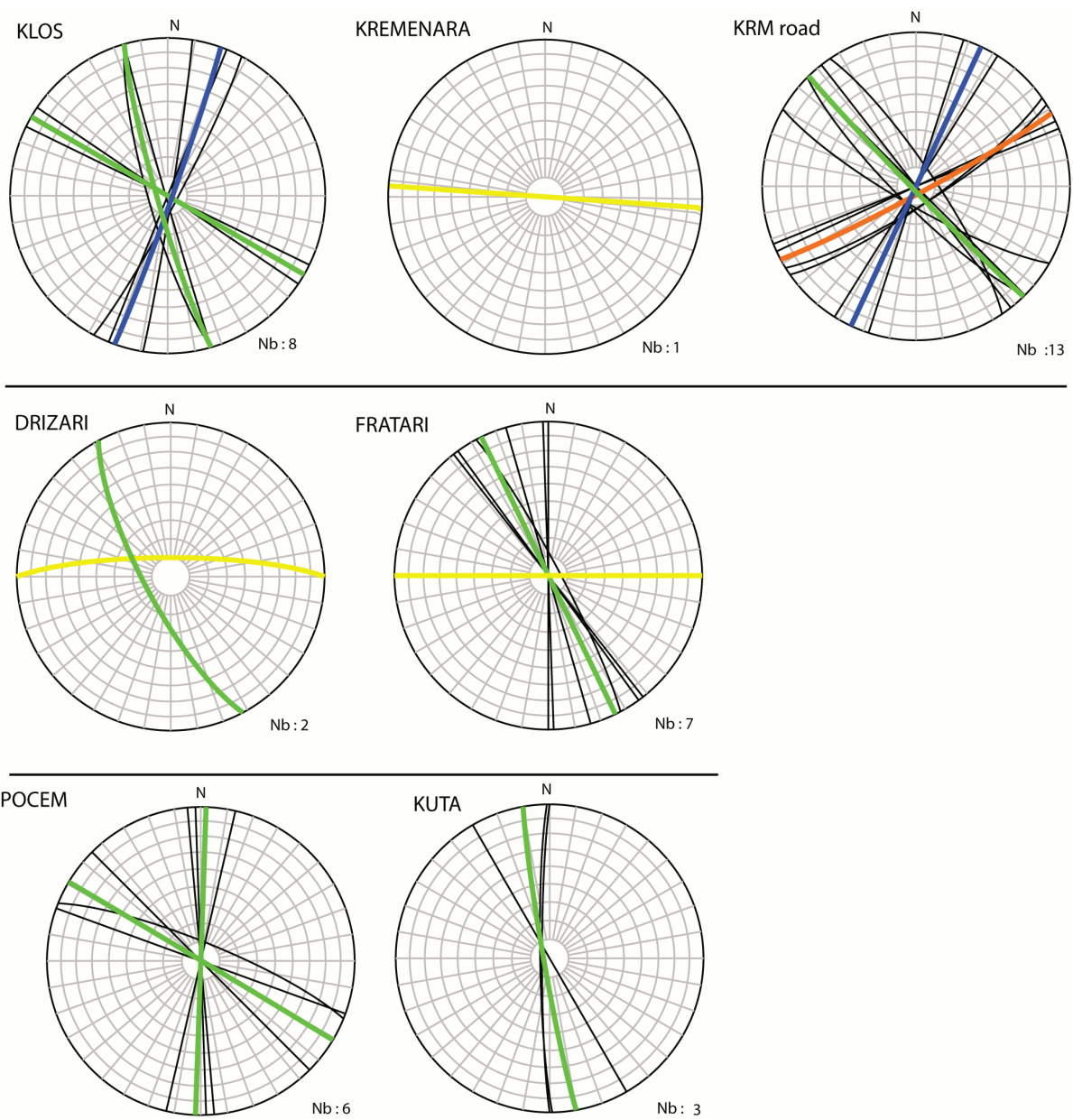


Figure 7.13. Raw data of the tectonic stylolites dated as post-folding.

Later on, the NE-SW tectonic stylolites developed only in the northern part of the Kremenara anticline (i.e. orange plane, KRM road), and relate to a NW-SE compression. The latter is perpendicular to the fold hinge located in the northern compartment of the anticline (i.e. compartment1, Figure 7.1). The last stage is less common and records a NS compression.

However some uncertainties still exist concerning the determination of the maximum principal stresses, since only planes of TS have been studied instead of their peaks.

7.2.2- Fractures

Backtilted and raw orientations of fractures are given respectively in the Figure 7.14 and Figure 7.15. After backtilting of the data, five main sets of fractures were determined as pre- to syn-folding (Figure 7.14).

The FRACT0 generation, which was observed everywhere in the anticline, is oriented N130° and possesses a subvertical dip (i.e. green planes in Figure 7.14). FRACT0 fractures are cut by the burial stylolites, suggesting a pre-folding origin and a development at relatively shallow depth

(several 100 of meters). They can be related to the burial stage, during the flexure of the foreland, developing fractures under an extensive regime. Alternatively, they could be associated to the onset of a SE-NW compression.

FRACT1 is oriented mainly N60° with subvertical dip, and is synchronous to the development of burial stylolites. This fracture generation is parallel to the main compression developing the folds and thrusts in the Ionian Basin. Consequently FRACT1 likely relates to a NE-SW horizontal compression (i.e. blue planes) and/or is associated to the burial stage, developing fractures under an extensive regime.

This stage was followed by the development of FRACT2, oriented NNE-SSW, i.e. corresponding with the dark blue plane in Figure 7.14. The latter predate the tectonic stylolites and should likely be related to a N110° oriented compression. FRACT3 corresponds to fractures developed mainly parallel to the bedding (i.e. yellow mean planes), and was recorded in many areas. However, the lack of cross-cutting relationships does not allow to place this generation precisely in the paragenesis.

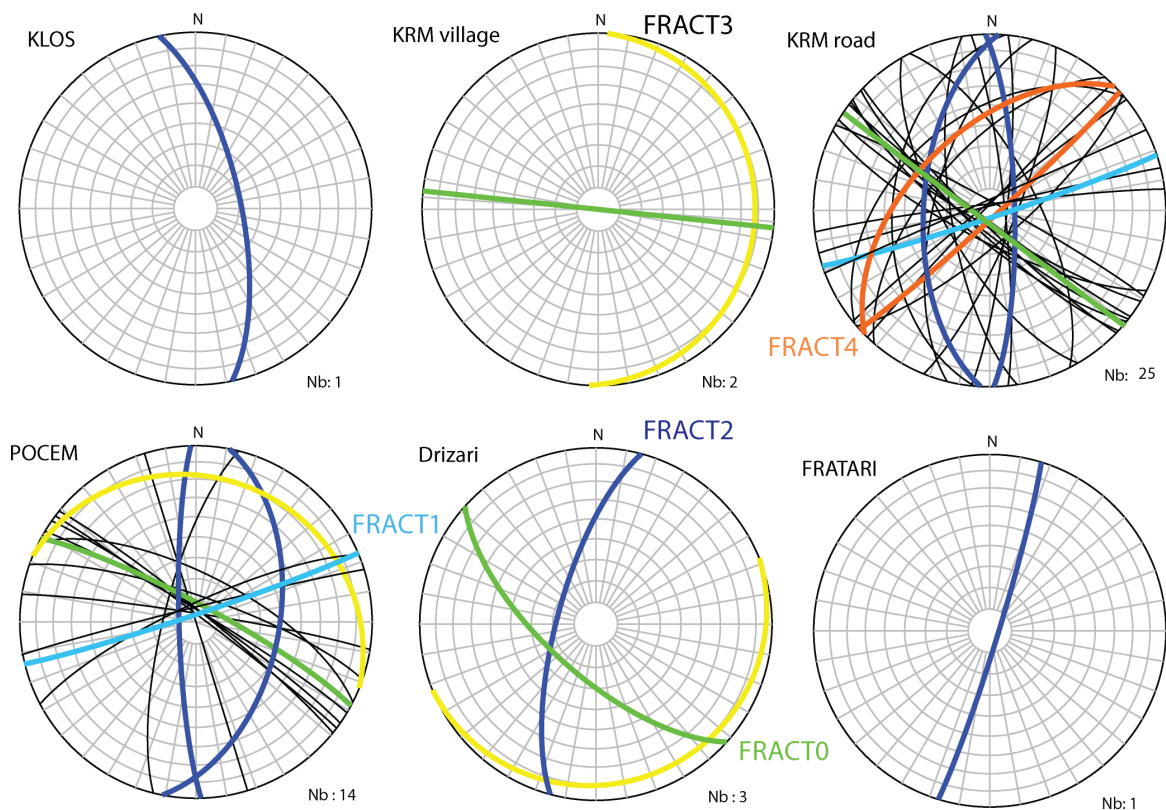


Figure 7.14. Backtilted data representation for recorded fractures.

The next stage, which was only encountered in the northern part of the anticline, consists of the development of FRACT4 (i.e. orange plane in Figure 7.14, KRM road). The latter have a NE-SW orientation, which is parallel to the fold hinge but also parallel to the compressive stress, which developed the folds and thrusts in the Albanides. Moreover FRACT4 is also perpendicular to the NW-SE faults, which compartmentalise the anticline, and not all fractures developed vertically. Consequently, this set of fracture can be related to the folding stage.

Concerning the fractures dated as post-folding, raw data are given in the Figure 7.15. Four main

generations of fractures were distinguished and relatively dated based on cross-cutting relationships between fractures. Their orientations are very similar to those of the fracture generations dated as pre-folding. The first set FRACT5, represented by the green mean planes in Figure 7.15, is oriented N120°, with subvertical dip. This generation is perpendicular to the fold hinge and similar to FRACT0. Consequently, FRACT5 can be related either to a second burial episode, developing fractures under an extensive regime or due to a SE-NW compression.

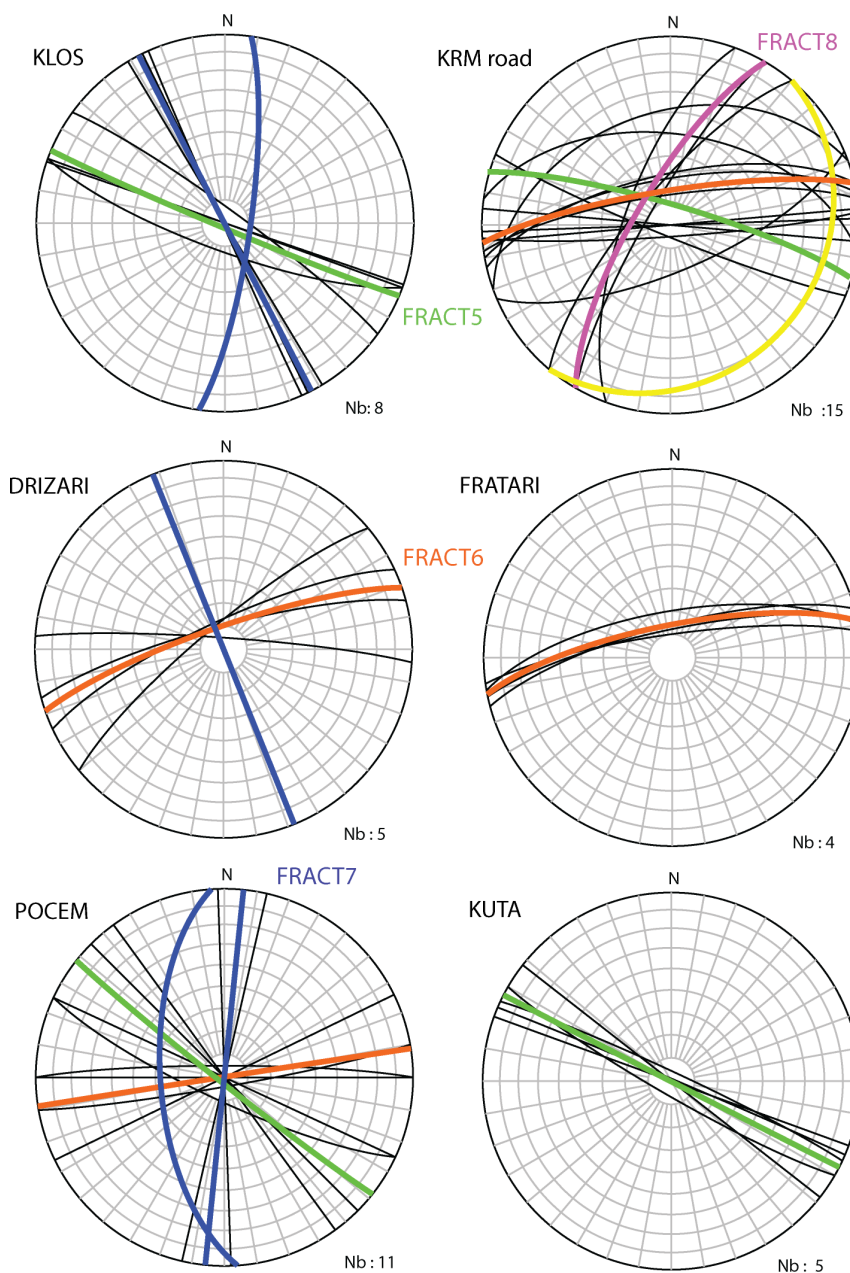


Figure 7.15. Presentation of the raw data of fractures, determined as post-folding.

The second fracture generation, i.e. FRACT6, is mainly oriented N70°, 85N (i.e. orange planes in Figure 7.15), and consistent with the main compression developing the NNW-SSE thrusts and folding structures in the Albanides. FRACT6 is also parallel to the fold hinge, suggesting also the development of fractures in the outer arc during the folding process. Ultimately, FRACT7 consists of only NS fractures, characterised by subvertical dip, i.e. blue mean planes in Figure 7.15. Their coeval maximum stress likely records a post-folding E-W compression. This change in the orientation of the maximum stress attests of the occurrence of a third tectonic phase. Under this regime, the NE faults would act as transfer zones with dominant dextral strike-slip motion and subsidiary normal displacement. This interpretation is in agreement with the work of Mantovani et al. (2002), who demonstrates an E-W compression during the Late Miocene. This new developed EW stress may play an important role in the structural evolution of the anticline. In fact, under this regime, the NW-SE transversal faults would act as sinistral strike-slip fault that uplifted and moved independently each compartments, changing their fold hinge. This interpretation can explain the present-day

variation of the fold hinge (Figure 7.1). Another way to interpret FRACT5 to FRACT7 is to consider that they relate to a vein system formed in response to the regional SE-NW compressional stress also responsible for folding, i.e. with a main compression stress oriented N110°.

FRACT6 and FRACT7 are oblique to the fold hinge and can then be attributed to the folding process, i.e. hinge-perpendicular conjugate shear fractures. This model is in agreement with the model proposed by Stearns and Friedman (1972), i.e. Figure 6.13.

The last generation of fractures, i.e. FRACT8, are mainly oriented N30° and have been only observed in the northern part of the anticline along the Kremenara road (purple plane in Figure 7.15, “KRM road”). FRACT8 shows the same orientations than FRACT4, developed during the pre-folding stage. Both have been only encountered in the northern part of the anticline. FRACT8 is parallel to the present-day fold hinge, occurring in the northern part of the anticline. Then, it likely relates to the folding of the structure.

Fracture generations		Tectonic evolution
FRACT0 - FRACT1	Pre- to syn-folding	Flexure of the foreland or NE-SW compression and NW-SE compression from the Eocene.
FRACT2		Folding stage, associated to the N110° oriented compression
FRACT3		Folding
FRACT4		
FRACT5	Post-folding	N120° oriented compression (fractures perpendicular to the fold hinge)
FRACT6		NE-SW compression, developing the frontal thrusts in the Albanides OR fractures developed in the outer arc during the folding
FRACT7		E-W compression, changing the fold hinge due to sinistral strike slip faults.
FRACT8		NE-SW compression OR NW-SE compression recording the continuity of the folding.

Table 7.1. Relative timing of the fracture generations in relation to the tectonic evolution of the Kremenara anticline.

These successive fracture sets record a complex deformation history. The Kremenara anticline shows a fold hinge, which is not parallel to the overall orientation of the folds and thrusts in the Albanides (Figure 7.1), but likely developed due to a SE-NW compressive stress. The main compressive stress, oriented NE-SW, and developing the frontal thrusts, is recorded by the development of three NW-SE faults, which cut the anticline in four compartments (Figure 7.1).

This suggests that the folding of this area occurred earlier than the onset of the NE-SW compression and has been afterwards faulted by the main compression developing the frontal thrusts. From then onwards, the Kremenara anticline probably developed duplex structures (Figure 7.5 and Figure 7.6).

A recapitulative paragenesis of the fracture development associated to the tectonic evolution of the Kremenara anticline is given in Table 7.1.

This interpretation can explain also the intense folding of the Eocene interval, showing small fold hinges oriented N30-40°, that is in agreement with the occurrence of a NW-SE principal stress σ_1 during the Late Eocene (Figure 7.9).

7.2.3- Oil occurrences

The main interest of the Kremenara anticline is the occurrence of oil staining in the dual porosity system. Many tectonic features, such as stylolites and fractures, are often cemented with calcite cements and partially oil stained, indicating that these tectonic elements acted as flow conduits. Then, according to the oil occurrence in the fractures, it is possible to propose a relative timing for the oil migration. Additionally, oil seeps occur mainly in the northern part of the anticline, i.e. in compartment 1, rather than in the other compartments. According to field observations, all fracture sets, located in the compartment 1, display oil staining except for the FRACT8 generation. This observation suggests that the oil migration likely predates FRACT8 development. In the other compartments, few oil occurrences are encountered in the matrix porosity. The latter suggests that a local structure, such as impermeable faults, must prevent oil migration across adjacent compartments. These impermeable faults may be filled with sediments coming from the flysch or partially cemented. The presence of oil seeps, especially in the northern part, points toward a tectonic reactivation, allowing the opening of cemented fractures. Based on the geological map (Figure 7.1), the three NW-SE faults, which compartmentalise the anticline, likely play a role in sealing these different compartments.

7.3- Vein development in the Kremenara anticline

7.3.1- Cal-1 cement

Cal-1 cement precipitates in FRACT0, oriented NW-SE with subvertical dip. These veins are cut by burial stylolites. Cal-1 cement consists of blocky and transparent calcite crystals, which display two sets of thin twins and some fluid inclusions (Figure 7.16). Under CL, the calcite crystals show an orange zoning similar to their

host-lithology. The central part, where many solid inclusions occur, displays a characteristic CL pattern, pointing towards the recrystallisation of the calcite crystals (Figure 7.16B).

7.3.2- Cal-2 cement

The next cement precipitates in FRACT1, oriented NE-SW with subvertical dip (backtilted data). These veins are synchronous to the development of burial stylolites (BPS), since they cut and are crosscut by the BPS. Cal-2 cement consists of blocky to elongated (Figure 7.17A) and transparent calcite crystals, which display numerous double sets of twinning, as well as some fluid and solid inclusions (Figure 7.17B). Under cathodoluminescence (CL), Cal-2 is characterised by a bright to dull sector-zonation (Figure 7.17A & D). The central parts of the veins show less luminescent crystals.

Moreover, the bright luminescent zones display many solid inclusions, a typical CL pattern of recrystallisation and some red-luminescent dolomite inclusions (Figure 7.17A). This vein generation contains also some brecciated zones (Figure 7.17B-C-D), including pieces of calcite cements, and insoluble residues. The calcite fragments are likely coming from a former fracture filling. It displays similar CL characteristics as their host calcite. The brecciated fragments also consist of microsparite, which could come from the recrystallisation of micritic fragments. These observations point to the occurrence of high pore fluid pressure, developing hydrofracturing (Figure 7.17B). This fracture was then re-opened and filled with subsequent blocky and transparent calcite crystals (Figure 7.17A), which are characterised by dull to non luminescent sector zones.

7.3.3- Cal-3 cement

This vein filling has been difficult to place into the relative paragenesis, since only few crosscutting relationships were encountered.

Cal-3 cement is characterised by blocky to elongated non-luminescent calcite crystals (Figure 7.18), displaying two sets of twins. This cement is found in re-used Cal-2 veins (Figure 7.19), i.e. FRACT1, or in FRACT4. This cement likely precipitates under high pore fluid pressure, since it brecciates the previous cements.

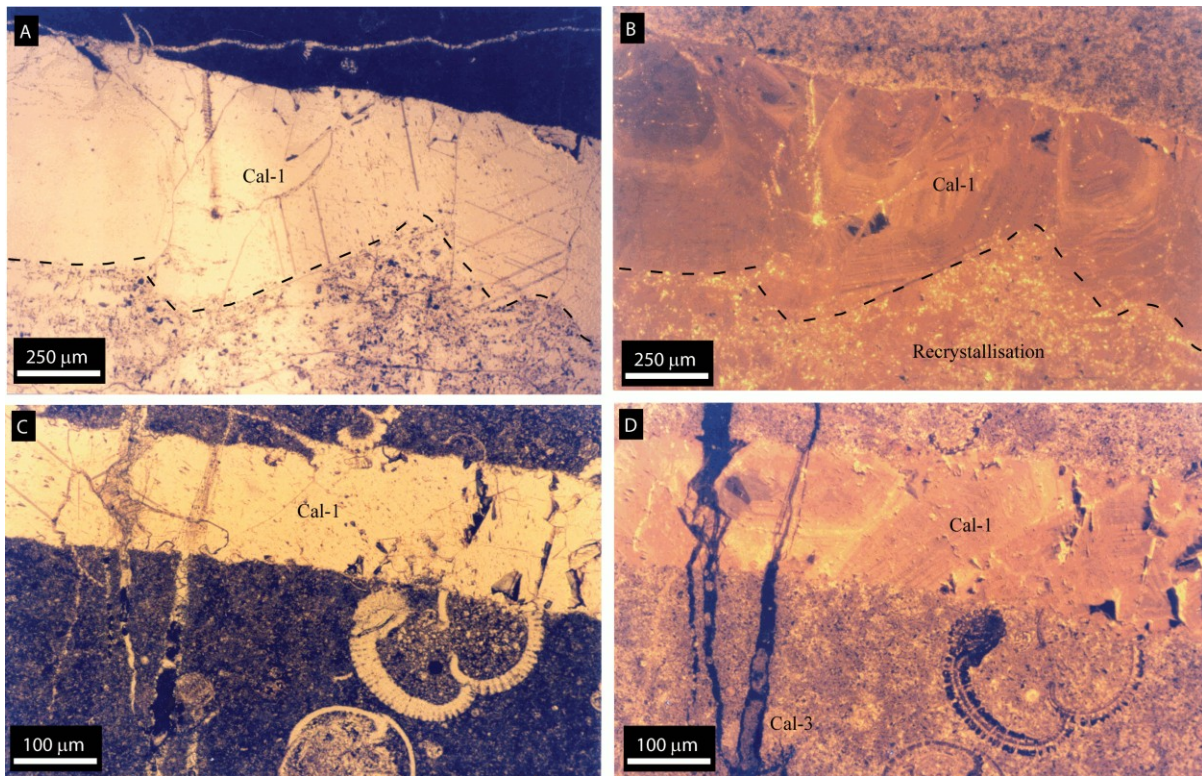


Figure 7.16. Photomicrographs of the Cal-1 cement: (A) - (B) Respectively transmitted light and CL views of the orange luminescent zoned calcite, precipitating along the border, whereas the central part displays a typical CL pattern of recrystallisation. (C) - (D) Respectively transmitted light and CL views displaying the crosscutting relationship of Cal-1 and a non-luminescent calcite vein, i.e. Cal-3.

7.3.4- Cal-4 cement

Cal-4 cement precipitated in FRACT5, oriented NW-SE. It postdates the development of burial stylolites and predates the N-S oriented stylolites, since in some places, Cal-4 cement is cut by the N-S oriented stylolites. This cement is made up of blocky to elongated calcite crystals. The crystals display only few twins and, as for the previous Cal-2 cement, show orange to dull luminescent sector zoning. Based on the typical CL pattern, showing many bright luminescent spots scattered in the vein, the Cal-4 cement is likely partially recrystallised (Figure 7.20).

These veins contain many brecciated zones, characterised by calcite fragments and non-carbonate impurities. The calcite grains should have been detached from the Cal-4 cement, since they display similar CL (Figure 7.20A & B).

These calcites possess a crack-seal fabric, as indicated by the occurrence of micro-structural

indicators, such as regularly spaced trails of pieces of wall-rock (Figure 7.20C & D). The latter are parallel to the vein wall and may contain also non-carbonate impurities.

7.3.5- Cal-5 cement

Cal-5 cement has only been encountered in FRACT1 and FRACT6 in the southern part of the anticline in the Poçem area. This cement postdates the development of burial stylolites and is in turn cut by tectonic stylolites. It is characterised by an intense brecciation (Figure 7.21), where the brecciated fragments are mainly composed of calcite crystals, coming from the former vein, i.e. Cal-2, non-carbonate impurities and possibly micritic fragments. The calcite fragments display orange to dull luminescent sector zoning and are surrounded by carbonate matrix. Some Fe-oxides are also scattered within the Cal-5 vein. This process of crystallisation likely suggests a hydrofracturing episode.

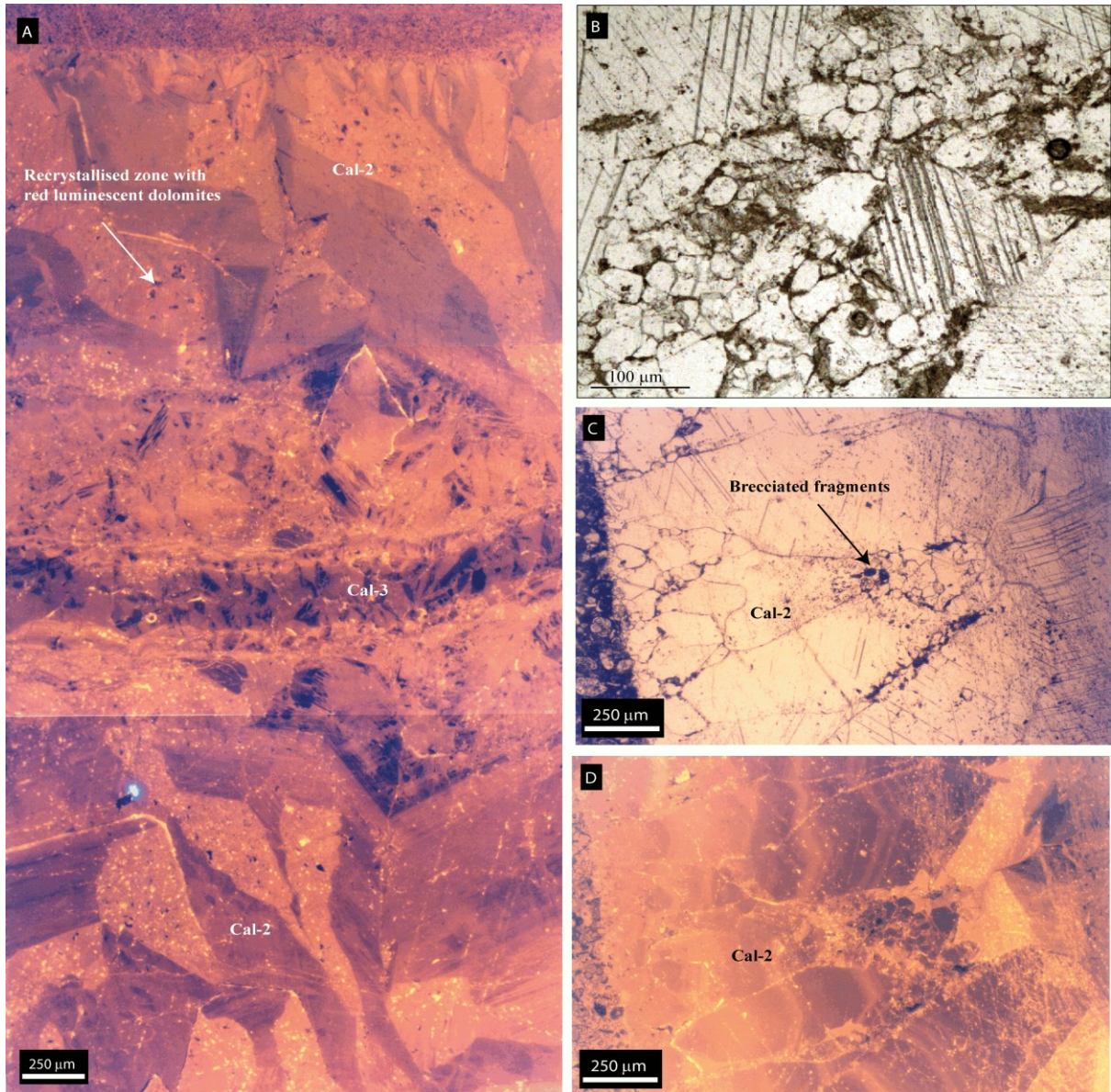


Figure 7.17. Photomicrographs of the Cal-2 cement: (A) CL view of Cal-2 cement, re-opened and filled by the same cement, suggesting a crack-seal process. The yellow luminescent areas display typical CL pattern of recrystallisation; (B) Transmitted light view of a brecciated fragment into Cal-2 vein; (C)-(D) Respectively transmitted light and CL views of Cal-2 vein, where brecciated fragments of the former cement occur.

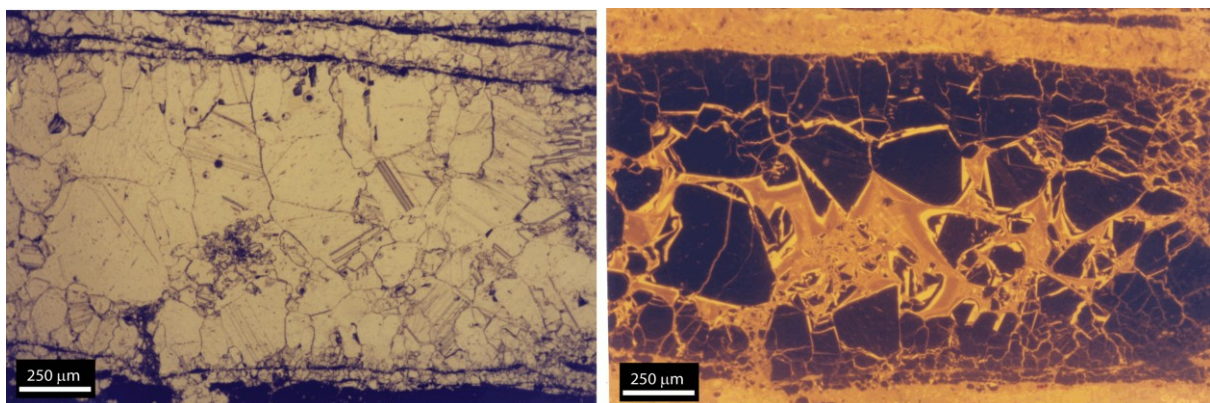


Figure 7.18. Respectively transmitted light and CL views of the Cal-3 cement. Notice the brecciation of the non-luminescent calcite cement by a younger bright luminescence cement.

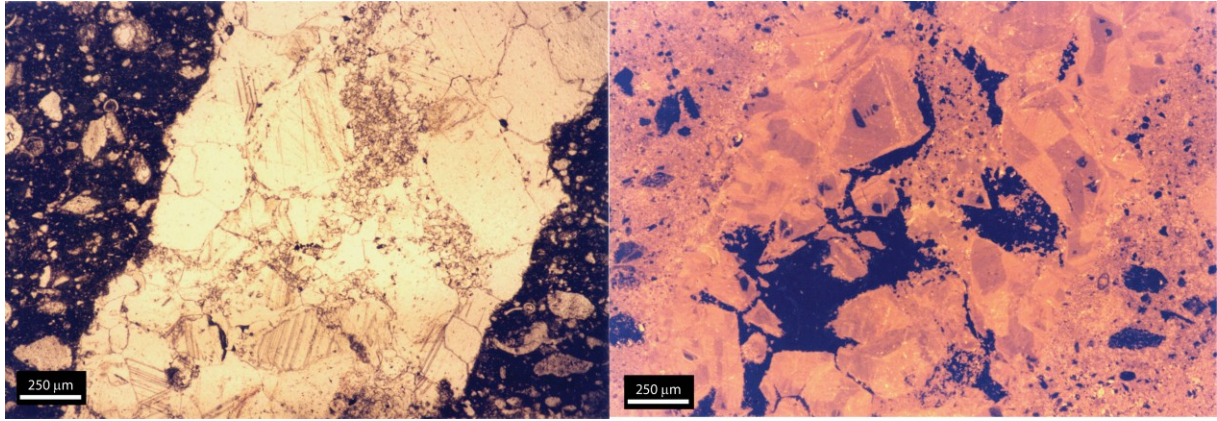


Figure 7.19. Transmitted light and CL views of Cal-3 cement, which postdates the previously brecciated Cal-2 cement.

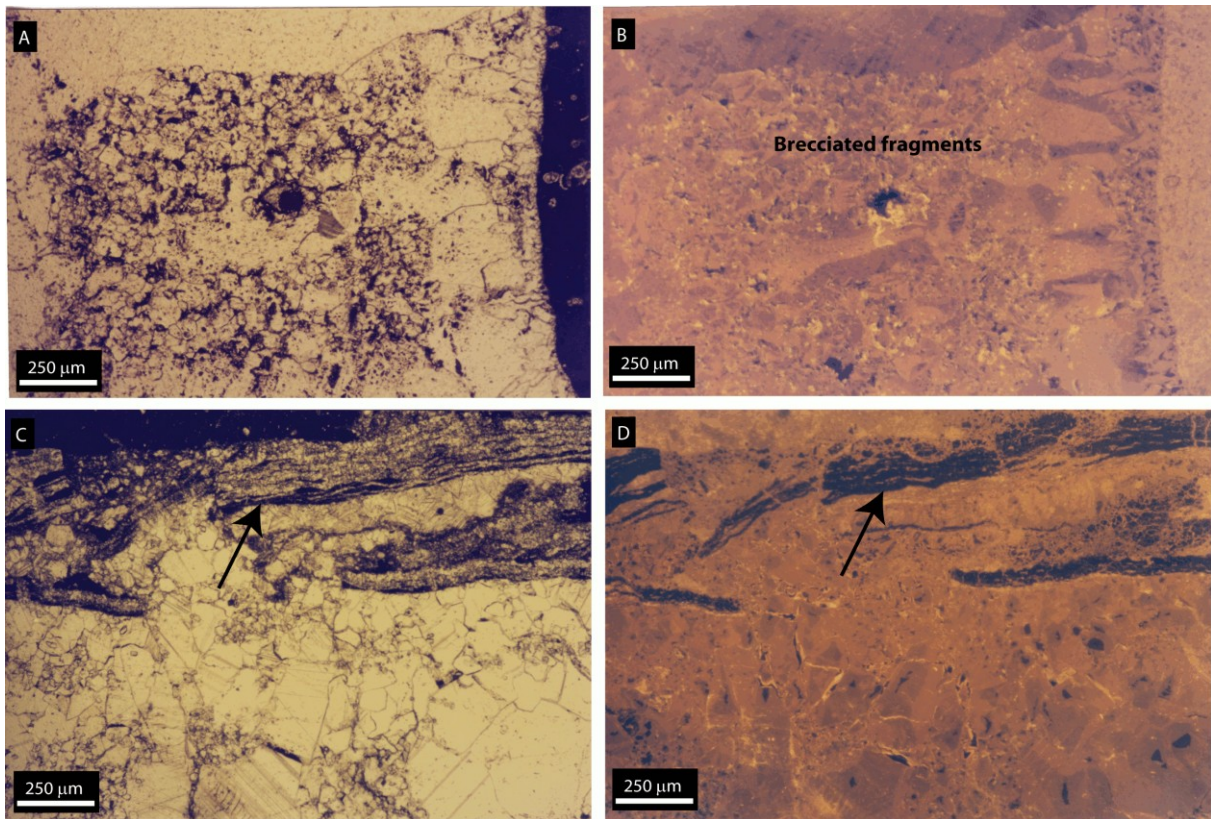


Figure 7.20. (A) & (B) Respectively transmitted light and CL views of the Cal-4 cement, characterised by numerous brecciated fragments, which likely originate from the former veins or can be attributed to sparitised micritic fragments. (C) & (D) Respectively transmitted light and CL views of the Cal-4 cement, displaying regularly spaced trails of wall rock, parallel to the opening of the vein (arrows). These fragments may contain pieces of micritic matrix and non-carbonate impurities

7.3.6- Cal-6 cement

Cal-6 cement precipitates in FRACT6 and consists of small blocky calcite crystals averaging 250µm in size. These crystals present numerous twins (Figure 7.22). Many dolomite crystals are scattered in Cal-6 and have a size up to 300 µm large. At present, the dolomite is altered, or recrystallised. Under CL, the calcite

displays an orange luminescence, which becomes brighter at the vicinity of altered and non-luminescent dolomite crystals. The vein was subsequently crosscut by tectonic stylolites, filled by hydrocarbon.

7.3.7- Cal-7 cement

The next fracture filling has been encountered in FRACT7, oriented N-S, and is characterised by blocky to elongated calcite crystals, i.e. Cal-7, with a size up to 600 μm long (Figure 7.23). Cal-

7 is dated as post-Serravalian, since this fracture set has been observed in this interval, during the post-folding stage. The calcite crystals are not twinned and display an orange to non-luminescent sector zoning.

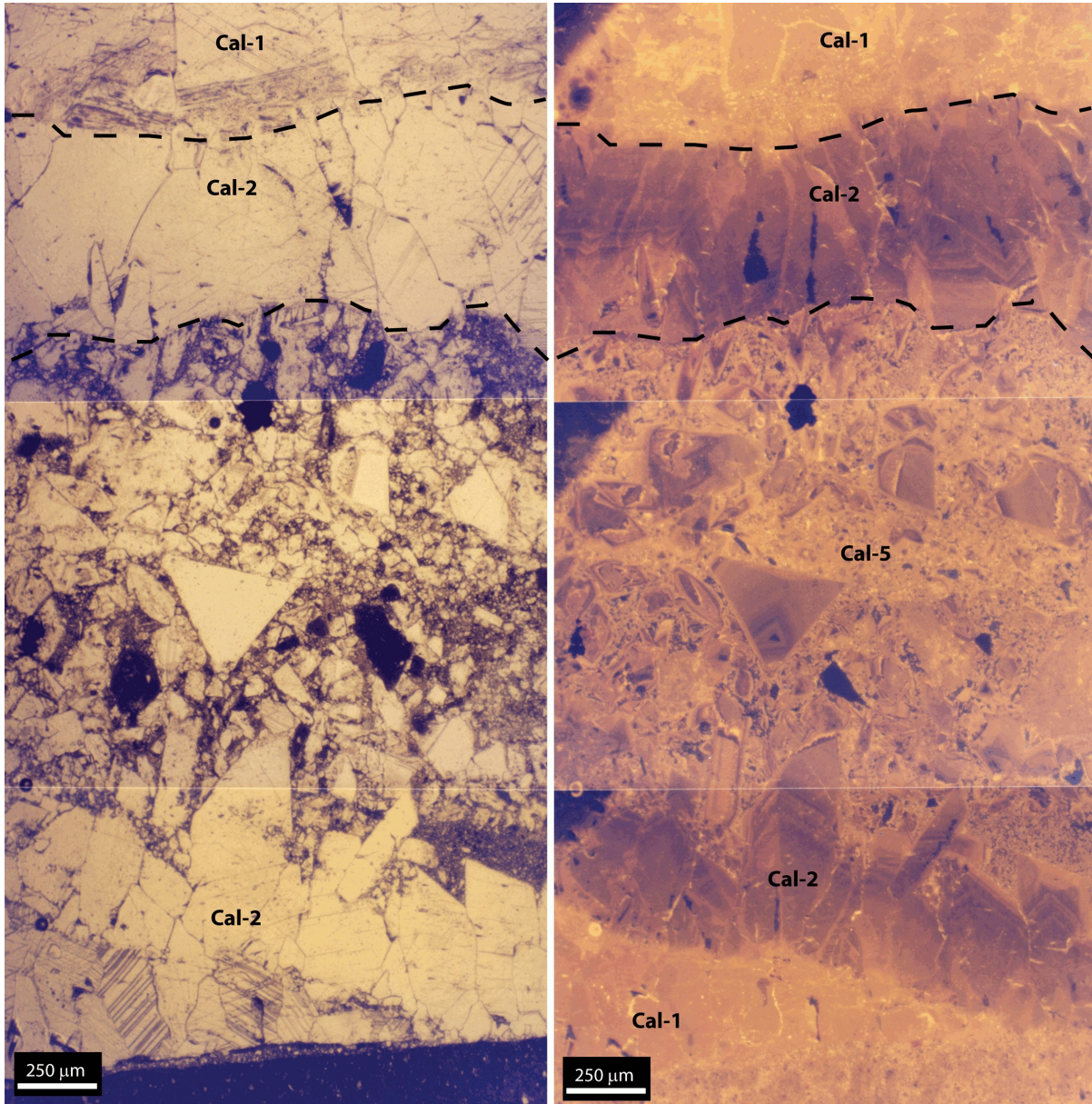


Figure 7.21. Respectively transmitted light and CL views of the Cal-5 cement, which brecciates the initial Cal-2 cement. Notice the intense brecciation of the vein and the occurrence of Fe-oxides (non-luminescent crystals). The matrix fragments in the brecciated vein display the same luminescence as the surrounded matrix.

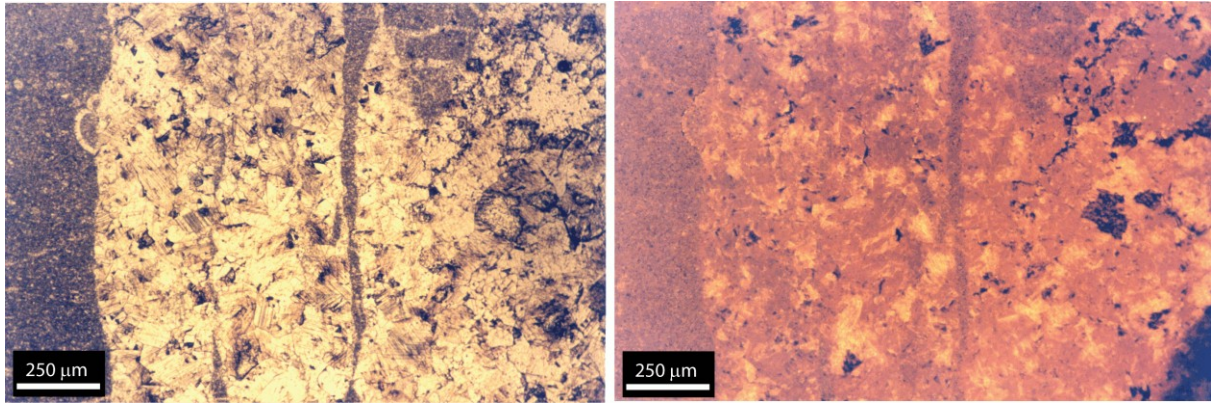


Figure 7.22. Respectively transmitted light and CL views of the Cal-6 cement, characterised by numerous brecciated fragments, which originate from the former veins.

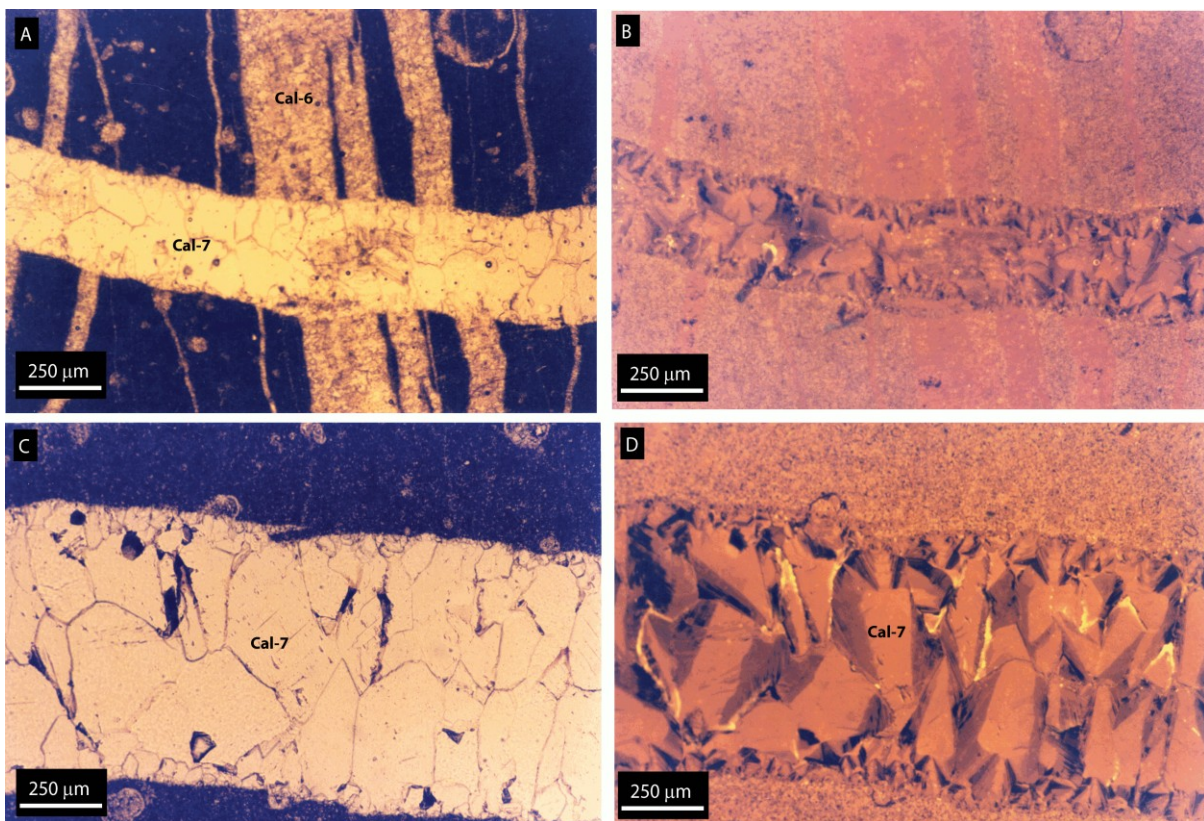


Figure 7.23. Photomicrographs of the Cal-7 cement. Respectively transmitted light and CL views: (A) – (B) of Cal-7 cement, which crosscut Cal-6 vein; (C) – (D) view on elongated calcite crystals, characterised by orange to non luminescent sector zoning.

7.4- Stable isotopes

Figure 7.24 and Figure 7.25 display stable isotope crossplots of $\delta^{18}\text{O}$ and $\delta^{13}\text{C}$ values respectively of the Upper Cretaceous to Eocene and Serravalian limestones and of the different diagenetic phases recognised in this study.

The studied Upper Cretaceous to Eocene host-rocks of the Kremenara anticline have $\delta^{18}\text{O}$ values comprised between -2.73 and -0.38 ‰ V-

PDB and $\delta^{13}\text{C}$ ranging from -0.42 to +3.22 ‰ V-PDB, consistent with the marine signature described by Veizer et al. (1999).

The Serravalian host-rock has a different isotopic signature, characterised by $\delta^{18}\text{O}$ varying from -1.72 and -0.89‰ V-PDB and $\delta^{13}\text{C}$ between -1.65 and +0.25 ‰ V-PDB.

The isotopic signature of Cal-1 shows a $\delta^{18}\text{O}$, plotting from -2.35 to -0.80 ‰ V-PDB and a

$\delta^{13}\text{C}$ from -0.80 and +1.28 ‰ V-PDB. The second fracture filling, Cal-2, covers a large area, determined by a $\delta^{18}\text{O}$ varying from -3.75 and +1.47‰ and a $\delta^{13}\text{C}$, plotting from -0.27 to +3.45 ‰ V-PDB. The isotopic signature of the brecciated veins, i.e. Cal-4, is characterised by $\delta^{18}\text{O}$ and $\delta^{13}\text{C}$, varying respectively from -3.00 to +2.84 ‰ V-PDB and from +0.16 and +2.10 ‰ V-PDB. The Cal-5 vein plots in a very narrow range with $\delta^{18}\text{O}$ from -2.64 to -2.71 ‰ V-PDB and exhibits $\delta^{13}\text{C}$ values from -0.86 to +1.11 ‰ V-PDB.

has a $\delta^{18}\text{O}$ varying between -3.10 and -0.03 ‰ V-PDB and a $\delta^{13}\text{C}$ from +0.76 to +1.44 ‰ V-PDB.

Except for the Cal-4 veins, which suggest an important hydrofracturing episode, all these signatures plot in a similar area, close to the signature of the Upper Cretaceous to Eocene marine carbonates (Chapter 4). This observation rather demonstrates that the fluid flow system was rock buffered and consequently the reactivity between fluid and host-rock was limited. The result is in agreement with the works realised in the same study area by Swennen et al. (1998), Van Geet et al. (2002), Breesch et al. (2007) and Dewever et al. (2007).

Cal-6 shows a $\delta^{18}\text{O}$ plotting between -4.87 and -0.53 ‰ V-PDB and a $\delta^{13}\text{C}$ from -0.71 to +1.98 ‰ V-PDB. The last determined vein, i.e. Cal-7,

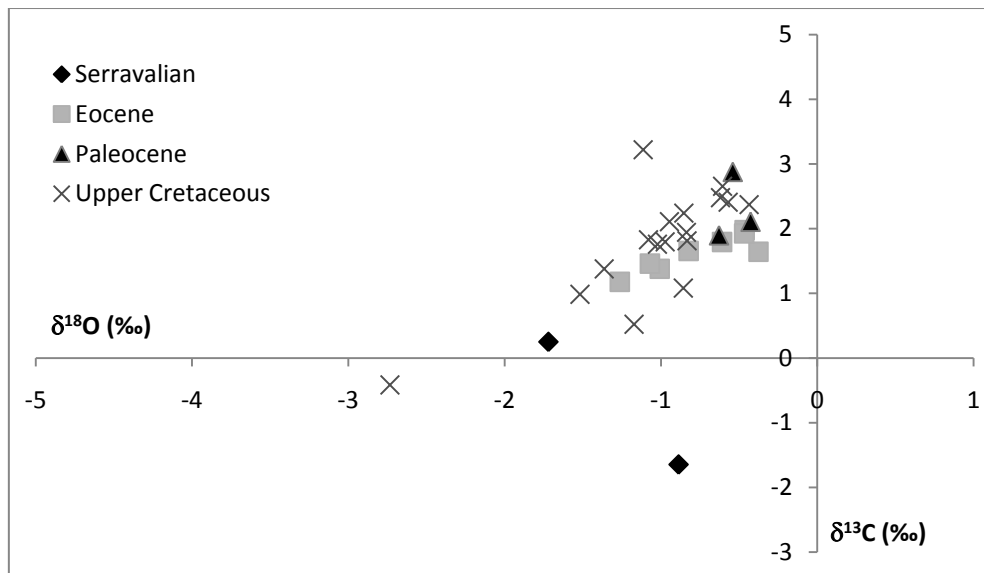


Figure 7.24. Carbon and oxygen isotopic signature of the matrix carbonates, which occur in the Kremenara anticline.

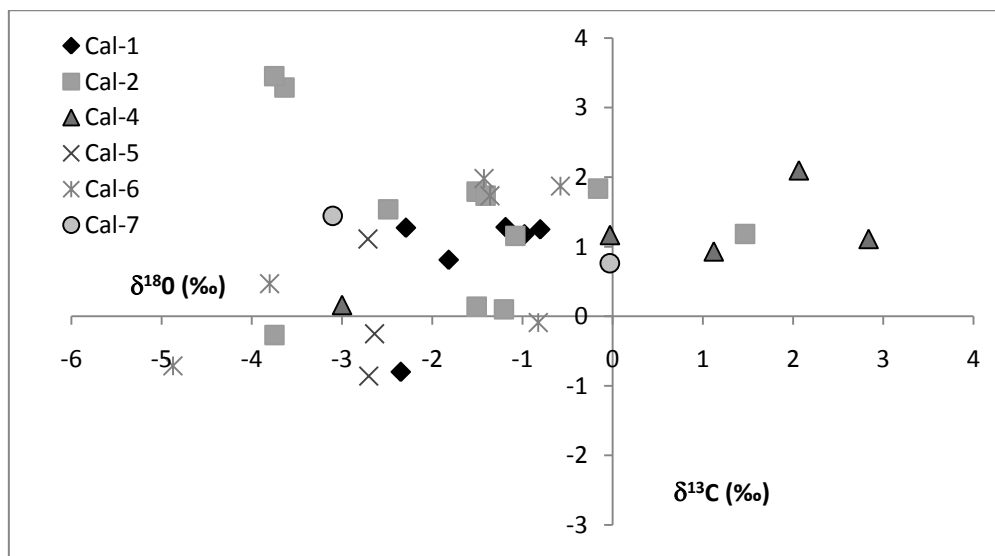


Figure 7.25. Carbon and oxygen isotopic crossplot of the successive calcite veins.

7.5- Interpretations

This diagenetic study is based on field observations, classical petrography, cathodoluminescence, and stable isotope ($\delta^{18}\text{O}$ and $\delta^{13}\text{C}$) signatures of vein cements. The fluid inclusion analysis was not successful due to the lack of stable fluid inclusions and does not appear in the report. Previous research was already in agreement with this observation, which is likely due to the occurrence of recrystallised calcite cements and/or to the successive compressive stresses. Based on

mutual cross cutting relationships (especially with stylolites) and petrographical characteristics, seven generations of veins have been recognised. The differentiation between hydrofractures, burial infill veins, those cemented by meteoric fluids or reused by oil migration allows to define the paragenetic sequence in this area. Until now, this study has unravelled a complex fracturing history (Figure 7.26) with the development of hydrofractures by overpressure conditions, whereby the fluid flow system was mainly rock buffered (Swennen et al., 1998, 2000; Van Geet et al., 2002).

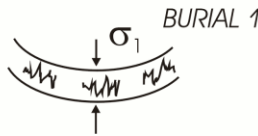
SYN/RE-DEPOSITIONAL		TIMING
EOGEN.	Early marine calcite cementation in platform settings	Pre-Oligocene
	Marine cementation in debris flows	
	Marine cementation in turbidites	
POST-DEPOSITIONAL		
MESOGENETIC	Fracturing/ FRACT0 / Cal-1 (N110° σ_1)	
	Compaction (bed parallel stylolite development) -hydraulic fracturing FRACT1 / Cal-2 (N70° σ_1)	
	Folding of the area (N110° σ_1)	
	Emersion of the area Re-opened FRACT1 / Cal-3 (N70° σ_1) FRACT4	
TELOGEN.	Fracturing -crack and seal vein cementation FRACT5 / Cal-4 (N110° σ_1) -hydraulic fracturing Re-opened FRACT1 / Cal-5 (N70° σ_1) FRACT6	
	Folding and faulting of the area (N110° σ_1) FRACT6 / Cal-6	
	Oil migration? Karst development/sedimentary infill FRACT7 / Cal-7 (E-W σ_1)	

Figure 7.26. Summary of the paleofluids and coeval paragenesis and its relationship with the tectonic evolution of the Kremenara anticline (adapted from Van Geet et al., 2002).

7.5.1- Pre-folding stage

The pre-folding stage is characterised by the development of fractures oriented N110° (FRACT0) and the subsequent precipitation of Cal-1. They predate the bedding-parallel compactional stylolites. Based on their CL and

isotopic signatures, Cal-1 likely developed during sedimentary burial of the reservoir. This cement is interpreted to relate to a N110° oriented compression.

Later on, the BPS developed simultaneously to the FRACT1 set, filled with Cal-2. This stage

accounts for the development of hydrofracturing that is demonstrated by the occurrence of brecciated fragments. This period is defined by the occurrence of a NE-SW compression and/or by a SE-NW extension, reflecting the flexure of the foreland contemporary with the burial in the basin. Based on the isotopic signature, the system was buffered by the host-rock. However, the most positive value of $\delta^{18}\text{O}$ of +1.47‰ V-PDB can likely be attributed to the occurrence of Cal-4 fragments in the vein, the latter displaying positive O-signature. A mixing of two cements could have been sampled for the isotopic analyses, explaining this positive value. Oppositely, the $\delta^{13}\text{C}$ values averaging +3.45‰ V-PDB are likely genetically linked to biodegradation-fermentation of hydrocarbons (Dimitrakopoulos & Muehlenbachs, 1987). The depleted $\delta^{18}\text{O}$ signature likely suggests that high temperature was involved. This is in agreement with the increase of the burial recorded by the development of BPS. This period could also be characterised by the generation of TS oriented NW-SE and NNW-SSE, since it predates the folding stage.

Cal-3 generation of veins postdates bedding-parallel stylolitisation but predates development of tectonic stylolites. Then, it can therefore be considered as syn-orogenic. Cal-3 precipitates in N70°, 90 fractures, associated to a NE-SW compression. The precipitation of non-luminescent calcite, which brecciates the previous Cal-2 vein, suggests the occurrence of high pore fluid pressure and a precipitation under oxic environment (Suchy et al., 2000). This cement therefore likely records the uplift and emersion of the Kremenara area. Based on the work of Swennen et al. (1998) and Nieuwland et al. (2001), this period corresponds to the Serravalian.

The folding of the structure is likely recorded by the development of FRACT3 and FRACT4 fracture sets, which show horizontal movement and generation of fractures in the outer arc of the fold respectively. An important observation here is a folding event, caused by a N110° compression that does not agree with the overall structure of the Ionian basin, which rather developed due to a N70° oriented compression. This stage is also characterised by the development of NE-SW oriented tectonic stylolites.

7.5.2- Post-folding stage

During the post-folding stage, some veins, such as Cal-4, formed by crack-seal process, whereas others, such as Cal-5, are characterised by an important internal brecciation. Therefore, these cements records episodes of high pore fluid pressure. More precisely, Cal-4, which cemented in FRACT5, is likely related to a N110° oriented compression, whereas Cal-5, cemented in FRACT6, was generated due to a N70° compression.

Both cements display similar CL features, characterised by orange to dull luminescence. The latter CL pattern suggests an evolution of the precipitation conditions, where no more cement precipitating under oxic environment is encountered. This likely records a second burial stage.

Based on isotopic results, Cal-4 is characterised by (1) several positive $\delta^{18}\text{O}$ values, attesting of a fluid system, which either was influenced by clay diagenesis (Boles and Franks, 1979) or interacted with Triassic evaporites and (2) a $\delta^{13}\text{C}$, suggesting a buffering by the host-rock (Van Geet et al., 2002). One negative $\delta^{18}\text{O}$ value of -3.00‰ V-PDB is similar to the host-rock signature and can be explained by a rock buffering.

Consequently two main principal maximum stresses occurred successively or even simultaneously during the post-orogenic stage. A N110°-oriented compression has been recorded in every location in the Kremenara anticline, whereas the N70°-oriented compression was only determined in the Poçem area, in the southern part. During this period, the NW-SE transversal faults likely formed, as they developed after the folding stage due to a NE-SW compression. These faults caused the compartmentalisation of the Kremenara anticline and the development of deep structures, which will play an important role in the petroleum system.

At this stage, FRACT6 was also cemented by Cal-6 cement, suggesting a still active N70° compression. This period was also associated to the oil migration through fractures, because all previous fracture sets display oil impregnation, with the exception of FRACT7.

The last recorded vein, i.e. Cal-7, is characterised by bright to non luminescent sector zoned calcite and precipitated in N-S oriented FRACT7. These

fractures either relate to an E-W compression or to the folding process, developed by a NNW-SSE compression. The existing CL pattern is often interpreted as meteoric cement, which formed at shallow depth and low temperatures (Meyers, 1974, 1978; Grover and Read, 1983). The bright zones reflect precipitation in a suboxic environment and the non-luminescent areas could have formed under oxic environment. This suggests that the Kremenara anticline has been uplifted and likely eroded before cementation took place. The orientation of

the FRACT7 may also be related to a reorientation of the compressional stress in the vicinity of the Vlora-Elbasan transfer zone (Swennen et al., 1998).

Finally, the last recorded fractures, which are uncemented, developed in the northern part of the anticline and demonstrate a NE-SW orientation. They likely relates to a NE-SW compression.

CHAPTER 8- Fluid-flow modelling

The aim of this part of the study is to gain some insights into the deformation/fluid flow history during the FTB development. Basin-scale modelling techniques are required to understand the velocity and trends of fluid migrations, pore fluid pressures, temperature evolution of the basin, natural hydrofracturing and the hydrodynamic behaviour of faults. However, before being able to perform a coupled thermal and fluid flow modelling, a good knowledge of the basin scale structural geometry and history is needed.

The present chapter summarises the workflow and the results of an integrated study using surface and subsurface geological data and IFP's basin modelling tools along a regional transect. 2D-coupled kinematic (forward)/stratigraphic modelling, realised by Barrier et al. (2003), was used to provide an intermediate boundary conditions for a regional 2D fluid flow modelling using the Ceres software (Schneider et al., 2002), allowing to elaborate a better structural scenario.

The chapter will present also the overall geological background of the studied transect and the input data. Implications of these results (1) to constrain the diagenetic and structural studies realised on different reservoir analogues and (2) to refine exploration strategies, presented and discussed in the conclusions.

8.1- Previous work: Coupled 2D-Kinematic/stratigraphic modelling

Barrier et al. (2003) compiled two balanced cross-sections in the Outer Albanides (Figure 8.1). In this part, the workflow of the 2D-kinematic/stratigraphic modelling she applied on these sections and the result sections, which will be used as input data for the Ceres modelling, is described.

8.1.1- Edition of the section

The first stage relates to the building of a regional structural balanced cross-section with lithological attributes, representative of the present-day deformation state of the studied area. In this study, the present-day cross-sections were build using geological maps, well data (ages, lithologies and seismic velocities from well logs and cuttings) and depth-converted interpreted

seismic data (Figure 8.2). In the Albanides, the seismic data provide also a strong control on the architecture of pre-, syn- and post-kinematic strata and their space-time relationships with faults and folds. These observations allow to sequentially retro-deform the present day cross-sections to reconstruct intermediate deformation states.

The methodology used first selects a specific stratigraphic horizon in the structural section. An approximate topographic profile selected for the chosen time step is drawn using the depositional environments (alluvial to deltaic and/or turbiditic deposits for example) within the sedimentation area. The paleo-topography is further extrapolated in the eroded domains. The selected horizon is then unfolded and unfaulted, keeping its length constant, to fit the topographic profile. Finally, the stratigraphic markers below the selected horizon are also restored with the same amount of deformation, while shallower horizons are successively deleted. Proceeding in this way from the more recent horizon to the older ones provides a series of cross-sections supplying time constraints for the kinematics, erosion and sedimentation in the studied area. The output from cross-section balancing (Figure 8.2) provides the pre-orogenic sections. These intermediate geometries are then used as an input data for forward kinematic modelling. A first geological model is thus built, that can be improved by a trial-error process using kinematic and stratigraphic numerical modelling.

8.1.2- Coupled Thrustpack-Dionisos forward kinematic and stratigraphic modelling

The 2D kinematic evolution of the Albanian sections was modelled with the Thrustpack software that uses an algorithm based on the kink-band method for fold-bend folds proposed by Suppe (1983). The Thrustpack simulations consist in performing a series of forward time steps to reproduce successive deformations (faulting, folding and flexure) on the basis of the geological restored cross-sections (Sassi and Rudkiewicz, 1999; Sassi et al., 2007). In this software, the observed geometry of the syntectonic deposits and of the coeval fault paths is drawn at each stage before applying the tectonic offsets. Former strata located above

erosional unconformities are then erased before to initiate the next kinematic stage.

Finally, the software calculates the compaction in the section between two deformation steps, depending on the lithologies given by the user for each new sedimentary layer. A reasonably good fit to the observed section geometry can be

obtained in this way, in spite of the restrictions imposed by the fold-bend fold model. There are however no real constraints on the topographic profiles reproduced into the Thrustpack modelling, except those approximated from the geological profile and the distribution of sand/shale.

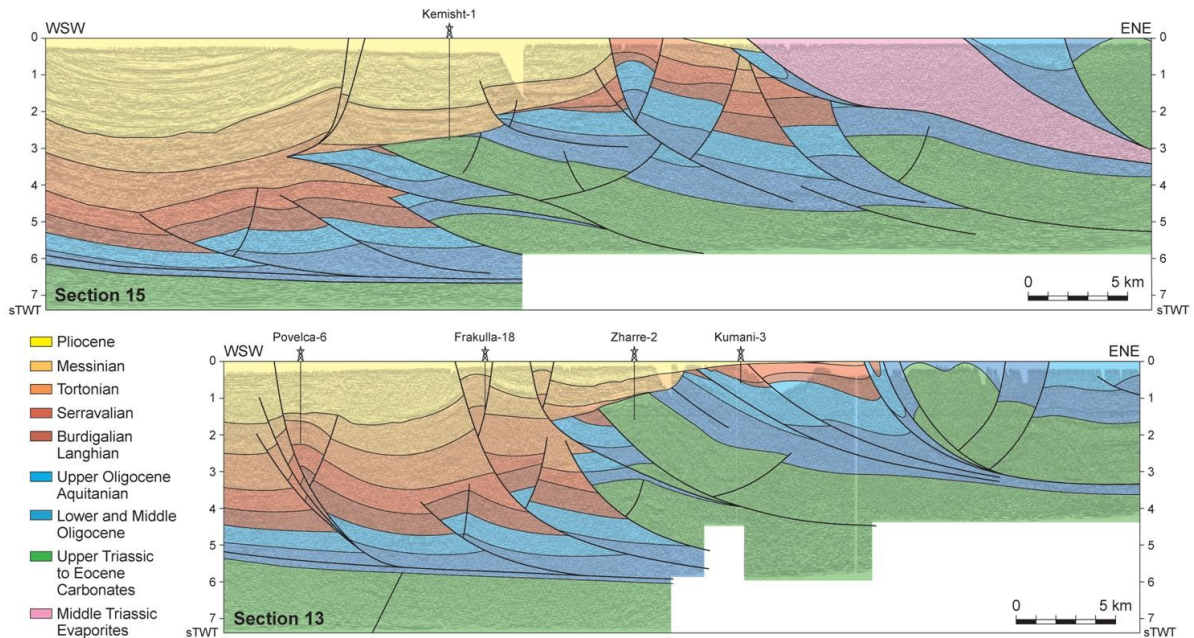


Figure 8.1. Two seismic profiles, which are located in the Outer Albanides, interpreted by Barrier et al. (2003).

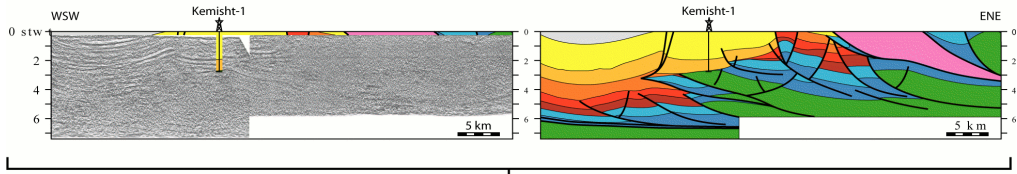
The 2D stratigraphic evolution of the Albanian sections was also modelled with the Dionisos software. The Dionisos software is a multi-lithological dynamic-slope forward computer model that uses deterministic physical laws to simulate the transport of sediments in 3D (Granjeon and Joseph, 1999). In the Dionisos simulations, the interactions between three main processes (accommodation, sediment supply and sediment transport) are numerically solved at each time step. The changes of accommodation are linked to the basin deformation, induced by tectonic movements and sediment loading, the sea level variations and the sediment compaction. The supply of sediments can either derive from the erosion of adjacent source areas (i.e. clastic sediments), or result from an in-situ production controlled by ecological rules and physical parameters such as water depth and wave energy (carbonates). The transport of

sediments is simulated using two sets of water-driven diffusive equations in order to reproduce the interaction between the long-term fluvial and gravity transport, and the shorter-term transport induced by catastrophic floods, slope failures and turbiditic flows. The numerical quantification of the interactions between accommodation, sediment supply and sediment transport leads to a 4D (x , y , z and t) model that represents the evolution of the stratigraphy and the topography of the studied area through time.

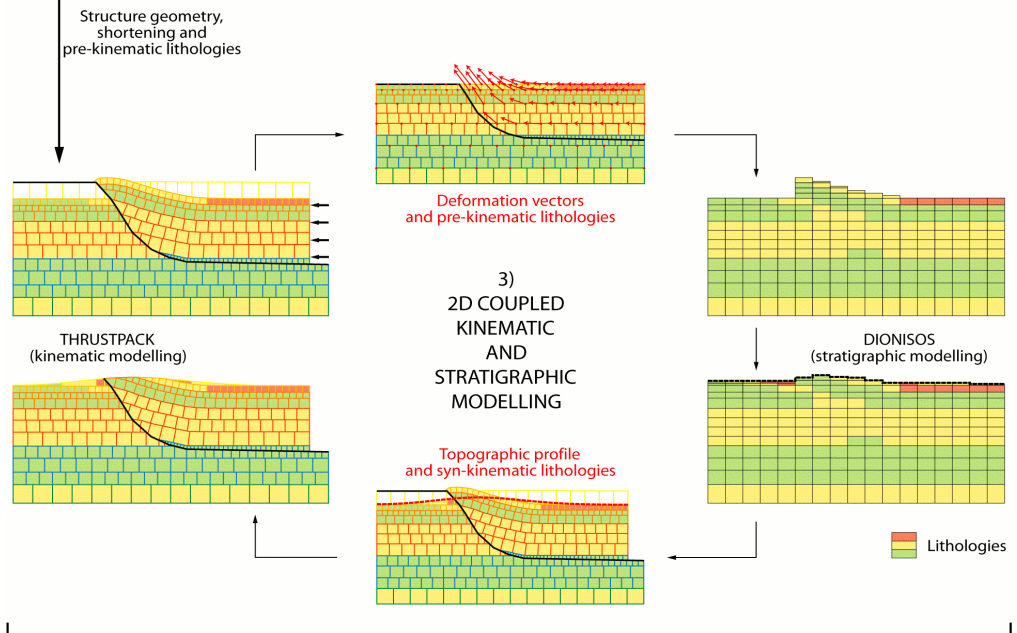
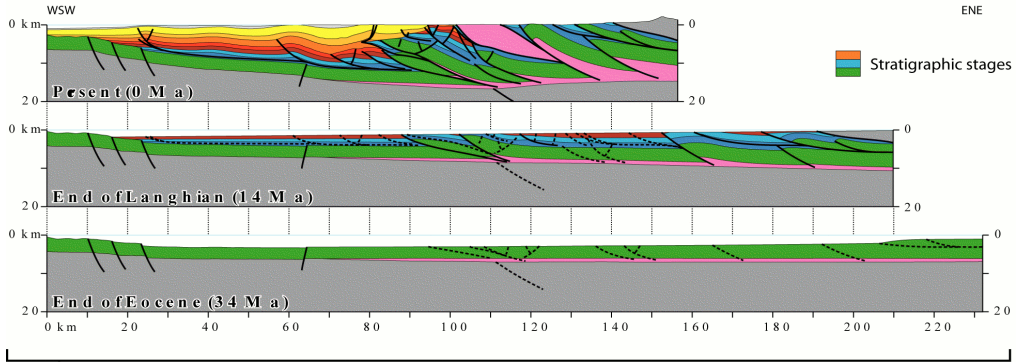
As many other stratigraphic computer model, Dionisos was first developed to simulate the vertical tectonic movements that are a component of the accommodation space. Although it can now reproduce some horizontal displacements such as listric normal growth faults, Dionisos is not yet able to reproduce such tangential offsets repeating layers as thrusting.

Figure 8.2. Workflow of the coupled structural/stratigraphic forward modelling. See explanation in the text.

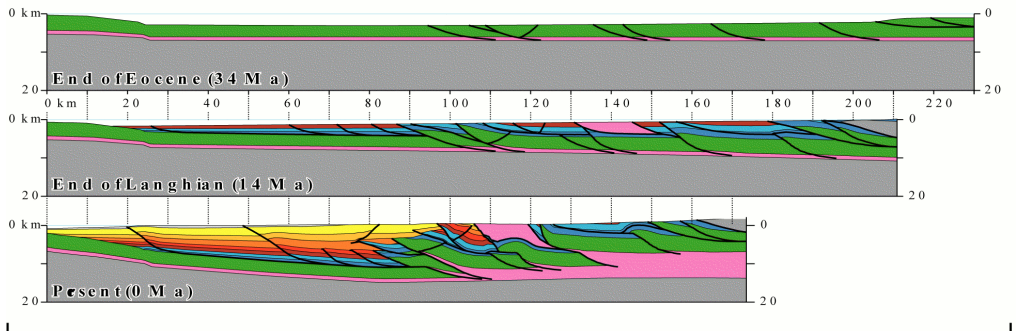
1) FIELD, WELL AND SEISMIC DATA INTERPRETATION



2) BALANCED CROSS-SECTION AND SEQUENTIAL RESTAURATION



4) KINEMATIC TEMPLATES FROM THRUSTPACK



5) 2D COUPLED THERMAL AND FLUID FLOW MODELLING (CERES)

This is why a newly developed coupling between the Thrustpack and Dionisos softwares was tested in this Albanian study. The coupled kinematic and stratigraphic modelling consists in a data exchange between the two softwares, each one supplying the other one with complementary information (Albouy et al., 2003; Barrier et al., 2003) (Figure 8.2). At the end of each kinematic stage, Thrustpack exports towards Dionisos the initial topography and lithologies of the model surface, as well as its vertical displacement vectors corresponding to the underlying thrusting, folding and flexural deformation. On the basis of these inputs, Dionisos incrementally performs a simulation of the accommodation changes, the sediment supply and the sediment transport on the duration of the same kinematic stage. Dionisos then sends back to Thrustpack a template for the final topographic profile of the stage, which in that case takes into account the physics of the erosional and depositional processes.

Incremental Thrustpack kinematic stages can finally be performed again using the new information on the topography and if needed, on the lithologies also calculated by Dionisos for the syntectonic deposits between the well data. At the end of this geological computation, the structural, stratigraphic and topographic knowledge of the area is considerably improved and the final geometric results of the Thrustpack modelling can be ultimately used as intermediate boundary conditions / templates for a regional 2D coupled thermal and fluid flow modelling using the Ceres software as described below.

8.2- Ceres workflow

The Ceres software, developed at IFP and commercialised by Beicip-Franlab, is a 2D-basin modelling that allows to model sedimentary basins and understand the petroleum systems in complex structural environments, such as salt-driven tectonic areas, (diapirism) and foreland fold-and-thrust belts, where blocks are displaced along faults (Schneider et al., 1993, 2002).

In addition to the simulation of overpressures and fracturing, the Ceres software is able to model the formation and evolution of the petroleum system by reconstructing the hydrocarbon generation and migrations but also to trace the changes in the water flow through time. In this way, a coupling of the thermal evolution, the diagenetic processes, the

deformation history and the fluid pathways is required to replace the fluid migrations within the kinematic evolution.

In this project, the fluid flow modelling was used to study essentially the impact of the faults on the fluid migration, to determine whether they acted as fluid barriers or drains, to quantify the fluid flow, and to reconstruct the pore fluid pressure history of the sub-thrust reservoirs, which govern the generation of hydrofractures.

To carry out such study, the work flow operates in three main steps (Schneider et al., 2002), which are the edition of the *initial section*, the *restoration* of the section and finally the *forward simulations*. Unlike Thrustpack, the use of Ceres implies a backward restoration.

8.2.1- Edition of the initial Ceres section

The *initial section* can be edited on the screen or using a template geometry imported directly from another study or other softwares, such as Thrustpack (i.e. the final section that is equivalent to present-day geometry). At this stage, it is recommended to use a structural software that is able to balance the section, such as Locace, 2D Move, Restore or 2D-GeoSec softwares (Gibbs, 1983; Moretti et al., 1988; Moretti and Larrère, 1989; Tozer et al., 2006). First, the number of horizons, the corresponding number of layers, the age of the horizons and the sea level (bathymetry) are edited with the chronostratigraphic editor. Subsequently, the geometry of the section is defined (Figure 8.3 A & B) and the geological markers and attributes (Figure 8.3 C to F) are assigned, including the horizons, faults, décollement levels, section boundaries and finally the lithologies, which may evolve spatially but not in time. The sub-domains are then defined as small independent kinematical units or “blocks”. The meshing, which is specific for each “block” (Figure 8.3 G), is built with no constraint coming from the other blocks. Geometrically, the initial section holds its sedimentary part, the brittle upper crust as well as the ductile lower crust and the Moho.

8.2.2- Restoration of the section

The section is then restored with a backward process, where the intermediate geometries built with Thrustpack are directly used as templates in Ceres to rebuild the eroded parts and to perform the displacements along faults.

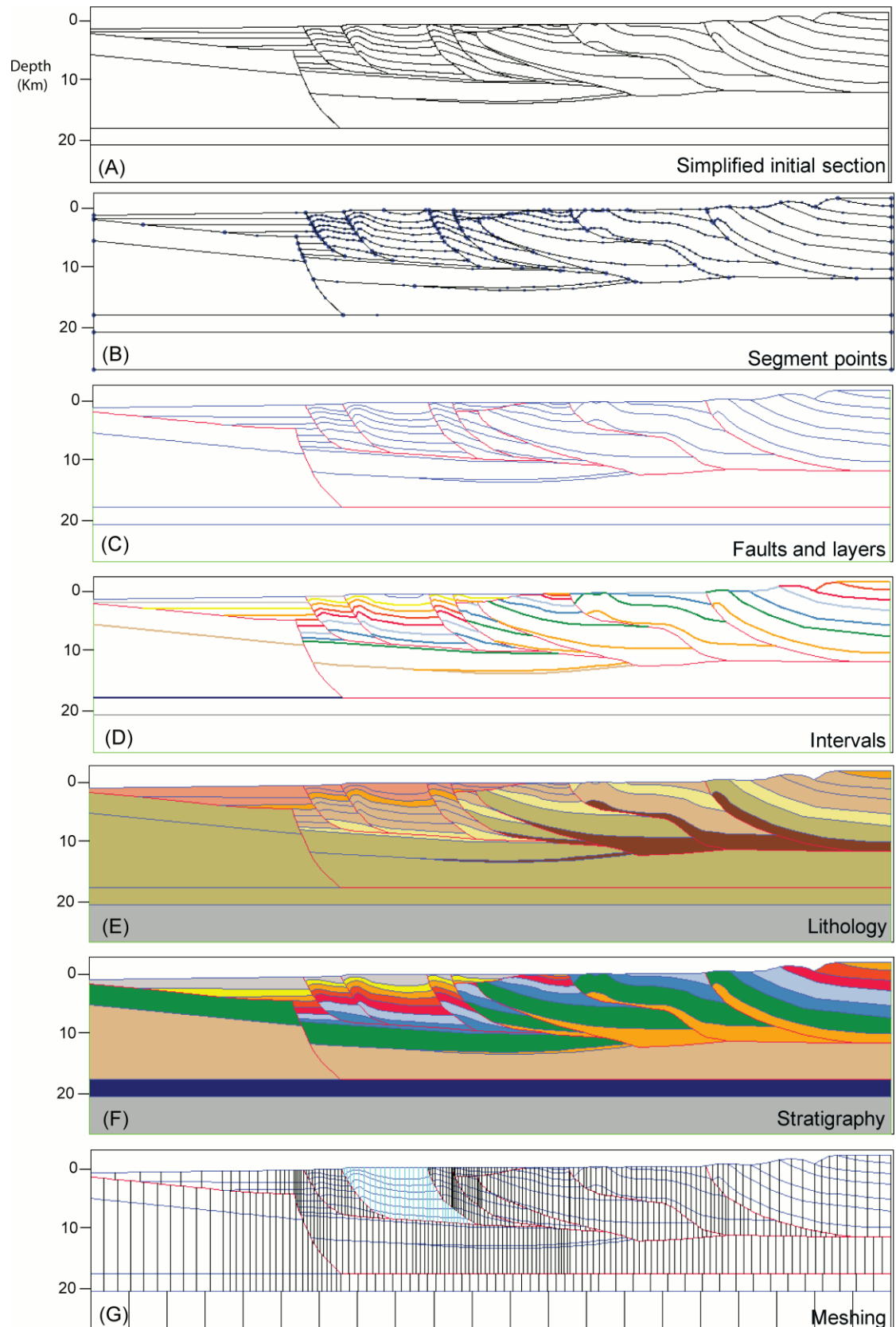


Figure 8.3. Main steps, defining the work flow of the section editor: (A) – (B) edition of the present-day geometry and the definition of segment points; (C) to (F) edition of the geological attributes; (G) definition of the kinematics blocs and building of the meshing for each bloc.

Once the erosion and the sedimentation are accounted for, the resulting section is automatically backstripped, restored and uncompacted using porosity-depth laws, which are related to the initial lithology distribution (Schneider et al., 2002). At this stage, the displacement along individual faults is applied using translations and vertical shear. As for the edition of the eroded parts, this operation may be facilitated by the use of templates as it was the case for the present study. Once the thickness is restored, the last step of the backward simulation requires the correction of local inconsistencies in the computed thicknesses that result from the use of the vertical shear as restoration mode. A correction of the eroded part may be also done at this stage. However, this step allows mainly to account for salt or mud tectonics and diapirism as well as related thickness modifications. These steps were done for each layer of the initial section at present. The final scenario of the restoration is then validated using input data derived from former kinematic studies.

8.2.3- Forward simulations

The last step is a forward modelling coupling the fluid flow simulations, the heat transfer, the hydrocarbon formation, the compaction and pore space evolution, the building up of overpressure, etc... To solve the problems of permeability and pore saturation in complex tectonic setting, Ceres defines several sub-domains, the boundaries of which being mainly defined by faults and model boundaries. The principal equations are mass conservation of solid and fluids (i.e. 3 phases: water, oil, gas), coupled with Darcy's law (porosity), modified Koseny-Carman's formula (intrinsic permeabilities; Schneider et al., 1996) and compaction law (Schneider et al., 2002). Compaction at basin and at geological time scale is supposed to be vertical, and thus, does not take into account the effect of layer-parallel shortening.

The faults represent fundamental objects for fluid flow migration in basin modelling (Yielding et al., 1999; Billi et al., 2003). They have a constant thickness and three options have been implemented to handle their permeabilities and long term behaviour. Faults can either be assumed as pervious (i.e. first option) or impervious (i.e. second option), being then considered as a flow barrier (Brown, 2003; Bretan et al., 2003). Alternatively their permeability can also evolve through times

according to the neighbouring lithologies (i.e. third option). This anisotropic behaviour can be modified also by taking into account the fault velocity (i.e. the strain rate). Whatever option is chosen, the faults are considered as inactive when their velocities are slower than the defined speed limit of 50m/Ma (i.e. a fixed threshold value by Ceres). In that case, the fault permeabilities are decreased by a factor $\alpha < 1$ (i.e. $K = \alpha K_f$). However, if the faults are active, i.e. determined by a velocity higher than the speed limit, their permeabilities increase by a factor $\alpha > 1$ (i.e. $K = \alpha K_f$). Then, the fluids will be able to migrate more easily through the faults. In the framework of this study, the three options have been modelled but only the third option, where the permeability is dependant to the lithologies on both sides, is illustrated in detail. A brief comparison with the two other options, considering the faults as either impervious or pervious, was carried out.

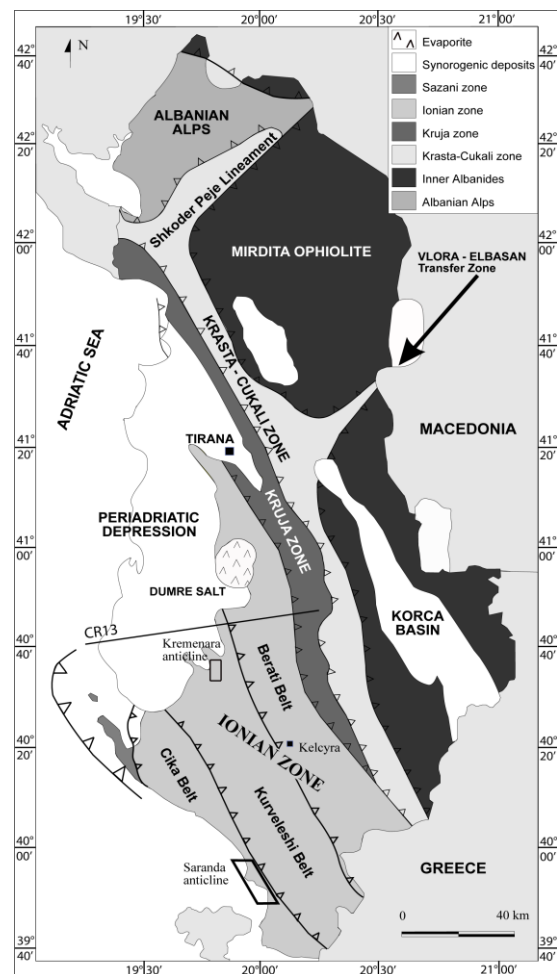


Figure 8.4. Structural map of the Albanides with location of the CR13 line, which represents the geological profile interpreted from seismic line.

8.3- Case study: the Albanides transect CR13

The east-west transect CR13 is located in the internal Albanides and passes south of the Vlora-Elbasan transfer zone, close to the location where most of the major Albanian oil fields occur, as indicated in the Figure 8.4.

The eastern part of the CR13 profile crosses various tectonic units, i.e. the Kurveleshi, the Berati and the Kruja units, which crop out at the surface. In the western part, the transect extends across the Peri-Adriatic Depression, which comprises the most external units.

As previously described, the first step consists in the construction of the initial section (i.e. present day stage). This has been performed with data coming from the interpreted seismic line (Figure 8.5 (1)) and the wells data. Due to numerical consideration, i.e. especially the restoration mode, the initial cross-section was simplified from the forward kinematic modelling to perform a backward fluid flow modelling using Ceres 2D. The principal simplifications essentially relate to the fault structures (i.e. flower structures, backthrust faults, ...), as indicated by red circles in the Figure 8.5.

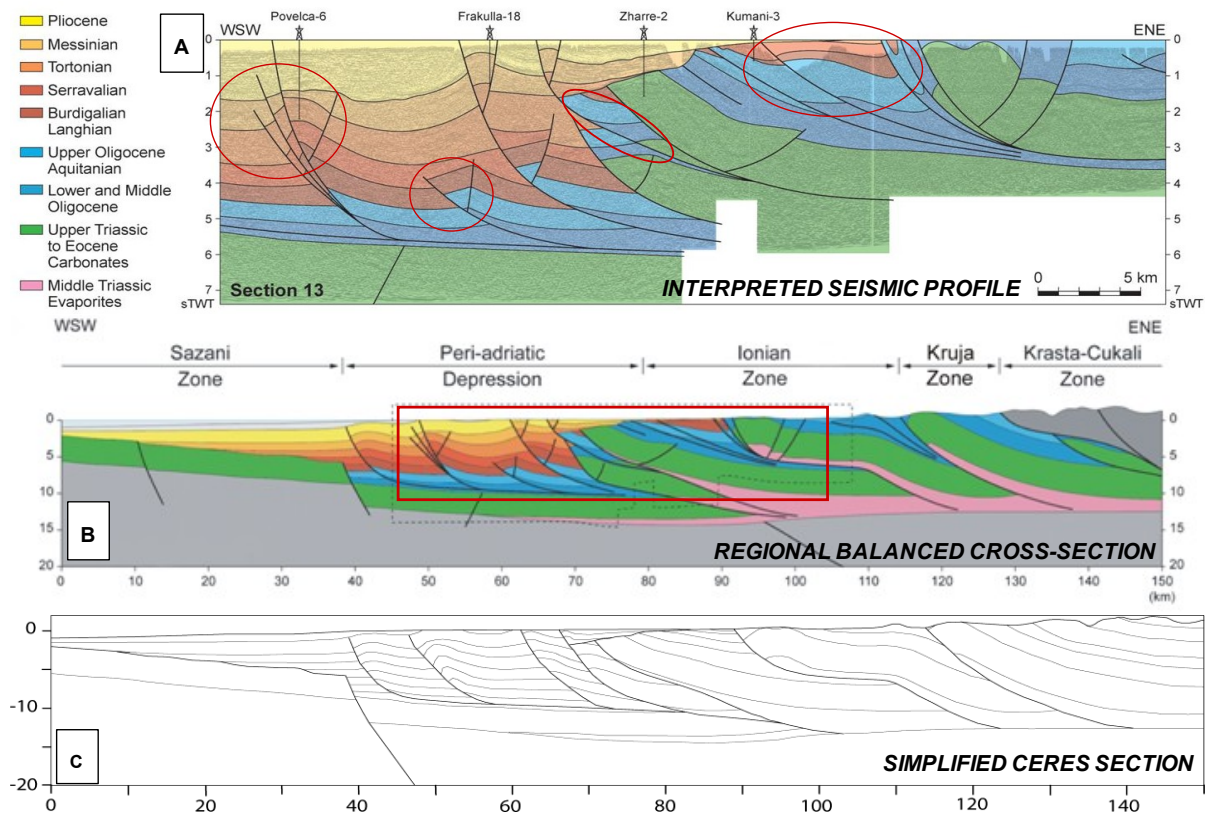


Figure 8.5. Successive steps for the simplification of the profile from the seismic interpretation to the Ceres section. The upper figure (A) represents the interpreted seismic profile, displaying its detailed geometry (from Barrier et al., 2003). The middle transect (B) is the regional balanced cross-section (from Barrier et al., 2003) and the lower profile (C) is the simplified section used for Ceres (fluid flow modelling). All the layers are represented but only the main faults can be implemented in the Ceres profile, due to numerical complexities. The areas with simplifications are indicated by red circles in the upper seismic profile.

8.3.1- The initial section

Figure 8.6 shows the simplified stratigraphic cross-section, which was used in the Ceres modelling. From east to west, the main tectono-stratigraphic assemblages comprise:

- The Kruja unit, representing the former Mesozoic platform during Triassic to Eocene

time, which separated two former basins, i.e. the Ionian and the Krasta-Cukali basins.

- The Berati and Cika tectonic units, which constitute a stack of basinal sediments. They have been deformed from the Oligocene onward (Swennen et al., 1999; Nieuwland et al., 2001) after the emplacement of the intern-most units. The Berati belt developed as an out-of-sequence

thrust from the Serravalian onward (Barrier et al., 2003)

- The Peri-Adriatic Depression (i.e. foreland) in the western part, made up of the Oligocene flysch and the Neogene molasse. This unit can reach a thickness locally up to 7 km.

As previously described, the kinematic evolution of the Albanides is strongly influenced by the occurrence of the Triassic evaporites, deposited during the rifting stage. These evaporites constitute the main décollement level in the Ionian Basin. In the western part of the profile, the décollement level changes to the base of the Oligocene flysch.

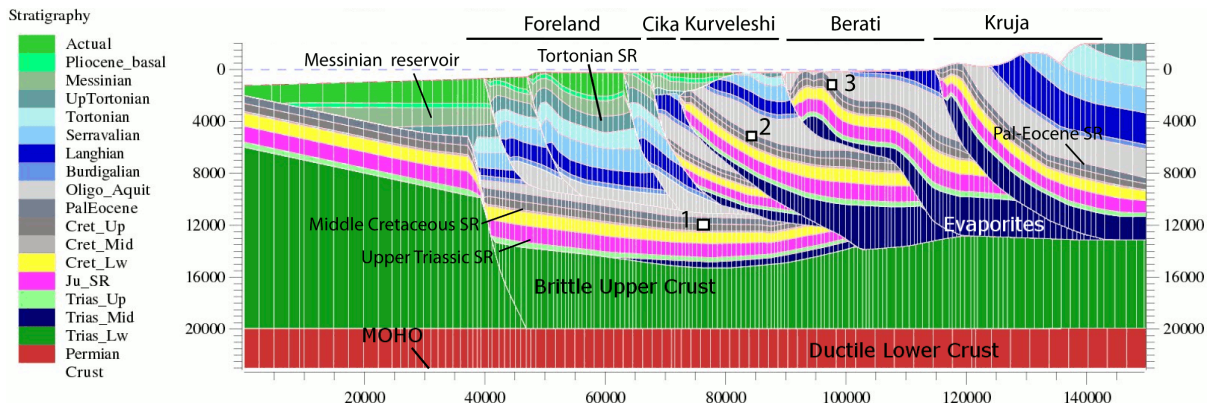


Figure 8.6. Distribution of geometries and lithologies of the present day CR13 section. The four main source rocks are indicated, i.e. the Upper Triassic, the Middle Cretaceous, the Paleocene-Eocene (Pal-Eocene), and the Tortonian source-rocks (SR). The locations “1”, “2”, and “3” were chosen to work out the distribution of the (over)pressure in the focussed Upper Cretaceous-Eocene carbonates interval along the profile through time.

8.3.2- Geological attributes

8.3.2.1- Distribution of the lithologies and porosities

The distribution of the lithologies is shown in the Figure 8.7. Their repartition is simplified and homogeneously distributed in stratigraphic intervals and in blocks. Small scale layers, such as intercalations of debris flow or individual organic-rich layers, were not taken into account due to numerical difficulties. Hence, the Upper Cretaceous to Eocene interval, which represents the main reservoir interval of the Ionian Basin, is characterised by a mudstone lithology, similar to the Lower Cretaceous interval. Another important simplification is the representation of the Upper Triassic to Jurassic source-rocks, which were regrouped into one thicker shale interval. The slumping horizons as well as the intercalated debris flows, occurring in the Upper Cretaceous to Paleocene reservoir interval, were not taken into account.

The resulting matrix porosity distribution displays an important feature, which is the low

porosity of the Oligocene flysch, made up of mixed sand-shale (30-70%) and of the Messinian - Early Pliocene. The latter consists of an evaporitic interval, which occurred homogeneously in the foreland. Another point is the preservation of 6-8% of matrix porosity in the upper Triassic, which is covered by the Upper Triassic - Lower Jurassic source rocks, characterised by a very low porosity.

Figure 8.8 displays the present-day distribution of the thermal conductivity, which is a function of the temperature and the lithologies. The Messinian and Triassic intervals have important values above $3\text{W}\cdot\text{m}^{-1}\cdot\text{C}^{-1}$, characterising a good conductivity due to the presence of evaporites. These evaporitic units will play an important role to transfer the heat from deeper levels towards the shallower surface, by following laterally the evaporitic intervals. In this case, the source rocks and reservoirs, located at a shallower depth and at the vicinity of evaporitic intervals, must increase their maturities.

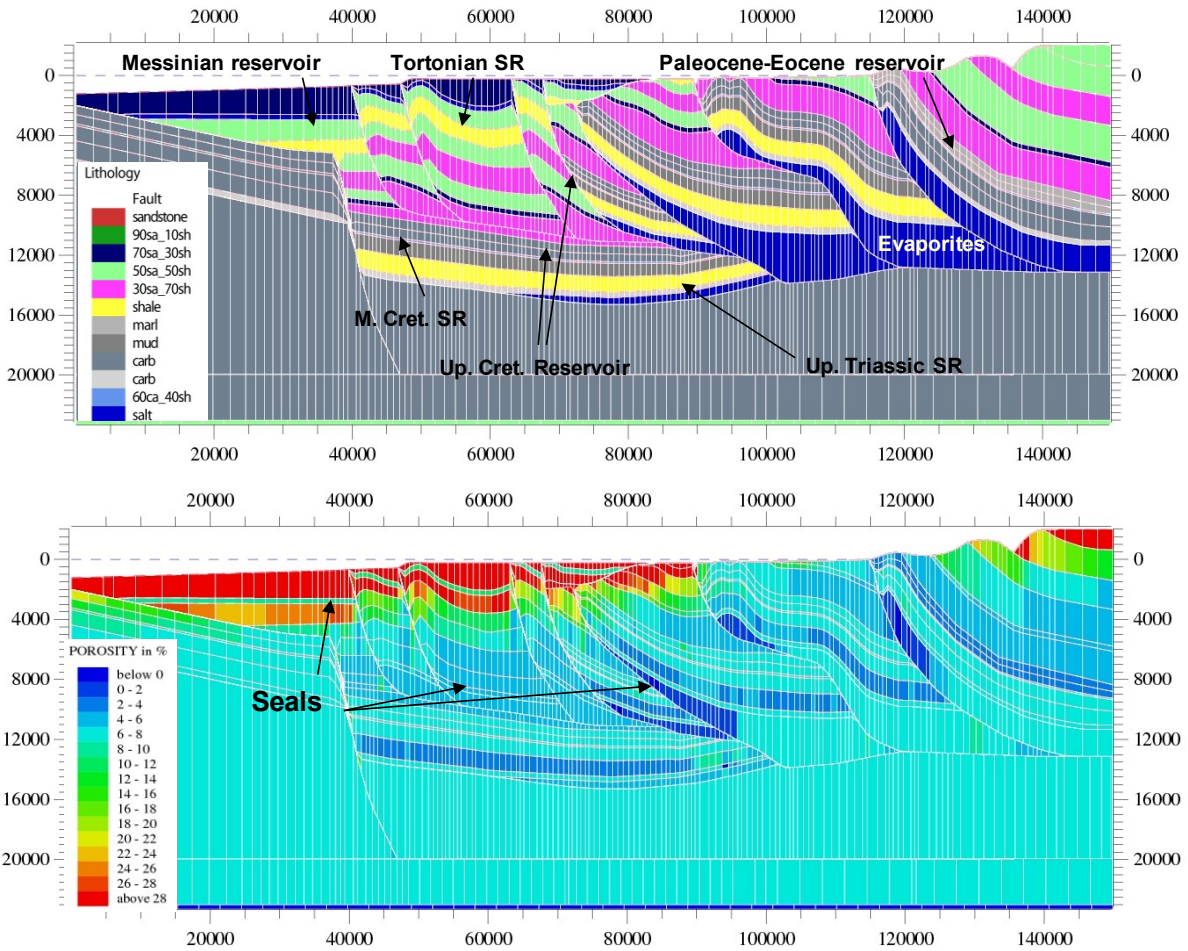


Figure 8.7. Distribution of the lithologies and of the resulting porosities in the CR13 section (Vertical and horizontal scales are respectively in kilometres and in meters).

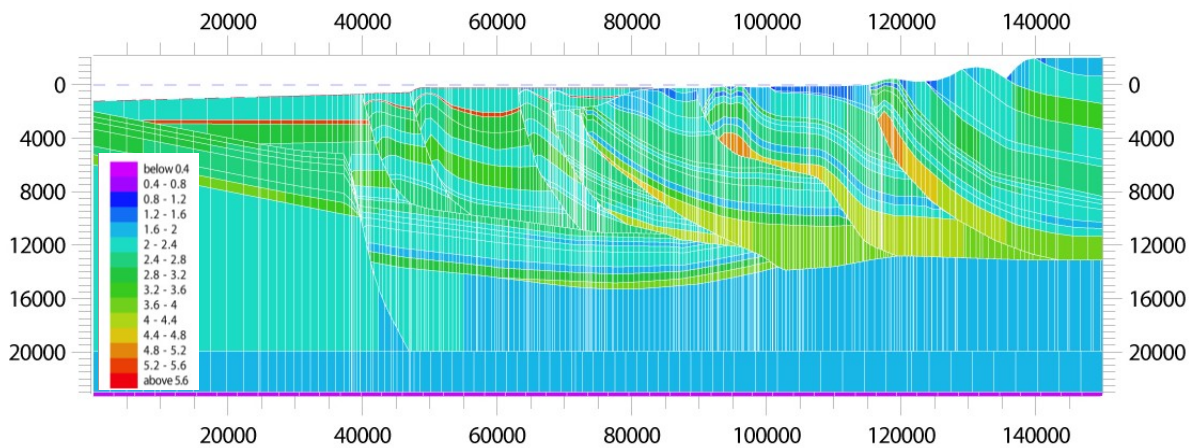


Figure 8.8. Distribution of the thermal conductivity (in $W.m^{-1}.^{\circ}C^{-1}$). Vertical and horizontal scales are respectively in kilometres and in meters.

8.3.2.2- Distribution of the source rocks, reservoirs and seals

For this modelling, four main organic-rich source-rock formations have been considered (Mattavelli et al., 1991; Curi, 1993; Speranza et al., 1995; Rigakis and Karakitsios, 1998): a) the Upper Triassic - Lower Jurassic blackshales, which are the main effective source rock, with TOC values up to 5,5%; b) the Middle Cretaceous bituminous shale and limestones with 1,5% of TOC; and c) the Paleocene – Eocene shaly limestone in the Kruja belt, where the TOC reached 3,5%. Their organic matter is of type I or type II of marine origin. A fourth source-rock, with organic matter of type III, occurs in the Peri-Adriatic Depression and consists of the Tortonian shales, with a TOC of mainly 3.5% (Velaj et al., 1999). They are indicated on the Figure 8.7.

As previously described, carbonate reservoirs range in age from the Upper Cretaceous to Eocene and essentially consist of pelagic facies of the Ionian Zone, characterised by a dual fracture-matrix porosity. Their reservoir

characteristics are largely enhanced by the presence of numerous open fractures. Other reservoir intervals, located in the Peri-Adriatic Depression, such as the Pliocene and Messinian sandstones, are oil/gas-bearing, sealed by the Messinian-Early Pliocene evaporites. The trapping mechanisms have a dominant stratigraphic control that must account for the seal capacity of the Oligocene flysch and the continuous Messinian evaporitic interval in the foreland. Alternatively, the sealing capacities can be modified by the occurrence of internal impervious faults and unconformities, as they occurred in the foreland. However, in places where the Oligocene flysch has been tectonically removed, the Triassic evaporites along the décollement level also constitute a composite stratigraphic and structural seal, i.e. in the Delvina oil field. These structures are well-defined, with the resulting porosity distribution in the Figure 8.7. According to the resulting porosity distribution, the Upper Triassic-Jurassic organic source-rock display also very low porosities and consequently has good stratigraphic seal characteristics.

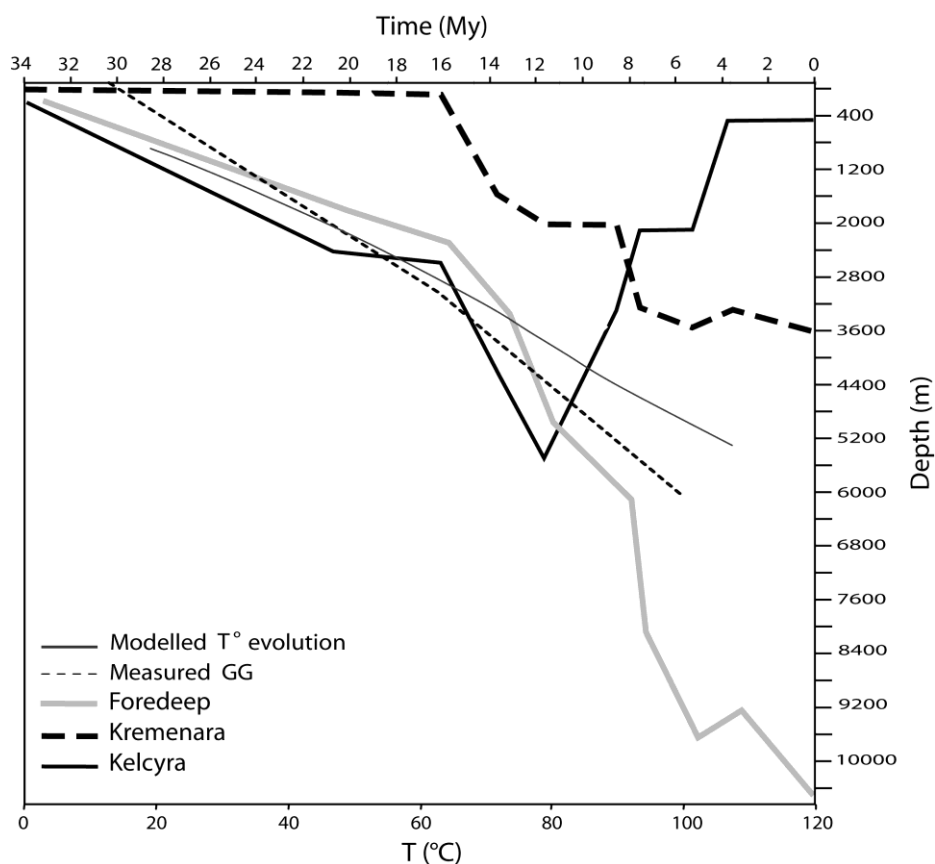


Figure 8.9. Burial curves of the main tectonic units, i.e. the foredeep, the Kurveleshi and the Berati belt. Two curves representing respectively the evolution of the geothermal gradient (input data) and the modelled temperature evolution through time (output data) are also indicated.

8.3.3- Burial curves of the studied tectonic units

The burial curves of the main tectonic units, represented on the Figure 8.9, have been derived from the kinematic modelling, described in the Figure 2.7. The burial curves show the evolution of three representative locations of the Upper Cretaceous petroleum reservoirs in the foredeep (1) and in the Kurveleshi (2) and the Berati (3) belts. Their actual depths were determined according to industry data and are indicated in the Figure 8.6. These curves were used in the previous chapters, with regard to the structural and diagenetic characterisation of reservoir analogues.

8.3.4- Limitations of the model

Although the input data of the petroleum attributes (i.e. kerogen and source rock editors) are very numerous, only few of them are well known. The main problem thus concerns the distribution of the lithologies. Due to numerical difficulties, lithologies have to be homogeneously distributed in a same block and therefore this small scale variation, such as local slumping intervals or lateral facies variations, cannot be taken into account. Their consideration would indeed increase largely the meshes, making consequently the restoration difficult.

In this project, three main generalisations were made:

- The first one relates to the distribution of the Triassic-Jurassic source rocks, which have been regrouped into one unique organic-rich layer, characterised by an homogeneous TOC and single type of organic matter.

- The second simplification occurs in the Upper Cretaceous – Eocene interval, which is characterised by a mudstone lithology (i.e. shaly carbonates), homogeneously distributed from west to east. Here, the occurrence of dual porosity, i.e. fractures and matrix, due to the presence of small-scale turbiditic and slumping horizons, could not be represented, minimising the real reservoir characteristics of this interval in the results (e.g. lateral and vertical connectivities within the reservoir interval).

- A third limitation is due to the simplified representation of the faults in the profile. Only the main faults are considered, involving the disappearance of some local structures, which may play an important role in

the petroleum system, such as flower structures or backthrust faults.

Consequently, the petroleum interpretation of the results should be made with caution, taking into account these simplifications, which were required to handle a realistic fluid flow modelling.

8.4- Thermal regime

Accurate forward structural modelling allows a direct control on the burial history of source rocks in foreland fold-thrust belt systems. However, one of the most important steps in the fluid flow modelling is the thermal calibration of the section, in order to predict a realistic maturity evolution of the source rocks, the timing of hydrocarbon generation and expulsion, and the possible way of hydrocarbon migration between the sources to the traps. In fact, the petroleum systems of a thrust belt are greatly affected by the thermal regime. First, the thermal regime controls source rock maturation and hydrocarbon expulsion and secondly, it affects the seal and reservoir rocks by controlling their deformational setting and diagenesis.

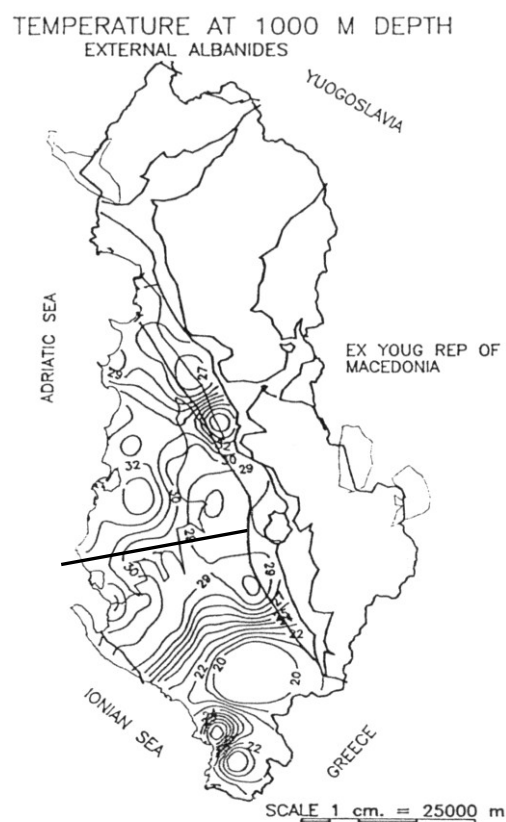


Figure 8.10. Actual geothermal gradient distributed in the southern part of Albania (from Frasheri et al., 1995). The black line represents the location of the CR 13 profile.

8.4.1- Initial data

Many paleothermometers have been used along the profile, such as Bottom Hole Temperature (BHT), present-day heat flow, temperature at the surface, crustal temperature, geothermal gradients (Figure 8.10, Figure 8.11), as well as petrophysical and laboratory data such as Vitrinite reflectance, Apatite Fission Tracks, microthermometry and Rock-Eval analyses. Even if the present-day temperature of buried reservoirs can be easily calibrated since this parameter is not too sensitive to its fluctuation through time, the difficult step remains to determine the best evolution of the heat flow in order to obtain an accurate present-day maturity repartition. In fact, the source rock maturation depends on the thermal history of the source rock section (Waples, 1992 a, b). In the case of source rocks deposited prior to thrusting, the thermal history of the precursor basin also becomes important.

8.4.2- Thermal Calibration

In the case of foreland-fold-thrust belts, the evolution of the heat flow, which occurs during the sedimentary filling of the flexured basin, is very difficult to determine, since folding and

thrusting stages are often associated with important sedimentation rates (i.e. flysch deposition). The intense flexuring may imply a blanketing effect in the thermal evolution due to low sedimentary compaction. It is usually followed by an important subsidence (i.e. filling of the accommodation space) during the episode of maximum shortening (Barrier et al., 2003). In this study, several hypotheses, based on the heat flow variation, have been tested, especially to determine the importance of the blanketing effect and to better constrain the model.

In the Albanides, low geothermal gradients exist at present, ranging from 15 to 20°C.km⁻¹ (Fraseri et al., 1995, 2005; Cermak et al., 1996) with generally an increase towards the east. These values are associated with anomalous surface heat flows as low as 30 to 40 mK.m⁻², with unclear distribution. In some places, strong variations of the temperature gradient are also observed mostly due to complex tectonic structures at the vicinity of salt diapirs (high conductivities), transfer zones (i.e. Vlora-Elbasan lineament) and local reversal in temperature gradient due to meteoric circulation through karst networks.

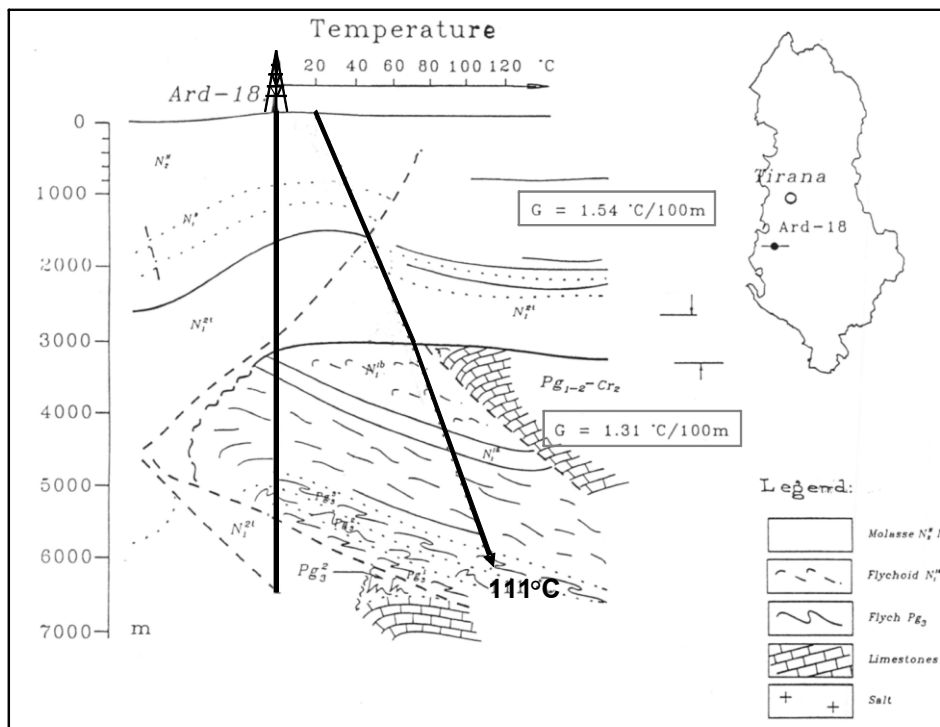


Figure 8.11. Geothermal profile from a well (i.e. Ard-18) located in the southern part of the Peri-Adriatic Depression (from Fraseri et al., 1995).

Here, two hypotheses, based on the heat flow variation will be precisely described. They are illustrated on the Figure 8.12. These two hypotheses correspond to the best fit obtained between computed temperatures and the actual thermal data. The heat flow variations were determined from the work realised by Allen and Allen (1990), consisting of a characterisation of the typical heat flow values for various types of sedimentary basins. The pre- to syn-rift period is characterised by high heat flow values, varying from 50 to 60 $\text{mW}\cdot\text{m}^{-1}\cdot\text{C}^{-1}$. These values are typical for active extensional basin with young rifts (Morgan, 1984). Then, the post-rift to passive margin period is defined by a decrease of the heat flow from 60 to 50 $\text{mW}\cdot\text{m}^{-1}\cdot\text{C}^{-1}$, i.e. hypothesis 1, and from 60 to 55 $\text{mW}\cdot\text{m}^{-1}\cdot\text{C}^{-1}$, i.e. hypothesis 2, which results of the thermal

subsiding rift and the beginning of the compressive regime. Afterwards, the Oligocene flysch and the Miocene molasse are deposited, accounting for a blanketing effect due to the fast sedimentation and the low compaction. This period is defined by a variation of the heat flow from 50-55 to 30 $\text{mW}\cdot\text{m}^{-1}\cdot\text{C}^{-1}$ and represents the most difficult period to calibrate in temperature. The two hypotheses presented here are only differentiated by the intensity of the blanketing effect.

The last stage shows homogeneous and low heat flow values of 30 $\text{mW}\cdot\text{m}^{-1}\cdot\text{C}^{-1}$, characterising the present-day thermal data. This heat flow evolution characterises the outer Albanides, i.e. the studied area, but does not reflect the heat flow evolution occurring in the hinterland.

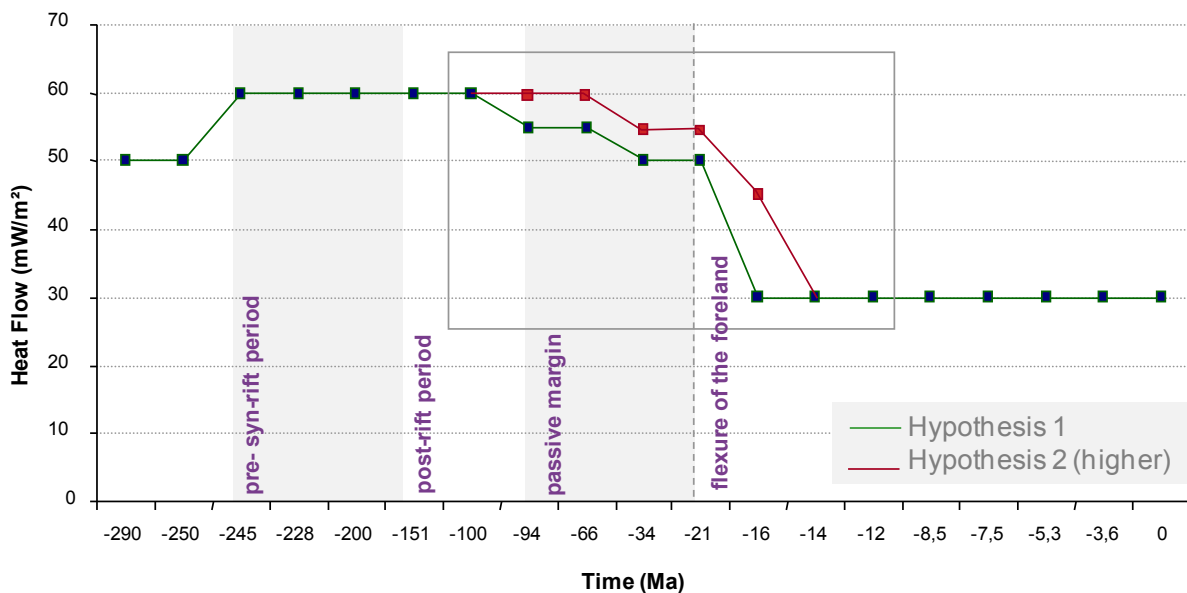


Figure 8.12. Heat flow variations through time for the studied E-W CR13 transect. Both hypotheses provide a good fit between the computed temperature and the present day data.

The two hypotheses based on heat flow variation (Figure 8.12) were tested to refine the calibration. Computed temperatures and R_o are reported in the Figure 8.13 with the actual geothermal gradient of $10^\circ\text{C}/\text{km}$, which evolves to $21^\circ\text{C}/\text{km}$ (Fraseri et al., 1995, 2005; Cermak et al., 1996) down and up to the Messinian sediments, i.e. at 3km depth. This change relates to the blanketing effect due to the fast sedimentation rate and the less compacted sediments. The low subsurface geothermal gradient can also be explained by the migration of meteoric fluid in karst networks, implying local cooling at the vicinity of fluid conduits.

With the present day data, the thermal calibration is quiet accurate for both hypotheses (Figure 8.13). However, the maturity can not be calibrated precisely, because no actual maturity data are located along the studied transect. The maturity values, represented in the Figure 8.13, characterised the Upper Triassic interval of the Sazani unit, the Lower Jurassic interval of the Cika unit and the Lower Cretaceous interval of the Kurveleshi unit, which are at present still covered by the Oligocene flysch. Consequently, the higher maturities might suggest that these sediments have been buried deeper than the post-Lower Cretaceous interval modelled with Ceres.

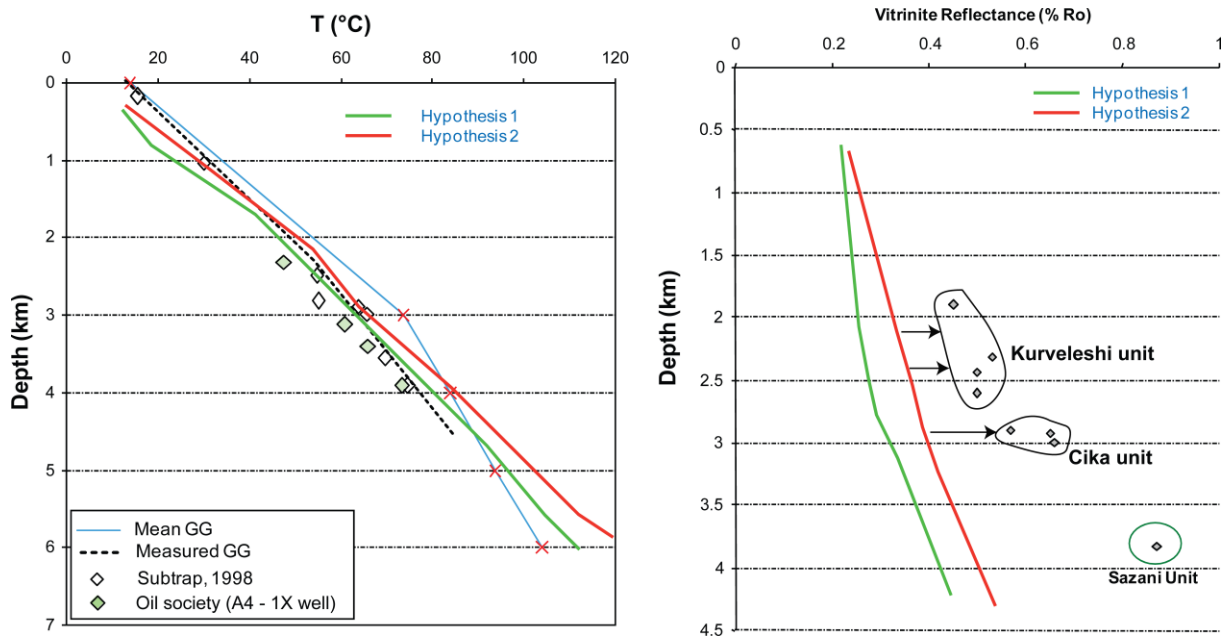


Figure 8.13. Present-day temperature and maturity evolutions for the two hypotheses, shown in Figure 8.12. The actual geothermal gradient and the thermal data, from industry data, used to calibrate the model are indicated in the diagrams. The dash line represents the modelled geothermal gradient from the computed temperature.

However, in order to balance the uncertainties, the hypothesis 2, characterised by higher maturity values, will be kept to carry on the fluid flow modelling. The resulting distributions of the temperature and the maturity are indicated on the Figure 8.14. The red-coloured wells indicate the locations of the present-day thermal data, from productive wells, used to constrain the model (Figure 8.13).

8.4.3- Maturity of the source-rocks

As previously described, source rock maturity is estimated either by the vitrinite reflectance values (Easy R_o ; Ardic, 1998), or through the transformation ratio (TR) that represents the advancement of the transformation of kerogen into hydrocarbon in percent. This has been computed for the four modelled source rocks: a) the Upper Triassic - Lower Jurassic black shales, which are the main effective source rock, with TOC values up to 5.5%; b) the Middle Cretaceous bituminous shale and limestones with 1.5% of TOC; c) the Paleocene - Eocene shaly limestone in the Kruja belt, where the TOC reached 3.5%, and d) the Tortonian shales in the Peri-Adriatic Depression. Their organic matter is of type I or II of marine origin, except for the source rocks in the PAD which is of type III.

8.4.3.1- Vitrinite reflectance

Sedimentary burial was already sufficient during the Aquitanian to already mature ($0.6\% < R_o < 1\%$) the Triassic source rocks in the still subsiding Ionian basin (Figure 8.15). Alternatively, shallower source rocks, i.e. the Middle Cretaceous black shales and the Paleocene-Eocene shaly limestones, remained largely immature ($R_o < 0.6\%$) until the Serravalian, when sedimentary burial ultimately forced them to enter the oil window ($0.6 < R_o < 1\%$).

During the Early Tortonian, the tectonic burial leads the Upper Triassic-Jurassic source rocks to partially enter in the dry gas window.

Since the Messinian (Figure 8.16), the Upper Triassic-Jurassic source rocks are overmature ($R_o > 2.2\%$) in the foreland, whereas in the thrust units they are still mature or in the condensate-gas window ($1\% < R_o < 1.4\%$). Only the top of the Kurveleshi belt is still immature, since this unit was uplifted at the onset of thrusting and consequently always remained at lower temperature. The Middle Cretaceous source rock is principally mature to immature in the Ionian tectonic units from the base to the top of the tectonic units. The maturity of the Paleocene-Eocene shaly limestone of the Kruja unit is higher and has reached the gas-condensate window.

At present, the majority of the source-rocks in the outer Albanides reached the condensate/wet gas window and some of them are overcooked, especially the source rocks, which have been underthrust beneath other tectonic units. Only the Kurveleshi unit, due to its early uplift and to the late out-of-sequence development of the Berati belt, demonstrates still an oil potential.

Finally, the model shows two main steps of maturation: the first one initiates during the sedimentary burial, which allows the Triassic to Lower Jurassic source-rocks to enter the oil window as early as the Aquitanian and to

increase the maturity of the shallower source rocks. Afterwards, during the syn-deformational stage, thrusting will help to keep the source rocks of allochthonous Ionian units in the oil window and to evolve slowly towards the condensate-wet gas window, whereas source rocks are overmature in the foreland from the Late Tortonian onward.

The variation in maturity of the Kurveleshi - Kruja belts can be explained by their early thrust emplacement during the Albanides evolution, allowing a low maturation of the source rocks.

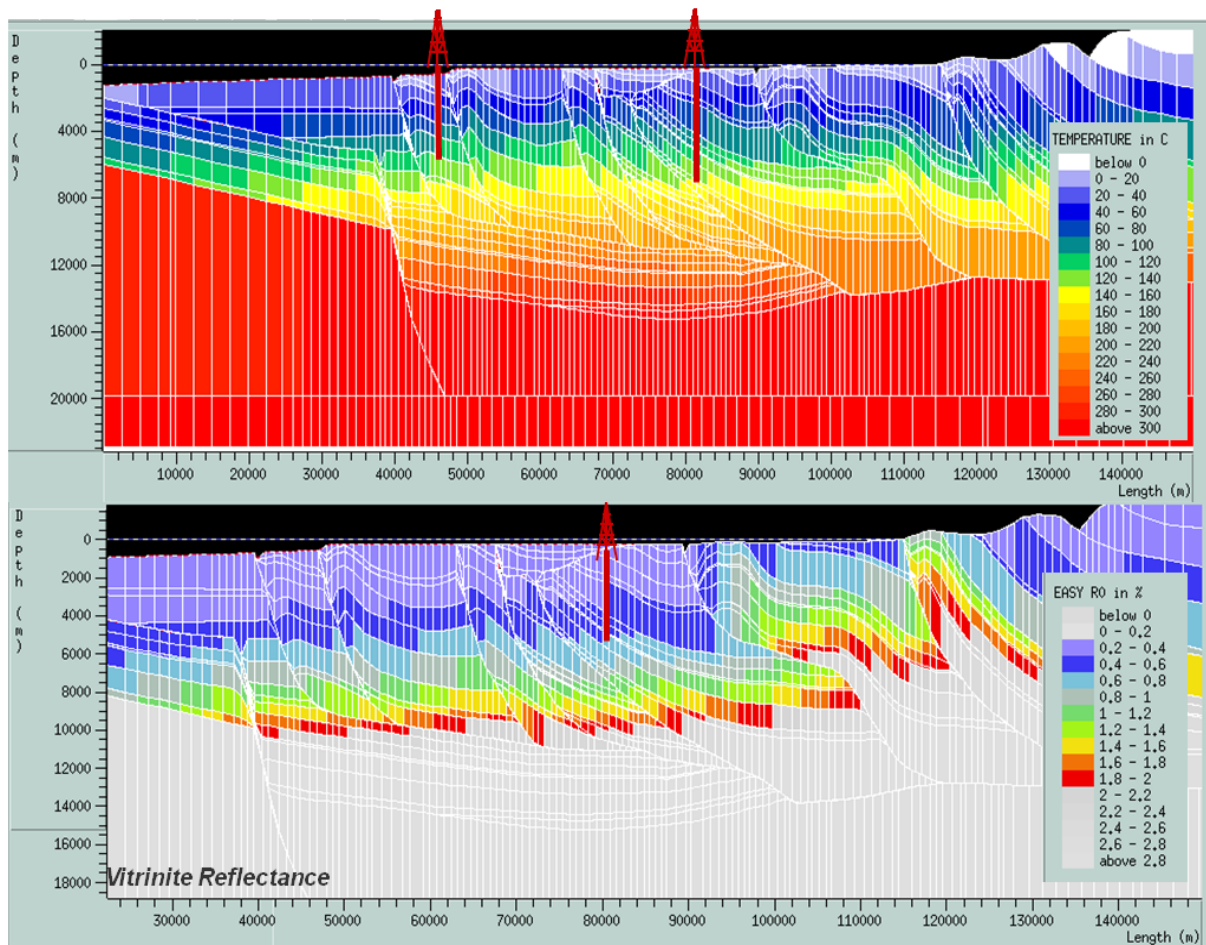


Figure 8.14. Ceres section showing the distribution of the temperature in °C (top) and the Ro in % (bottom) for the hypothesis 2. The productive wells used to constrain the model are indicated in red.

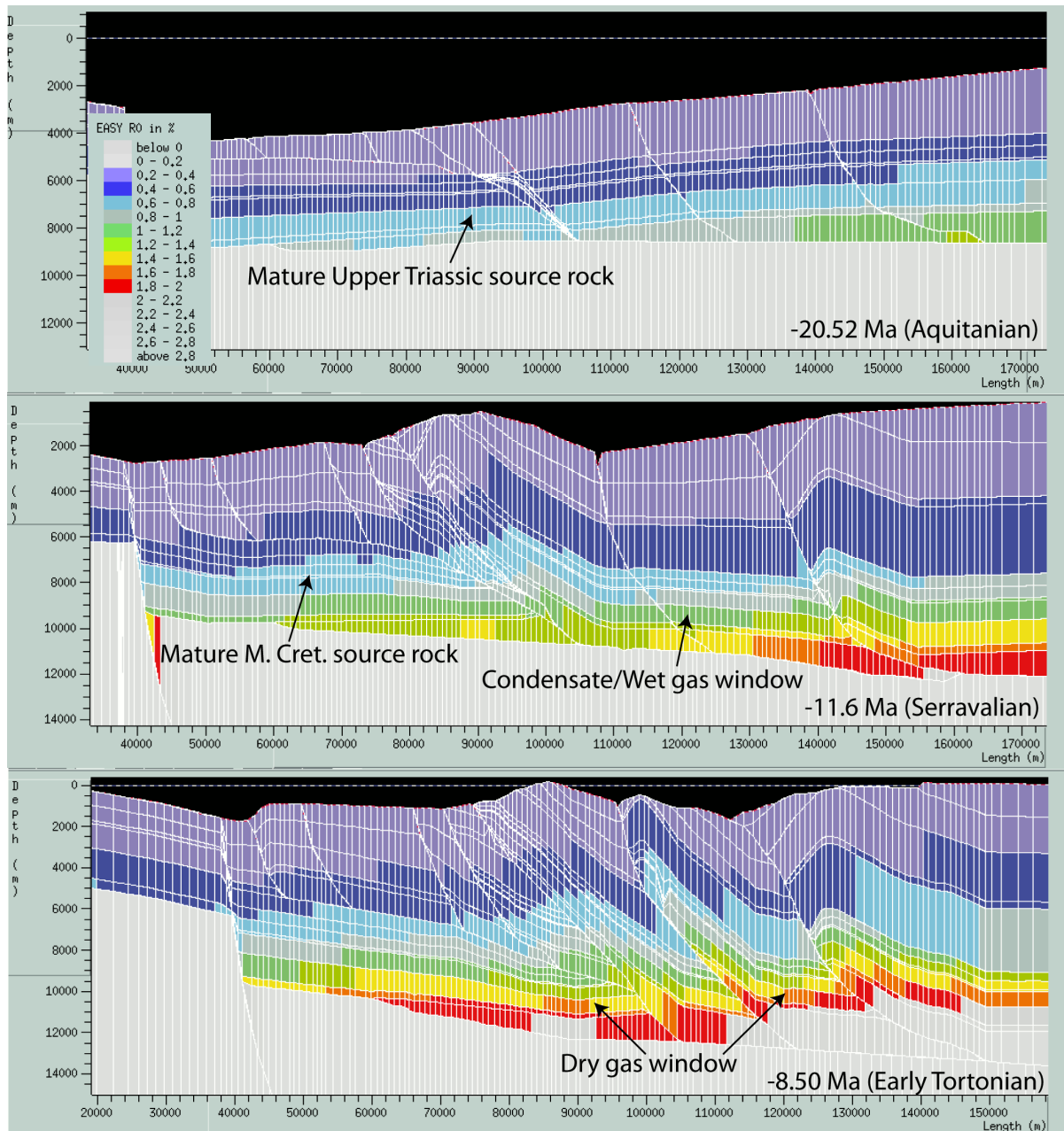


Figure 8.15. Repartition of the maturity (Vitrinite reflectance in %) along the CR13 profile from the Aquitanian to the Early Tortonian.

8.4.3.2- Transformation ratio

In the CR13 profile, the transformation ratio (i.e. TR) distribution shows that the majority of the source rocks are mostly overcooked due to the important thickness of the overlying sediments. However, some locations have been preserved and did not reach TR higher than 60%, with still an oil potential. This is the case for the source rocks located above 5-6km depth, except SR in the Berati belt, due to its out of sequence development, implying a later uplift and then a longer overcooking of the Triassic source rock.

The Figure 8.18 shows the evolution of the transformation ratio for the Triassic to Lower Jurassic source rocks, which are located in the foredeep structures and in the upper part of the Kurveleshi belt. It shows that the source-rocks in the foreland are at present overcooked, with no longer oil potential. In the Kurveleshi belt, the Triassic to Lower Jurassic source-rock reached abruptly their main phase of transformation, when the Berati unit became thrust over the frontal units. It still displays at present an oil potential.

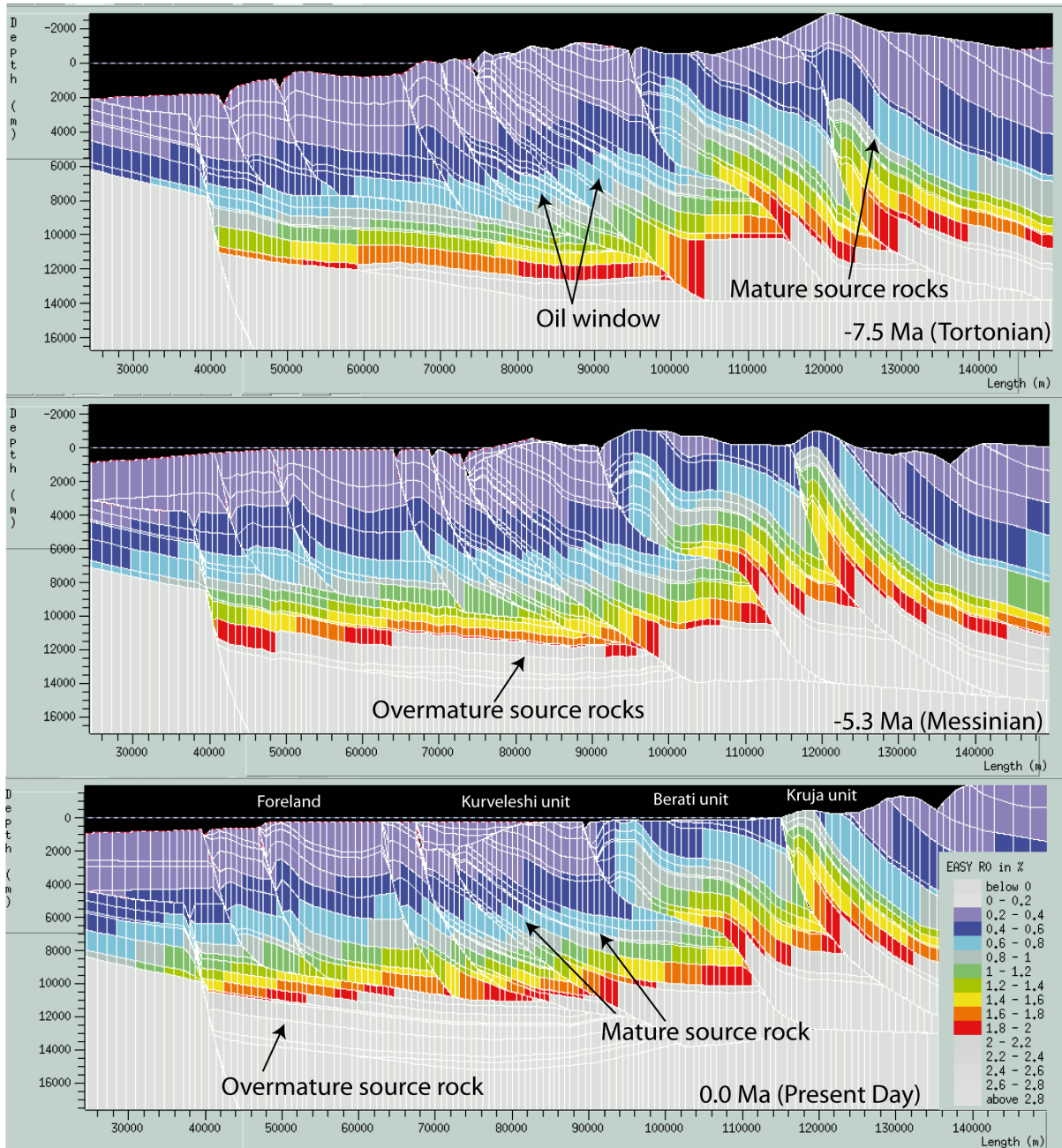


Figure 8.16. Continuation of the Figure 8.15, showing the Ro evolution from the Tortonian to the present-day.

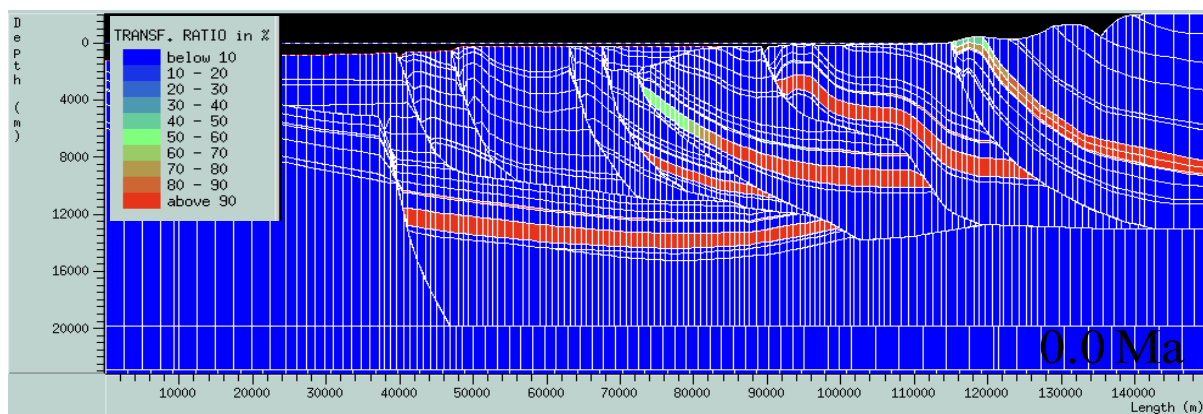


Figure 8.17. Distribution of the transformation ratio in the frontal thrust units at present-day.

8.5- Pressure evolution

From previous structural and diagenetic studies realised in different reservoir analogues in the Ionian Zone, it is clear that several episodes of high pore-fluid pressure occurred from the pre-deformational stage onward, i.e. during flexure of the basin. With realistic values of

permeabilities for the different lithologies, the Ceres software is able to reproduce the evolution of the hydraulic head and overpressures through time and consequently, to estimate a timing of the high pore-fluid pressure episodes, which were mentioned in the previous chapters.

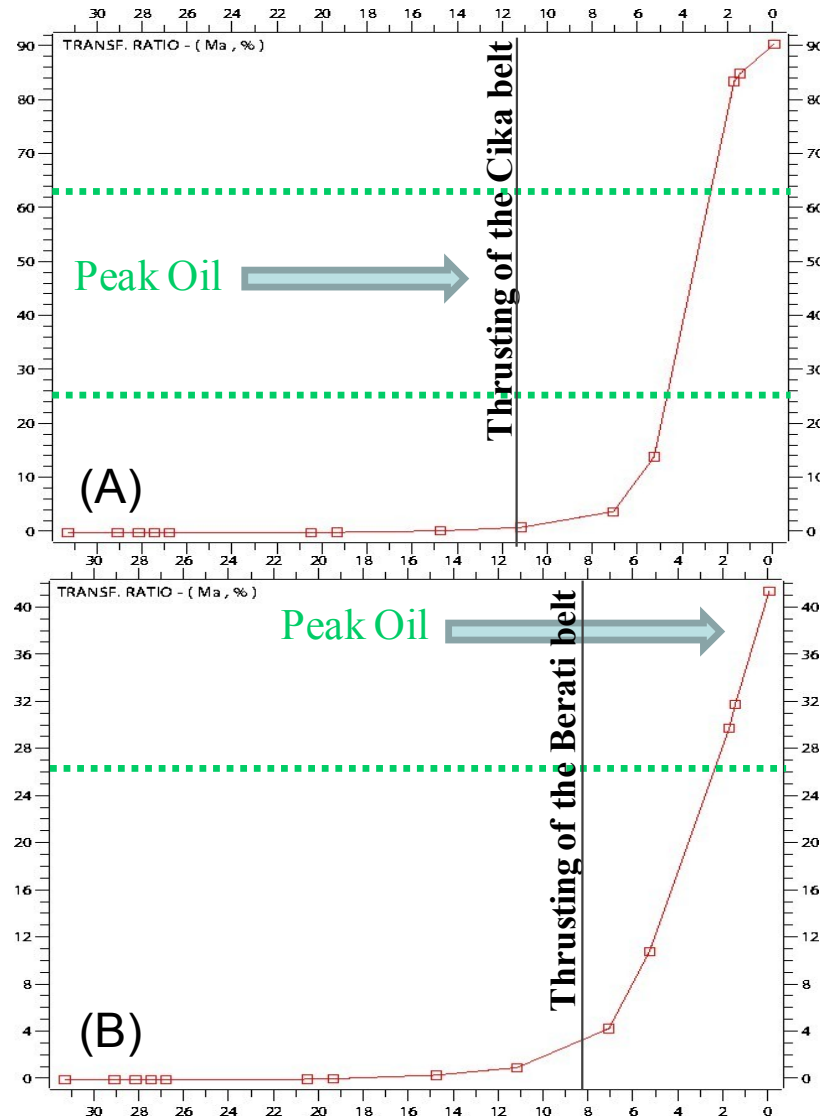


Figure 8.18. Evolution of the transformation ratio for the Triassic to Lower Jurassic sources rocks, located in (A) the foreland and in (B) the upper part of the Kurveleshi belt. The peak oil corresponds to the main transformation phase, varying between 25 and 65% of transformed organic matter (Houseknecht and Hayba, 1998). The vertical and horizontal scales correspond respectively to the transformation ratio in % and the time in Ma.

8.5.1- Hydraulic head

The bathymetry and the topography play a fundamental role, by directly controlling the hydraulic head, the development of overpressure, when permeability barriers occur, and consequently the fracture generation.

Unfortunately, the evolution of the sea level through time is not precisely determined in literature and often only a depth range, characterising a sedimentary environment, is proposed.

Due to numerical difficulties, a change of the sea level is impossible to imply after the validation of the kinematic scenario. Therefore, this parameter was tested by the way of the eustatism, i.e. sea level fluctuations. Several hypotheses related to the bathymetry evolution were simulated to determine the incidence of this parameter on the generation of fractures and overpressures and to constrain the model. Two of them are described below (Figure 8.19): (1) the first one, shown by a dashed line, corresponds to

the initial evolution, which appears in the kinematic evolution (Figure 2.7), without any sea level change; and (2) the second hypothesis, i.e. the black line, is characterised by a shallower marine sedimentation during the syn- to post-deformational stage. The bathymetry of the second hypothesis was reduced by 1 km maximum, compared to the hypothesis 1 (Figure 2.7; i.e. first hypothesis), during the syn-deformational stage.

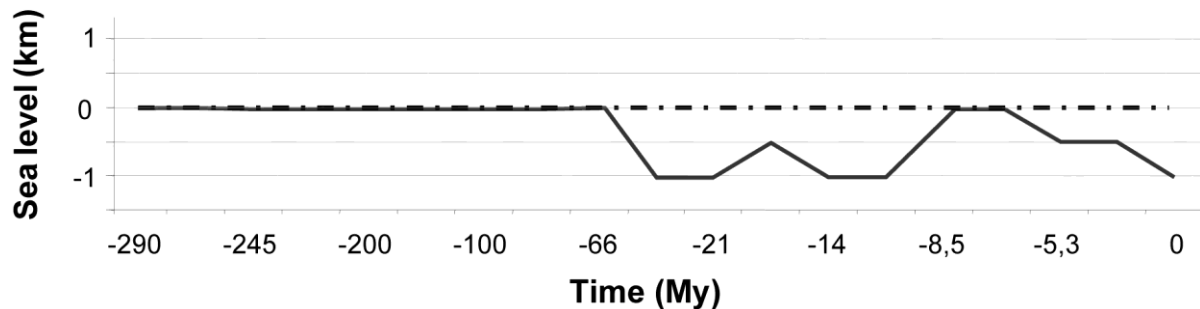


Figure 8.19. The diagram shows the variation of the eustatism, i.e. sea level, for the two tested scenarios. The dashed and the black lines correspond respectively to the first and the second scenarios described in the text. The second hypothesis is defined relatively to the sea level evolution used for the first hypothesis.

The results of the hydraulic head distribution are given in the Figure 8.20, for hypothesis 1, and Figure 8.21, for hypothesis 2. The hydraulic head corresponds to a specific measurement of the water pressure and is expressed in units of length. It allows also determining the fluid movements associated to the compressive lateral/vertical stresses and to the meteoric fluid infiltration via high topographic reliefs. Both hypotheses are characterised by a similar sea level in the Tortonian, i.e. during the -8.5 and -7.5 Ma time interval. However, each scenario has still a distinct distribution of the hydraulic head. Then, it is obvious that a variation of the bathymetry will affect the subsequent stages, when permeability barriers, such as continuous and non-porous sedimentary intervals, occur. In fact, vertical compaction during the burial stage implies the dewatering of the sediments, which may cause the development of horizontal barriers. Scenario 1 is characterised by higher pressure values, especially in the thrust belt, from the Serravalian to the Tortonian, whereas in the Peri-Adriatic Depression, these high pressure values occurred during the later stages. This observation is important since it is directly

associated with the development of hydraulic fracturing (Schneider et al., 1999).

Concerning the influence of the topography, both scenarios demonstrate high values of hydraulic head in the shallow levels of the Kurveleshi and the Kruja units during the Tortonian. These values reflect the infiltration of meteoric water via high topographic reliefs. Meteoric water allows to recharge the system and then increase the hydraulic head, promoting the generation of hydrofractures. In detailed, this meteoric water migrates downward and laterally into tectonic units. For example, meteoric water, which was infiltrated in the Kruja topographic relief, migrated through the matrix porosity and across the main thrust fault towards the Oligocene flysch deposits of the Berati unit. In this case, the fault acts as fluid conduits. However, similar meteoric water was infiltrated by topographic reliefs in the Kurveleshi belt, but was stopped along the footwall of the Berati thrust fault, promoting only downward and westward migration. The latter could be explained by a control of the matrix porosity, favouring migrations through the flysch and molasse sediments instead of the fine-grained Mesozoic carbonates.

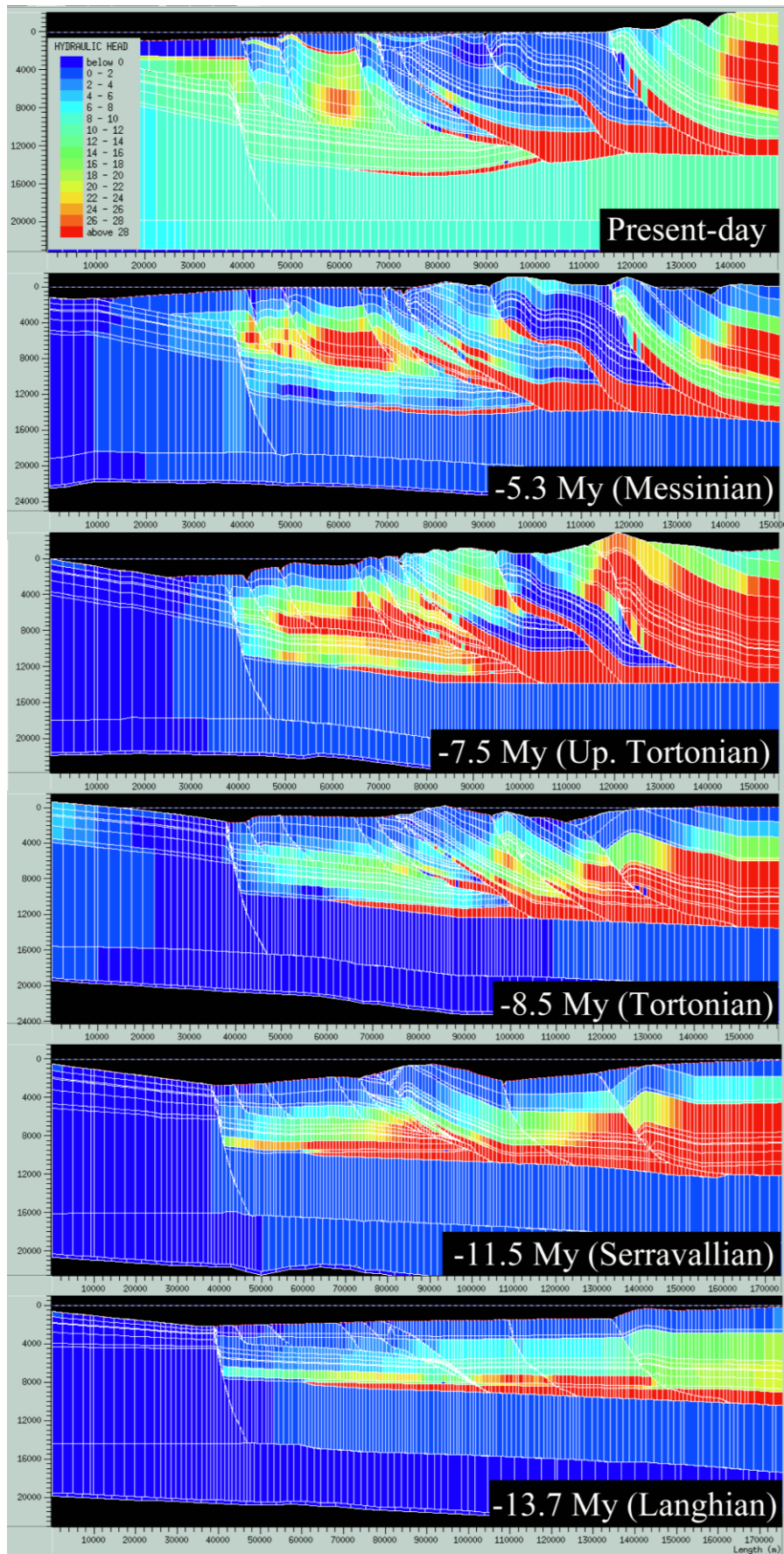


Figure 8.20. Evolution of the hydraulic head (water pressure) through time (Scenario 1). For explanation, see text.

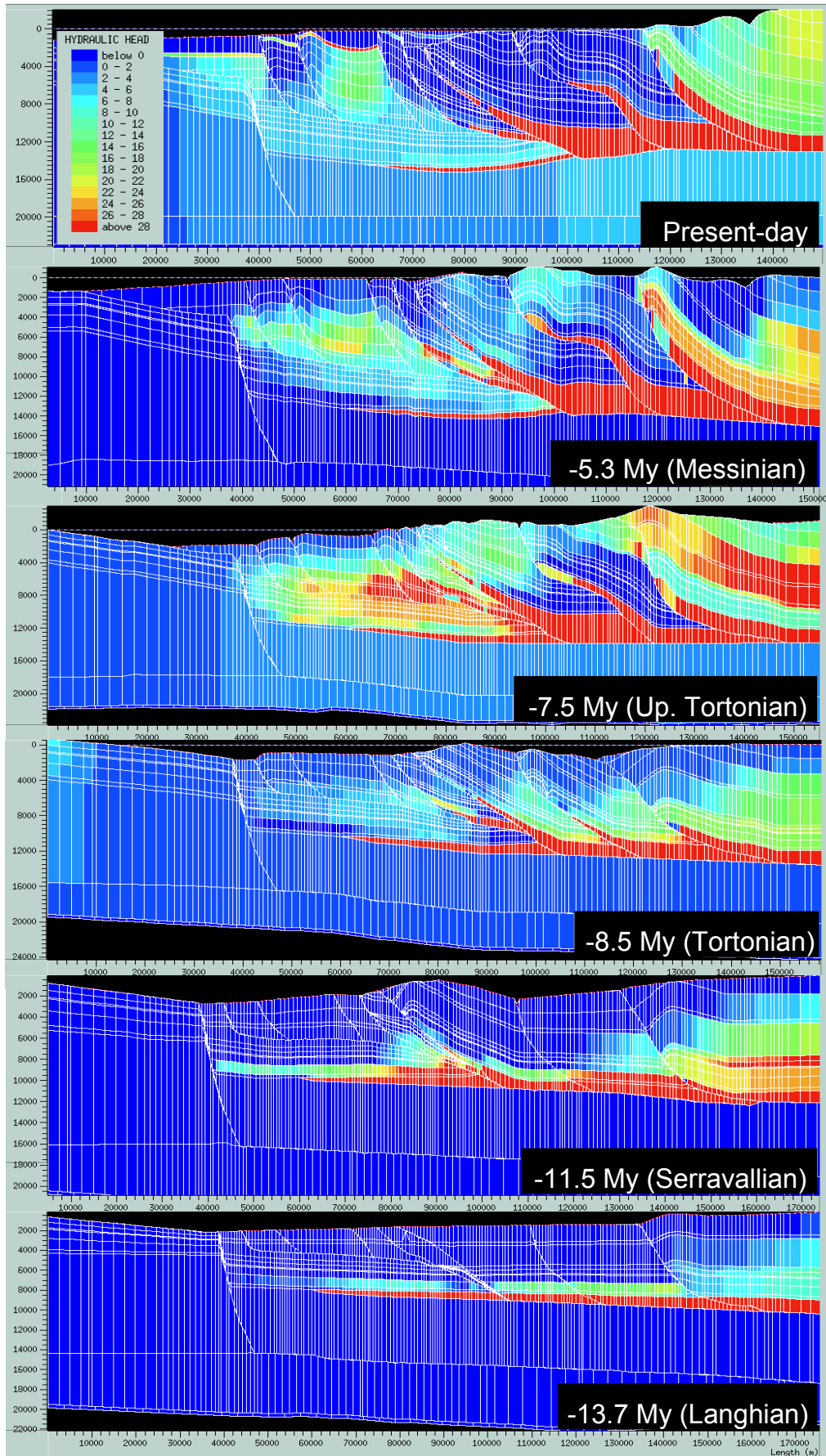


Figure 8.21. Hydraulic head (water pressure) evolution through time (Scenario 2). For explanation, see text.

8.5.2- Generation of overpressure

The estimation of the overpressure regime is linked to the spatial distribution and lateral/vertical connectivity of seals and potential conduits for the fluids, as well as the rates of HC generation and charge of HC fluids during the deformation.

The distribution of the overpressure through time for three representative locations of the actual

reservoir emplacements and for both scenarios discussed above is shown on the Figure 8.22. The three locations are distributed in different thrust belt locations, i.e. the Kurveleshi and the Berati belts, which are associated to the Kremenara and the Kelcyra reservoirs respectively as well as a location situated in the foreland.

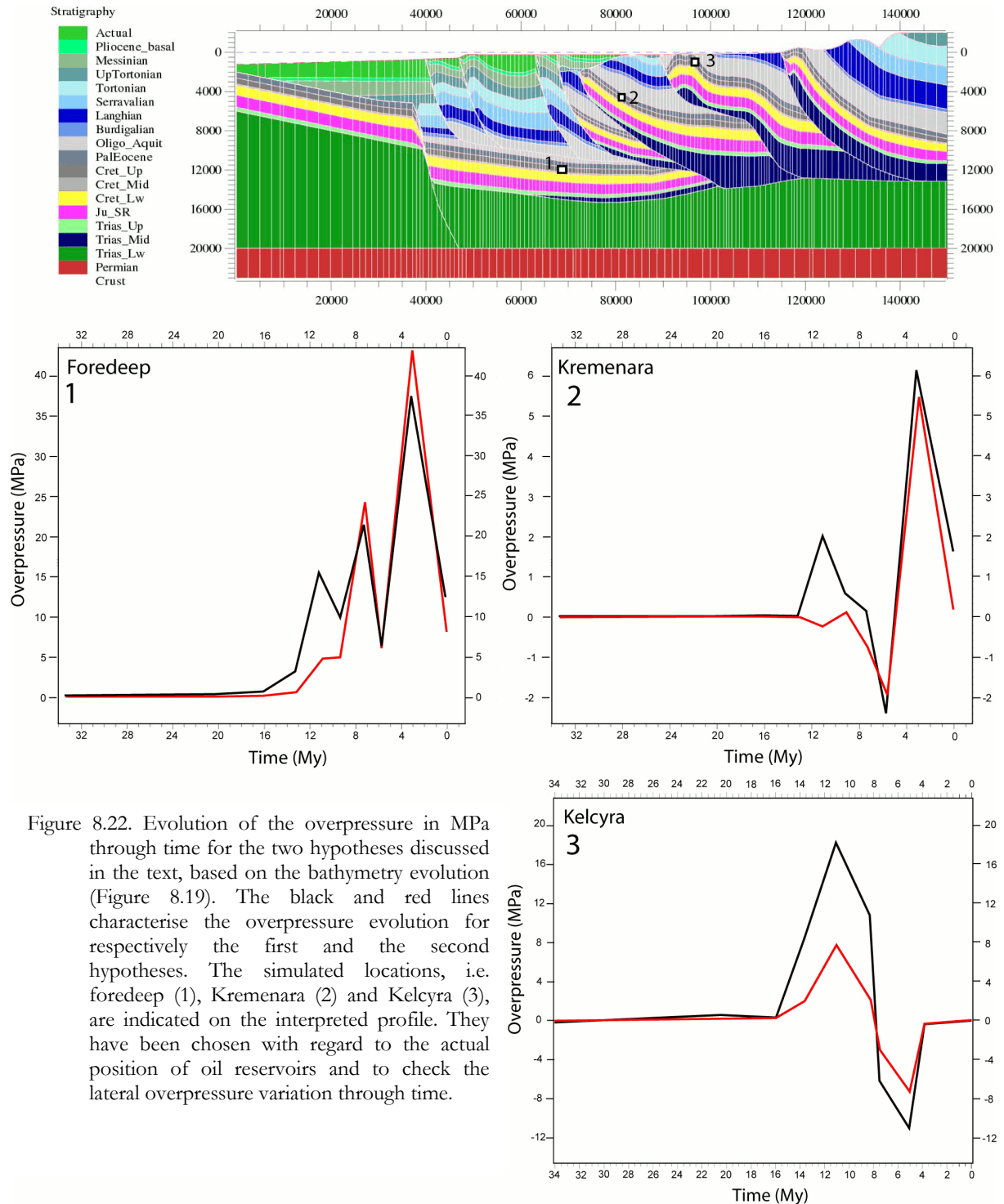


Figure 8.22. Evolution of the overpressure in MPa through time for the two hypotheses discussed in the text, based on the bathymetry evolution (Figure 8.19). The black and red lines characterise the overpressure evolution for respectively the first and the second hypotheses. The simulated locations, i.e. foredeep (1), Kremenara (2) and Kelcyra (3), are indicated on the interpreted profile. They have been chosen with regard to the actual position of oil reservoirs and to check the lateral overpressure variation through time.

The black and red curves (Figure 8.22) characterise the evolution of the overpressure as controlled by the bathymetry for the first and the second hypotheses respectively. The two hypotheses record practically the same trends, with only a difference recorded during the Serravalian (i.e. at -11.6 My).

An homogeneous state of overpressure of 15-20 MPa is recorded during the Serravalian (-11.6 My) in the Ionian Zone for both scenarios, likely related to the onset of the thrusting. Only the Kurveleshi unit, i.e. Kremenara reservoirs displays the lowest pressure (i.e. 2 MPa) since this unit has been simultaneously uplifted, decreasing the hydrostatic pressure (i.e. hydraulic head).

Afterwards, a second overpressure regime occurs in the foredeep and frontal thrust belts (i.e. Tortonian, -8.5 My), and is characterised by overpressures reaching up to 22 to 25 MPa. This episode likely relates to the maximum shortening of the thrust units, increasing dramatically the horizontal compression. No overpressure regime is recorded in the thrust belts because of the uplift and erosion of the tectonic units, causing a decrease of the hydrostatic pressure. The emersion of a thrust unit is translated by a decrease of the overpressure in the negative values. The last recorded overpressure period is encountered in the foreland, characterising by pressures reaching up to 38-45 MPa, and in the frontal thrust belts, i.e. Kremenara. This period can be explained by a rapid sedimentation rates in the Peri-Adriatic Depression (PAD), which allows to bury the most western units and the foreland, increasing the vertical compaction. This stage is also characterised by the activation of compressive structures in the PAD.

The successive periods of overpressure are directly related to a coupling of the horizontal (i.e. main compression) and vertical stresses (i.e. compaction). During the deformational stage, the overpressure fronts are moving from the thrust belts towards the foreland, which is shown by an increase of the overpressure intensity. This evolution is then strongly related to the evolution of the hydraulic head, as illustrated in the Figure 8.20 and Figure 8.21.

8.5.3- Fracturing episodes

The increase of the overpressure and hydraulic head may point to fracturing events. The evolution of fracturing is immediately associated

to the vertical/horizontal pressures, the water flux and the mechanical properties of the lithologies. Figure 8.23 shows the distribution of the fracturing potential through the deformational stage of the outer Albanides. The fracturing evolves parallel to the evolution of the overpressure, giving a similar evolutionary trend.

The fracturing ratio is an estimate of the possible intensity of fracturing and is purely indicative. It is based on overall physical-mechanical properties of rocks, since no input data was used to calibrate the model.

At the onset of the main compression, i.e. Burdigalian, the Upper Cretaceous to Eocene limestones and the Oligocene flysch are likely to be highly fractured in the Kruja zone as well as the Upper Triassic-Lower Jurassic source rocks, located in the western part of the basin. From the Serravalian onward, the fracturing of the Upper Cretaceous to Eocene intervals are homogeneously distributed all along the profile. Only the Kurveleshi unit, which is characterised by lower hydraulic head and overpressure, displays a lower fracturing ratio.

From the Early Tortonian onward, an increased fracturing ratio is recorded in the Peri-Adriatic Depression. Notice that the Messinian-Early Pliocene strata, which consists of an evaporitic layer, seals the underlying highly fractured pre-Messinian reservoirs. At present, many gas/oil fields (Swennen et al., 1999; Zelilidis et al., 2003) are trapped in these areas.

8.6- Fluid flow

Once the kinematic model is developed and subsequently constrained in temperature and pressure, the last step in the Ceres workflow consists of the forward modelling coupling the fluid flow simulations, the heat transfer, and the hydrocarbon formation.

The Ceres software allows to simulate a triphasic system, i.e. oil, gas and water. In this study, only the water and the hydrocarbon flows were studied. The main goal has been to characterise their migration pathways and velocities, which also relate directly to the behaviour of the faults, and to test different hypotheses (oil density, fault behaviour). Moreover, the quantification of the fluid velocity in the sedimentary basin will allow to constrain the previous diagenetical models in time.

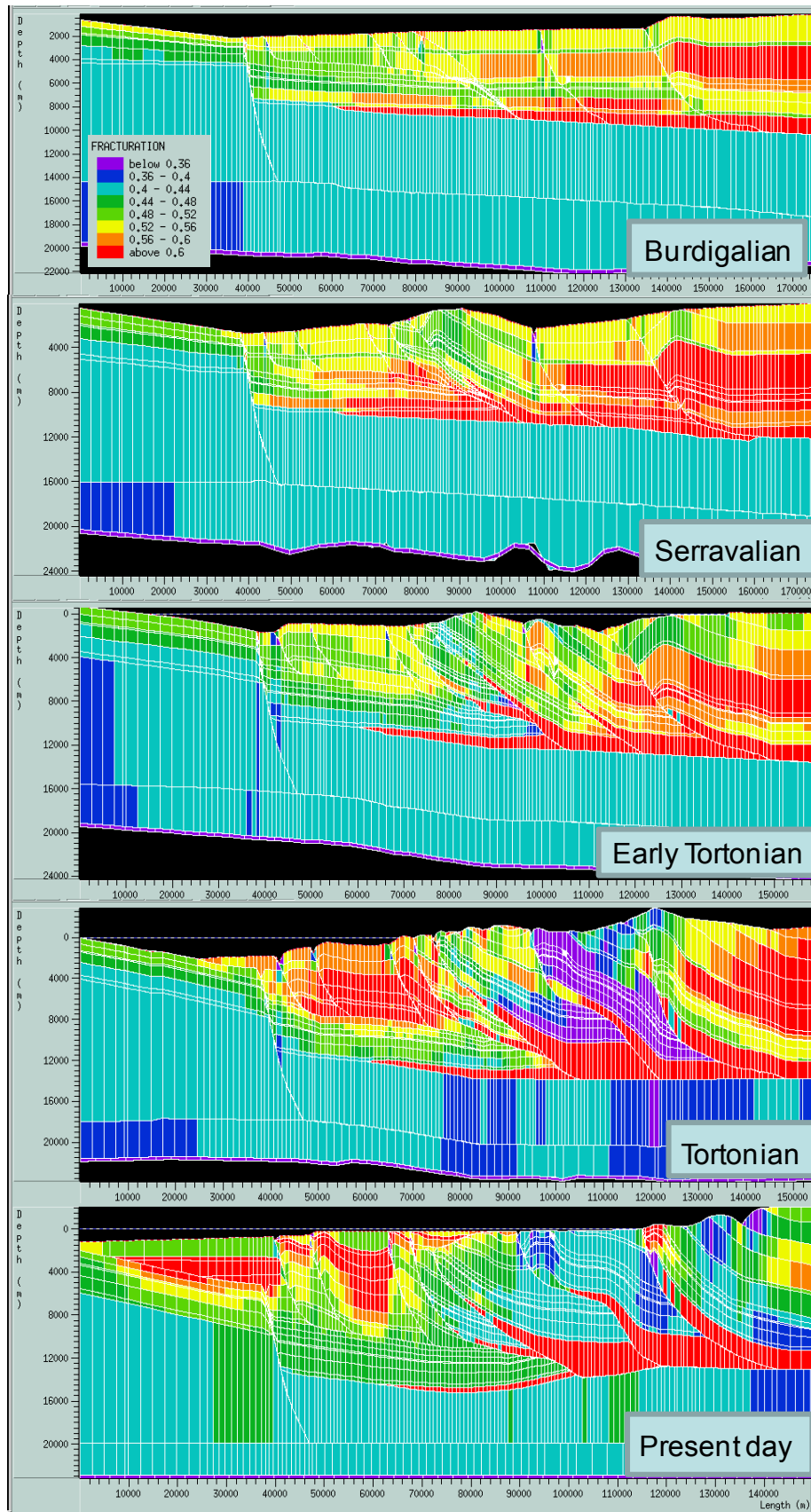


Figure 8.23. Evolution of the fracturing during the main steps of the deformational period, based on the second hypothesis (i.e. shallower marine sedimentation). The fracturing ratio is an estimate of the possible intensity of fracturing and is purely indicative. It is based on overall physical-mechanical properties of rocks, since no input data was used to calibrate the model.

8.6.1- Water migration

The water flow is directly associated to the compaction of the sediments, decreasing the porosity and expelling pore fluids, to the topography, allowing the infiltration of water from high elevation areas and indicating topography driven flow, and to the compression, with the development of squeegee episode of pore fluids expulsion.

From the deposition of the Upper Cretaceous-Eocene reservoirs until the Burdigalian, the water flow remained dominantly vertical due to the compaction-driven dewatering of the sediments (Figure 8.24). Limited lateral water escape, which occurred in the eastern part of the Albanides, was essentially developed due to the increase of the tectonic compression, i.e. horizontal stress. Both horizontal and vertical

water escapes characterise fluid flow driven by compaction, including components of both vertical and horizontal compaction. The low porosity of the overlying sediments of the Oligocene flysch may also explain these lateral migrations, which have an average velocity of 50m/My (Figure 8.26). During this period, the main thrusts were not yet developed.

Modelled lateral deep water migration (i.e. velocities averaging 50m/My) intensified in the Mesozoic lithologies from the Serravalian onward (Figure 8.25), due to the decrease of the porosity of the overlying sediments and the increase of the horizontal compression. Vertical fluid migration occurs also and consists of pore fluids expelled from the young sedimented layers due to burial compaction.

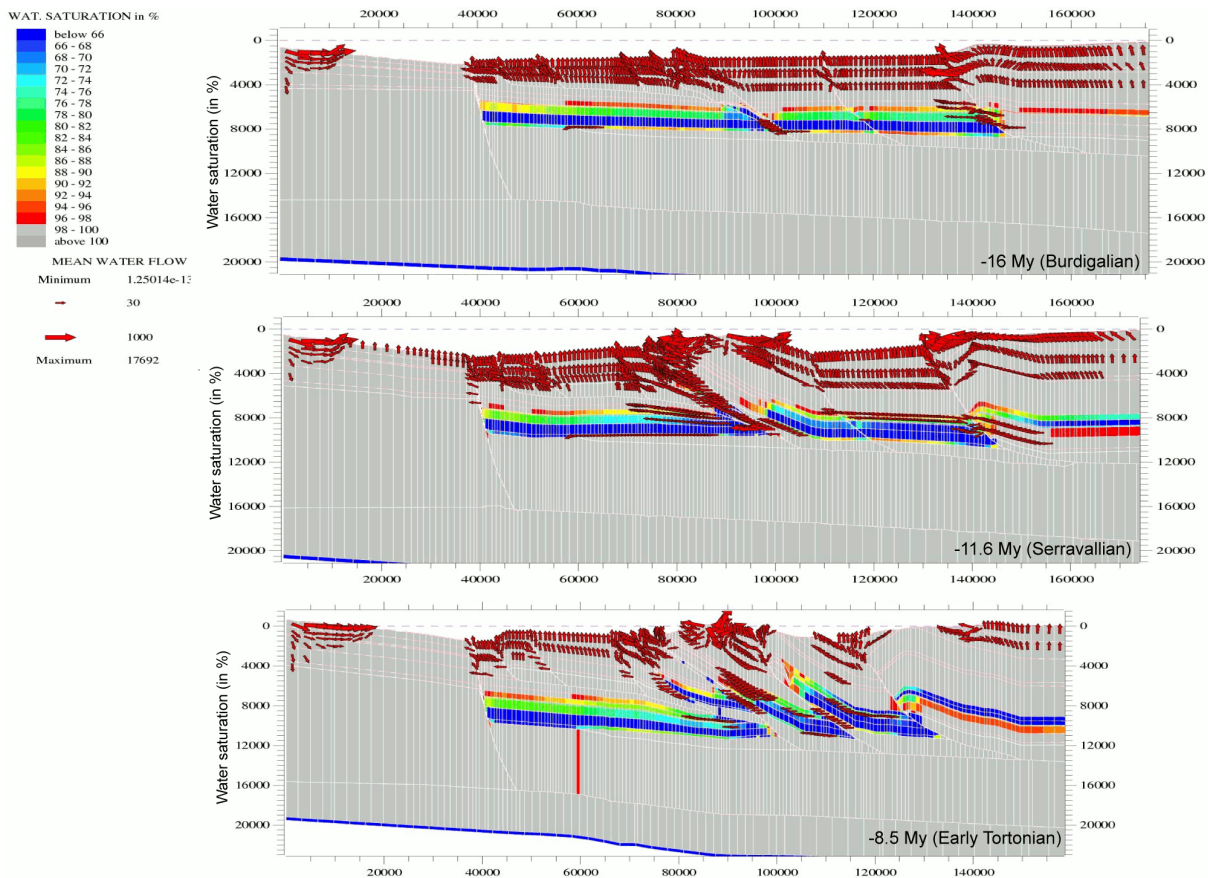


Figure 8.24. Water migration pathways from the Burdigalian until the Early Tortonian shown by red arrows. The water flow is expressed in m/My. For discussion, see text.

The onset of the thrusting of the Cika/Kurveleshi units causes an increase of the lateral fluid flow in the frontal zone of the outer Albanides as well as of the water flow velocity, varying from 40 to

120m/My. Notice that the fluid velocity is higher in the upper part of the Cika unit than in the lower part of the same tectonic unit or in the Kurveleshi (Figure 8.26). In fact, the emersion of

the Kurveleshi unit allows the infiltration of water via high topography relief, characterised by higher velocities, reaching up to 1 km/My. The meteoric water infiltration allows to increase largely and locally the hydraulic head, promoting likely the generation of fractures. This fluid moves downward and out into the neighbouring foreland and tectonic units (i.e. Cika belt) in the direction of decreasing hydraulic head (Nemcok et al., 2005). This process is enhanced by the development of active and pervious faults, since no evaporitic décollement level occurs in this area.

During the Early Tortonian, the three main thrusts were active. The evaporites, located along the décollement levels, prevented the water migration to occur between tectonic units, resulting in closed systems. From then onwards, fluid flow was driven by compression and compaction. Deep fluids were expelled laterally towards shallower levels in the Mesozoic fractured intervals. Notice that the latter are sealed by the Oligocene flysch. Vertical water escapes occurred locally in the shallower levels, due to dewatering of younger sediments as well as fluid flow driven by topography, since the Kurveleshi unit was still emerged.

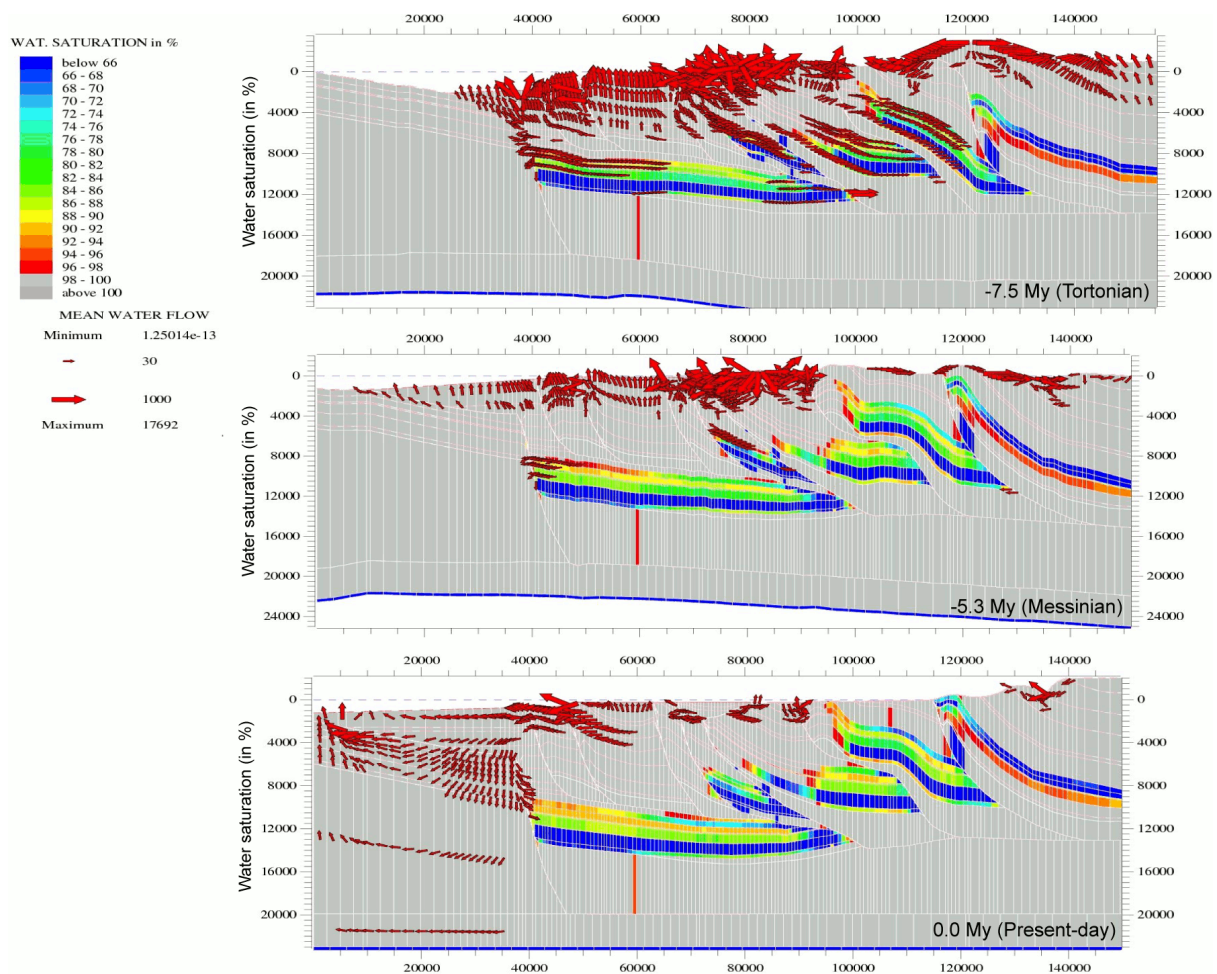


Figure 8.25. Water migration pathways from the Tortonian onward, described by red arrows. The water flow is expressed in m/My. For discussion, see text.

During the Tortonian, a main change occurred in the fluid pathways. The modelled water flow was characterised by a dominantly downward migration in the Mesozoic carbonates, allowing the meteoric fluid flow to reach deeper levels in

the fold-and-thrust belt system, with a velocity averaging 40 m/My. The shallower level, still characterised by fluid flow driven by topography, still displays high fluid velocities of 70-120 m/My. This change in the migration

pathways likely relates to the increase of the hydraulic head and the overpressure in the foreland. The water moved towards areas with lower hydraulic pressure.

From the Messinian onward (i.e. 5.3 My), the outer Albanides are characterised by still downward meteoric water migration from topographic elevated areas, but with velocity finally decreasing towards 0 m/My. Vertical upward water flow consisting of the dewatering of young sediments still occurs in the foreland.

The present-day situation displays lateral fluid migration in the Peri-Adriatic Depression towards the Sazani platform, which is characterised by lower pore-fluid pressures. These fluids migrate also towards pervious, i.e. permeable, faults (i.e. compressive structures in the Peri-Adriatic Depression), which have been activated during the late deformational stage, because the Messinian-Pliocene evaporites act as a flow barrier.

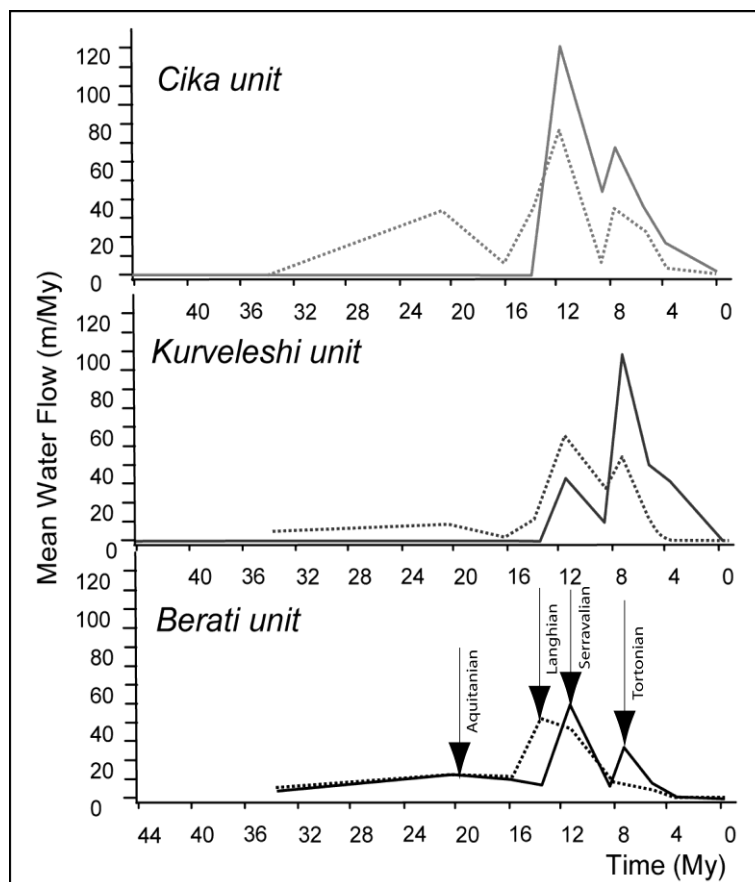


Figure 8.26. Modelled velocity of the water flow (in m/My) through time. The dashed lines and the full lines correspond respectively to the eastern and western part of the Upper Cretaceous intervals for each tectonic units.

8.6.2- Oil migration and HC charge through time

The four source rocks were tested independently and together in order to determine their own petroleum system. In this study, gas generation and secondary cracking could not be taken into account due to numerical difficulties. Consequently, late stage development of gas reservoirs in the Peri-Adriatic Depression, which

are sealed by the Messinian/Pliocene evaporites or local unconformities, cannot be modelled.

Water saturation has been modelled since it is complementary to the oil saturation. This part will describe in parallel the influence of several input parameters, such as the density of the oil and the behaviour of the faults, which are fundamental in understanding the fluid flow modelling, but difficult to estimate.

In fact, some parameters could vary through time, especially the density, due to diagenetic

processes, making difficult to determine their initial states.

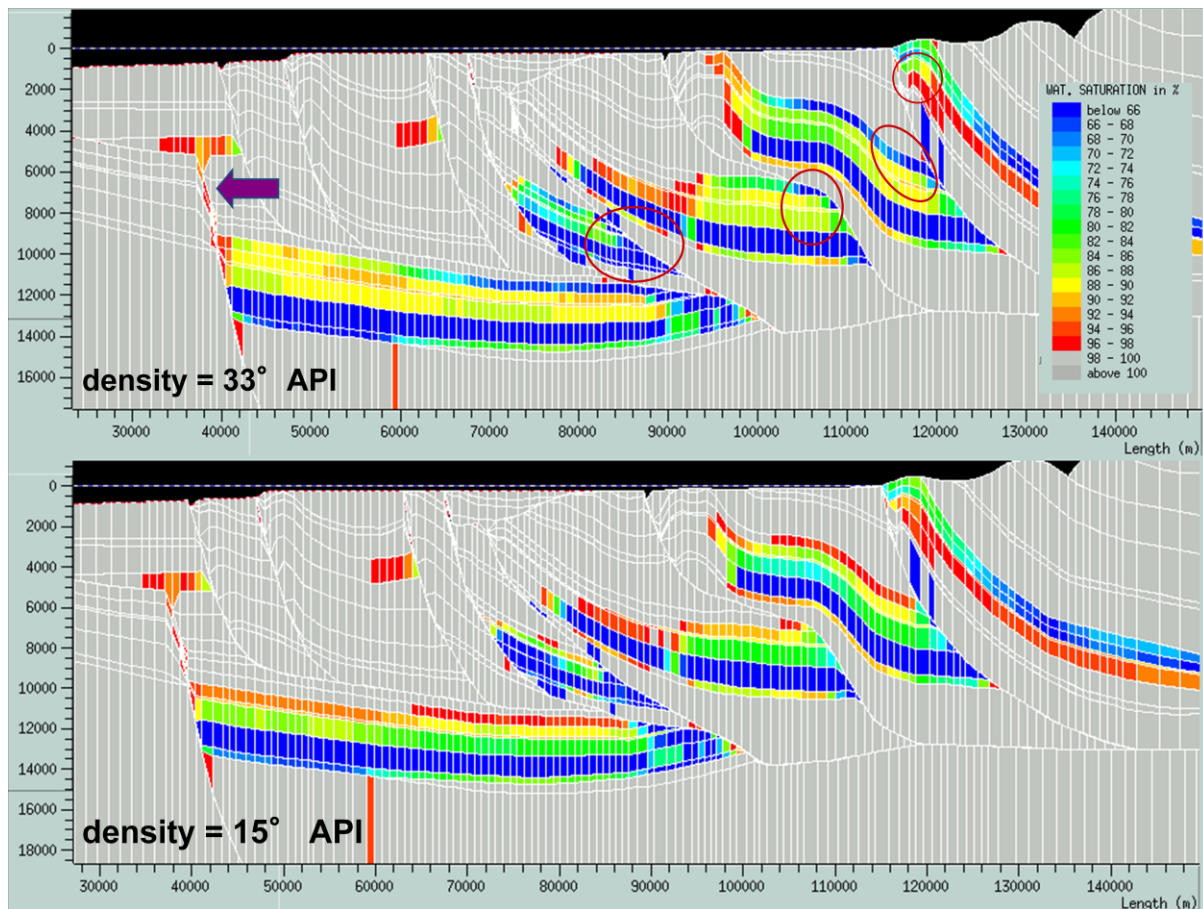


Figure 8.27. Distribution of the water saturation at present-day for the two tested oil densities, i.e. 33 and 15 °API. Notice that the decrease in water saturation is complementary to the oil saturation. A density of 33°API corresponds to light oil and 15°API characterises heavy oil. The main differences are highlighted by red circles.

8.6.2.1- Incidence of the oil density

A more realistic fluid flow modelling would require the input of the true oil density. Unfortunately, different types of oil, in terms of density, have been recovered in Albania, whose API degrees fluctuate in a range of values comprised between 9 to 37 °API corresponding to densities from 840 to 1000 kg.m⁻³ (Sedjini et al., 1994).

Hence, the migration has been simulated for the two main oil densities (i.e. 33°API or 876 kg.m⁻³ and 15° API or 980 kg.m⁻³) to clarify whether these two types of oil have been expelled from different source rocks, or if this density variation relates to late diagenetic processes such as biodegradation or secondary cracking of the hydrocarbons. The distribution of the water saturation in percent for the two hypotheses is

shown on the Figure 8.27. The differences, used to determine the best density, are encircled in a red colour. By using light oil, i.e. 876 kg.m⁻³, some accumulations occur in the Upper Cretaceous reservoirs and reach the surface, especially in the Berati unit. In the case of heavy oil, the migration cannot reach the actual reservoirs and the oil remains into the Upper Jurassic to Lower Cretaceous interval. These observations suggest that the oil in the Ionian Zone is likely characterised by a light density.

Several parameters and model results point towards the biodegradation of the hydrocarbon in a post-deformational stage, since the migration of heavy oil would not be able to reach the Upper Cretaceous-Eocene reservoir intervals (model with an oil density of 15°API) and because the amount of free hydrocarbons in the samples

remains too high (i.e. Rock-Eval pyrolysis) to have been subjected to a secondary cracking. Moreover this observation is in agreement with the single burial stage determined in the Ionian Zone in this study. A second burial episode would be in favour of a secondary cracking of the oil, releasing free hydrocarbon.

From these first models, the known oil-bearing reservoirs are accounted for by the model, but other untested reservoirs, such as the Triassic dolomites, sealed by the Triassic-Lower Jurassic source rocks according to the model results, could still account for interesting but yet unknown accumulations with oil saturation higher than 45%.

8.6.2.2- Function of the fault behaviour

The pre-deformational stage is characterised by early generated hydrocarbons, which migrated vertically up- and down dip as early as the Oligocene-Aquitainian until the Burdigalian-Langhian (Figure 8.28). During this early migration stage, developing during the foreland flexuring, the main faults acted as fluid conduits allowing the oil of the Triassic-Lower Jurassic source rock to be trapped in the reservoirs of the Kruja unit (Figure 8.29).

From the Serravalian onward, the evolution is still characterised by up- and down dip vertical hydrocarbon migrations (Figure 8.29) but accounts also for east- and westward migrations in the foreland, particularly towards the Italian offshore. This is attested by direct oil-source rock correlations in the Aquila field, which relates to a distal Triassic source (Albpetrol, 1995). The specificity of the period is a change in the fault behaviour. The presence of evaporites along the décollement level enables to block the oil migration through the faults, even if foreland fold-and-thrust belt evolution and the strain rate would rather predict that the faults without evaporites should be pervious during such period.

From the Tortonian onward, the hydrocarbons are trapped in the Upper Cretaceous-Eocene fractured carbonate reservoirs. This period is characterised by the major expulsion and migration of hydrocarbon in connection with the

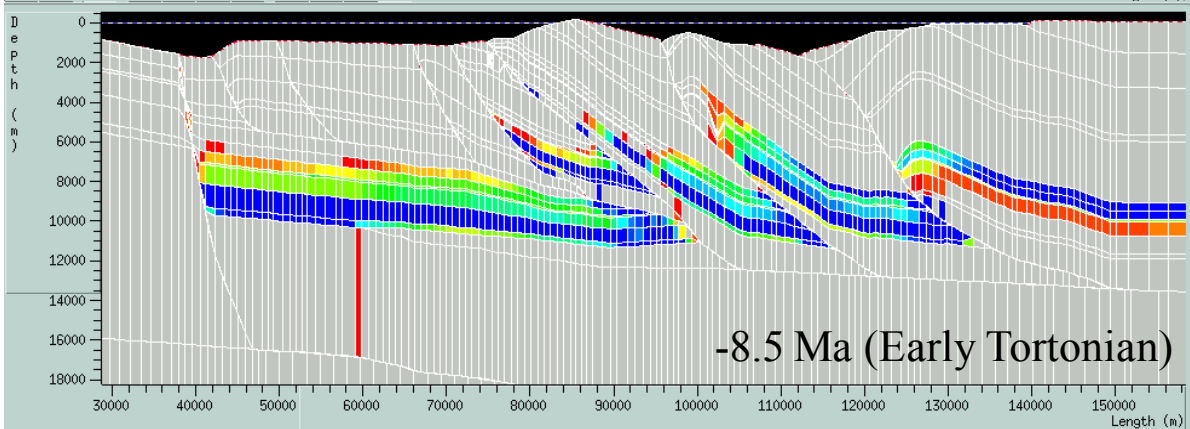
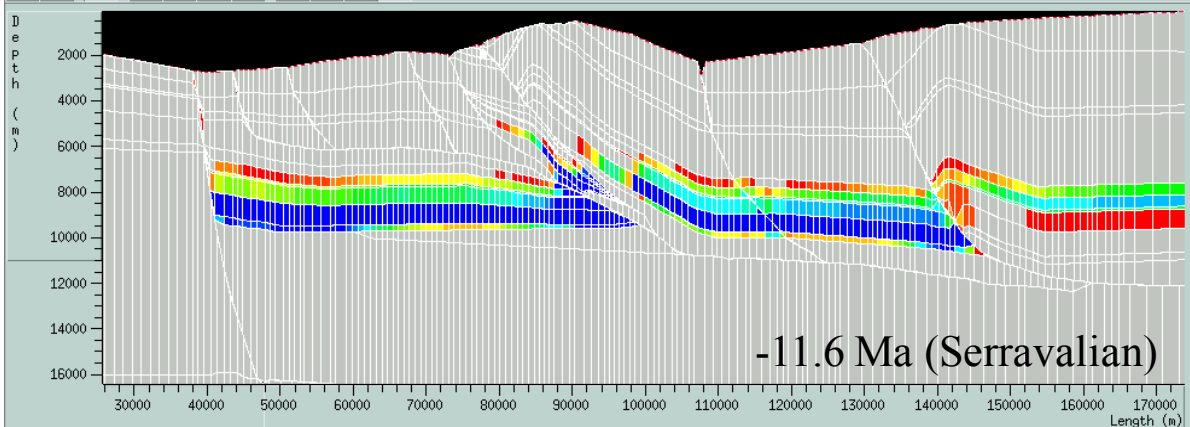
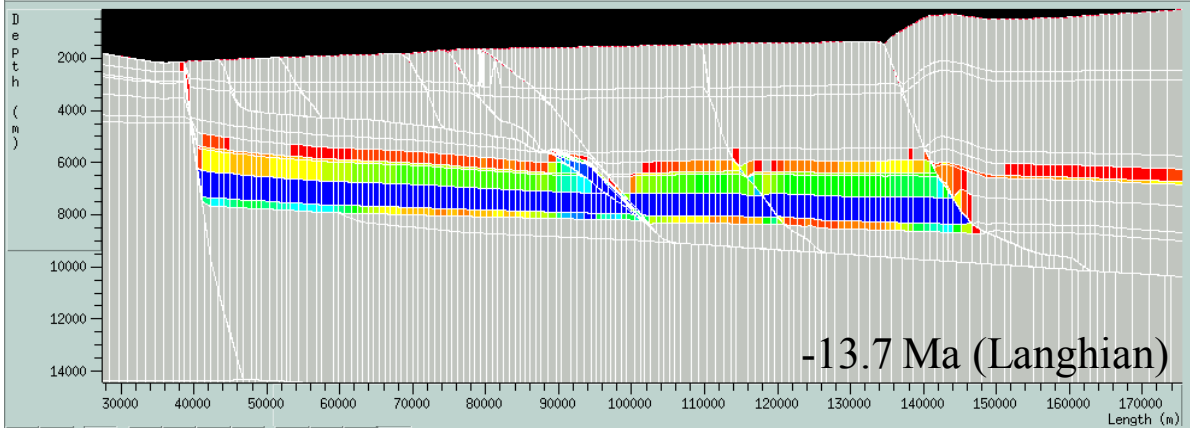
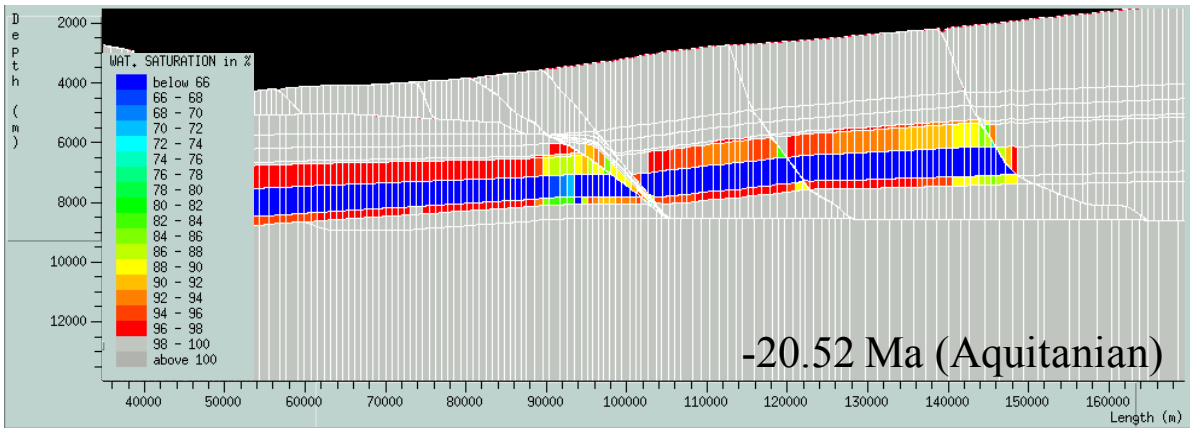
maximum shortening and thermal burial. Alternatively, hydrocarbons migrate along faults in the Cika unit before reaching the sandstone intervals of the foreland and the Italian offshore, where no evaporite exists.

Since the Messinian, the migration pathways are relatively short and partly up- and down-dip but other important pathways are east and downward (i.e. reflux). This period is characterised by a shift of the hydraulic head from the thrust belt toward the foreland, where many compressive structures are formed.

The latter allows a change in the faults behaviour, from fluid conduits in the foreland to fluid barriers in the thrust belt. This is due to the constraint of the software, which considers the fault as inactive, when the speed of the displacements is lower than 50m/Ma.

The evolution of the compressive stress enables to develop oil reservoirs in the foreland, i.e. in the Messinian oil-bearing sandstones. This period is also characterised by the maturation and the up- and down-dip vertical expulsion of hydrocarbon from Tortonian shales, i.e. source-rocks. Finally, the sealed faults have completely compartmentalised the fluids within the thrust belt, isolating independent volumes of rocks since the onset of the orogeny.

These results of fluid flow modelling account for the hypothesis of fault permeability being dependant from the neighbored lithologies (i.e. third option). When considering that the faults are pervious (i.e. first option) all along the FTB evolution, the fluid migration remains unchanged. In fact, the occurrence of evaporites along the décollement level stops the migration pathways of fluids along the faults. However, when considering the second option, i.e. the hypothesis with impervious faults, results are quite different especially in the foreland, where reservoirs can no longer be charged by hydrocarbons, as they become isolated from the kitchen areas. This hypothesis does not reflect the present-day situation, showing oil reservoirs in the foreland.



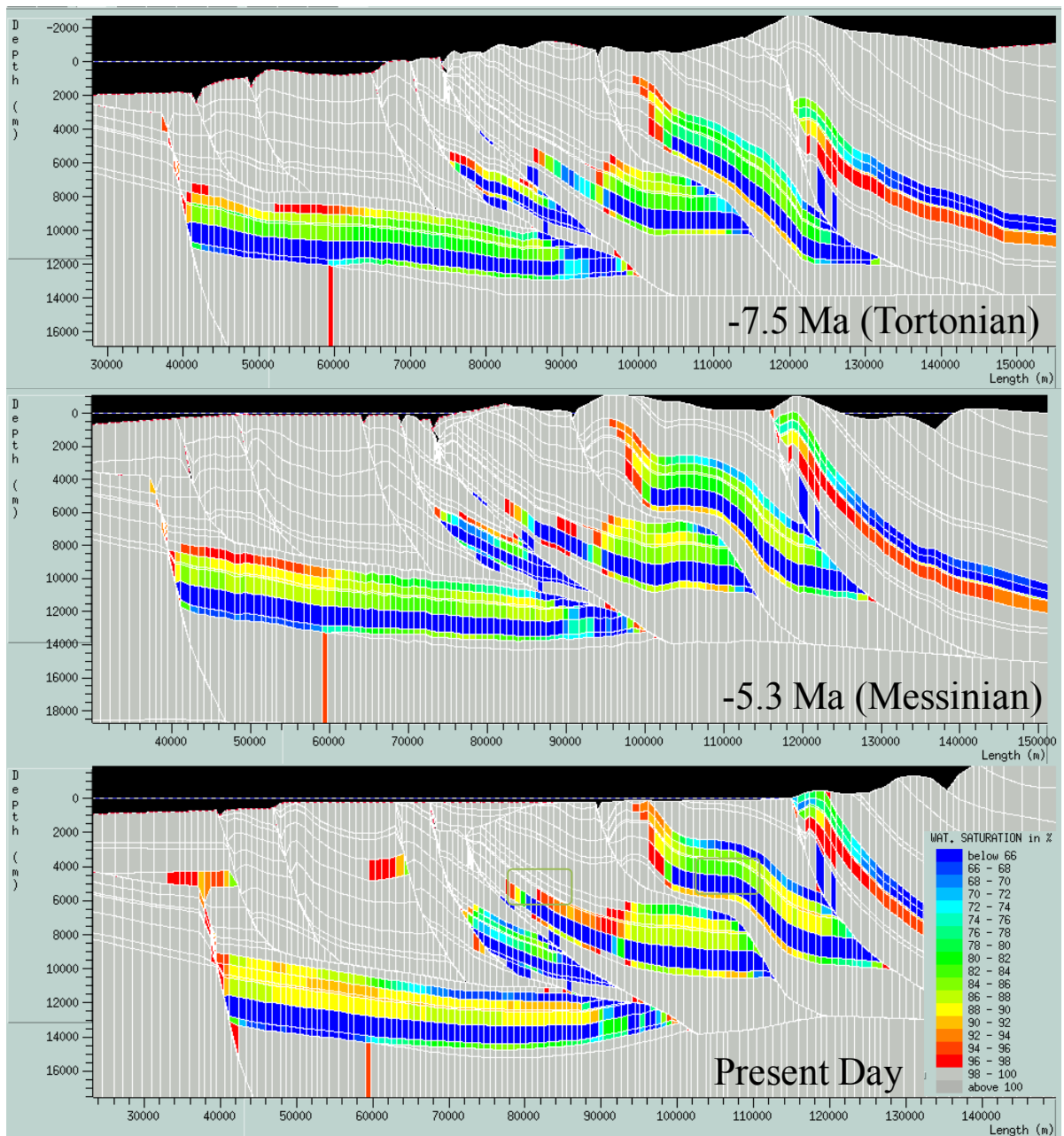
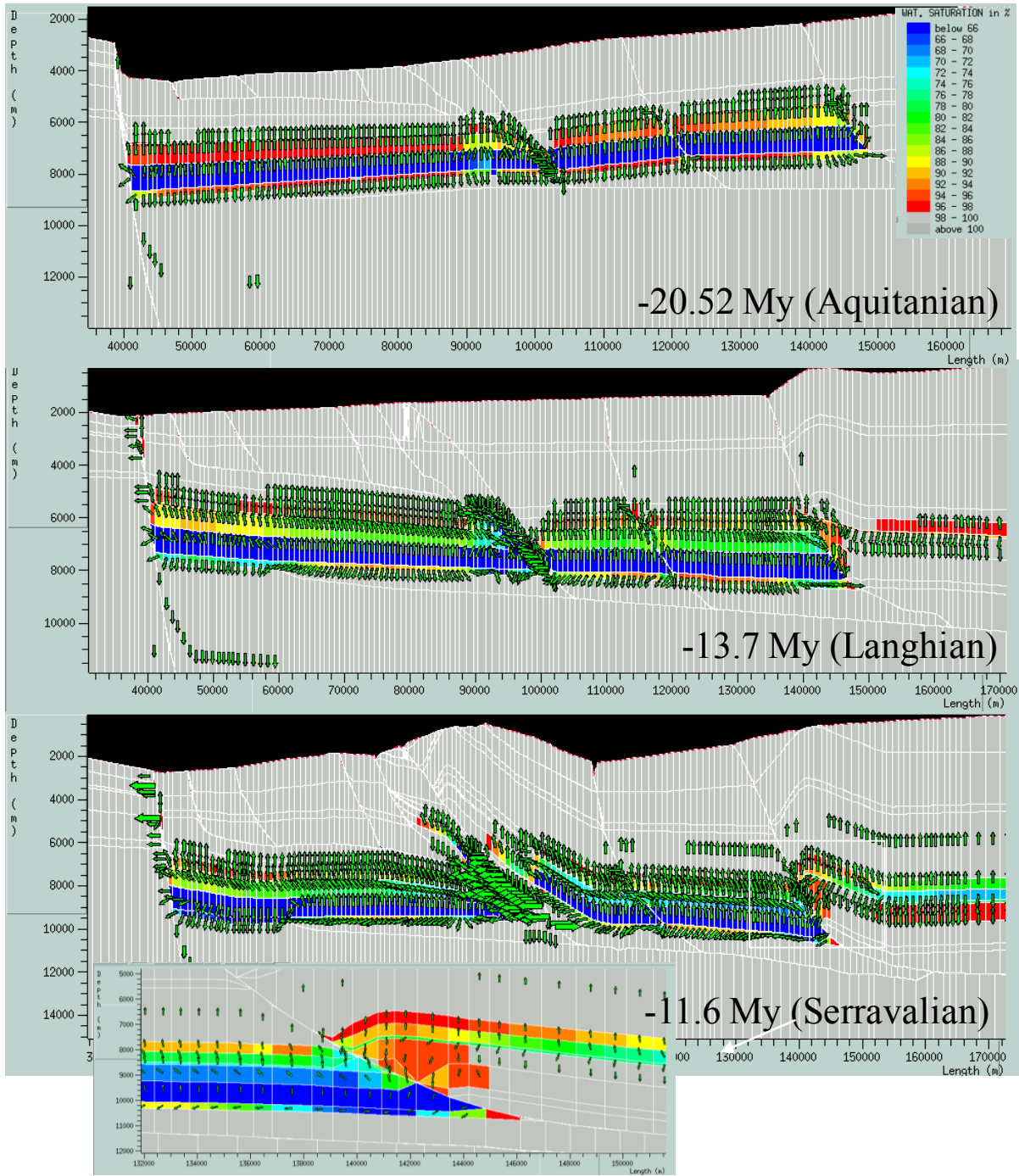


Figure 8.28. Evolution of the water saturation for light oil density from the Aquitanian to present-day, for estimating time of oil expulsion of a source rock and primary migration. Notice that the accumulations of hydrocarbon in the Upper Cretaceous to Eocene carbonates are located beneath the thrusts, sealed by Triassic evaporites and the Oligocene flysch.



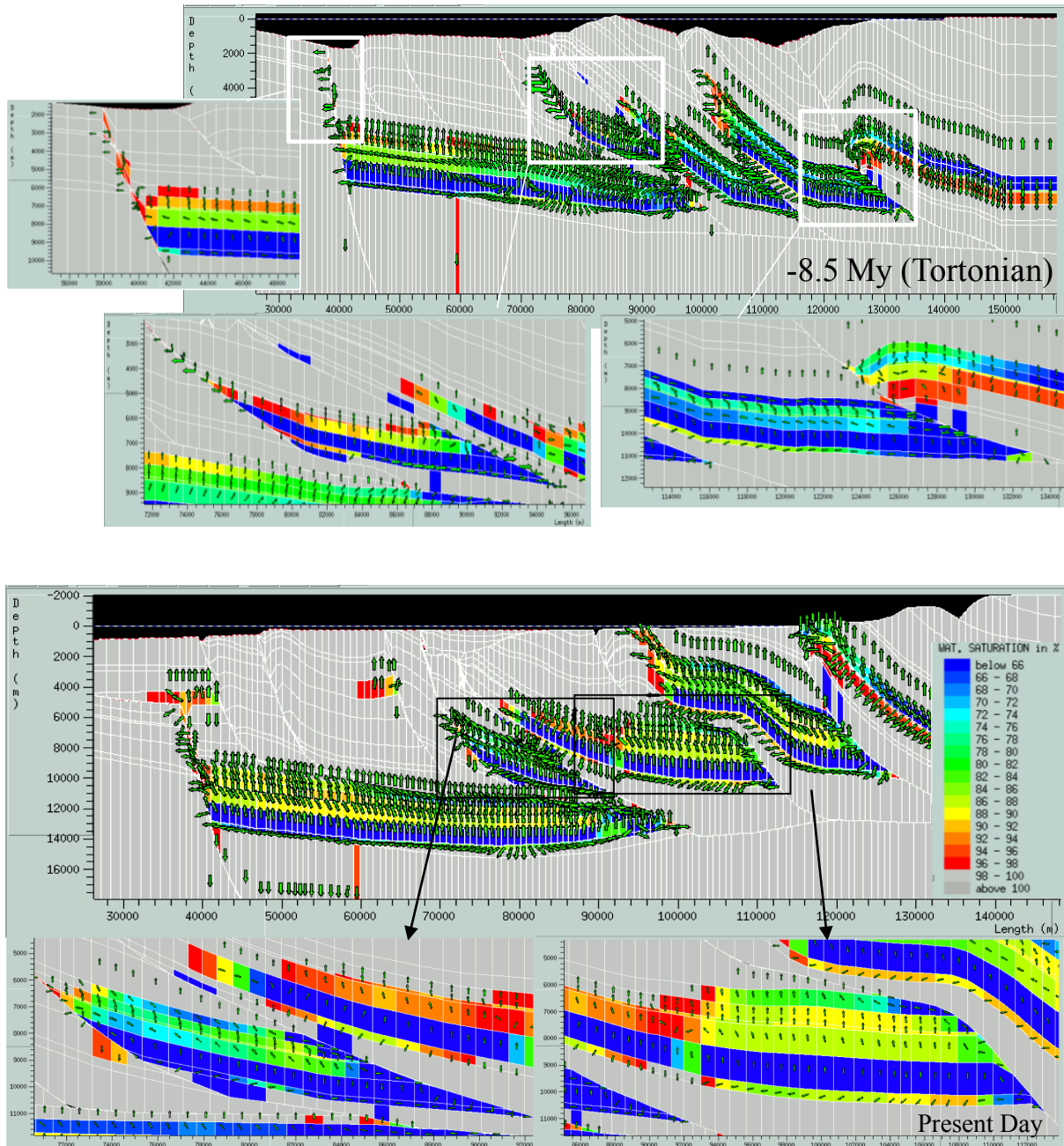


Figure 8.29. Water saturation (= oil accumulation) with the oil migration pathways from the Aquitanian to the present-day with illustrations of some detailed zones. The size of the arrows is proportional to the migration velocities, varying approximately from 0.04 to 4.5 m/My.

8.7- Conclusions

Ceres is a new tool that enables to perform basin modelling in very complex structures of the foothills, where faults and salt tectonics may constrain the petroleum system (Schneider et al., 2002). It can provide values for the velocity of the paleofluid migrations and for the paleopressures.

A recapitulative summary, which characterises each main step of the kinematic evolution, according to the overpressure distribution and the evolution of the petroleum system, is given in the Table 8.1.

Figure 8.30 summarises the main water flow pathways according to the geodynamic evolution. The following major results from the fluid flow modelling were recognised:

Timing	Kinematic evolution	Hydraulic head intensity			Overpressure (MPa)	Fracturing			Source-rock maturation
		PAD	Krm	Kel		PAD	Krm	Kel	
Aquitanian	- Flexure of the Ionian Basin								- Triassic: oil window
Burdigalian	- Thrusting of the Kruja unit - Flexure of the Ionian Basin	-	+	++		++		++	
Serravallian	- Thrusting of the Cika, Kurveleshi and Kruja unit - Burial of the Berati unit	+	+	+++	For deep: 5-15 Kremenara: 2 Kelcyra: 17	++	+	+++	- M. Cret.: oil window - Triassic: condensate gas window
Early Tortonian	- Out-of-sequence development of the Berati unit - Tectonic subsidence of the Kurveleshi unit	++	++	++		+		+	- M. Cret.: condensate/wet gas window - Triassic (deep level): dry gas window; (shallow level): oil window
Tortonian	- Maximum shortening - Important subsidence in the foreland - Uplift and erosion of the most internal belts	+++	++	-	For deep: 25	+++	+	-	- Triassic (deep level): dry gas window; (shallow level): oil window
Messinian / Pliocene	- Increase of the flexure in the foreland - Activation of the compressive structures in the foreland - Erosion of the upper part of the Kruja unit	+++	+	-	For deep: 40 Kremenara: 6	+++	+		- M. Cret.: condensate/wet gas window to overmature - Triassic (deep level): dry gas window; (shallow level): oil window
Present-day	- Erosion of the Oligocene flysch, causing the partial emersion of the Upper Cretaceous-Eocene reservoirs - Still active compressive structures in the foreland	+++	-	-		+++	-		- Triassic (foreland): overmature - Tortonian shale: oil window

Table 8.1. Characterisation of the main steps of the deformation. PAD, Krm and Kel refer to the three main studied areas, which are respectively the Peri-Adriatic Depression, Kremenara and Kelcyra.

(1) The water fluid migrations are dominantly vertical until the Burdigalian (stage 1) and consist of compaction-driven dewatering of the sediments. The beginning of the horizontal compression (stage 2) causes the increase of the fluid velocity and development of main thrusts, which act as fluid barriers, since evaporites constitute the main décollement horizons. From this stage onward, deep sourced-fluid flow driven by compaction, including vertical and horizontal components, governs the fluid system. It migrates laterally along the stratifications with velocities averaging 50m/My (stage 3). From the Serravalian onward, some topographic reliefs emerge, allowing the infiltration of meteoric water into the system with high velocities reaching up to 1km/My (stage 4), promoting locally and largely the increase of the hydraulic head. These fluids move downward and towards the neighbored foreland and tectonic units in the direction of lower hydraulic head. The main change occurs in the Tortonian, which is characterised by a displacement of the hydraulic head from the fold-and-thrust belt towards the foreland (stage 5). From this period onward, the meteoric fluid infiltrates and migrates downward towards lower hydraulic head, i.e. deep level. The last stages are also characterised by fluid flow dominantly driven by topography in the thrust belts, but with a decreasing velocity. The foreland displays high overpressure regime, activating the pervious compressive structures and allowing lateral fluid flow to migrate towards the Sazani platform. The latter were previously sealed by the evaporitic layer of the Upper Messinian.

(2) Concerning the petroleum system, it was demonstrated that only light oil (33°API) from Mesozoic source rocks (i.e. Upper Triassic - Lower Jurassic) migrated since the Langhian onward, ultimately reaching the Upper Cretaceous–Eocene reservoir interval in Tortonian times (i.e. maximum shortening). At present, the hydrocarbons in place are biodegraded, likely due to important meteoric fluid migrations during the post-folding stage, which is in agreement with the chemistry of cemented fractures.

In a future model, it should be fruitful to simulate the gas migration and to study the possible secondary oil cracking, in order to confirm the hypothesis of the light oil migration.

(3) At present, the source rocks located in the foredeep are overmature. Due to the early uplift of the tectonic units, the Triassic and Cretaceous source rocks located in the thrust belts have still an oil potential, especially in the shallower levels. However, the main oil potential remains in the foreland, where the Tortonian shales enter recently in the oil window. Related HC are confined below the Upper Messinian evaporites, being trapped due to local impervious faults or unconformities.

Notice that many small faults, backthrusts or flower structures were simplified during the initial section creation, whereas they may account for other oil and gas reservoirs. The same comment can be made due to the simplification of the lithologies, which usually play a major role in the petroleum system, as they control lateral facies variations, unconformities and high porosity intervals, developing local reservoirs and entrapment structures. The dual porosity, which characterises the main reservoirs in the Ionian Zone, is not well represented here since only the matrix porosity is taken into account in the model. The porosity of the fractures does not enter in the simulation of the fluid migration.

Moreover, due to numerical difficulties, the secondary cracking and the gas migration could not be simulated in this project. Consequently, the evolution of the petroleum system, except the source rocks maturation and the first oil migration, is not fully representative of the actual state, occurring in the Albanides.

(4) An important result of the Ceres modelling relates to the fault permeabilities. In fact, the main generations of fluids, which were petrographically and geochemically characterised during this study, account for intense fluid-rock interaction with the Triassic evaporites, located either in diapirs (during the pre-deformational stage) or along the décollement level. According to the fluid flow modelling, the faults act principally as flow barriers during the FTB development due to the occurrence of evaporites (non-permeable), except in the foreland, where they act as fluid conduits. Ultimately, some contradictions still exist between observations and modelling results, which point towards the current limitations of the software, as local fractures and successive changes in their porosity-permeability

properties related to diagenetic processes, which

are not taken into account.

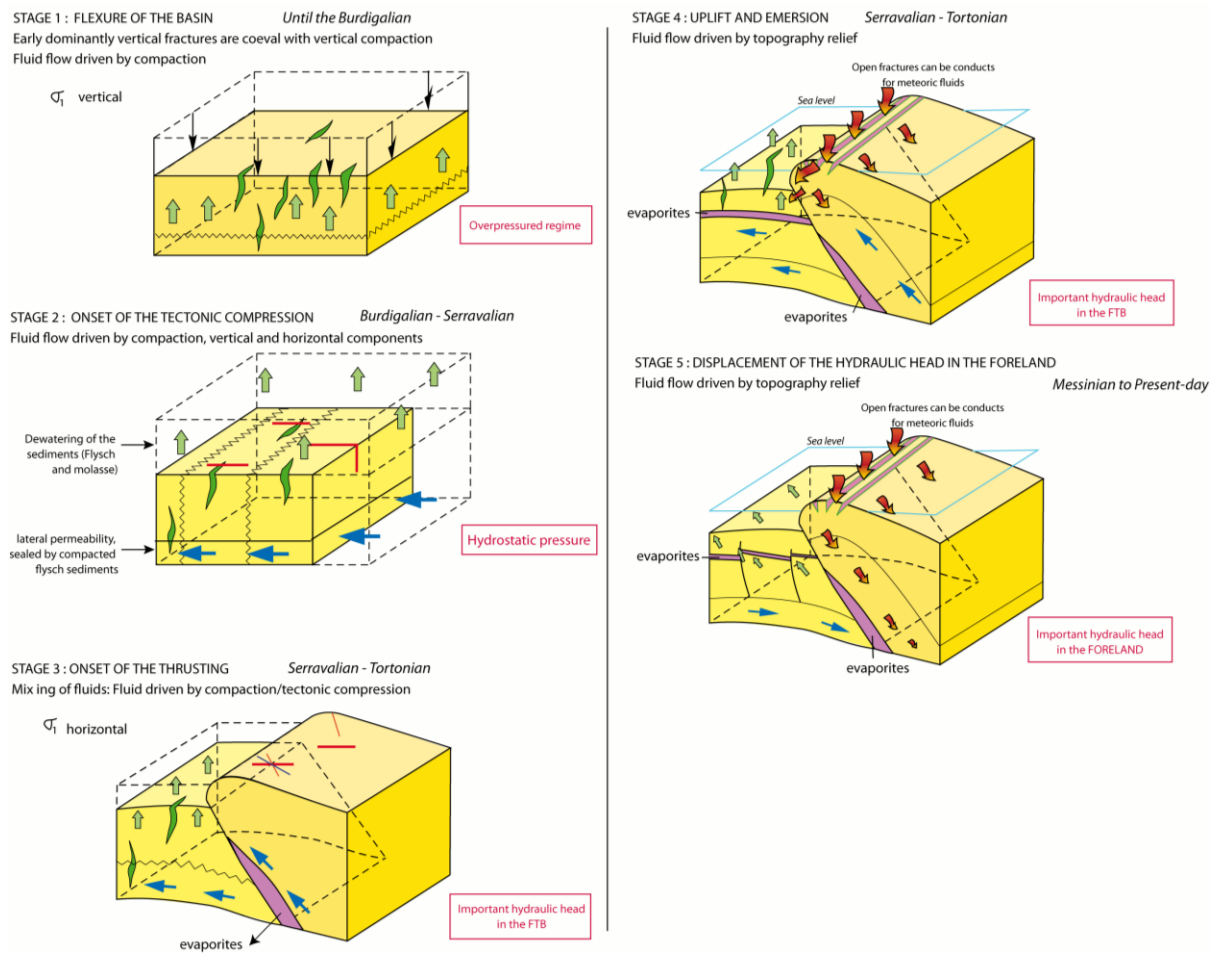


Figure 8.30. Summary of the main steps in the water flow modelling according to the tectonic evolution of the Albanides.

CHAPTER 9- Deformation / Fluid flow history

This chapter summarises the regional/local diagenetic processes encountered in the different studied areas, i.e. the Kelcyra area, the Saranda and the Kremenara anticlines, which were addressed in the previous chapters. The main differences and resemblances in diagenetic evolution are discussed and subsequently placed into the kinematic and fluid flow model, describing the evolution of the Albanides FTB (Chapter 8).

A summary of the main different diagenetic processes determined in the three studied areas is given in Figure 9. 1. The processes have been placed in the tectonic evolution of the Albanides according first to the development of stylolites

(compaction or tectonic), which mainly relate to regional sedimentological and tectonic evolution, and secondly to hydrofracturing episodes, recorded by studying infill cements in fractures and the fluid flow modelling. In fact, the fluid flow modelling allows a simulation of the evolution of the overpressure through time according to the studied locations. These overpressuring periods can be considered as good time markers to place the determined diagenetic processes in the tectonic evolution of the Albanides. In this case study, two episodes of overpressuring were recorded, which allow to precise the timing of each paragenesis.

Age	Saranda	Kremenara	Kelcyra	Events
Pre-Burdigalian	BURIAL COMPACTION FRACT1 FRACT2 + TS oriented N40° Cal-1 cement	FRACT0 Cal-1	BURIAL COMPACTION >= 800 m Fracturing FRACT1 Cal-1 cement	REGIONAL FLEXURING
	FRACT3 Tectonic Stylolites (N170°) FRACT4 Cal-2 cement	BURIAL COMPACTION FRACT1 (compression oriented N70°) Cal-2 hydraulic fracturing		
Burdigalian		FRACT2 (N110° σ1) FRACT3- FRACT4 Folding Cal-3 cement (non-luminescent cement) Emerision	FRACT1 Cal-2 (meteoric origin) < 3 km	COMPRESSIONAL STRESS oriented N110°
Langhian-Serravalian		FRACT5 (N110° σ1) 2nd burial stage Crack and seal vein cementation Cal-4	FRACT2 1-2.5 km Cal-3 cement (brecciated fragments with Dol-2, Dol-1)	1st Overpressure regime N110° compression
	Tectonic Stylolites (N110°) FRACT5 FRACT6 Cal-3 cement Max. burial (1.5 - 5.5km) Pressure solution cleavage (TS N120°) to accomodate the folding Folding	FRACT6 Hydraulic fracturing (N70° σ1) Cal-5	Cal-4 cement (fibrous calcite) FRACT3 Tectonic Stylolite (TS) Fracturing New-FRACT2 Cal-5 cement (crack-seal vein) Cal-6 cement	2nd Overpressure regime N70° compression
Tortonian	Cal-4 cement (meteoric cement) Cal-5 cement (meteoric cement)	FRACT6 Faulting of the area Cal-6	Tectonic Stylolite (TS)	THRUSTING and uplift
	FRACT7 Dissolution of the cherts	Oil migration? Overturning Cal-7 (E-W σ1)	Dol-1 cement (+ Strontianite, Barite) 6 km Dol-3 cement (+ Barite) New-FRACT2 FRACT4 Cal-7 cement (poor in Sr-content) Selective dissolution (dolomite)	OVERTHRUSTING and OUT-OF-SEQUENCE development EMERSION

Figure 9. 1. Summary of the main diagenetic processes determined in the three studied areas, placed into the tectonic evolution of the Albanides. Processes taking place in the beginning of the diagenetic history are indicated in the upper part of the figure, those that occurred at the end are given in the lower figure part.

9.1- Fracturing vs. kinematic evolution of the Albanides

During the Albanide development, three main principal compressional stresses have been

determined: the first one is oriented N110° and plays a major role in the pre-thrusting stage. The second compression is oriented N70° and occurred from the pre-orogenic stage to the post-

deformational period. It relates to the development of fold-and-thrust belts, occurring in the Ionian Zone. The last compressive stress is oriented N90° and is recorded in the post-orogenic stage at the vicinity of the transfer zone.

9.1.1- Pre-orogenic stage

The burial stage is associated by the development of burial stylolites in the Cretaceous to Eocene carbonates of the former Ionian basin. This stage relates to the regional flexure, which generates also NW-SE oriented fractures. However in the Kremenara area, which is located in the centre of the flexure, this first fracturing event predates the generation of BPS.

Subsequently, a N70°-oriented compression occurred and developed tectonic stylolites oriented N170° and fracture set oriented NE-SW. In the Kremenara anticline, this fracture set is developed synchronously to the development of BPS, suggesting a fracturing at shallow depth in between 800 and 2000 m on average. These fractures are subsequently filled by a fluid under high pressure in the Kremenara anticline, based on the occurrence of brecciated oligomict fragments in the calcite cements. Moreover the isotopic signature of these cements is rock buffered, indicating that only a limited reactivity existed between the fluid and the host-rock.

The following stage is characterised by the replay of the N110°-oriented compression, which is associated to the folding of the Kremenara anticline. In fact, this anticline shows a fold hinge, which is not in agreement with the main compression developing the folds and thrusts in the Ionian Zone. This folding stage has been placed here in the paragenesis because first the main N110° compression predates the thrusting process and secondly, because the majority of the fracture sets, such as the crack-seal or brecciated veins, determined in the Kremenara anticline, are post-folding. Then, the folding of the Kremenara developed fractures in the outer arc of the fold and is followed by the uplift of the area. This stage is characterised by the cementation of a fluid under oxic environment, suggesting the emersion of the Kremenara anticline. The latter is in agreement with the work realised in the Kremenara anticline by Breesch et al. (2007). At this period, no folding stage is recorded in the Cika unit, where only NW-SE oriented fractures are generated and filled with cement, buffered by the host-rock. Based on the isotopic analyses, an

increase of the burial is recorded in the Saranda area.

The emersion of the Kremenara area allowed the infiltration of water from the surface through the reservoir intervals. This early forebulge, i.e. high topography relief, can also be related to the occurrence of meteoric cement in the Berati belt. Large amount of fluid likely moved downward and laterally towards the eastern belt, which was possible, since no thrust fault, which acts as flow barriers, existed at that time. During its transfer, this fluid may interacted with Triassic evaporites; located in diapirs, allowing an enrichment in Sr of the diagenetic fluids.

9.1.2- Generation of overpressures

The next period is characterised by the generation of two overpressure stages, related respectively to a N110° and a N70°-oriented compression. These orientations do not differ from those described in the previous paragraph, but relate to an increase of the pore fluid pressure, associated with the two main overpressuring periods recorded in the fluid flow modelling.

The first overpressuring stage is characterised by the development of crack-seal and brecciated veins, occurring respectively in the Kremenara anticline and in the Kelcyra area. Both generations are associated to a N110°-oriented compression. The fractures are filled with calcite cement, associated with many brecciated fragments (Kelcyra), containing Triassic dolomites, phyllosilicates, ... The latter suggests that the fluid probably interacted with Triassic evaporites, in relation to fluid flow directed along the diapirs. The second episode of high pore fluid pressure is characterised by the generation of crack-seal and brecciated veins and is related to a N70° oriented compression. During this period, no overpressuring stage has been recorded in the frontal unit, i.e. the Cika belt. However, this period can be associated to the folding of the Saranda anticline.

9.1.3- Thrusting stage

The above mentioned high pore fluid regimes developed prior to the development of the thrusting stage in the Ionian Basin. The Kurveleshi and the Cika units developed during the Serravalian, under a N70°-oriented main compression. This process allows the uplift of the units and the subsequent emersion of the

Saranda anticline, allowing the infiltration of meteoric fluid into the reservoir succession. This stage is also recorded in the Kremenara area by the possible formation of transversal NW-SE faults, which compartmentalise the anticline. At this period, the Berati belt is still undeformed and only tectonic stylolites, oriented NW-SE are observed. This reflects the caterpillar type progression of tectonic deformation and fluid flow expulsion during the development of the foreland and thrust development.

9.1.4- Overthrusting and out-of-sequence development

The next main tectonic period is characterised by the overthrusting of the Kremenara and the Saranda anticlines. This period is likely associated to the out-of-sequence development of the Berati belt. Based on field observations and the crosscutting relationships between fractures, the oil migration occurring in the Kremenara anticline is associated to this stage. The development of the Berati unit from the Tortonian onwards allows the migration of deep fluids, expelled laterally towards shallower subsurface levels. This period is characterised by the circulation of sulphate-rich fluids, which were derived from Triassic evaporites located along the décollement level. The latter acted as a conduit for deep sourced fluids. This interpretation is in agreement with the result of the fluid flow modelling, suggesting deep water migration in the eastern-belts.

9.1.5- Onset of an E-W compression

The final recorded tectonic period is related to the occurrence of a N90° oriented compression and was only determined in the Kremenara anticline. This orientation of the maximum stress attests of the occurrence of a third tectonic phase. Under this regime, NE-SW transversal faults would act as sinistral strike slip faults. This is in agreement with the work of Mantovani et al. (2002), who demonstrates an E-W compression during the Late Miocene-Pliocene.

After this period, the three studied areas reached the surface, allowing the infiltration of meteoric fluids within Upper Cretaceous-Eocene carbonates. The latter implies selective dissolution of the dolomitic phases and the silica nodules as well as a recrystallisation of the carbonate matrix.

9.2- General conclusion

This thesis research illustrates an integrated workflow for carbonates reservoir characterisation, coupling kinematic, fluid characterisation and thermal evolution of a fold-and-thrust belt system and associated foreland basin, which has been developed to improve the overall knowledge of the fluid migration and the petroleum system in complex tectonic systems (overpressures, evaporitic diapirs, major erosional events, ...). Such multi-scale study, from outcrop and petrography to basin-scale fluid modelling was performed in the Albanide FTB, which constitutes a unique natural laboratory for the study of active processes in an emerged tectonic wedge. These regional integrated approaches allowed to precise the timing of deformation and erosion of the cementation and dissolution episodes, to estimate the velocity of the fluids and their evolving chemistry during migration, giving evidence of important water-rock interaction.

The main diagenetic processes are dependent on the fracture characteristics (orientations, ...) and the fluid flow, e.g. fracture opening, fluid velocity, vicinity to the main faults, allowing either large influx of exotic water or instead precluding rock interactions, ... Once the different episodes of a specific reservoir have been identified, basin modelling can help to validate possible scenarios, based on thermal evolution and faults behavior, evolving through time and to place the characterised fluids (i.e. oil and water) into the kinematic evolution of the FTB.

Bibliography

- Albouy E., Casero P., Eschard R., Barrier B., and Rudkiewicz J.L., 2003. Coupled Structural/Stratigraphic Forward Modeling in the Central Apennines. AAPG Annual Convention, May 11-14, 2003, Salt Lake City, Utah.
- Albpetrol, 1992. Petroleum exploration opportunities in Albania: 1st onshore licensing round in Albania: 13p. Fier
- Albpetrol, 1993. Petroleum exploration opportunities in Albania: 1st onshore licensing round in Albania. Publicity brochure, Western Geophysical, London.
- Albpetrol, 1995, Petroleum exploration opportunities in Albania: 1st onshore licensing round in Albania: nov., 23-26.
- Albpetrol, 1995. Recent developments in exploration and oil production and the future in the free market economy. 1965 – 1995, 30 years Oil and Gas Institute, 23-26.
- Aliaj Sh., 1987. On some fundamental aspects of the structural evolution of the outer zone of the Albanides. *Bull. Geol. Sci.* 4, 2–11 (in Albanian with English abstract).
- Allen P.A., and Allen J.R., 1990. *Basin Analysis: Principles and Applications*. Blackwell Scientific Publications, Cambridge, 451 pp.
- Anderson T.F., and Arthur M.A., 1983. Stable isotopes of oxygen and carbon and their application to sedimentologic and paleoenvironmental problems. In: Arthur, M.A., Anderson, T.F., Kaplan, I.R., Veizer, J., and Land, L.S. (Editors), *Stables isotopes in sedimentary geology*, Volume 10, Columbia, SEPM Short Course, 1-15.
- Andrews L.M., and Railsback L.B., 1997. Controls on stylolite development: Morphologic, lithologic, and temporal evidence from bedding-parallel and transverse stylolites from the U.S. Appalachians. *Journ. Geol.*, 105, 59-73.
- Ardic C., 1998. Quantitative Basin Modeling, Hydrocarbon Generation and Migration History of the Moose Mountain Area, Rocky Mountain Foothills, Alberta. PhD Thesis, Univ. Calgary.
- Bakiaj H., and Bega Z., 1992. Lushnje-Elbasan transversal fault as an important feature of the external Albanides- an interpretation. 4th EAPG Conf. and Tech. Exhibition, Paris.
- Banner J.L., 1995. Application of the Trace-Element and Isotope Geochemistry of Strontium to studies of Carbonate Diagenesis. *Sedimentology*, 42, 5, 805-824.
- Barker C.E., 1986. Notes on cathodoluminescence microscopy using the technosyn stage, and a bibliography of applied cathodoluminescence. USGS Microfiche, I. 19, 76,86-85.
- Barnaby R.J., and Rimstidt J.D., 1989. Redox conditions of calcite cementation interpreted from Mn and Fe contents of authigenic calcites. *GSA Bull.* 101, 795-804.
- Barrier L., Albouy E., Guri S., Rudkiewicz J.L., Bonjakes S., Muska K., and Eschard R., 2005. Coupled structural and sedimentary mass balances in the Central Albanides. Soc. Géol. de France, Soc. Geol. España, ILP Conference, Thrustbelts and foreland basins, Paris, December 2005, Abs., 47-49.
- Barrier L., Guri S., Albouy E., Bonjakes S., Rudkiewicz J.L., Muska K., and Eschard R., 2003. Tectonique et sédimentation dans les Albanides centrales. Intern IFP report, IFP-RB30, QKSHH, 55p.
- Bathurst R.G.C., 1971. Carbonate sediments and their diagenesis. In: *Developments in Sedimentology*, 12, Elsevier, Amsterdam, p. 620.
- Baudin F., Dercourt J., Herbin J.P., and Lachkar G., 1988. Le Lias supérieur de la zone ionienne (Grèce) : une sédimentation riche en carbone organique. Paris, *Comptes rendus à l'Académie des Sciences*, II, 307, 985-990.
- Baudin F., Herbin J.P., and Vandenbroucke M., 1990. Mapping and geochemical characterisation of the Toarcian organic matter in the Mediterranean Tethys and Middle East, *Organic Geochemistry*, 16, 677-687.

- Baudin F., Herbin J.P., Bassoulet J.P., Dercourt J., Lachkar G., Manivit H., and Renard M., 1989. Distribution of organic matter during the Toarcian in the Mediterranean Tethys and Middle East. In: A. Huc, ed., *Deposition of organic facies*, AAPG Studies in Geology, 30, 73-91.
- Bergbauer S., and Pollard D.D., 2004. A new conceptual fold-fracture model including pre-folding joints, based on the Emigrant Gap anticline, Wyoming, Geological Society of America Bulletin, 116, 294-307.
- Billi A., Samvini F., and Storti F., 2003. The damage zone-fault core transition in carbonate rocks: implications for fault growth, structure and permeability. *Journal of Structural Geology*, 25, 1779-1794.
- Bodnar R.J., and Bethke P.M., 1984. Systematic of stretching in fluid inclusions -1 : Fluorite and sphalerite at 1 atmosphere confining pressure. *Econ. Geol.*, 79, 141-161.
- Bodnar R.J., 1993. Revised equation and table for determining the freezing-point depression of H₂O-NaCl solutions. *Geochimica et Cosmochimica Acta*, 57, 3, 683-684.
- Boggs Jr S., and Krinsley D., 2006. *Application of Cathodoluminescence Imaging to the Study of Sedimentary Rocks*. New York, Cambridge University Press, 165 p.
- Boles J.R., and Franks S.G., 1979. Clay diagenesis in Wilcox sandstones of Southwest Texas; implications of smectite diagenesis on sandstone cementation. *Journal of Sedimentary Research*, 49, 1, 55-70.
- Bons P.D., 2000. The formation of veins and their microstructures. In: Jessell, M.W. and Urai, J.L., Editors, 2000. *Stress, Strain and Structure: A Volume in Honour of W.D. Means*. *Journal of the Virtual Explorer* vol. 2.
- Bouma A.H., 1962. *Sedimentology of some Flysch deposits: A graphic approach to facies interpretation*. Elsevier, 168 p.
- Bradbury H.J., and Woodwell G.R., 1987. Ancient fluid flow within foreland terrains, in: *Fluid Flow in Sedimentary Basins and Aquifers*, Goff, J.C., and Williams, B.P.J, eds., Geological Society Special Publication 34, 87-102.
- Brand U., 1991. Strontium isotope diagenesis of biogenic aragonite and low-Mg calcite. *Geochimica et Cosmochimica Acta* 55, 505-513.
- Breesch L., Swennen R., and Vincent B., 2007. Fluid flow reconstruction in hanging and footwall carbonates : Compartmentalization by Cenozoic reverse faulting in the Northern Oman Mountains (UAE). *Marine and Petroleum Geology*, in press.
- Breesch L., Swennen R., Dewever B., and Mezini A., 2007. Deposition and diagenesis of carbonate conglomerates in the Kremenara anticline, Albania: a paragenetic time marker in the Albanian foreland fold-and-thrust belt. *Sedimentology*, 54, 483-496.
- Bretan P., Yielding G., and Jones H., 2003. Using calibrated shale gouge ratio to estimate hydrocarbon column heights. *AAPG Bulletin*, 87, 397-413.
- Brown A.A., 2003. Capillary pressure and fault sealing. *American Association of Petroleum Geologists Bulletin*, 87, 381-396.
- Burke W.H., Denison R.E., Hetherington E.A., Koepnick R.B., Nelson H.F., and Otto J.B., 1982. Variation of seawater Sr⁸⁷/Sr⁸⁶ throughout Phanerozoic time. *Geology*, 10, 516-519.
- Burns S.J., and Baker P.A., 1987. A geochemical study of dolomite in the Monterey Formation, California: *Journal of Sedimentary Petrology*, 57, 128-139.
- Cazenave S., Duttine M., Villeneuve G., Chapoulie R., and Bechtel F., 2003. Cathodoluminescence orange (620nm) de la calcite. I. Rôle du manganèse et du fer. *Annales de Chimie Science des Materiaux*, 28, 1, 135-147.
- Cazzola C., and Soudet H.J., 1993. Facies and reservoir characterization of Cretaceous-Eocene turbidites in the Northern Adriatic, in AM Spenser ed., *Generation, Accumulation and Production of Europe's Hydrocarbon III: Eur. Assoc. Petrol., Geosciences*, 191-207.

- Cermak V., Krest M., Kucerova L., Safanda J., Frasher A., Kapedani N., Lico R. and Cano D., 1996. Heat flow in Albania. *Geothermics*, 25, 1, 91-102.
- Chaftez H.S., 1972. Surface diagenesis of limestone. *Journal of Sedimentary Petrology*, 42, 325-329.
- Collaku A., Cadet J.-P., Melo V., Bonneau M., 1990. Sur l'allochtonie des Albanaises : mise en évidence de fenêtres à l'arrière de la nappe ophiolitique de la Mirdita (Albanie). *C.R. Acad. Sci. Paris*, 2, 311, 1251-1258.
- Connolly J.A.D., 1990. Calculation of multivariable phase diagrams: an algorithm based on generalized thermodynamics. *American Journal of Science*, 290, 666-718.
- Cooper M., 1992. The analysis of fracture systems in subsurface thrust structures from the foothills of the Canadian Rockies. In : K.R. McClay, Editor, *Thrust Tectonics*, Chapman and Hall, London, 391-405.
- Cooper S.P., Goodwin L.B., and Lorenz J.C., 2006. Fracture and fault patterns associated with basement-cored anticlines: The example of Teapot Dome, Wyoming. *AAPG Bulletin*, 90, 12, 1903-1920.
- Cox S.F., 1987. Antitaxial crack-seal microstructures and their relationship to displacement paths. *Journal of Structural Geology*, 97, 779-787.
- Curi F., 1993. Oil generation and accumulation in the Albanides Ionian Basin. In: *Generation, Accumulation and Production of Europe's Hydrocarbons III*, Spencer A.M. (ed.), Special publication of the European Association of Petroleum Geoscientists, 3, 281-293.
- Dalipi H., Kondo A., Pejo I., Ikonomi J., and Mecaj B., 1971. Stratigraphy of the deposits of the Mesozoic in southern and western Albania (Outer Albanides). *Nafta* 22, 227-253; Zagreb.
- Danelian T., De Wever P., and Vrielynck B., 1986. Datations nouvelles fondées sur les faunes de Radiolaires de la série jurassique des Schistes à Posidonies (zone ionienne, Epire, Grèce). *Revue de Paléobiologie*, Genève, 5, 1, 37-41.
- De Paola N., Collettini C., Trippetta F., Barchi M.R., and Minelli G., 2007. A mechanical model for complex fault patterns induced by evaporite dehydration and cyclic changes in fluid pressure. *Journal of Structural Geology*, 29, 1573-1584.
- Denison R.E., Koepnick R.B., Fletcher A., Howell M.W., and Callaway W.S., 1994. Criteria for the retention of original seawater $^{87}\text{Sr}/^{86}\text{Sr}$ in ancient shelf limestones. *Chem. Geol. (Isotope Geoscience Section)*, 112, 131-143.
- Dercourt J., Ricou L.E., and Vrielynck B., 1993. (Eds.) *Atlas Tethys Palaeoenvironmental Maps*, Beicip-Franlab.
- Dercourt J., Zonenshain L.P., Ricou L.E., Kazmin V.G., Le Pichon X et al., 1986. Geological evolution of the Tethys belt from the Atlantic to the Pamirs since the Lias. *Tectonophysics*, 123, 241-315.
- Dercourt J., et al., 1980. Les zones externes de l'édifice Hellénique. In: Dercourt, J. et al., (Eds.), *Géologie des Pays Européens*, 26th Int. Geology Congress, Paris. Dunod, Paris, 361-371.
- Deweever B., Breesch L., Mezini A., and Swennen R., 2007. Sedimentological and marine eogenetic control on porosity distribution in Upper Cretaceous carbonate turbidites (central Albania). *Sedimentology*, 54, 2, 243-264.
- Dickson A.D., Smalley P.C., Raheim A., and Stijfhoorn D.E., 1990. Intracrystalline carbon and oxygen isotope variations in calcite revealed by laser microsampling. *Geology*, 18, 809-811.
- Dickson J.A.D., 1965. A modified staining technique for carbonates in thin section. *Nature*, 205, 587.
- Dickson J.A.D., 1966. Carbonate identification and genesis as revealed by staining. *Journal of Sedimentary Petrology*, 36, 491-505.
- Dimitrakopoulos R., and Muehlenbachs K., 1987. Biodegradation of petroleum as a source of ^{13}C enriched carbon dioxide in the formation of carbonate cement. *Chemical Geology (Isotope Geoscience Section)*, 65, 283-291.

- Drivet E., and Mountjoy E.W., 1997. Dolomitization of the Leduc Formation (Upper Devonian), southern Rimbey-Meadowbrook Reef Trend, Alberta. *Journal of Sedimentary Research*, 67, 411-423.
- Duggan J.P., Mountjoy E.W., and Stasiuk L.D., 2001. Fault-controlled dolomitisation at Swans Hills Simonette oil field (Devonian), deep basin west-central Alberta, Canada. *Sedimentology*, 48, 301-323.
- Dulaj A., and Basha M., 1998. Genetic Relations of Hydrocarbons in the central part of Kurveleshi belt and northern part of the Cika belt, Albania. Paper 4-21 presented at the 60th EAGE Conference and Technical Exhibition, Leipzig, June.
- Elderfield H., 1986. Strontium Isotope Stratigraphy. *Palaeogeography Palaeoclimatology Palaeoecology*, 57(1), 71-90.
- Evans E.H., Day J.A., Palmer C.D., Price W.J., Smith C.M.M., and Tyson J.F., 2006. Atomic spectrometry update. Advances in atomic emission, absorption and fluorescence spectrometry and related techniques. *Journal of Analytical Atomic Spectrometry*, 21, 1-34.
- Ferket H., 2004. Sedimentology, diagenesis and fluid flow reconstruction in the Laramide fold-and-thrust belt of Eastern Mexico (Cordoba platform): implications for petroleum exploration. PhD Thesis, K.U.Leuven, 281 p.
- Ferrill D.A., Morris P., Evans M.A., Burkhard M., Groshong R.H., and Onasch C.M., 2004. Calcite twin morphology: a low-temperature deformation geothermometer. *J. Struct. Geol.*, 26, 8, 1521-1529.
- Ferrill D.A., and Groshong Jr. R.H., 1993. Kinematic model for the curvature of the northern Subalpine Chain, France. *J. Struct. Geol.*, 15, 523-541.
- Ferrini V., Martarelli L., De Vito C., Cina A., and Deda T., 2003. The Koman Dawsonite and Realgar-Orpiment deposit, North-eastern Albania: Inferences on processes of formation. *The Canadian Mineralogist*, 41, 413-427.
- Flores G., Pieri M., Sestini G., 1991. Geodynamic history and petroleum habitats of the SE Adriatic region. In: Spencer AM (ed), Generation, accumulation and production of Europe's hydrocarbons. Spec. Publ. EAPG 1. Oxford University Press, Oxford, 389-398.
- Frank D., and Arthur M.A., 1999. Tectonic forcings of Maastrichtian ocean-climate evolution. *Paleoceanography* 14, 103-117.
- Fraseri A., 2005. Geothermal regime and hydrocarbon generation in the Albanides. *Petroleum Geoscience*, 11, 347-352.
- Fraseri A., Kapedani N., Lico R., Canga B., and Jareci E., 1995. Geothermy of external Albanides. Symposium ALBPETROL, November 1995.
- Fraseri A., Nishani P., Bushati S., Hyseni A., 1996. Relationship between tectonic zone of the Albanides, based on results of geophysical studies. In: Ziegler, P.A., Horwath, F. (Eds.), Peri-Tethys Memoir 2: Structure and Prospects of Alpine Basins and Forelands. Mem. Musee Hist. Nat. Paris, 170, 485-511.
- Friedman I., and O'Neil J.R., 1977. Compilation of stable isotope fractionation factors of geochemical interest. In: Fleischer, M. (Editor), Data of Geochemistry. United States Geol. Survey Prof. Paper, 440, 1-12.
- Gealey W.K., 1988. Plate tectonic evolution of the Mediterranean-Middle East region. *Tectonophysics*, 155, 285-306.
- Gibbs A., 1983. Balanced cross-section construction from seismic sections in the areas of extensional tectonics, *Journal of Structural Geology*, 5, 153-160.
- Given R.K., and Wilkinson B.H., 1985. Kinetic control of morphology composition and mineralogy of abiotic sedimentary carbonates. *Journal of Sedimentary Petrology*, 55, 109-119.
- Godfroid J., 2007. Sedimentologie en diagenese van Boven-Krijt platform carbonaatgesteenten in de Kruja zone (Kruja, Albanië). Master project, K.U.Leuven.
- Goldstein R.H., 2001. Fluid inclusions in sedimentary and diagenetic systems. *Lithos*, 55, 159-193.

- Gotze J., Plotze M., and Habermann D., 2001. Origin, spectral characteristics and practical applications of the cathodoluminescence (CL) of quartz - a review. *Mineralogy and Petrology*, 71, 225-250.
- Granjeon D., and Joseph P., 1999. Concepts and applications of a 3D multiple lithology, diffusive model in stratigraphic modelling. In: Numerical experiments in stratigraphy, Harbaugh J.W. et al. (eds), SEPM Special Publications, 62, 197-210.
- Griggs D., and Handin J., 1960. Observations on fracture and a hypothesis of earthquakes. In: Griggs, D. and Handin, J., eds., *Rock Deformation - A Symposium*. Geol. Soc. Am. Memoir, 79, 347-373.
- Groshong Jr R.H., 1988. Low-temperature deformation mechanisms and their interpretation: *GSA Bull.* 100, 1329-1360.
- Grover G., and Read J.F., 1983. Paleoaquifer and deep burial related cements defined by regional cathodoluminescent pattern, Middle Ordovician carbonates, Virginia. *Am. Assoc. Petrol. Geol. Bull.*, 67, 1275-1303.
- Halley R.B., Pierson B.J. and Schlager W., 1984. Alternative diagenetic models for Cretaceous talus deposits, DSDP Site 536, Gulf of Mexico, in R.T. Buffler and W Schlager eds., *Init. Repts. DSDP*, 11: Washington (U.S. Govt. Printing Office), 397-408.
- Harper G.D., and Tartarotti P., 1996. Structural evolution of Upper layer, Hole 896A. In: J.C. Alt, H. Kinoshita, L.B. Stokking and P.J. Michael, Editors, *Proc. ODP, Sci. Results*, 148, Ocean Drilling Program, 245-259.
- Hendry J.P., Trewin N.H., and Fallick A.E., 1996. Low-Mg calcite marine cement in Cretaceous turbidites: Origin, spatial distribution and relationship to seawater chemistry. *Sedimentology*, 43, 5, 877-900.
- Hess J., Bender M.L., and Schilling J.G., 1986. Evolution of the ratio of strontium-87 to strontium- 86 in seawater from Cretaceous to Present. *Science*, 231, 979-984.
- Houseknecht D.W., and Hayba D.O., 1998. Modeling oil generation in the undeformed part of the Arctic National Wildlife Refuge 1002 area, in ANWR Assessment Team, ed., *The oil and gas resource potential of the Arctic National Wildlife Refuge 1002 area, Alaska: U.S. Geological Survey Open-File Report 98-34*, p. HG1-HG24.
- Hudson J.D., 1977. Stable isotopes and limestone lithification. *Journal of the Geological Society of London*, 133, 637-660.
- Ineichen G., 1934. Il petrolio in Albania. *Proceed. World Petrol. Cong.*, London 1933, I, 58-61.
- Ingle J. D., and Crouch S.R., 1988. Infrared spectroscopy. In: *Spectrochemical Analysis*. Prentice Hall Inc., Upper Saddle River, NJ., 404-436.
- Jenkyns, H.C., 1988. The Early Toarcian (Jurassic) anoxic event: Stratigraphic, sedimentary and geochemical evidence. – *Amer. J. Sci.* 288, 101-151.
- Jørgensen N.O., 1987. Oxygen and carbon isotope compositions of Upper Cretaceous chalk from the Danish sub-basin and the North Sea Central Graben. *Sedimentology*, 34, 559-570.
- Karakitsios V., 1989. Données nouvelles sur la stratigraphie des formations jurassiques de la série ionienne (Epire, Grèce). Conséquences paléogéographiques et tectoniques. *Bull. Soc. Géol. Grèce*, XXIII, 2, 59-74.
- Karakitsios V., 1990. Chronologie et géométrie de l'ouverture d'un bassin et de son inversion tectonique: le bassin ionien (Epire, Grèce). PhD Thesis, Univ. Paris VI, 300p.
- Kaufmann B., Schauer M., and Reinhold C., 1999. Concentric-zoned calcite cements of Middle Devonian carbonate mounds of the Mader Basin (eastern Anti-Atlas, Morocco) – a combined cathodoluminescence and microprobe study. *Neues Jahrbuch für Geologie und Paläontologie, Abhandlungen*, 214, 95-110.
- Kodra A., and Bushati S., 1991. Paleotectonic emplacement of the ophiolites of Mirdita zone. *Bull. Shk. Gjeol.*, 1, 99-108 (in Albanian).

- Kodra A., Gjata K., and Bakalli F., 1993. Les principales etapes de l'évolution paleogeographique et geodynamique des Albanides internes au cours du Mesozoique. *Bulletin de la Societe Geologique de France*, 164, 61-67.
- Krajcar-Bronić I., Horvatinčić N., and Obelić B., 1998. Two decades of environmental isotope records in Croatia, Reconstruction of the past and prediction of future level. *Radiocarbon*, 40(1), 399-416.
- Lacombe O., Malandain M., Vilasi N., Amrouch K., Roure F., 2008. From paleostresses to paleoburial in fold-thrust belts: Preliminary results from calcite twin analysis in the Outer Albanides. *Tectonophysics*, doi:10.1016/j.tecto.2008.10.023.
- Lajunen L.H.J., 1992. Spectrochemical Analysis by Atomic Absorption and Emission, Royal Society of Chemistry. In: Manly, R., (1995). *Environmental Analytical Chemistry*, Ch. 12., eds. F.W. Fifield and P.J. Hains, 249-79.
- Land L.S., 1980. The isotopic and trace element geochemistry of dolomite: The state of the art. In: Zenger, D.H., et al., eds., *Concepts and models of dolomitization: Society of Economic Paleontologists and Mineralogists Special Publication 28*, 87-110.
- Laubach S.E., Reed R.M., Olson J.E., Lander R.H., and Bonnell L.M., 2004. Coevolution of crack-seal texture and fracture porosity in sedimentary rocks: cathodoluminescence observations of regional fractures. *Journal of Structural Geology*, 26, 967-982.
- Lazzari A., 1964. Albania. *Encyclopedia del petrolio e del gas naturale*, Colombo, Roma, I, 190-200 (in Italian).
- Le Pichon X., and Angelier J., 1979. The Hellenic arc and trench system: a key to the neotectonic evolution of the eastern Mediterranean area. *Tectonophysics*, 60, 1-42.
- Lind I.L., 1993. Stylolites in chalk from Leg 130, Ontong Java Plateau. In: W.H. Berger, J.K. Kroenke and L.A. Mayer (Editors). *Proceedings of the Ocean Drilling Program, Scientific Results*, 130, 112-125.
- Lohmann K.C., 1988. Geochemical Patterns of Meteoric Diagenetic Systems and Their Applications to Studies of Paleokarst. In: N.P. James and P.W. Choquette (Editors), *Paleokarst*. Springer Verlag, New-York, 58-80.
- Luciani V., Giusberti L., Agnini C., Backman J., Fornaciari E., and Rio D., 2007. The Paleocene-Eocene Thermal Maximum as recorded by Tethyan planktonic foraminifera in the Forada section (northern Italy). *Marine Micropaleontology*, 64, 3-4, 189-214.
- Lula E., 2002. Sedimentpetrological study of the Cretaceous carbonates in the Kruja Zone (central and south of Albania). Master project, K.U.Leuven, 116 p.
- Machel H.G., and Burton E.A., 1991. Factors governing cathodoluminescence in calcite and dolomite, and their implications for studies of carbonate diagenesis. In: C. Barker and O.C. Kopp (Editors), *Luminescence Microscopy and spectroscopy: qualitative and quantitative applications*. Society of economic paleontologists and mineralogists short course. Society of economic paleontologists and mineralogists, Tulsa, 37-57.
- Machel H.G., Mason R.A., Mariano A.N. and Mucci A., 1991. Causes and emission of luminescence in calcite and dolomite. In: Barker, C.E. and Kopp, O.C. (eds.), *Luminescence microscopy and spectroscopy: qualitative and quantitative applications*. SEPM, 9-25.
- Macovei G., 1938. *Les gisements de pétrole : Géologie statistique, Economie, Masson et Cie*, Paris, 502p.
- Magyar B., 1982. *Guide-Lines to Planning of Atomic Spectrometric Analysis*. *Studies in Analytical Chemistry*, 4, 273p.
- Mantovani E., Albarello D., Babbucci D., Tamburelli C. and Viti M., 2002. Trench arc-back arc systems in the Mediterranean area: examples of extrusion tectonics. In: Rosenbaum G., and Lister G. S., 2002. *Reconstruction of the evolution of the Alpine-Himalayan orogeny*. *Journal of the Virtual Explorer*.

- Marfil R., Caja M.A., Tsige M., Al-Aasm I.S., Martin-Crespo T., and Salas R., 2005. Carbonate-cemented stylolites and fractures in the Upper Jurassic limestones of the Eastern Iberian Range, Spain: A record of palaeofluids composition and thermal history. *Sedimentary Geology*, 178, 237-257.
- Marku D., 1992. Oil production history in Albanian oil fields and their perspective. In: *The first onshore negotiation round*, Fier.
- Marshall D. J., 1988. *Cathodoluminescence of Geological Materials*. Boston, Unwin Hyman, 146 p.
- Matano F., Barbieri M., Di Nocera S., and Torre M., 2005. Stratigraphy and strontium geochemistry of Messinian evaporite-bearing successions of the southern Apennines foredeep, Italy: implications for the Mediterranean "salinity crisis" and regional palaeogeography. *Palaeogeography, Palaeoclimatology, Palaeoecology*, 217, 1-2, 87-114.
- Mattavelli L., Novelli L., and Anelli L., 1991. Occurrence of hydrocarbons in the Adriatic basin. In Spencer A.M., ed., *Generation, accumulation and production of Europe's hydrocarbons*, Springer. European Assoc. Petrol. Geosc., Spec. Publ. 1, Oxford, 369-380.
- Mayer-Gürr A., 1953. Albania. In: Illing C.V., ed., *The world's oil fields, The Science of Petroleum*. Oxford Univ. Press, VI, 1, 52-53.
- McArthur J.M., and Howarth R.J., 2004. Sr-isotope stratigraphy: the Phanerozoic $^{87}\text{Sr}/^{86}\text{Sr}$ -curve and explanatory notes. In: F. Gradstein, J. Ogg and A.G. Smith, Editors, *A Geological Timescale*, CUP, 7, 589 pp.
- McArthur J.M., 1994. Recent trends in strontium isotope stratigraphy. *Terra Nova* 6, 331-358.
- McArthur J.M., Kennedy W.J., Chen M., Thirlwall M.F., and Gale A.S., 1994. Strontium isotope stratigraphy for the Late Cretaceous: direct numerical calibration of the Sr-isotope curve for the U.S. Western Interior Seaway. *Palaeoceanography, Palaeoclimatology, Palaeoecology*, 108, 95-119.
- Meço S., 1988. *Konodontet dhe stratigrafia e depozitimeve paleozoike e triasike ne zonen e Korabit*. Disertacion, 359 p. Tirana.
- Meço S. and Aliaj S., 2000. *Geology of Albania. Beiträge zur Regionalen Geologie der Erde*, Gebrüder Borntraeger, Berlin, 246 p.
- Melim L.A., Westphal H., Swart P.K., Eberli G.P., and Munnecke A., 2002. Questioning carbonate diagenetic paradigms: evidence from the Neogene of the Bahamas. *Marine Geology*, 185, 27-53.
- Melo V., Aliaj Sh., Kora A., Xhomo P., Naso F., Lula K., Gjata V., and Hoxhe V., 1991b. Tectonic windows of the external zones in the eastern regions of Albanides. *Bul. Shk. Gjeol.*, 1, 21-29 (in Albanian).
- Melo V., Shallo M., Aliaj Sh., Xhomo A., and Bakia H., 1991a. Thrust and nappe tectonics in geological structure of Albanides. *Bul. Shk. Gjeol.* 1, 7-20 (in Albanian).
- Meyers W.J., 1974. Carbonate cement and stratigraphy of the Lake Valley Formation (Mississippian) Sacramento Mountains, New Mexico. *J. Sediment. Petrol.*, 44, 837-861.
- Meyers W.J., 1978. Carbonate cements: their regional distribution and interpretation in Mississippian limestones of southwest New Mexico. *Sedimentology*, 25, 371-400.
- Miller J., 1988. Cathodoluminescence microscopy. In: Tucker, M. (ed.), *Techniques in Sedimentology*. Blackwell Scientific Publications, 174-190.
- Misha V., Bandilli L., Bare V. and Xhufi C., 1999. The structure modelling and extending of the prospect targets for oil and gas in Albania territory, estimation of their prognoses. Paper presented at the Workshop 'National Program for Research and Development: Geology, Exploration and Processing of Minerals', December, Ministry of Public Economy and Privatization, Tirana.
- Moldovanyi E.P., and Lohmann K.C., 1984. Isotopic and petrographic record of

- phreatic diagenesis: Lower Cretaceous Sligo and Cupido formations. *Journal of Sedimentary Petrology*, 54, 972-985.
- Monopolis D., and Bruneton A., 1982. Ionian sea (western Greece): Its structural outline deduced from drilling and geophysical data. *Tectonophysics*, 83, 227-242.
- Moore C.H., 2001. Carbonate reservoirs: porosity evolution and diagenesis in a sequence stratigraphic framework. *Developments in sedimentology*, 55, 444 pp.
- Moorkens T.H., and Döhler M., 1994. Albania/Albanien. In: *Regional Petroleum Geology of the world, Part I* (Ed. H. Kulke), *Beträge zur Regionalen Geologie der Erde*, 21, 325-342.
- Moretti I., and Larrère M., 1989. LOCACE: Computer-Aided Construction of Balanced Geological Cross-section. *Geobyte*, 4, 1-24.
- Moretti I., Colletta B., and Vially R., 1988. Theoretical model of block rotation along circular faults. *Tectonophysics*, 153, 313-320.
- Morgan P., 1984. The thermal structure and thermal evolution of the continental lithosphere, *Phys. Chem. Earth*, 15, 107-193.
- Mucci A., and Morse J.W., 1983. The incorporation of Mg^{2+} and Sr^{2+} into calcite overgrowths: influence of growth rate and solution composition. *Geochimica et Cosmochimica Acta*, 47, 217-233.
- Muço B., 1994. Focal mechanism solutions for Albanian earthquakes for the years 1964-1988. *Tectonophysics*, 231, 311-323.
- Muço B., 1998. Twenty years seismic monitoring of induced seismicity in northern Albania. *Pure Appl. Geophys.*, 153, 151-162.
- Muska K., 2002. Thermicité, transferts et diagenèse des réservoirs dans les unités externes des Albanides (Bassin Ionien). PhD Thesis, UPMC Paris VI, IFP Report 56850, 205 p.
- Nader F., 2003. Petrographic and Geochemical Study of the Kesrouane Formation (Jurassic), Mount Lebanon: Implications on Dolomitization and Petroleum Geology. Unpublished PhD Thesis, K.U.Leuven, Leuven, 382 p.
- Nader F.H., Swennen R., and Ellam R., 2004. Reflux stratabound dolostone and hydrothermal volcanism-associated dolostone: a two-stage dolomitization model (Jurassic, Lebanon). *Sedimentology*, 51, 2, 339-360.
- Nader F.H., Swennen R., and Keppens E., 2008. Calcitization/dedolomitization of Jurassic dolostones (Lebanon): results from petrographic and sequential geochemical analyses. *Sedimentology*, 55, 5, 1467-1485.
- Nelson R.A., 1985. *Geologic Analysis of Naturally Fractured Reservoirs*. Gulf Publishing Company, Houston, Texas, 320 p.
- Nemcok M., Schamel S., and Gayer R., 2005. *Thrustbelts - Structural Architecture, Thermal Regimes and Petroleum Systems*. Cambridge University Press.
- Nickel E., 1978. The present status of cathode luminescence as a tool in sedimentology. *Mineral Science and Engineering*, 10, 73-99.
- Nicolaides S., and Wallace M.W., 1997. Pressure dissolution and cementation in an Oligotropical limestone (Clifton Formation). Otway Basin, Australia. In: *Cool water Carbonates* (Eds N.P. James and J.A.D. Clarke). *SEPM Spec. Publ.*, 56, 249-261.
- Nielsen P., Swennen R., and Keppens E., 1994. Multiple-step recrystallization within massive ancient dolomite units: an example from the Dinantian of Belgium. *Sedimentology*, 41, 467-584.
- Nieuwland D.A., Oudmayer B.C., and Valbona U., 2001. The tectonic development of Albania: explanation and prediction of structural styles. *Marine and Petroleum Geology*, 18, 161-177.
- O'Neil J.R., Clayton R.N., and Mayeda T.K., 1969. Oxygen isotope fractionation between divalent metal carbonates. *Journ. Chem. Physics*, 51, 5547-5558.
- Pagel M., Barbin V., Blanc P., and Ohnenstatter D., 2000. *Cathodoluminescence in Geosciences*. Berlin, Springer-Verlag.
- Papa A., 1970. Conceptions nouvelles sur la structure des Albanides (presentation de la

- carte tectonique de l'Albanie au 1/500 000). *Bull. Soc. Géol. France*, 7, 1096-1109.
- Papa A., and Kondo A., 1968. Reflections about the Sazani zone and its transition to the Ionian zone, *Bull. Tirana Univ., Nat. Sci.* 2, 44-47, in Albanian.
- Paulucci, G., Novelli, L., Bongiorno, D., Cesaroni, R. (1988). Deep offshore exploration in the southern Adriatic Sea.-O.T.C. (Offshore Technology Conference, Houston, Texas, May 1988) Pap. 5730, 413-421; Houston
- Petroconsultants, 1991. *Hydrocarbon Discoveries*, Petroconsultants, Londra.
- Railsback L.B., and Andrews L.M., 1995. Tectonic stylolites in the "undeformed" Cumberland Plateau of southern Tennessee. *Journal of Structural Geology*, 17, 911-915.
- Railsback L.B., 1993. Contrasting styles of chemical compaction in the Upper Pennsylvanian Dennis limestone in the Midcontinent region, USA. *Journal of Sedimentary Petrology*, 63, 61-72.
- Ramsay J.G., and Huber M.I., 1987. *The techniques of modern structural geology: v.2: Folds and fractures*: London, Academic Press, 462 p.
- Ramsay J.G., 1967. *Folding and fracturing of rocks*: McGraw-Hill Book Company, New York, 560 p.
- Ramsay J.G., 1980. The Crack-seal mechanism of rock deformation. *Nature*, 284, 135-139.
- Richter D.K., and Zinkernagel U., 1981. Zur Anwendung der Kathodolumineszenz in der Karbonatpetrographie. *Geologische Rundschau*, 70, 1276-1302.
- Rigakis N., and Karakitsios V., 1998. The source rock horizons of the Ionian basin (NW Greece). *Marine and Petroleum Geology*, 15, 593-617.
- Robertson A., and Shallo M., 2000. Mesozoic-Tertiary tectonic evolution of Albania in its regional eastern Mediterranean context. *Tectonophysics*, 316, 197-254.
- Rocher M., Lacombe O., Angelier J., Deffontaines B., and Verdier F., 2000. Cenozoic folding and faulting in the North Pyrenean Foreland (Aquitaine Basin, France): insights from combined structural and paleostress analyses. *J. Struct. Geol.*, 22, 5, 627-645.
- Roedder E., 1984. Fluid inclusions. *Mineral. Soc. Am. Rev. Mineral.*, 12, 1-644.
- Rosenbaum J., and Sheppard S.M., 1986. An isotopic study of siderites, dolomites and ankerites at high temperatures. *Geochimica Cosmochimica Acta*, 50, 1147-1150.
- Rouchy J.M., 1982. La genèse des évaporites messiniennes de Méditerranée. *Mem. Muséum Nat. Hist. Nat., serie C*, t.L.1, Paris, 267 pp.
- Roure F., and Sassi W., 1995. Kinematics of deformation and petroleum system appraisal in Neogene foreland fold-and-thrust belts. *Petroleum Geosciences*, 1, 253-269.
- Roure F., Cacas M.C., Sassi W., Swennen R., Ferket H., Van Geet M., Frizon de la Motte D., Grelaud S., Ortuno S., Jaswal T., and Muska K., 1998. Critical parameters for the appraisal of carbonate reservoirs in foothills areas. IFP-SUBTRAP report 4563-4.
- Roure F., Nazaj S., Muska K., Fili I., Cadet J.P. and Bonneau M., 2004. Kinematic evolution and petroleum systems: an appraisal of the Outer Albanides. In: McKlay, ed., *Thrust Tectonics and Hydrocarbon Systems*, AAPG Mem. 82, 24, 474-493.
- Roure F., Prenjasi E., and Xhafa Z., 1995. Petroleum Geology of the Albanian Thrust Belt. AAPG International Conference and Exhibition Nice, Post-Conference Guide-Book, 100 p.
- Roure F., Swennen R., Howell D.G., 2000. Subthrust reservoir appraisal. World Petroleum Conference, Proceedings, Calgary, Alberta, Canada.
- Roure F., Swennen R., Schneider F., Faure J.L., Ferket H., Guilhaumou N., Osadetz K., Robion Ph., and Vandeginste V., 2005. Incidence and importance of Tectonics and natural fluid migration on reservoir evolution in foreland fold-and-thrust belts. In: Brosse E. et al., eds., *Oil and Gas*

- Science and Technology, Oil and Gas Science and Technology, *Revue de l'IFP*, 60, 67-106.
- Rutter E.H., 1983. Pressure solution in nature, theory and experiment. *Journal of the Geological Society of London*, 140, 725–740
- Salvini F., and Storti F., 2004. Active-hinge-folding-related deformation and its role in hydrocarbon exploration and development - insights from HCA modeling. In: *Thrust Tectonics and Petroleum Systems*. Edited by K. R. McClay, American Association of Petroleum Geologists Memoir 82, 453-472.
- Sans M., Verge J., Gomis E., Pare J.M., Schiattarella M., Travé A., Calvet F., Santanach P., and Doucet A., 2003. Layer parallel shortening in salt-detached folds: constraint on cross-section restoration. *Tectonophysics*, 372, 85–104.
- Sassi W., and Rudkiewicz J.L., 1999. THRUSTPACK version 6.2: 2D integrated maturity studies in thrust areas. IFP internal report n° 45372, 79 p.
- Sassi W., Graham R., Gillcrust R., Adams M., and Gomez R., 2007. The impact of deformation timing on the prospectivity of the Middle Magdalena sub-thrust, Colombia. *Geological Society, London, Special Publications*, 272, 473-498.
- Sazhdanaku F., Gjoka M., Kamberi Th., and Gjini A., 1999. Geological setting of sandstone reservoirs in Kreshpan-Patos-Marinëz-Kononjë and Kuçova-Arrës-Rasë-Pekisht regions based on existing geological-geophysical field data and re-evaluation of gas and oil reserves. Paper presented at the Workshop 'National Program for Research and Development: Geology, Exploration and Processing of Minerals', December. Ministry of Public Economy and Privatization, Tirana.
- Schneider F., Devoitine H., Faille I., Flauraud E., and Willien F., 1999. A New 2D Basin Modeling Tool for HC Potential Evaluation in Faulted Area. Application to the Congo Offshore and to the Bolivian Sub Andean zone. *AAPG Hedberg Research Conference*, Colorado Spring, May 9-13.
- Schneider F., Devoitine H., Faille I., Flauraud E., and Willien F., 2002. Ceres-2D: A numerical prototype for HC potential evaluation in complex area. *Oil and Gas Science and Technology, Revue de l'IFP*, 54, 6, 607-619.
- Schneider F., Potdevin J.L., Wolf S., and Faille I., 1996. Mechanical and Chemical Compaction Model for Sedimentary Basin Simulators. *Tectonophysics*, 263, 307-317
- Schneider F., 2003. Basin modelling in complex area: Examples from eastern Venezuela and Canadian foothills. *Oil and Gas Science and Technology, Revue de l'IFP*, 58, 2, 313-324.
- Scholle P., and Arthur M.A., 1980. Carbon isotopic fluctuations in pelagic limestones: Potential stratigraphic and petroleum exploration tool. *AAPG*, 64, 67-87.
- Sedjini B., Constantinescu P., and Piperi T., 1994. Petroleum exploration in Albania, in B. Popescu, ed., *Hydrocarbons of Eastern Central Europe*, 1-28.
- Sejdini B., 1990. On the exploration and geology of oil and minerals in Albania. – Annex 1: Hydrocarbon generation potential, Ionian Zone, Kruja Zone, Krasta Zone, Tortonian and Pliocene deposits of Peri-Adriatic Depression. 18p.; Annex 2: Stratigraphy. 21p. – Symposium on hydrocarbon exploration opportunities in Central-Eastern Europe and the USSR; Petroconsultants, Geneva.
- Shackleton N.J., and Kennett J.P., 1975. Paleotemperature history of the Cenozoic and the initiation of Antarctic glaciation: oxygen and carbon isotopic analysis in DSDP sites 277, 279 and 281. *Initial Reports of the Deep Sea Drilling Project*, 29, 743-755.
- Shackleton N.J., 1986. Paleogene stable isotope events. *Paleogeogr. Paleoclim. Paleoecol.*, 57, 91-102.
- Shallo M., 1990. Ophiolitic melange and flyschoidal sediments of the Tithonian-Lower Cretaceous in Albania. *Terra Nova*, 2, 470-488.
- Shallo M., 1991. Albanian ophiolites. *Sci. Rep.*, Tirana, Albania, 247 pp. (in Albanian).

- Shallo M., 1992. Geological evolution of the Albanian ophiolite and their platform periphery. *Geol. Rundsch*, 81, 681-694.
- Shepherd T.J., Rankin A.H. and Alderton D.H.M., 1985. A practical guide to fluid inclusions studies, Blackie, London.
- Sorel D., Bizon G., Aliaj S., and Hasani L., 1991. Essai de synthèse sur l'âge et la durée des phases compressive des Hellénides externes (Grèce nord-occidentale et Albanie), depuis le Miocène. *Bull. Soc. Géol. France*.
- Speranza F., Islami I., Kissel C., and Hyseni A., 1995. Paleomagnetic evidence for Cenozoic clockwise rotation of the external Albanides. *Earth and Planetary Sc. Letters*, 129, 121-134.
- Stearns D.W., and Friedman M., 1972. Reservoirs in fractured rock. In: King R.E., Editor, 1972. Stratigraphic oil and gas fields classification, exploration methods and case histories. AAPG Memoir 16, 82-106.
- Stearns D.W., 1968. Certain aspects of fracture in naturally deformed rocks. In: Reicher, R. E., (Ed.), National Science Foundation Advanced Science Seminar in Rock Mechanics. Air Force Cambridge Research Laboratory Special Report, 97-118.
- Suchy V., Heijlen W., Sykorova I., Muechez P., Dobes P., Hladikova J., Jackova I., Safanda J., and Zeman A., 2000. Geochemical study of calcite veins in the Silurian and Devonian of the Barrandian Basin (Czech Republic): evidence for widespread post-Variscan fluid flow in the central part of the Bohemian Massif. *Sedimentary Geology*, 131, 201-219.
- Suppe J., 1983. Geometry and kinematics of fault-bend folding. *American Journal of Science*, 283, 684-721.
- Surić M., Juračić M., Horvatinčić N. and Krajcar Bronić I., 2005. Late Pleistocene - Holocene sea-level rise and the pattern of coastal karst inundation: records from submerged speleothems along the Eastern Adriatic Coast (Croatia). *Marine Geology*, 214 (1-3), 163-175.
- Swennen R., and Dugar M., 1997. Diagenesis of Late Cretaceous to Paleocene carbonates in the Rur Valley Graben (Molenbeersel borehole, NE Belgium). *Annales de la Société Géologique du Nord*, 5, 2, 215-226.
- Swennen R., Muska K., and Roure F., 2000. Fluid circulation in the Ionian fold and thrust belt (Albania): Implications for hydrocarbon prospectivity. *Journal of Geochemical Exploration*, 69, 629-634.
- Swennen R., Van Geet M., Roure F., Müller C., Nazaj S., Mushka K., and Zaimi L., 1998. Subtrap Albanian transect across the Ionian Basin and Kremenara anticline. IFP-SUBTRAP report, n° 45635-1.
- Tagari D., 1993. Etude néotectonique et sismotectonique des Albanides: analyse des déformations et géodynamique du Langhien à l'Actuel. PhD Thesis, Paris XI, Orsay.
- Townend J., and Zoback M.D., 2000. How faulting keeps the crust strong. *Geology*, 28, 5, 399-402.
- Tozer R.S.J., Butler R.W.H., Chiappini M., Corrado S., Mazzoli S., and Speranza F., 2006. Testing thrust tectonic models at mountain fronts: where has the displacement gone ?. *Journal of the Geological Society*, London, 163, 1-14.
- Travé A., Calvet F., Sans M., Verges J., and Thirlwall M., 2000. Fluid History Related to the Alpine Compression at the Margin of the South Pyrenean Foreland Basin; the El Guix Anticline. *Tectonophysics*, 321, 1, 73-102.
- Travé A., Calvet F., Soler A., and Labaume P., 1998. Fracturing and fluid migration during Palaeogene compression and Neogene extension in the Catalan Coastal Ranges, Spain. *Sedimentology*, 45, 1063-1082.
- Tucker M.E., 1995. Techniques in sedimentology. Blackwell science, Oxford, 394 p.
- Turner F.J., Griggs D.T., and Heard H.C., 1954. Experimental deformation of calcite crystals. *Geol. Soc. Am. Bull.* 65, 883-934.
- Underhill J.R., 1988. Triassic evaporites and Plio-Quaternary diapirism in Western Greece. *Jour. Geol. Soc.*, London, 145, 269-282.

- Valbona U., and Nazaj S., 1990. Mbi ndertimin gjeologjik te rajonit Mlik-Durres-Rodon. Nafta dhe Gazi, Fieri, 45-58 (in Albanian).
- Van Geet M., 1997. Giagenetische studie van de carbonaatsequentie in de Ionische Zone (Albanië) met special aandacht voor de ontwikkeling van gefractureerde carbonaatsequenties. Master thesis, K.U.Leuven.
- Van Geet M., Swennen R., Durmishi C., Roure F., and Muchez P., 2002. Paragenesis of Cretaceous to Eocene carbonate reservoirs in the Ionian foreland fold-and-thrust belt (Albania): relation between tectonism and fluid flow. *Sedimentology*, 49, 697-718.
- Veizer J., 1983. Trace elements and isotopes in sedimentary carbonates. In: R.J. Reeder, Editor, *Carbonates. Mineralogy and Chemistry, Reviews in Mineralogy and Geochemistry*, 11, 1, 265-299.
- Veizer J., 1983b. Chemical diagenesis of carbonates: theory and application of trace element technique. In: M.A. Arthur, T.F. Anderson, I.R. Kaplan, J. Veizer and L.S. Land, Editors, *Stable Isotopes in Sedimentary Geology*, Society of Economic Palaeontologists and Mineralogists Short Course, 10, 3, 1-100.
- Veizer J., Ala D., Azmy K., Bruckschen P., Buhl D., Bruhn F., Carden G.A.F., Diener A., Ebner S., Godderis Y., Jasper T., Korte G., Pawellek F., Podlaha O.G., and Strauss K., 1999. $\text{Sr}^{87}/\text{Sr}^{86}$, $\delta^{13}\text{C}$ and $\delta^{18}\text{O}$ evolution of the Phanerozoic seawater. *Chemical Geology*, 161, 1-3, 59-88.
- Veizer J., and Hoefs J., 1976. The nature of $^{18}\text{O}/^{16}\text{O}$ and $^{13}\text{C}/^{12}\text{C}$ secular trends in sedimentary carbonate rocks. *Geochim. Cosmochim. Acta*, 40, 1387-1395.
- Velaj T., and Xhufi C., 1995. The evaporite effect on the tectonic style of the internal Ionian subzone of the Albanides. The 57th EAGE Conference and Technical exhibition, Glasgow, Abst., p. 574.
- Velaj T., 2001. Evaporites in Albania and their impact on the thrusting processes: *Journal of the Balkan Geophysical Society*, 4, 1, 9-18.
- Velaj T., Davison I., Serjani A., and Alsop I., 1999. Thrust tectonics and the role of evaporites in the Ionian Zone of the Albanides. *AAPG Bull.*, 83, 9, 1408-1425.
- Vilasi N., Malandain J., Barrier L., Callot J.P., Amrouch K., Guilhaumou N., Lacombe O., Muska K., Roure F., and Swennen R., 2009. From outcrop and petrographic studies to basin-scale fluid flow modelling: the use of the Albanian natural laboratory for carbonate reservoir characterisation. *Tectonophysics*, 474, 367-392.
- Vilasi N., Swennen R., and Roure F., 2006. Diagenesis and fracturing of Paleocene-Eocene carbonate turbidite systems in the Ionian Basin: The example of the Kelcyra area (Albania). *Journal of Geochemical Exploration*, 89, 409-413.
- Vranaj A., Shallo M., and Xhomo A., 1997. *Geology of Albania*. Tirana, Albania, 394 pp. (in Albanian).
- Walkden G.M., and Berry J.R., 1984. Syntaxial overgrowths in muddy crinoidal limestones: cathodoluminescence sheds new light on an old problem. *Sedimentology*, 31, 251-267.
- Waples D.W., Kamata H., and Suizi M., 1992a. The art of maturity modeling, Part 1: Finding a satisfactory geologic model. *American Association of Petroleum Geologists Bulletin*, 76, 31-46.
- Waples D.W., Kamata H., and Suizi M., 1992b. The art of maturity modeling, Part 2: Alternative models and sensitivity analysis. *American Association of Petroleum Geologists Bulletin*, 76, 47-66.
- Welz B., 1985. *Atomic absorption spectrometry*. VCH Verlag, Weinheim, Germany.
- Whitaker A.E., and Bartolomew M.J., 1999. Layer parallel shortening: A mechanism for determining deformation timing at the junction of the central and southern Appalachians. *American Journal of Science* 299, 238-254.
- Xhomo A., Kondo A., Papa A., Balluku I., Kanani J., Alixaj N., and Nasi V., 1971. La transgression tithono-néocomienne dans la zone ionienne d'Albanie. *Ann. Inst. Geol. Publ. Hung.*, Budapest, 2, 567-575.

- Yielding G., Øverland J.A., and Byberg G., 1999. Characterization of fault zones for reservoir modeling: An example from the Gullfaks Field, Northern North Sea, American Association of Petroleum Geologists Bulletin, 83, 925–951.
- Zappatera E., 1994. Source rock distribution model of the Periadriatic region. AAPG Bulletin, 78, 3, 333–354.
- Zelilidis A., Piper DJW., Vakalas J., Avramidis P., and Getsos K., 2003. Oil and gas plays in Albania: do equivalent plays exist in Greece? - Journal of Petroleum Geology, 26, 1, 29-48.

